Coupled Hydro-Mechanical Modelling of Gas Migration in Saturated Bentonite

Guanlong Guo

Thesis submitted to the University of Ottawa
in partial fulfillment of the requirements for the
Doctorate in Philosophy degree in Civil Engineering

Under the supervision of
Prof. Mamadou Fall

Department of Civil Engineering
Faculty of Engineering
University of Ottawa

Abstract

Bentonite is regarded as an ideal geomaterial for the engineering barrier system of a deep geological repository (DGR) where nuclear wastes are disposed, as it has several desirable properties for sealing the nuclear wastes, including low permeability, low diffusion coefficient, high adsorption capacity and proper swelling ability. Nevertheless, gas migration in saturated bentonite may undermine the sealing ability of the geomaterial. Previous experimental studies showed that the gas migration process is accompanied by complex hydromechanical (HM) behaviors, such as gas breakthrough phenomenon, development of preferential pathways, build-up of water pressure and total stress, nearly saturated state after gas injection test, localized consolidation, water exchange between clay matrix and developed fractures and self-sealing process. These experimentally observed behaviors should be properly modelled for conducting a reliable performance assessment for the geomaterial over the lifespan of DGR. In this thesis, two different coupled HM frameworks, i.e., one based on double porosity (DP) concept, referred to as coupled HM-DP framework, and the other on phase field (PF) method, referred to as coupled HM-PF framework, are proposed to simulate the gas migration process in saturated bentonite.

For the coupled HM-DP framework, the saturated bentonite is assumed as a superposition of a MAcro-Continuum (MAC) and a MIcro-Continuum (MIC). Two-phase flow is only allowed in the MAC, whereas the MIC is impermeable to both water and gas. Nevertheless, the water can transfer between the MIC and the MAC under the water pressure gap. The first coupled HM model in this framework is based on a double effective stress concept. Mechanical behaviors of the MAC and the MIC are respectively governed by Bishop-type effective stress and Terzaghi's effective stress. The model can well simulate the evolutions of both gas pressure and gas outflow rate, the water exchange between clay matrix and developed pathways, the high degree of saturation and the consolidation of clay matrix. To account for the development of preferential pathways, the damaging effect has been introduced in the framework. In this improved model, Bishop-type effective stress for the MAC is replaced by the independent stress state variables, i.e., net normal stress and suction, since using the net normal stress is

beneficial to simulating tensile failure under high gas pressure. Numerical results showed that the damage-enhanced model can well describe the effect of the development of preferential pathways on the build-up of water pressure and total stress. In addition, the proposed hysteretic models for intrinsic and relative permeabilities make the coupled HM framework more flexible to reproduce the experimental results.

To explicitly simulate the development of preferential pathways, a coupled HM-PF framework is developed by using Coussy's thermodynamic theory and the microforce balance law. The coupled HM-PF framework is implemented in the standard Finite Element Method (FEM). To avoid the pore pressure oscillation and enhance the computational efficiency, a stabilized mixed finite element, in which linear shape functions are selected for interpolating all primary variables, is adopted to discretize the whole domain. In the developed framework, swelling pressure (initial stress) is accounted for by introducing a modified strain tensor that is the sum of the strain tensor due to deformation and the strain tensor calculated from the initial stress. The numerical results showed that the developed coupled HM-PF framework can capture some important behaviors, such as the discrete pathways, localized gas flow, built-up of water pressure and total stress under constant volume condition and nearly saturated state in clay matrix. A spatially autocorrelated random field is introduced into the framework to describe the heterogeneous distribution of HM properties in bentonite. The heterogeneity is beneficial to simulating the fracture branching and the complex fracture trajectory. Numerical results showed that some factors, such as Gaussian random field, coefficient of variation, boundary condition and injection rate, have significant influences on the fracture trajectory.

At the end of the thesis, the obtained numerical results are synthesized and analyzed. Based on the analysis, the pros and cons of the developed numerical models are discussed. Corresponding to the limitations, some recommendations are proposed for future studies.

Acknowledgement

I would like to express my sincere gratitude to my supervisor, Dr. Mamadou Fall, for his continuous supports to my Ph.D study over the past five years. These supports include not only the patient guidance and the warm encouragement to my research, but also the invaluable advice on my academic career. Over the past five years, his passion and dedication to research have continuously inspired me to become a creative and rigorous researcher. These supports and inspirations will continue to benefit my future studies.

I am so grateful to Dr. Sai Vanapalli for his constructive suggestions to my research and precious supports to my career development. He is also the person who sparks my great interests in unsaturated soil mechanics that is important to my Ph.D study. My appreciation is also extended to Dr. Jon Harrington in British Geological Survey for providing the experimental data.

I would like to extend my sincere appreciation to Dr. Liang Cui, Dr. Gongda Lu, Dr. Shunchao Qi and Dr. Bin Chen for their insightful advice on my research. I am grateful to Penghai, Junping, Sada, Ken, Jianxiong and other colleagues and friends for their generous helps to my study and life in the past years.

I gratefully acknowledge China Scholarship Council and University of Ottawa for providing the financial support for my research program.

Last but not least, I deeply appreciate my parents, my brother and his families for their consistent supports and encouragements during my study in Ottawa. Without their supports and encouragements, I could not imagine how hard it will be to complete the research.

Table of Contents

List of Figures

List of Tables

List of Abbreviations

BBM	Barcelona Basic Model
CM	Corey's Model
CRM	Cubic Root Model
CSC	Constant Stress Condition
CVC	Constant Volume Condition
CZM	Cohesive Zone Model
DAM	Damage
DCF	Dilatancy-Controlled Flow
DEM	Discrete Element Method
DES	Double Effective Stress
DGR	Deep Geological Repository
DP	Double Porosity
DPM	Drucker-Prager Model
EBS	Engineering Barrier System
EFM	Embedded Fracture Model
FC	Fractured Continuum
FDEM	Finite-Discrete Element Method
FEM	Finite Element Method
FPM	Fractured Porous Media
FPZ	Fracture Process Zone
GFC	Griffith Fracture Criterion
HM	Hydro-Mechanical
LBM	Lattice Boltzmann Method
LEFM	Linear Elastic Fracture Mechanics
MAC	Macro-Continuum
MCM	Mohr-Coulomb Model
MGM	Mualem-van Genuchten Model

MIC	Micro-Continuum
MIP	Mercury Intrusion Porosimetry
ODE	Ordinary Differential Equation
PC	Porous Continuum
PDE	Partial Differential Equation
PF	Phase Field
PLM	Power Law Model
RBSN	Rigid-Body-Spring Network
RFC	Rankine-type Fracture Criterion
RVE	Representative Volume Element
THCM	Thermo-Hydro-Chemo-Mechanical
UDEC	Universal Distinct Element Code
WRC	Water Retention Curve
XFEM	Extended Finite Element Method

List of Symbols

Greek Symbols

α_B	Biot's coefficient	ϖ	Fluid phase (l liquid and g gas)
α_w	Wetting angle	ρ_s	Density of solid phase
α	Fluid component (w : water and g : gas)	$\rho_{\beta\alpha}$	Density of fluid α in subcontinuum β
β	Subcontinuum (f, p, M, m)	ρ	Averaged density of mixture
β_{sw}	Moisture swelling coefficient	σ'_{Mp1}	1st principal net normal stress in MAC
Γ_w	Water exchange term	σ'_a	ath principal effective stress
γ_c	Compressibility of capillary tube	σ'_c	Excess value of gas pressure over total stress
γ	External microscopic traction force	σ_{cr}	Critical tensile stress
ε_0	Critical tensile strain	σ_{gw}	Surface tension
ε_a	ath principal strain, $a = 1,2,3$	σ_t	Tensile strength
ε_{eq}	Equivalent strain	$\boldsymbol{\sigma}'^{\pm}$	Positive or negative part of effective stress tensor
ε_n	Strain normal to embedded fracture	$\boldsymbol{\sigma}_0$	Initial stress tensor
ε_{nl}	Nonlocal equivalent strain	$\boldsymbol{\sigma}'_C$	Constitutive stress tensor
ε_{nl}^M	Maximum nonlocal equivalent strain	$\boldsymbol{\sigma}'_n$	Net normal stress tensor
$\varepsilon_{\beta v}$	Total volumetric strain of subcontinuum β	$\boldsymbol{\sigma}'_\beta$	Effective stress for subcontinuum β
$\varepsilon_{\beta v}^{el}$	Elastic volumetric strain of β	$\boldsymbol{\sigma}$	Total stress tensor
$\varepsilon_{\beta v}^{pl}$	Plastic volumetric strain of β	$\boldsymbol{\sigma}'$	Effective stress tensor
ε_{sv}	Volumetric strain due to suction	ς	External microscopic body force
ε_v	Total volumetric strain	τ_d	Tortuosity for diffusion
$\tilde{\boldsymbol{\varepsilon}}$	Modified strain tensor	Φ_{int}	Dissipation of skeleton
$\boldsymbol{\varepsilon}_0$	Fictious initial strain tensor	φ_f	Dissipation due to fluid flow
$\boldsymbol{\varepsilon}_n$	Strain tensor corresponding to $\boldsymbol{\sigma}'_n$	φ_{th}	Dissipation due to heat transfer
$\boldsymbol{\varepsilon}_{pl}$	Plastic strain tensor	ϕ_{cr}	Critical porosity
ε_{sw}	Swelling strain	ϕ_e	Accessible porosity for diffusion
$\boldsymbol{\varepsilon}^{\boldsymbol{e}}$	Elastic strain tensor	ϕ_t	Total porosity
$\boldsymbol{\varepsilon}_\beta$	Strain tensor of subcontinuum β	ϕ_α	Volume percentage occupied by fluid α
$\boldsymbol{\varepsilon}$	Strain tensor of porous media	ϕ_β	Porosity of subcontinuum β
η	Entropy	ϕ	Porosity
κ_s	Elastic stiffness corresponding to suction	χ	Bishop's coefficient
κ_β	Slope of swelling line of subcontinuum β	Ψ_s	Free energy of skeleton
κ	Historical maximum value of ϵ_{nl}	$\psi_0^{e\pm}$	Tensile/compressive part of elastic strain energy
λ_p	Slope of normal consolidation line of PC	ψ^c	Fracture surface energy
λ	Lamé parameter	ψ_{cr}	Critical fracture energy
μ	Lamé parameter	ψ^e	Elastic strain energy
μ_α	Dynamic viscosity of fluid α	ψ_s	Free energy of solid matrix
ν	Poisson's ratio	ω_α^ϖ	Mass fraction of fluid α in phase ϖ
ξ_w	Water transfer coefficient	Ω^e	Domain of a single element

$\boldsymbol{\xi}$	Internal microscopic stress	Ω	Domain of studied domain
π_{eq}	Equivalent pore pressure	$\partial\Omega$	Boundary of studied domain
π	Internal microscopic body force		

Latin Symbols

a_c	Capillary spacing area	$\boldsymbol{k}_\beta$	Intrinsic permeability of subcontinuum β
a	Average fracture spacing	l	Characteristic length for phase field
b	Fracture aperture	M_v	Viscosity ratio
C_L	Land trapping coefficient	M	Molar mass of the gas
C_s	Storage coefficient	m, n	Shape parameter of van Genuchten model
c_w	Compressibility of water	$\boldsymbol{n}_f$	Unit normal vector to fracture
$\mathbb{C}$	Elastic compliance tensor	$\boldsymbol{n_a}$	ath principal vector, $a = 1,2,3$
$\mathbb{D}$	Elastic stiffness tensor	$\boldsymbol{n}$	Unit normal vector to the outer boundary
$\overline{D}_\alpha^\varpi$	Diffusion coefficient in free solution	$\bar{p}_\beta$	Averaged pore pressure in subcontinuum β
D_α^ϖ	Apparent diffusion coefficient	p_c	Capillary pressure
d_L^ϖ	Longitudinal dispersivity coefficient	p_c'	Pre-consolidation pressure
d_T^ϖ	Transversal dispersivity coefficient	p_{gev}	Gas entry value
$\boldsymbol{D}'^\varpi$	Dispersion tensor	p_{my}'	Mean yielding effective stress
d	Variable for damage or phase field	p_n'	Net mean stress
E	Young's modulus	p_α	Pressure of fluid α
e_v	Void ratio of porous media	p_β'	Mean effective stress for subcontinuum β
e_β	Void ratio of subcontinuum β	$p_{\beta\alpha}$	Pressure of fluid α in subcontinuum β
e	Internal energy per unit volume	$\boldsymbol{q}$	Heat flux
G_c	Critical fracture energy release rate	R	Universal gas constant
G	Shear modulus	r_T	Heat source
$\boldsymbol{g}$	Gravitational acceleration	r_c	Radius of capillary tube
h_e	Size of element	S_α	Degree of saturation of fluid α
H_M^+	Historical maximum elastic strain energy	S_e	Effective degree of saturation
h	Hysteretic parameter	S_{gi}	Gas saturation at the reversal point
H	Henry's constant	S_{gim}	Maximum gas saturation
$\boldsymbol{i}_\alpha^\varpi$	Non-advective flux of fluid α in phase ϖ	S_{gt}	Trapped gas saturation
I	Internal power of microscopic force system	S_{gtm}	Maximum trapped saturation
$\boldsymbol{J}$	Jacobian matrix	$S_{\beta\alpha}$	Degree of saturation of fluid α in subcontinuum β
K_{IC}	Fracture toughness	s	Suction
K_m^{el}	Elastic bulk modulus for MIC	T	Absolute temperature
K_m^{pl}	Plastic bulk modulus for MIC	U	Free energy of interface
K_s	Bulk modulus of solid grain	$\boldsymbol{u}$	Displacement vector

K_{sc}	Bulk modulus associated with suction	V^e	Volume occupied by a meshing element
K_α	Bulk modulus of fluid α	V_t	Total volume of porous media
K	Bulk modulus of porous media	V_β	Volume occupied by subcontinuum β
k_n	Normal stiffness of boundary	$\boldsymbol{v}_{r\beta\alpha}$	Relative velocity of fluid α in subcontinuum β
k_{rg}^d	Relative permeability on bounding drainage curve	$\boldsymbol{v}_s$	Velocity of solid phase
$k_{r\alpha}$	Relative permeability of fluid α	$\boldsymbol{v}_{\beta\alpha}$	Absolute velocity of fluid α in subcontinuum β
$\boldsymbol{k}_{ef}$	Intrinsic permeability of embedded fracture	$\boldsymbol{v}_{\beta\alpha}^D$	Darcy's velocity of fluid α
$\boldsymbol{k}_{in}$	Intrinsic permeability tensor	W	External power of microscopic force system
$\boldsymbol{k}_{mat}$	Intrinsic permeability of porous matrix	w	Fracture aperture

Chapter 1 Introduction

1.1 Background

The extensive use of nuclear power has resulted in a large volume of nuclear wastes that may pose great threats to public health and the sustainable development of nuclear power. A commonly accepted way to manage the produced nuclear wastes is to deposit them in a deep geological repository (DGR). DGR is a multi-barrier system, consisting of an engineering barrier system (EBS) and a natural geological barrier (the host rock), to prevent the lethal radionuclides from leaking into the biosphere (Jove-Colon 2013; Rodwell et al. 1999). Bentonite is considered as an ideal geomaterial for the EBS owing to several desirable properties, such as low permeability and diffusion, proper swelling ability and high adsorptive capacity (Villar and Lloret 2008; Wang et al. 2013a; Xu et al. 2017; Xu et al. 2016). Over the lifespan of the DGR, these desirable properties may be negatively affected by the thermo-hydro-chemo-mechanical (THCM) processes that take place in the DGR and the engineering barrier material. In particular, gas generation and migration may undermine the sealing ability of the geomaterial (Graham et al. 2012; Ye et al. 2014). The gas migration process in bentonite has been (is being) studied, either experimentally or numerically, in many research projects related to nuclear waste disposal, such as FORGE project, DECOVALEX-2019 and EURAD (Daniels and Harrington 2017; Garcia et al. 2020; Harrington et al. 2017b; Yu and Weetjens 2009). More details about the subtopic of DECOVALEX-2019 that is associated with gas migration in bentonite are presented in Appendix A.

Gas can be generated from several physicochemical processes, i.e., metal corrosion, water radiolysis, radioactive decay of nuclear wastes and microbial degradation (Graham et al. 2012; Ye et al. 2014; Yu and Weetjens 2009). For the Swedish KBS-3 repository concept, a copper canister with an iron lining are adopted to store the nuclear wastes. The precondition of gas generation is that the outer shell of copper canister can be penetrated by groundwater (Rodwell et al. 1999). As the copper is highly resistant to the corrosion of groundwater, the canister is expected to keep intact for a long time. At the onset of gas generation, the heat releasing stage

is expected to have finished and the barrier material to have reached full saturation (Brown 1999; Graham et al. 2012; Rodwell et al. 1999; Ye et al. 2014). Since the saturated bentonite has a high hydraulic resistance to gas flow, i.e., low intrinsic permeability and high gas entry pressure, gas pressure may reach a very high value in the canister. The highly pressurized gas may bring about complex hydromechanical (HM) processes in bentonite. Correctly evaluating the influence of the HM processes on the sealing ability of bentonite is important to conduct reliable performance assessments for DGRs.

1.2 Problem Statement

Previous studies agree that there are four basic transport mechanisms for gas migration in porous media with low permeability, including the advection/diffusion of dissolved gas, visco-capillary two-phase flow, dilatancy-controlled flow and macro-fracture flow (Marschall et al. 2005; Nagra 2008; Ye et al. 2014). The former two mechanisms only involve hydraulic processes, while the latter two mechanisms are characterized by complex coupled HM processes. Therefore, modelling the advection/diffusion of dissolved gas and visco-capillary two-phase flow is relatively straightforward once the hydraulic properties are properly determined. In contrast, more efforts are required to simulate the complex HM behaviors of dilatancy-controlled flow and macro-fracture flow. Previous experimental studies have shown that dilatancy-controlled flow is a dominant mechanism for gas migration in saturated bentonite (Graham et al. 2012; Gutiérrez-Rodrigo et al. 2015; Harrington and Horseman 2003; Harrington et al. 2017b; Horseman et al. 1999). The dilatancy-controlled gas flow is characterized by various HM behaviors, such as the gas breakthrough, development of preferential pathways, build-up of water pressure and total stress, nearly saturated state after gas injection test, localized consolidation of clay matrix and self-sealing process (Graham et al. 2012; Harrington et al. 2017b; Harrington et al. 2019b; Hoch et al. 2004; Rodwell et al. 1999). Previous numerical models mainly focused on reproducing the involved hydraulic processes, such as gas pressure at the injection boundary and gas outflow rate at the outflow boundary. In contrast, the mechanical behaviors during gas migration process were numerically studied to a less extent. Nevertheless, these mechanical behaviors are closely associated with

the evolution of preferential pathways that directly influence the sealing ability of the bentonite material. The developed pathways may serve as the preferential channels for radionuclide transport (Rodwell et al. 1999; Yu and Weetjens 2009). Therefore, coupled HM models that can describe the complex HM processes are necessary to be developed to gain a comprehensive understanding of gas transport in bentonite.

1.3 Objectives

The primary objective of this research work is to develop a series of novel and robust numerical models that can realistically simulate gas migration in saturated bentonite as well as the accompanied HM behaviors. These models are expected to enhance current understandings of gas transport processes in low permeable media and to serve as numerical tools to conduct performance assessments for DGRs. The main objective is further divided into the following sub-objectives:

(1) To review previous experimental and numerical studies on gas migration in saturated bentonite, and identify the research gaps in these numerical studies;

(2) To develop novel and robust HM models that can reliably describe the key experimentally observed behaviors, including gas breakthrough, build-up of water pressure and total stress, nearly saturated state after gas injection test, consolidation of clay matrix and water exchange between fractures and clay matrix. This sub-objective is achieved by the following two steps:

   1) To develop a coupled HM model that can differentiate the double pore structures in saturated bentonite;
   2) To extend the developed coupled HM model by accounting for damaging effect and hysteresis of intrinsic permeability.

(3) To develop novel coupled HM models that can explicitly simulate the development of preferential pathways. This objective includes the following two steps:

   1) To develop a stable and efficient coupled HM model that can explicitly simulate the fractures propagation driven by the highly pressurized gas;
   2) To examine the effects of swelling pressure and heterogeneity of HM properties

on the development of preferential pathways.

1.4 Research Approaches and Numerical Tool

1.4.1 Research Approaches

To develop novel numerical models that can simulate the gas migration process and the HM behaviors observed in experiments, a flowchart of research approaches is proposed as Figure 1.1. The specific steps that are followed by this study are listed as:

(1) A comprehensive literature review is conducted to summarize or synthesize previous numerical models for gas migration in saturated bentonite and then to identify the research gaps of previous numerical studies.

(2) Mixture theory and thermodynamic laws are employed to construct general coupled HM frameworks to simulate the complex HM behaviors during gas migration in saturated bentonite. The specific governing equations and constitutive models in the frameworks are developed based on the experimental behaviors of interest. In this thesis, double porosity (DP) concept and phase field (PF) method are incorporated into the coupled HM frameworks, thus leading to a coupled HM-DP framework and a coupled HM-PF framework.

(3) In the coupled HM-DP framework, the saturated bentonite is assumed as a superposition of two subcontinua, i.e., MAcro-Continuum (MAC) and MIcro-Continuum (MIC). The HM interactions between the two continua are explicitly modelled to describe more experimentally observed behaviors. In addition, the damaging process, the hysteresis of permeability and heterogeneous distribution of HM properties will be incorporated into the framework to enhance its ability to simulate the gas migration process.

(4) In the coupled HM-PF framework, the PF method is adopted to simulate the discrete pathways induced by the highly pressurized gas. The PF method can regularize a sharp discontinuity into a diffusive zone. Thus, it can be implemented into a standard Finite Element Method (FEM). The swelling pressure, boundary condition and heterogeneity of HM properties will be examined in terms of their effects on the gas migration process.

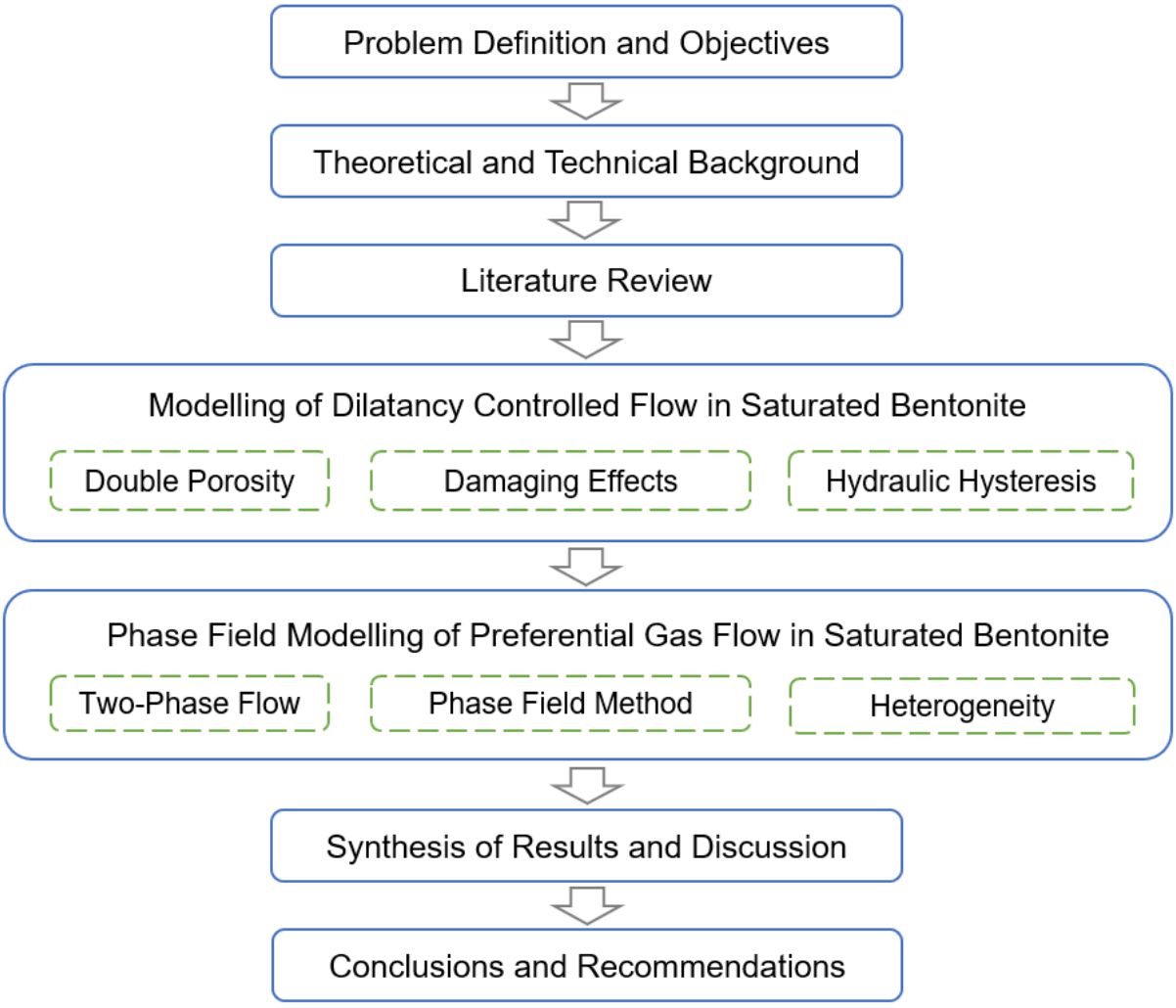

Figure 1.1 Flowchart of research approach

1.4.2 Numerical Tool

The coupled HM models developed in this thesis are implemented into commercial software, i.e., COMSOL Multiphysics. COMSOL is a FEM-based simulator that is powerful to solve complex coupled Partial Differential Equations (PDE). The PDEs for a specific physics can be easily implemented into its corresponding module embedded in COMSOL. For example, the governing equation for fluid flow in porous media is implemented in Darcy's Module, whereas the mechanical behavior is simulated by using Solid Mechanics Module. General PDEs developed by users can be achieved by using some general modules, such as Coefficient Form PDE, General Form PDE and Weak Form PDE. The temporal and spatial discretization for the coupled PDEs is automatically manipulated by the software. Time integration is achieved by using the backward differentiation formulas which is a fully implicit and adaptive

integration method. More details about the spatial and temporal discretization are given in Appendix B. There are two types of solvers that are available in COMSOL to solve the coupled PDEs, i.e., fully coupled solver and segregated solver. In this thesis, these functionalities have been employed to construct the coupled HM models for simulating gas migration in saturated bentonite.

1.5 Thesis Organization

This thesis consists of seven chapters, as shown in the flowchart in Figure 1.2. A summary of each chapter is provided as follows.

Chapter One is a general introduction on the research topic at hand, including research background, problem statement and objectives. In addition, research approaches that are used to achieve the objectives are introduced briefly.

Chapter Two includes a technical background of the current research topic and a literature review on it. The technical background includes an introduction of nuclear waste types, the basic HM properties of bentonite, the main gas generation mechanisms and the gas transport behaviors in the barrier material. Moreover, a comprehensive literature review of previous numerical models that are used to simulate gas migration in saturated bentonite is conducted. These models include hydraulic models, mechanical models and fracture propagation models. These models are carefully examined with respect to their benefits and limitations in simulating the gas migration process. Based on the discussion, some recommendations for improving the previous numerical models are provided.

Chapter Three presents a coupled HM-DP framework that is developed based on mixture theory and thermodynamic laws. Two coupled HM models are developed in this framework. In the first model, a double effective stress concept is utilized to govern the mechanical behavior of the bentonite sample during gas migration. This model can concurrently capture the dilation of the whole porous media and the consolidation of clay matrix, both of which contributes to the dilation of gas flow pathways. In addition, a simple hysteretic model for relative permeability of gas is adopted in the framework to describe the effect of gas entrapment on the gas migration process. This coupled HM framework is further extended by accounting

for damaging effect, hysteresis of intrinsic permeability and heterogeneity of HM properties. The proposed damage model has enhanced the coupled HM-DP framework to describe the build-up of water pressure and total stress. The hysteretic model makes the framework more flexible to reproduce the experimentally observed behaviors.

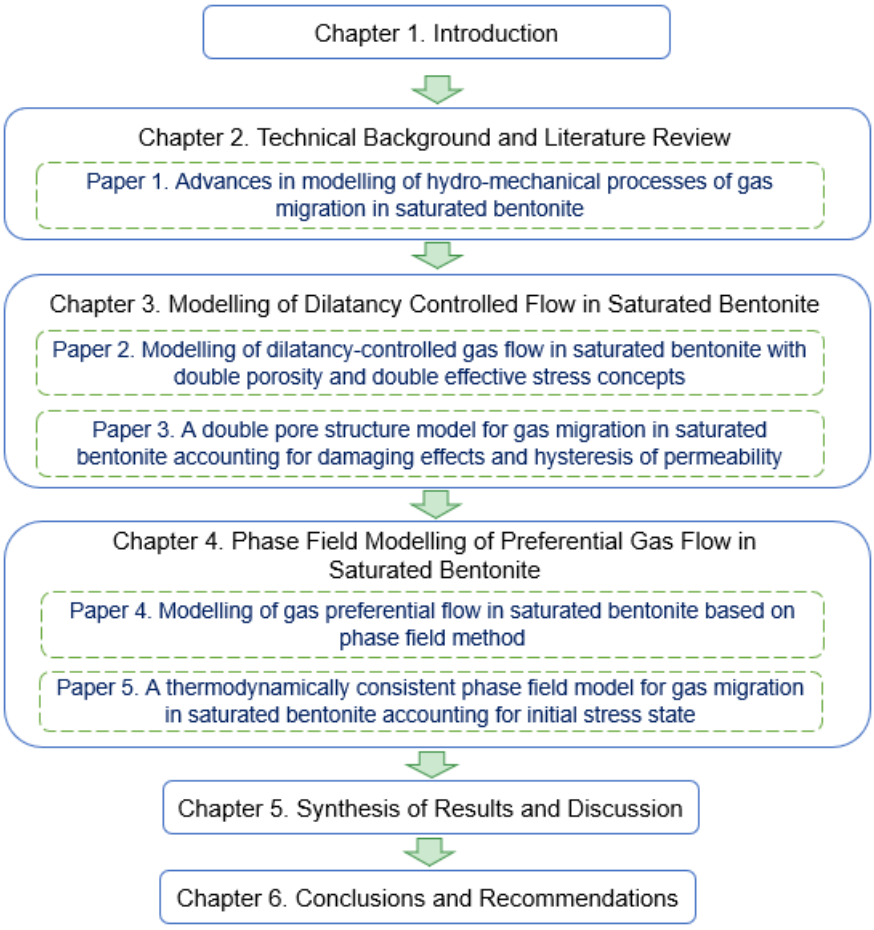

Figure 1.2 Thesis structure

Chapter Four focuses on simulating the development of preferential pathways as well as the accompanied HM behaviors. In this chapter, an efficient and stable coupled HM-PF framework is developed by using Coussy's thermodynamic theory for unsaturated porous media and microforce balance law. A spatially autocorrelated random field is introduced into the framework to simulate the heterogeneous distribution of HM properties. Numerical issues and corresponding solutions associated with the coupled HM model are discussed in detail. Several factors, such as Gaussian random field, coefficient of variation, boundary condition and injection rate, are examined in terms of their effects on the fracture trajectory and the

evolution of gas pressure. As an improvement, a modified strain tensor is introduced in the PF method to account for the effect of swelling pressure on the gas migration process.

Chapter Five synthesizes the numerical results obtained from the proposed coupled HM frameworks. Comprehensive discussions on the pros and cons of the developed HM models are conducted based on the analysis for these results. The original contributions of this thesis are presented at the end of this chapter.

Chapter Six presents the main conclusions and recommendations for future works.

Chapter 2 Technical Background and Literature Review

2.1 Introduction

This chapter covers the technical background related to gas migration process in saturated bentonite and the literature review of existing models to describe the gas migration process. In Section 2.2, the main types of nuclear waste and deep geological repository concept will be introduced. In Section 2.3, three basic HM properties (i.e. swelling pressure, permeability and water retention property) that may have important influences on the gas migration process are discussed. In Section 2.4. Gas generation mechanisms in a repository and four gas transport processes that may take place in low permeable media are briefly discussed. Moreover, some key HM behaviors observed in either laboratory tests or in-situ tests are summarized and discussed in Section 2.5. In addition, the state of the art of modelling the gas migration process is reviewed in Section 2.6 from several aspects, including hydraulic models, mechanical models and fracture propagation models. Finally, some conclusions will be drawn in Section 2.7.

2.2 Nuclear Waste Types and Repository Concept

2.2.1 Main Types of Nuclear Waste

The majority of nuclear wastes are created in nuclear power plants and military activities. In contrast, a relatively small amount of nuclear wastes results from industrial, medical and scientific activities (Miller et al. 2000). According to the level of radioactivity, the produced nuclear wastes can be classified into three categories (Fall and Nasir 2012; Freiesleben 2013; IAEA 2019; Miller et al. 2000; Shehata 2015):

High-Level Waste (HLW) includes spent fuel and the nuclear wastes created during reprocessing of spent fuel. This type of nuclear waste accounts for around 3% of the volume of all nuclear wastes from nuclear power plants, but more than 95% of the radioactivity produced by the power plant (Freiesleben 2013; IAEA 2019). During the period of radioactive decay, HLW can generate a significant amount of heat. The heat load exerted by HLW on the wall of emplacement chamber exceeds 200 W/m^2 (Freiesleben 2013).

Intermediate-Level Waste (ILW) includes resins, chemical sludge and materials contaminated during reactor decommissioning. ILW represents around 7% of the volume of all radioactive waste, but only about 4% of the total radioactivity. The heat generated by ILW is not significant. The heat load exerted by ILW on the wall of the emplacement chamber is less than 200 W/m^2. Therefore, the temperature increase cannot exceed 3K (Freiesleben 2013).

Low-Level Waste (LLW) includes paper tissues, protective clothing and materials used during normal reactor operations. LLW accounts for around 90% of the volume of all radioactive waste but only 1% of the total radioactivity (Freiesleben 2013). As LLW contains very limited amounts of long-lived radionuclides, it does not generate heat during the period of disposal.

2.2.2 Deep Geological Repository Concept

It is a common way to deposit the nuclear wastes into a DGR. A repository concept involves the type of waste, container design, emplacement techniques, backfill materials and host rocks (Rodwell et al. 1999). A representative example of a repository concept is the KBS-3 system, see Figure 2.1. The KBS-3 repository was developed by Swedish Nuclear Waste Management Company (Svensk Kärnbränslehantering AB (SKB 2011)) to dispose spent nuclear fuel. Basic processes of disposing the nuclear wastes are briefly discussed as follows based on the SKB report (Svensk Kärnbränslehantering AB (SKB 2011)). The KBS-3 repository is a multiple-barrier system, which mainly consists of a canister, buffer materials and host rocks. As shown in Figure 2.1, spent fuel pellets are first packed into metal cladding tubes that are then assembled into a unit called boiling water reactor fuel assembly. Then, the fuel assemblies are embedded into iron inserts with a 5 cm thick copper shell covered. These copper canisters are emplaced in vertical disposal holes drilled in a deposition tunnel. Bentonite clay is used to fill the space between the canister and the deposition tunnel. When all vertical holes are filled with copper canisters, the deposition tunnel is backfilled. This disposal process is repeated for every deposition tunnel until all vertical disposal holes have been filled with canisters. The tunnel system of the KBS-3 repository is constructed in a bedrock that is 400-700 m below ground surface. Finally, the main tunnels and shafts are backfilled up to the

ground surface (SKB 2011).

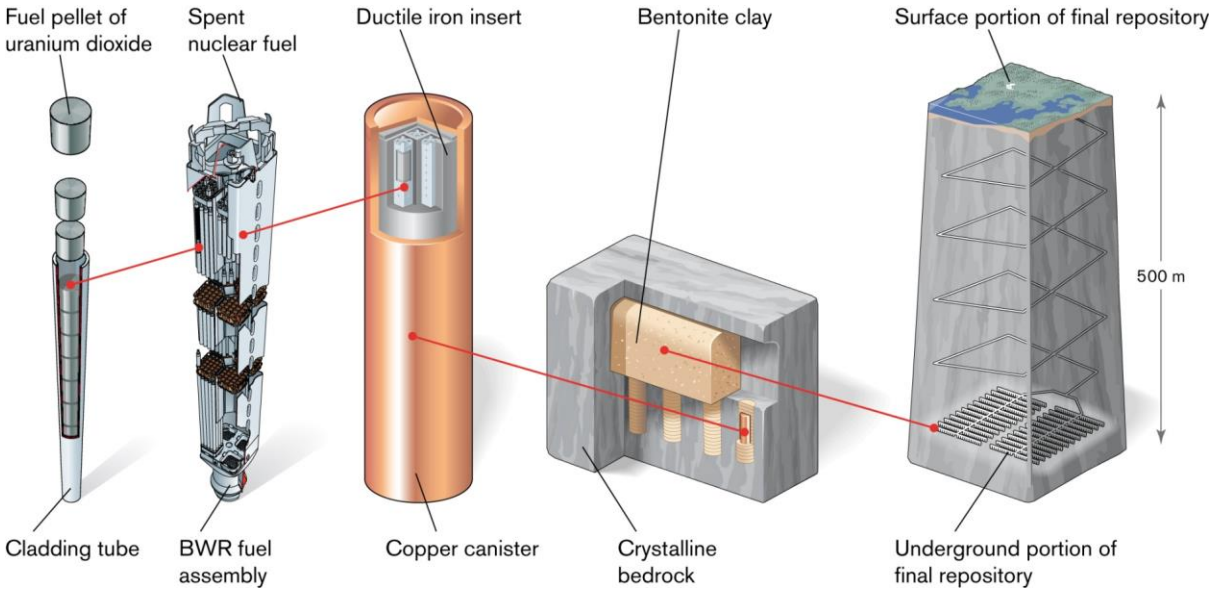

Figure 2.1 KBS-3 repository concept (SKB 2011)

2.3 Basic Hydro-Mechanical Properties of Bentonite

In this section, the HM properties of bentonite that have significant influences on the gas migration process, including swelling pressure, permeability and water retention capability, will be discussed.

2.3.1 Swelling Pressure

Previous experimental studies showed that gas initially infiltrates the saturated bentonite when the gas pressure reaches the sum of swelling pressure and porewater pressure (Graham et al. 2012; Harrington and Horseman 2003; Horseman et al. 1999). Thus, swelling pressure is an important factor controlling the gas migration process in saturated bentonite. In this section, the swelling pressure will be discussed from both physical and engineering viewpoints.

2.3.1.1 Clay-water interaction

The development of swelling pressure is a result of interactions between clay minerals and water molecules (Rodwell et al. 1999). The adsorbed water in clay minerals is mainly formed through two types of clay/water interaction, i.e. mineral surface hydration and cation hydration, (Tripathy et al. 2004; Zhu et al. 2013), see Figure 2.2. Mineral surface hydration is a physical

process that water molecules are adsorbed by mineral surfaces that are negatively charged due to isomorphous substitution. Cation hydration implies that water molecules are adsorbed by exchangeable cations embedded in clay sheets. Gibbs free energy of water molecules in the adsorbed state is less than its counterpart in a free state (Rodwell et al. 1999). As a result, water transfer occurs under the gradient of Gibbs free energy between the adsorbed water in clays and the external free water. The free water is adsorbed by the mineral surfaces or the exchangeable cations after infiltrating clay particles until an equilibrium state is reached. After adsorbing the external water molecules, the swelled clay particles tend to compress the surrounding particles. The resultant force is ultimately transmitted to rigid boundaries, thus leading to the development of swelling pressure (Rodwell et al. 1999). The swelling pressure in clays with a high proportion of montmorillonite is considered to be the effective stress to which the clay is subjected (Horseman et al. 1999; Rodwell et al. 1999).

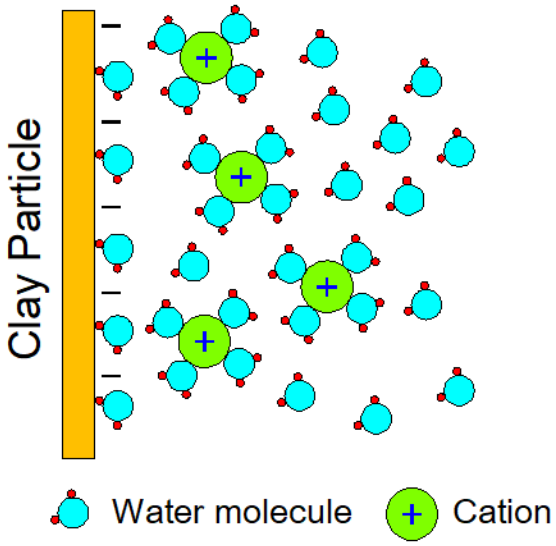

Figure 2.2 Schematic of clay-water interaction

2.3.1.2 Engineering factors

From the engineering viewpoint, the swelling pressure of bentonite is mainly influenced by dry density and water content (Villar and Lloret 2008). Under saturated condition, a higher dry density leads to a higher swelling pressure, since there are more expansive minerals per unit volume that can adsorb external water molecules. For practical purposes, the swelling pressure is generally estimated by using an exponential function of the dry density, see Figure

2.3.

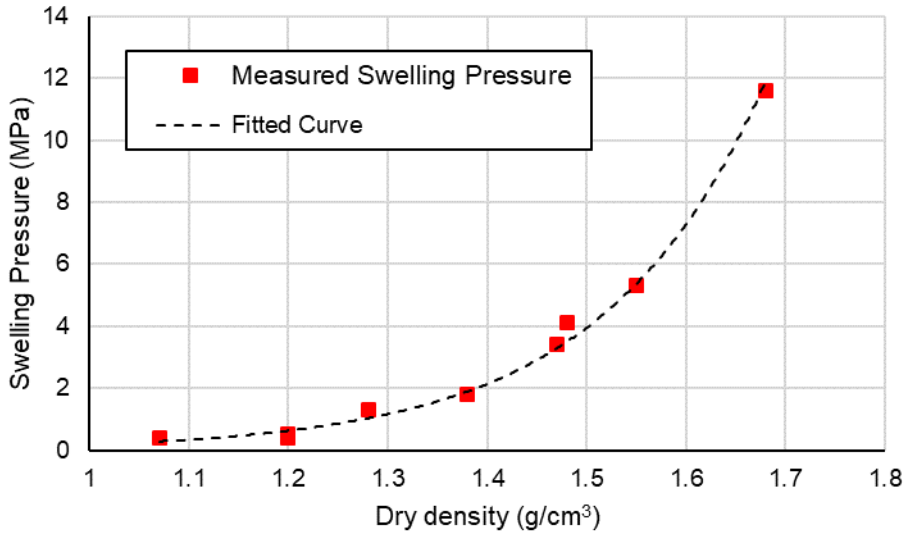

Figure 2.3 Relationship between swelling pressure and dry density of MX80 bentonite (from (Villar 2005))

In contrast, the effect of water content on the swelling pressure is more complex, as the water content significantly influences the evolution of pore structure in bentonite. It is widely accepted that unsaturated expansive soils present a bimodal pore size distribution. There are two types of pore structure in the soils, i.e., inter-aggregate pores (macro-pores) and intra-aggregate pores (micro-pores) (Gens and Alonso 1992). At low water content, hydration preferentially takes place at the surface of clay aggregates, whereas micro-pores in the aggregates are assumed to be unaffected (Cui et al. 2008; Wang et al. 2012). This process leads to the first swelling stage. With the increase of water content, the clay aggregates gradually break into smaller clay particles, causing the collapse of the inter-aggregate pores (Gens and Alonso 1992; Sánchez et al. 2016). As a result, the swelling pressure experiences a reduction trend after reaching the first peak. As the wetting process continues, clay interlayers will be hydrated. This leads to the second increase of swelling pressure until the full saturation is reached (Wang et al. 2012). Although the development of swelling pressure is a complex process during the wetting process, it was found that the final swelling pressure (at saturated state) under constant volume condition may not depend on the wetting path (Wang et al. 2012). Therefore, the swelling pressure of bentonite at saturated state is primarily controlled by the dry density (Villar and Lloret 2008).

2.3.2 Permeability

Permeability is an important property that directly controls the transport of water, gas and radionuclides in bentonite. Experimental studies have shown that the permeability of bentonite is governed by dry density, water content, pressure gradient, and type of adsorbed cation (Pusch 1980; Villar 2005; Villar et al. 2014a). This study mainly focuses on the effect of dry density and water content on the permeability. For the saturated bentonite with a high dry density, there is less void space available for fluid flow. In addition, more water molecules are adsorbed on the mineral surface, forming a thicker immobile water film. This water film further decreases the pore space for fluid flow. Thus, the bentonite with higher dry density has a lower permeability. As seen in Figure 2.4, the intrinsic permeability of Mx-80 bentonite decreases exponentially with the increase in dry density.

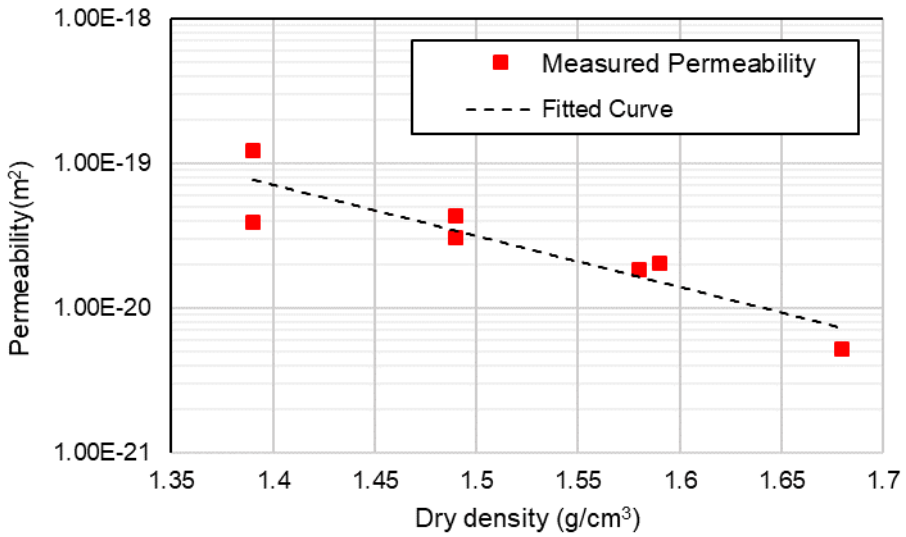

Figure 2.4 Relationship between permeability and dry density of Mx-80 bentonite (Modified from (Villar 2005))

Under unsaturated condition, the effect of water content on the permeability of expansive soils is two-fold. Firstly, water content plays an important role in the evolution of pore structure, as discussed in Section 2.3.1. The inter-aggregate pores are the main conduits for fluid flow in clays, whereas the intra-aggregate pores are much less permeable to both water and gas. Thus, the strong interaction between microstructure and macrostructure can significantly affect the intrinsic permeability. However, it is still difficult to quantitatively evaluate the influence of

pore structure on the permeability of unsaturated expansive soils. Generally, the permeability of bentonite is simply expressed as an empirical function of porosity in which the parameters are determined by model calibration (Sánchez et al. 2016). On the other hand, the water content also influences the relative permeability (Tawara et al. 2014). Mualem–van Genuchten model and power law model are widely used to describe the relationship between the relative permeability and the effective degree of saturation (Mualem 1976; Mualem 1978; van Genuchten 1980).

2.3.3 Water Retention Capability

Water retention capability is a key component that governs the two-phase flow process in porous media. Gas will infiltrate a saturated porous medium when the gas pressure exceeds the water pressure by a critical gas entry value (Vanapalli et al. 1996). Water retention curves for Mx80 bentonite are shown in Figure 2.5 in which the samples have three different dry densities (i.e. 1.5 g/cm^3, 1.65 g/cm^3, and 1.8 g/cm^3 which correspond to void ratios of 0.83, 0.66, 0.53, respectively) (Seiphoori et al. 2014).

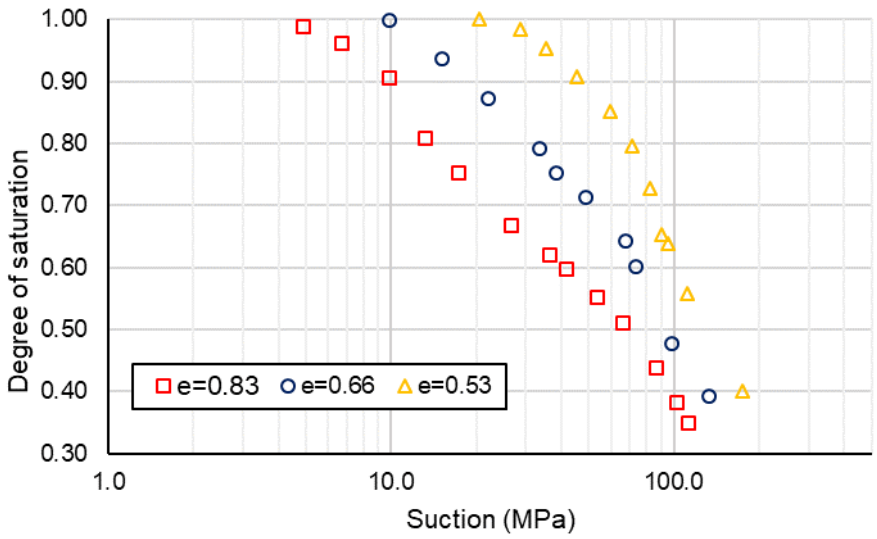

Figure 2.5 Water retention behavior of Mx80 bentonite (modified from (Seiphoori et al. 2014))

Figure 2.5 shows the gas entry value increases with the decrease of void ratio (increase of dry density). In (Seiphoori et al. 2014), the gas entry value was expressed as an exponential function of the void ratio. As discussed in Section 2.3.2, the saturated bentonite with high dry density contains more clay minerals and therefore can adsorb more water molecules, both of

which lead to a high gas entry value. As seen in Figure 2.5, the Mx80 bentonite remains almost fully saturated even under a high suction. The gas pressure that is required to infiltrate into the saturated bentonite may even exceed the local total stress to which the sample is subjected. Under such a condition, the highly pressurized gas may induce a microfracture network through which gas migrates through the bentonite. As a result, little water can be drained from the bentonite. This was widely observed in previous experimental studies, as seen in (Harrington and Horseman 2003; Harrington et al. 2017b; Horseman et al. 1999; Pusch and Forsberg 1983).

2.4 Main Gas Generation and Transport Mechanisms

2.4.1 Main Gas Generation Mechanisms

Gas generation mechanisms in repositories depend on the physicochemical environment, the disposal method and the waste type (Fall and Nasir 2012; Rodwell et al. 1999). There are three main mechanisms contributing to gas generation in repositories, including corrosion of metallic materials (e.g. wastes or packaging materials), radiolysis of water and organic materials and microbial degradation of organic wastes. The significance of the three gas generation mechanisms depends on the type of waste and the repository environment.

2.4.1.1 Corrosion of metallic materials

Corrosion of metallic materials is considered as the dominant mechanism for gas generation in almost all disposal situations (Rodwell et al. 1999). The metallic materials that can be corroded in a repository include metallic components of the disposed waste, the metallic parts of waste packages and the metallic materials for constructing the repository (Fall and Nasir 2012). Corroding agents for the metallic materials may include: (1) oxygen in the repository and the residual air in waste packages; (2) residual water in the waste, the backfill material and the packaging material; (3) the groundwater; (4) the water in the host rock (Rodwell et al. 1999). Shortly after the closure of a DGR, the whole repository is in an oxidizing environment. The free oxygen will be consumed rapidly by the corrosion of the aforementioned metallic materials (Miller et al. 2000). The chemical reactions of the corrosion processes can be formulated as

$$2\,Fe + O_2 = 2\,FeO \tag{2.1}$$

$$2\,Fe + 2\,H_2O + O_2 \rightarrow 2\,Fe(OH)_2 \tag{2.2}$$

After the exhaustion of oxygen in repositories by the aerobic corrosion processes, hydrogen is generated under the anaerobic condition. The chemical reactions for hydrogen generation are formulated as

$$Fe + 2\,H^+ \rightarrow Fe^{2+} + H_2 \tag{2.3}$$

$$Fe + 2\,H^+ + 2\,OH^- \rightarrow Fe(OH)_2 + H_2 \tag{2.4}$$

For the KBS-3 repository system, gas is initially generated when groundwater penetrates the copper shell and reacts with the iron inserts (Rodwell et al. 1999). As the copper shell is highly resistant to the corrosion of groundwater, gas generation is expected to take place thousands of years after the closure of DGR (Metcalfe et al. 2008). As a result, it is expected that the buffer material has reached a full saturated state and the heat release of nuclear wastes has been completed at the onset of gas generation (Rodwell et al. 1999; Ye et al. 2014). This is the reason why the saturated bentonite and the isothermal condition were adopted in most of previous experimental studies. However, it should be noted that the hydrothermal conditions of the buffer material at the onset of gas generation depend on the selected repository concept. In a repository for HLW with canisters that are entirely made of iron or steel, gas will be produced and transported much earlier than its counterpart in the KBS-3 repository (Rodwell et al. 1999). As a result, the thermal gradient and the unsaturated condition should be taken into account when studying, either experimentally or numerically, the gas generation and transport processes in a repository for HLW with canisters that are entirely made of iron or steel (Rodwell et al. 1999). However, this scenario has not yet been considered in previous experimental studies on this topic.

2.4.1.2 Radiolysis

Radiolysis is a radiolytic process in which chemical compounds can be decomposed by radiation. The decomposition of water by radiolysis makes the main contribution to the gas

generation of this mechanism. The amount of the generated gas linearly depends on the applied radiation dose. According to the location where the radiolysis takes place, two types of radiolysis are defined, i.e. internal radiolysis and external radiolysis (Rodwell et al. 1999). The internal radiolysis occurs in the waste and its package, whereas the external radiolysis takes place in the backfill material or the host rock (Fall and Nasir 2012). In general, the gas generated by radiolysis is not as significant as that by corrosion (Miller et al. 2000). The gas generation due to radiolysis of LLW can be neglected, since the radiation dose rate for LLW is very low. For HLW stored in containers with thin walls, the gas generation rate due to external radiolysis can reach a value that is comparable to the corrosion-induced generation rate (Rodwell et al. 1999).

2.4.1.3 Microbial degradation

There are three main prerequisites for gas generation by microbial degradation, i.e. the existence of micro-organisms in the repository, the availability of water and the presence of nutrients (Rodwell et al. 1999). In addition, the microbial activities are also influenced by several environmental factors, including temperature, pH value, oxygen supply, salinity, radiation and pressure. Considering these conditions, gas generation by microbial degradation mainly takes place in LLW repositories which contain a larger amount of organic materials (Rodwell et al. 1999). In contrast, HLW does not contain organic materials and its high radiation will inhibit the microbial activity. Therefore, the gas generation in HLW repositories due to microbial degradation is insignificant. It is generally accepted that the gas generation rate for L/ILW repositories is much higher than that for HLW repositories, since the former repositories contain more organic and metallic materials than the latter repositories (Fall and Nasir 2012; Miller et al. 2000; Rodwell et al. 1999).

2.4.2 Basic Gas Transport Mechanisms

Previous studies have shown that there are four basic transport mechanisms in porous media of low permeability, i.e., advection/diffusion of dissolved gas, visco-capillary two-phase flow, dilatancy-controlled flow and macro-fracture flow (Marschall et al. 2005). The characteristics of these four transport mechanisms depend on the properties of the buffer

material (including dry density, degree of saturation, and pore water chemistry) and boundary condition (Graham et al. 2012; Hoch et al. 2004; Rodwell et al. 1999).

2.4.2.1 Advection/diffusion of Dissolved Gas

The advection/diffusion of dissolved gas is a flow process that involves both advective and diffusive transport. Advective transport for gas is a passive transport process during which the dissolved gas carried by its host fluid is transported along with the fluid. Henry's law is used to determine the solubility of gas in the porewater, while Darcy's law to describe the water flow driven by the gradient of water pressure (Nagra 2008). By contrast, diffusive transport is an active transport process, as it is driven by the gradient of gas concentration in the porewater. This transport process is governed by Fick's and Henry's laws. The key parameters that control the advective-diffusive transport process include Henry's coefficient, diffusion coefficient, tortuosity, and accessible porosity and permeability of the porous medium (Nagra 2008; Rodwell et al. 1999). The advective-diffusive transport process is a pressure-dependent process in which the increase of gas pressure can increase the volume of dissolved gas and then enhance the advective flow (Marschall et al. 2005). However, the transport capacity of this mechanism is very low in comparison with the other three mechanisms (Nagra 2008).

2.4.2.2 Visco-capillary Two-Phase Flow

Visco-capillary two-phase flow is characterized by the process that the porewater in a porous medium is displaced by gas under the effect of viscous and capillary forces (Bear 1972; Rodwell et al. 1999). The key property that controls the two-phase flow behavior is the gas entry value which is the difference between gas pressure and water pressure that is required to displace the porewater from the initially fully saturated porous media. The gas entry value for a capillary tube is determined by the Young-Laplace equation (Laplace 1805; Young 1805):

$$p_{gev} = \frac{2\sigma_{gw}\cos\alpha_w}{r_c} \tag{2.5}$$

where p_{gev} is the gas entry value, σ_{gw} is the surface tension at the interface between gas and water, r_c is the radius of the capillary tube and α_w is the wetting angle.

Once gas enters the porous medium, the gas content is governed by the water retention model as discussed in Section 2.3.3. The fluid (gas or water) flow is described by a generalized Darcy's law. The semi-theoretical models given by (Luckner et al. 1989; Mualem 1976; van Genuchten 1980), are widely used to describe the relative permeability of water and gas. For practical use in expansive clays, the relative permeability is commonly expressed as a power function of the effective degree of saturation (Arnedo et al. 2013; Olivella and Alonso 2008). It should be noted that hysteresis is often observed in water retention curve and relative permeability model when the porous medium experiences several wetting-drying cycles. The hysteresis is associated with the pore structure and different wetting angles in advancing and receding processes (Fredlund et al. 2012). In previous models on this research topic, the hysteresis is rarely considered due to the lack of experimental data.

2.4.2.3 Dilatancy-controlled Gas Flow

Dilatancy-controlled gas flow involves strong couplings between hydraulic and mechanical process (Graham et al. 2012; Harrington et al. 2019b). Since the pore size of saturated bentonite is extremely small, the required gas pressure for gas entry may be even higher than the total stress to which the bentonite is subjected. When the gas pressure exceeds the local total stress, a series of microfractures are expected to develop. The expansion of the microfractures results from the compression of water, consolidation of clay particles and dilation of the whole sample (Rodwell 2005). Therefore, the dilatancy for this flow mechanism means the dilation of the developed microfractures. Within the microfractures, the gas entry value is substantially reduced, while the intrinsic and relative permeabilities are greatly increased. As a result, gas preferentially flows through the developed microfracture network (Graham et al. 2012). It is worth noting that due to the non-uniform distribution of stress state and HM properties, microfractures may develop locally when the gas pressure has not yet reached the global minimum principal stress (Marschall et al. 2005; Rodwell 2005). Therefore, the heterogeneous distribution of HM properties and local stress state may play an important role in the development of preferential pathways.

2.4.2.4 Macro-fracture Flow

When gas pressure exceeds the sum of the minimum principal stress and the tensile strength of the porous medium, macroscopic tensile fractures are expected to develop along the direction perpendicular to the minimum principal stress (Nagra 2008; Ye et al. 2014). This process is similar to the hydraulic fracturing process, but it is more complicated due to the capillary effect. As the fracture aperture is much larger than the pore size of surrounding porous matrix, a single gas flow is more likely to take place in the developed fractures (Marschall et al. 2005). Different from the microfractures developed during the dilatancy-controlled gas flow, the developed fractures in this mechanism are comparable to the sample size (Rodwell 2005). The occurrence of macroscopic fracturing in compacted bentonite has been validated in radial flow tests (Rodwell 2005).

2.5 Experimental Observations

The commonly used bentonite materials for gas injection tests include Mx80, FEBEX and GMZ bentonite. At present, all of the tests were performed under isothermal condition. Most of these tests were conducted on saturated bentonite under constant volume condition.

2.5.1 Gas Entry and Breakthrough

Gas breakthrough pressure is the pressure above which a significant gas outflow is observed at the downstream end of the bentonite sample. Gas entry pressure is the value at which the gas initially appears at the outflow boundary (Rodwell et al. 1999). Due to the difficulties of measuring gas entry pressure, monitoring the gas breakthrough pressure was preferred in previous experiments.

Most of laboratory and in-situ tests have demonstrated that gas initially enters the saturated bentonite when the gas pressure reaches the total stress, i.e. the sum of the swelling pressure and the back-water pressure (Graham et al. 2012; Horseman et al. 1999; Nash et al. 1998). The existence of a critical gas pressure that is comparable to the swelling pressure was also verified in (Pusch et al. 1985). As seen in Figure 2.6, the gas entry pressure is closer to the total stress, while the gas breakthrough pressure is slightly higher than the total stress. This is because a

higher gas pressure may be necessary to form an effective microfracture network to connect with the outflow filters (Graham et al. 2012; Harrington and Horseman 2003). In the LArge-scale Gas Injection Test (Lasgit) carried out at the Aspo Hard Rock Laboratory, it was also found that the gas pressure needs to reach the total stress for triggering a major gas entry event (Cuss et al. 2011). It is worth noting that the initial gas movement had been detected in the buffer material when gas pressure had not yet reached the applied stress (Cuss et al. 2014b; Cuss et al. 2011). This phenomenon may be attributed to the non-uniform distribution of the HM properties and stress state in the buffer material.

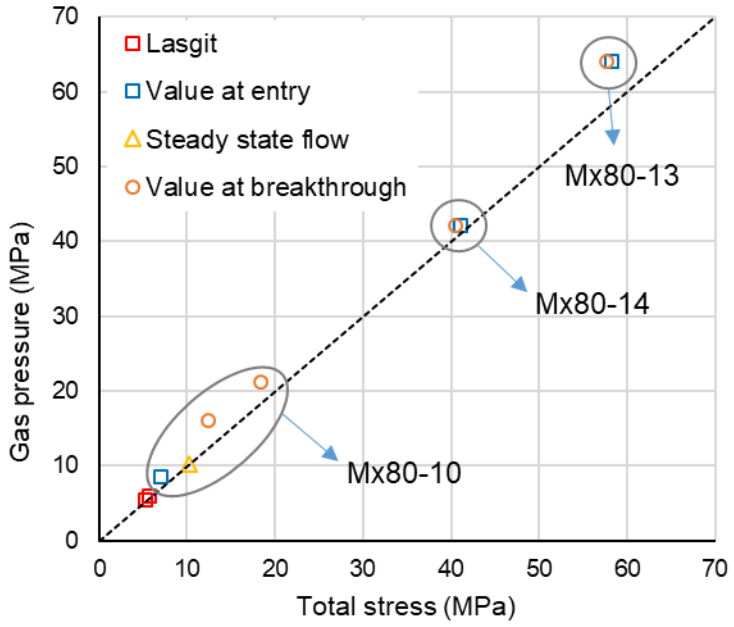

Figure 2.6 Relationship between gas pressure and total stress (Graham et al. 2016)

Dry density and initial degree of saturation of the tested bentonite are important factors controlling the gas breakthrough pressure. As discussed in Section 2.3, bentonite with a high dry density has high swelling pressure, high gas entry value and low permeability. These properties significantly inhibit gas transport in saturated bentonite. Previous gas injection tests on saturated bentonite showed that the gas breakthrough pressure increases with the increase of dry density (Graham et al. 2002; Gutiérrez-Rodrigo et al. 2015; Pusch et al. 1987; Villar et al. 2014b). In addition, the initial degree of saturation may have significant influences on the gas breakthrough. Experimental studies on Canadian Avonlea bentonite, as seen in (Graham et al. 2002), showed that there was a critical degree of saturation below which the gas

breakthrough behavior was not observed. This may be caused by the air-filled channels that had existed prior to gas injection (Graham et al. 2002). The experimental study on FEBEX bentonite also showed that the initial degree of saturation may influence the gas transport mechanism (Gutiérrez-Rodrigo et al. 2015). For a degree of saturation higher than a critical value, the dilatancy-controlled flow is a dominant transport mechanism, whereas for a lower degree of saturation, the two-phase flow is the dominant one.

The gas breakthrough phenomenon may be a time-dependent process. The experimental studies in (Graham et al. 2002) showed that the time necessary for gas breakthrough decreased inversely with the increase of gas pressure. Based on the time-dependent feature, the authors concluded that the gas breakthrough phenomenon is fundamentally caused by the advective process in interconnected macropores where water is replaced by the highly pressurized gas. This gas breakthrough mechanism was also adopted in (Tawara et al. 2014; Ye et al. 2014) to construct numerical models for simulating the gas migration process. However, recent experimental or numerical studies on Mx80 bentonite, as seen in (Graham et al. 2012; Harrington et al. 2017b), indicated that the advective process needs to be coupled with the mechanical process to fully reproduce the gas migration process in bentonite.

2.5.2 Preferential Pathways

For saturated bentonite, the extremely small pore size significantly inhibits the gas infiltration. Under such condition, the highly pressurized gas can trigger a series of preferential pathways for gas migration in the sample. The development of preferential pathways during gas migration in saturated bentonite has been widely validated in previous experimental studies. In (Horseman et al. 1999; Pusch et al. 1985), gas bubbles were observed at numerous discrete points on the surface of the tested bentonite sample when the sample was immersed in the glycerol or monomer compound. This implies that gas migrates in the bentonite sample through discrete pathways. In some experiments, like those in (Donohew et al. 2000; Wiseall et al. 2015), the generated pathways in clay paste were directly observed. The almost fully saturated state of bentonite sample after gas injection test, as observed in (Harrington and Horseman 2003; Horseman et al. 1999; Pusch and Forsberg 1983), also indicated that the gas was more

likely to transport through a small number of discrete pathways, thus leaving the clay matrix to keep fully saturated. Moreover, the couplings between water pressure, gas pressure, gas outflow and total stress also indirectly validated the development of preferential pathway. The radial gas flow test in (Harrington and Horseman 2003) showed that the gas outflow distributed nonuniformly between the sink arrays. Thus, this may be caused by the heterogeneous distribution of the preferential pathways developed in saturated bentonite. In addition, significant disturbances of the stress field in both magnitude and direction were always observed before the major gas outflow events (Harrington et al. 2017b). This experimental behavior is closely associated with the evolution of orientation and aperture of the developed pathways.

The developed pathways present high instabilities in terms of spatial and temporal evolution (Graham et al. 2012; Harrington and Horseman 2003). Specifically, the major gas outflow may switch between different outflow filters during gas injection test (Graham et al. 2012). The developed pathways may not be utilized as conduits for gas flow in the subsequent injection cycles (Harrington and Horseman 2003). These unstable features are closely associated with the formation and sealing of the pathways. The evolution of orientation and aperture of the pathways can induce significant chaotic behaviors of stress field, which is reflected by the changes in both magnitude and direction (Harrington et al. 2017b). Due to the instabilities of the pathways, the evolution of permeability is highly unpredictable. As a result, the measured gas pressure or outflow rate presents strong fluctuations during the gas injection test.

2.5.3 Fully Saturated State

Most of previous experimental studies showed that the tested bentonite sample after gas injection test remains almost fully saturated (Harrington and Horseman 2003; Horseman et al. 1999; Pusch and Forsberg 1983). In saturated bentonite, the majority of water molecules are tightly bound in clay particles. This part of immobile water significantly decreases the effective pore space for fluid flow. Therefore, gas preferentially flows through pre-existing larger connected pores or generated pathways, both of which only occupy a tiny proportion of the

whole pore volume. As a result, the tested sample can remain an almost fully saturated state.

2.5.4 Shut-in Pressure

Shut-in pressure, also called the capillary threshold pressure, is an asymptotic value to which the gas pressure decays after gas injection is stopped (Horseman et al. 1999). This value is regarded as the minimum gas pressure to maintain the aperture of the developed fractures (Harrington and Horseman 2003). The gas injection tests conducted under constant volume condition, i.e., Mx80-8 and Mx80-10 test, showed that the shut-in pressure is the sum of the swelling pressure and the porewater pressure (Harrington and Horseman 2003). This shut-in response is associated with the closure of the discrete pathways due to the decrease of gas pressure.

2.5.5 Self-sealing Process

The developed preferential pathways during gas migration process are highly unstable. After the termination of gas injection, the developed preferential pathways may abruptly collapse, leading to the recovery of sealing ability. This is observed in the evolution curve of gas outflow of the 1-D flow test in (Daniels and Harrington 2017). In addition, rehydrating the tested bentonite sample contributes to the recovery of the tensile strength and the sealing ability. The gas injection tests on the rehydrated sample showed that the previous gas breakthrough pressure can be reproduced (Gutiérrez-Rodrigo et al. 2015; Harrington et al. 2012). The fundamental self-sealing process may involve complex interactions between clay minerals, adsorbed water, free water and gas. This behavior has not yet been systematically studied by far.

2.5.6 Water Pressure and Total Stress

Evolutions of water pressure and total stress were mainly examined in laboratory and in-situ tests conducted by researchers from British Geological Survey. Under constant volume condition, the porewater pressure and total stress evolve rapidly as the preferential pathways develop in the saturated bentonite, as seen in (Daniels and Harrington 2017). Once the flow pathways are formed, the highly pressurized gas can significantly compress the surrounding

clay matrix, leading to an increase of porewater pressure and total stress. Thus, the evolutions of porewater pressure and total stress have indirectly reflected the pathway propagation events. A stress analysis conducted in (Harrington et al. 2017b) showed that there must be strong stress disturbances before any major gas outflow events took place. This indicates that the formation of an effective microfracture network is a prerequisite for the gas breakthrough behavior. Therefore, analyzing the evolution of total stress or porewater pressure is a good way to investigate the gas migration process in saturated bentonite.

2.6 Review of Hydro-Mechanical Modelling of Gas Migration in Saturated Bentonite

To conduct reliable performance assessments for DGR, many numerical models have been proposed in previous studies to simulate the gas migration process in bentonite. In this PhD manuscript, the state of the art of modelling the gas migration process is reviewed from several aspects, including materials, key experimental findings, hydraulic models, mechanical models and fracture propagation models. The findings and conclusions of this review are detailed in the technical paper presented in Appendix C as well as summarized below.

Gas migration in saturated bentonite is accompanied by complex coupled HM behaviors, as discussed in Section 2.5. To simulate the coupled HM behaviors, previous numerical models on this topic were generally developed in the framework of Biot's consolidation theory or mixture theory. Both Bishop-type effective stress and independent stress state variables (net normal stress and suction) were adopted to construct the mechanical models in previous numerical studies. Both types of stress state variables have their benefits and limitations when used for simulating the mechanical behaviors of bentonite under high gas pressure. Thus, it is still open for discussion that which stress state variable is more appropriate for the current research topic. The previous mechanical models on this topic cover linear elasticity, nonlinear elasticity, plasticity, damage and swelling. The elastoplastic models and damage models are proposed for simulating the possible shear failure and tensile failure caused by the high gas pressure. Thus, these inelastic models have accounted for the development of microfracture network in an implicit way. The swelling model can describe the expansion of clay matrix

during the wetting process. Thus, this model is beneficial in describing the closure and the self-sealing behavior of the developed fractures.

The gas transport in saturated bentonite is generally modelled by the generalized Darcy's law. To account for the mechanical effect on fluid flow, the intrinsic permeability has been expressed as a function of specific mechanical variables, such as porosity, volumetric strain, tensile strain, plastic strain and damage variable. Previous intrinsic permeability models are classified into five types, i.e. gas-pressure-based model, porosity-based model, strain-based model, damage-based model and Embedded Fracture Model (EFM). The capability of an intrinsic permeability model highly depends on the amount of physical or geometrical information it conveys. Compared with the other four types, the EFM has accounted for the physical basis, as well as incorporated more geometrical features of fractures, including fracture aperture, spacing and orientation. Thus, the EFM and its variations are the most widely used permeability models to simulate the gas migration process in saturated bentonite. Compared with the diverse intrinsic permeability models, the adopted relative permeability models are relatively uniform, mainly including Mualem-van Genuchten model and power law model. In almost all numerical models, van-Genuchten model is used to describe the water retention behavior. To account for the effect of the development of preferential pathways on the water retention behavior, the gas entry value is generally coupled with the intrinsic permeability (which is also controlled by the pathways) through a cubic root model.

It is desirable to explicitly simulate the fracturing process to reproduce the complex coupled HM behaviors. Three types of fracturing models are introduced, Rankine-type fracture criterion, Linear Elastic Fracture Model (LEFM) and Cohesive Zone Model (CZM). As the LEFM mainly concerns the elastic strain energy, it is not suitable to simulate the fracturing in saturated bentonite which may undergo plastic deformation. The Rankine-type fracture criterion has been examined from the viewpoint of Gibbs free energy. The experimental finding that gas starts to entry the saturated bentonite when gas pressure reaches the sum of swelling pressure and the porewater pressure, has validated the rationality of Rankine-type fracture criterion. The CZM may be the most desirable approach to simulate the gas-driven fracturing

in saturated bentonite, since it has been widely used to simulate the hydraulic fracturing in rocks and desiccation cracking in soils. However, more experimental works need to be conducted to determine the required parameters of CZM for saturated bentonite. Currently, numerical approaches that can explicitly simulate the gas-driven fracturing in saturated bentonite are relatively few and the existing ones performed less satisfactorily. Some potential approaches, such as phase field method, XFEM and TOUGH-UDEC model, can be further studied and improved to simulate the fracturing process in bentonite.

As summarized above, previous numerical studies on this topic have provided a comprehensive coupled HM framework to simulate the gas migration process. However, more numerical studies are necessary to be conducted to improve the framework. For example, the double porosity concept can be introduced to simulate the localized consolidation and water transfer between fractures and clay matrix. A physically based damage model is necessary to be developed to account for the development of preferential pathways. In addition, the preferential pathways need to be explicitly modelled to realistically simulate the coupled HM behaviors.

2.7 Conclusions

Substantial quantities of gas could be produced in DGRs for radioactive wastes (LLW, ILW, HLW) from several physicochemical processes, such as metal corrosion, water radiolysis and microbial degradation. About 94-97% of radioactive waste produced by nuclear plants are constituted of ILW and ILW. ILW and ILW produce no significant amount of heat. Thus, the temperature effect is irrelevant in the assessment of gas migration in DGR for LLW and ILW. HLW can produce a significant amount of heat. However, in DGR for HLW the production of gas occurs when groundwater penetrates the copper canister and then reacts with the iron insert. As the copper shell is highly resistant to the corrosion of groundwater, it is assumed that the bentonite buffer material has reached full saturation and the heat release of HLW has been completed at the onset of gas generation. Therefore, previous experimental studies on this topic are mainly conducted on saturated bentonite under the isothermal condition.

The initial dry density of bentonite sample significantly influences the HM properties that

control the gas migration process, including intrinsic permeability, gas entry value and swelling pressure. Bentonite sample with higher dry density contains more expansive minerals and therefore, can adsorb more water molecules. This leads to higher swelling pressure and smaller pore spaces that are available for fluid flow. As a result, the high dry density also contributes to a lower intrinsic permeability and a higher gas entry value.

The gas migration in saturated bentonite is characterized by several key HM behaviors, including gas breakthrough, development of preferential pathways, fully saturated state after gas injection test, build-up of water pressure and total stress, localized consolidation and "shut-in" pressure and self-sealing process. Previous numerical models were developed in the framework of Biot's consolidation theory or mixture theory to simulate these HM behaviors. The developed mechanical models have covered linear elasticity, nonlinear elasticity, plasticity, damage and swelling. The hydraulic models are coupled with mechanical models by defining the intrinsic permeability model as a function of specific mechanical variables. At present, the numerical approaches for explicitly simulating the development of preferential pathways are relatively few.

Chapter 3 Modelling of Dilatancy-controlled Gas Flow in Saturated Bentonite with Double Porosity Concept

3.1 Introduction

MIP results showed that the bentonite at saturated state presented a bimodal pore size distribution, whereas the μ-CT images captured the fissures between clay grains in the saturated bentonite sample, as discussed in Appendix C. The interconnected larger pores or fissures may serve as the preferential flow pathways under high gas pressure. Previous numerical models rarely examined the effect of the double pore structure on the gas migration process. Hoch et al. (2004) proposed a coupled HM model that considers the double pore structure to simulate the gas migration in saturated bentonite. However, the evolutions of porosities were expressed in a rather empirical way. The obtained results showed that the developed coupled HM model was less satisfactory to describe the experimental results. To overcome these issues, a novel coupled HM framework that accounts for the double pore structure is developed in this chapter. The saturated bentonite is considered as a superposition of two subcontinua. The mechanical behavior of each subcontinuum is governed by its own stress state variable and constitutive model. Therefore, the evolution of each porosity can be modelled in a more rigorous way. Furthermore, the proposed framework is enriched by incorporating the hysteresis of relative/intrinsic permeability, the consolidation of clay matrix, the damaging effect and the heterogeneity of HM properties, which makes it more flexible to describe the experimentally observed behaviors.

3.2 Modelling of Dilatancy-Controlled Gas Flow in Saturated Bentonite With Double Porosity and Double Effective Stress Concepts

Published in Engineering Geology Volume 243, 4 September 2018, Pages 253-271

Guanlong Guo, Mamadou Fall

Abstract

Dilatancy-controlled gas flow is a dominant process of gas migration in saturated bentonite. In this paper, a fully coupled hydro-mechanical model, which incorporates the concepts of double porosity and double effective stress, is developed to simulate the gas migration process. Double effective stress is derived based on the first law of thermodynamics and the mixture theory. The volumetric strain which is work-conjugated to each effective stress level is explicitly included in mass balance equations. Thus, the resultant mass balance equations are more robust from the viewpoint of thermodynamics. The developed coupled hydro-mechanical model is satisfactorily validated against the results of three laboratory tests conducted under different mechanical boundary conditions. In general, the model can well simulate the main experimental behaviors, including gas breakthrough, volume dilation, matrix consolidation, build-up of water pressure and "shut-in" pressure. Two important processes that contribute to the development of preferential pathways, i.e., dilation of the fractured porous media and consolidation of the porous continuum, have been successfully identified by the developed model.

Keywords: Gas breakthrough; Bentonite; Double porosity; Double effective stress; Gas entrapment; Hydro-mechanical processes

3.2.1 Introduction

Large volumes of nuclear waste have been generated due to the extensive use of nuclear power and advancements in nuclear power technology. Therefore, finding ways to safely and efficiently manage such hazardous nuclear waste is important to ensure the sustainable development of nuclear power. A widely accepted solution is to deposit nuclear waste into a deep geological repository (DGR) with a multi-barrier system to prevent lethal radionuclides from leaking into the biosphere. The multi-barrier system consists of an engineering barrier system (EBS), mainly including a copper canister and buffer materials, and a natural barrier system (Jove-Colon 2013), see Figure 3.1. Bentonite is considered to be an ideal buffer material for an EBS because it has some desirable properties, such as low permeability, proper swelling property and high adsorptive capacity (Villar and Lloret 2008; Wang et al. 2013a; Xu et al. 2017; Xu et al. 2016). During the lifespan of a DGR, three main physicochemical processes, i.e., metal corrosion, water radiolysis and bio-degradation, give rise to the generation of gas, which may negatively affect the desirable properties of bentonite when the gas pressure reaches a certain value (Graham et al. 2012; Ye et al. 2014; Yu and Weetjens 2009). Therefore, investigating the influence of gas migration process on the sealing ability of bentonite is very important for carrying out comprehensive performance assessments of DGRs.

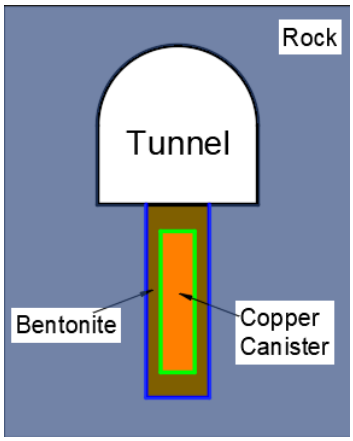

Figure 3.1 Multi-barrier system of deep geological repository

As the copper canister which is used to contain nuclear waste in an EBS is highly resistant to corrosion, the initiation of gas generation is sufficiently delayed for the bentonite to reach full saturation (Brown 1999; Graham et al. 2012; Rodwell et al. 1999; Ye et al. 2014).

Therefore, most of the existing tests on gas migration have been conducted on saturated bentonite. Studies in the extant literature agree that there are four basic processes of gas migration in porous media with low permeability: the advection/diffusion of dissolved gas, visco-capillary two-phase flow, dilatancy-controlled flow and macro-fracture flow (Marschall et al. 2005; Nagra 2008; Ye et al. 2014). Most of experimental results showed that dilatancy-controlled flow is a predominant mechanism for gas migration in saturated bentonite (Graham et al. 2012; Gutiérrez-Rodrigo et al. 2015; Horseman et al. 1999). It is a physical process that is characterized by different hydro-mechanical (HM) behaviors, such as gas breakthrough, the development of preferential pathways, volume dilation, consolidation of the clay matrix, and void interaction (Graham et al. 2012; Hoch et al. 2004; Rodwell et al. 1999).

The models that are used to simulate gas migration in saturated bentonite-based materials mainly include modified two phase flow models, fracture propagation models as well as conventional coupled HM models based on continuum mechanics (Arnedo et al. 2013; Brown 1999; Nash et al. 1998; Olivella and Alonso 2008; Tawara et al. 2014; Ye et al. 2014). For more information on the current models, readers can refer to the literature provided in Alkan and Muller (2008); Rodwell et al. (1999). In terms of modified two phase flow models, gas breakthrough phenomenon generally occurs at a critical gas pressure over which gas permeability dramatically increases (Tawara et al. 2014; Ye et al. 2014). As these models do not incorporate any mechanical variables, there are limitations in their use to describe the mechanical effects, such as the confining pressure or the mechanical boundary conditions, on the changes of permeability (Xu et al. 2013). By contrast, the fracture propagation model is more likely to capture the real physical process of gas migration in buffer materials, but limited by complex mathematical treatments and the application to field conditions (Hoch et al. 2004; Nash et al. 1998; Swift et al. 2001). Recently, new numerical theories and algorithms which include phase field method, cohesive zone model, extended finite element method (XFEM), etc., are potential alternatives for modeling fracture propagation in porous media (Cajuhi et al. 2018; Carrier and Granet 2012; Salimzadeh and Khalili 2015a). However, most of these models

are only applicable to saturated porous media, and further studies are necessary to incorporate multiphase flow.

To date, the widely adopted model for this case is the coupled HM model developed within the framework of Biot's consolidation theory. Features such as damage, plasticity, anisotropy, embedded fractures, etc., have been introduced to capture more experimentally observed behaviors of dilatancy-controlled flow (Arnedo et al. 2013; Fall et al. 2014; Nguyen and Le 2014; Olivella and Alonso 2008; Xu et al. 2013). Due to the simplicity and flexibility, the embedded fracture model (EFM) has been widely used in coupled HM models to explain the development of preferential pathways (Arnedo et al. 2013; Gerard et al. 2014; Gonzalez-Blanco et al. 2016; Olivella and Alonso 2008). However, the EFM is essentially a strain-controlled permeability model enriched by cubic law. Although the EFM can be conceptually regarded as a kind of pore space, these fractures do not occupy any pore spaces independently from the viewpoint of governing equation. This is because the evolutions of both normal pores and embedded fractures are lumped into the same set of governing equations. This is inconsistent with the traditional double porosity model in which the evolution of each type of porosity is described by its own governing equation. Therefore, it is better to regard the embedded fractures as a series of imaginary fractures which mainly modify the hydraulic properties, like intrinsic and relative permeability. Rutqvist and Stephansson (2003) proposed the concepts of indirect coupling and direct coupling. The direct coupling may be represented by the coupling term in governing equations, such as the effective stress term in the momentum balance equation or the volume strain term in the mass balance equation. In contrast, the indirect coupling is reflected by the changes of properties in either hydraulic or mechanical constitutive models. For example, the permeability is influenced by strain, or Young's modulus is influenced by suction. Based on the analysis above, the traditional EFM is a kind of indirect coupling. As a result, the consolidation of clay matrix on the opening of fractures may not be well described by the EFM which is essentially based on a single porosity approach. This limitation may lead to difficulties in simulating the development of preferential pathways under a constant volume condition which restricts the dilation of the tested sample. Considering the

limitations of pre-existing coupled HM models, this paper aims to develop a new coupled HM model, based on the concepts of double porosity and double effective stress, to better simulate the experimentally observed behaviors of gas migration in saturated bentonite.

3.2.2 Conceptual Model for Dilatancy-controlled Flow

Before developing a mathematical model for gas migration in saturated bentonite, a conceptual model for the basic HM processes will be developed in this section. To do so, the concepts of double porosity and double effective stress are proposed first, and then, simplifications and assumptions of the concepts are elaborated.

3.2.2.1 Double porosity concept

It is commonly known that bentonite samples form a double pore structure after gas breakthrough because of the development of preferential pathways. In contrast, there is controversy about the pore structure of bentonite before gas breakthrough takes place.

It is widely accepted that unsaturated expansive soils have a double pore structure, i.e. inter-aggregate pores and intra-aggregate pores (Gens and Alonso 1992). The pore size distribution of clays with a double pore structure depends on the degree of saturation. With an increase in water content, elementary clay particles may flake off from the clay aggregate, and consequently, the inter-aggregate pores are gradually reduced (Wang et al. 2013a). When the active clay reaches full saturation, single pore size is predominantly observed throughout the void space based on the mercury intrusion porosimetry (MIP) (Monroy et al. 2010), as seen in Figure 3.2.

However, other researchers have argued that saturated expansive clays also form a double pore structure. Ye et al. (2014) assumed that there are large interconnected pores in saturated bentonite, see Figure 3.3, which may serve as flow pathways for gas under high pressure. Based on this assumption, Ye et al. (2014) proposed a modified two-phase flow model to simulate the gas migration process. In addition, other researchers have indicated that there may exist clay stacks where tightly bound water resides, as well as “interstack” voids where the water is loosely bound (Hoch et al. 2004; Pusch and Hökmark 1990). Taking into consideration the current issue at hand in which the gas pressure is extremely high, the loosely bound water may

be replaced by gas, and then the “interstack” voids serve as the preferential pathways for gas transport. In order to avoid explicitly simulating the fracture propagation and maintain the modelling consistency prior to and after the gas breakthrough, it is assumed here that the saturated bentonite sample also has a double pore structure before gas breakthrough.

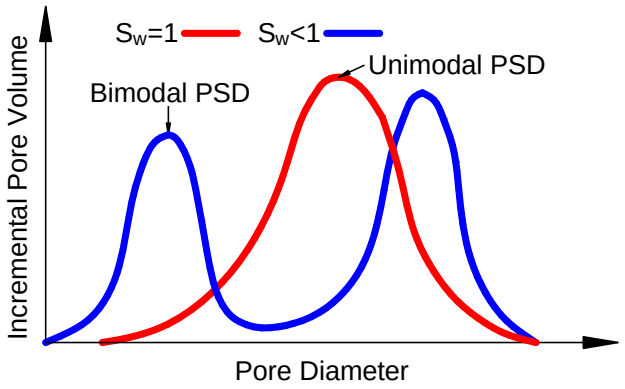

Figure 3.2 Pore size distribution of expansive clays

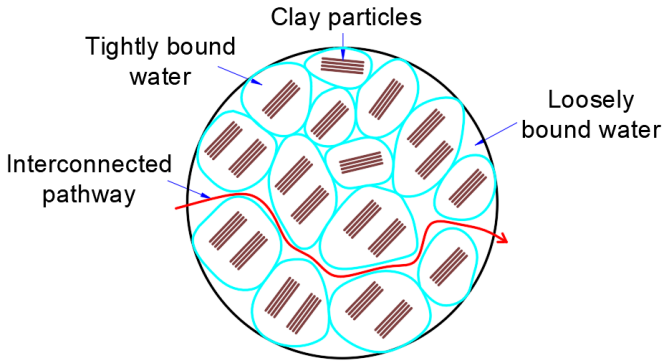

Figure 3.3 Interconnected pores in saturated bentonite (Modified from Zhu et al. (2013) and Ye et al. (2014))

3.2.2.2 Double effective stress concept

In conventional coupled HM models, porous media with a double pore structure are assumed to consist of two overlapping continua (Sánchez et al. 2016). Typically, the mechanical behaviors of double porosity media are considered to be governed by a single effective stress concept; for example, see Choo et al. (2016); Khalili (2008); Salimzadeh and Khalili (2015b). However, the single effective stress concept does not seem adequate to differentiate the mechanical contribution from each continuum when they behave rather differently. For the

current issue at hand, the development of preferential pathways is accompanied by both the dilation of the entire sample and the consolidation of clay matrix around fractures (Hoch et al. 2004; Nash et al. 1998; Swift et al. 2001). As these two processes present mutual contradiction from the mechanical viewpoint, it is difficult for a single effective stress concept to govern them simultaneously. Therefore, defining an effective stress concept for each continuum may be the best way to capture their mechanical behaviors. Meanwhile, the model may be more capable of explaining complex mechanical processes of double porosity media.

Double effective stress concept, which is used to a lesser extent in comparison to its single counterpart, is mainly adopted to govern the mechanical behaviors of fractured rocks or expansive soils. Elsworth and Bai (1992) and Nair et al. (2005) proposed the use of double effective stress concept for fractured rocks in which the fractured and the porous continuum are controlled by their own constitutive models. However, the two constitutive models were merged again based on the assumption of linear elasticity. By contrast, an entirely separate constitutive model for each subcontinuum is generally used for unsaturated expansive clays (Alonso et al. 1999; Gens and Alonso 1992; Mašín 2013; Sanchez et al. 2005; Sánchez et al. 2016; Vilarrasa et al. 2015). Sánchez et al. (2016) developed a coupled thermo-hydro-mechanical (THM) model for clay pellets with a double structure, in which there are two mechanical constitutive models, one for the macrostructure and one for the microstructure, that are linked through an interaction function. In this coupled model, the mechanical behaviors of the macrostructure of clay pellets are governed by the well-known Barcelona Basic Model (BBM), while the microstructure behaves like a nonlinear elastic material. This double porosity model provides a satisfactory outcome in terms of reproducing the two swelling steps of the clay pellets. It should be noted that the BBM used in their study is based on two independent stress state variables (i.e. net normal stress and suction), but other constitutive models based on effective stress concept can be used in lieu, such as the hypoplastic model in Mašín (2013), or the bounding surface model in Li et al. (2016). These works in the literature provide the basis for constructing a framework to model the gas migration process by using the concepts of double porosity and double effective stress.

In the extant literature, thermodynamics theories have been widely used to validate the concepts of effective stress proposed for single/double porosity media in saturated/unsaturated conditions (Borja and Koliji 2009; Houlsby 1997; Li et al. 2016; Zhao et al. 2010). To the best of the authors' knowledge, Li et al. (2016) were the first to derive a thermodynamically based double effective stress concept for unsaturated clays based on the approach in Houlsby (1997). By contrast, Borja and Koliji (2009) proposed another approach in which a single effective stress concept for unsaturated double porosity media was derived based on mixture theory and the first law of thermodynamics. Their approach will be extended in this paper to derive a thermodynamically based double effective stress concept for double porosity media. Readers can refer to Eqs. (D.1)-(D.19) in Appendix D for more details on the derivation process.

3.2.2.3 Conceptual model

The aim of this study is to assess whether the concepts of double porosity and double effective stress can capture more experimentally observed behaviors. In order to propose a proper conceptual model, some simplifications and assumptions are made as follows.

- The bentonite sample is assumed to be a fractured porous medium (FPM), which consists of two overlapping but independent subcontinua, i.e. a fractured continuum (FC) and a porous continuum (PC). The interaction between the two subcontinua is described by the water exchange and the porosity transformation between pores and fractures.
- The volume averaging theory is applicable for both the FC and the PC. In order to ease the understanding about the porosity transformation between the FC and the PC, and its effects on hydraulic properties, the FPM is simplified as a series of squares termed as "matrix" and two sets of orthogonal fractures, as shown in Figure 3.4(a) and (b). However, the HM properties of both subcontinua are assumed to be isotropic and homogeneous for simplicity.

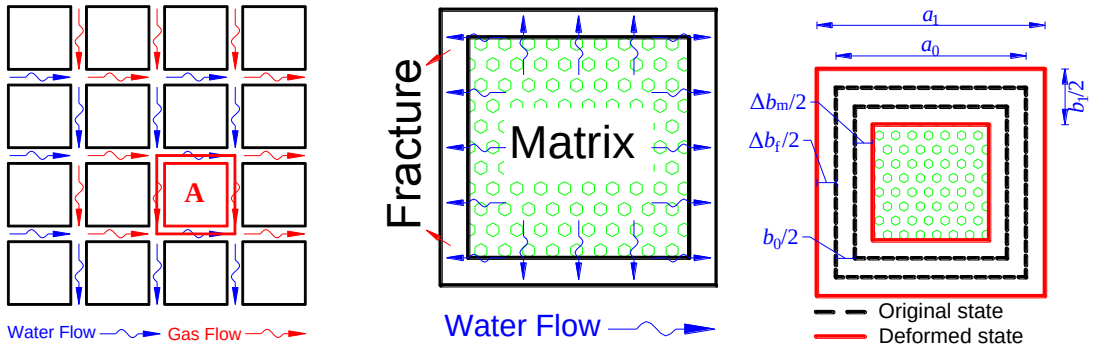

(a) Fractured porous medium (b) Element A (c) Deformation of element A

Figure 3.4 Schematic of REV of bentonite sample (a_0, a_1, b_0 and b_1 are the fracture spacings and apertures prior to and after deformation, respectively; Δb_m and Δb_f are the incremental apertures from the consolidation of the PC and the dilation of the FPM, respectively)

- Visco-capillary two-phase flow takes place in the FC. Due to the extremely small pore size, the PC remains saturated during the whole simulation, and the water flow within the PC is neglected for simplicity. However, the water can initially transfer into the FC, and then flow out of the sample, as seen in Figure 3.4(a) and 4(b). A similar assumption is also adopted by Navarro et al. (2015).
- Figure 3.4(c) shows that the original aperture is b_0, and the aperture after deformation is b_1. The opening/closure of fractures in the FC (represented by $b_1 - b_0$) results from the dilation of the FPM (Δb_f) and/or the consolidation of the PC (Δb_m). This conceptual model has an advantage over the single porosity model when addressing constant volume condition because the opening of fractures under a constant volume can be realized through the transformation from pores to fractures, which could significantly increase the permeability of gas phase.
- The FC and PC are subjected to the same total stress but different void pressures. This gives two different effective stresses to govern the mechanical behavior of each subcontinuum.
- The dissolution of gas into water and the vaporization of water into gas are not considered here for simplicity. The solid grains are assumed to be incompressible. The

small deformation theory is applied, and isothermal conditions are assumed. Tension and compression are taken to be positive for stress and pressure, respectively.

3.2.3 Governing Equations

3.2.3.1 Mass balance equations

In this section, the mass balance equations for the FC and the PC will be derived based on the conceptual model given in Section 3.2.2.3. The porosity and volumetric strain rate for each subcontinuum have been defined by Eq. (D.1) and Eqs. (D.6)-(D.7), respectively in Appendix D. Then, the total porosity and total volumetric strain rate can be expressed as:

$$\phi_t = \frac{V_f + V_p}{V_t} = \phi_f + \phi_p \tag{3.1}$$

$$\dot{\varepsilon}_v = \frac{dV_f + dV_p}{V_t dt} = \dot{\varepsilon}_{fv} + \dot{\varepsilon}_{pv} \tag{3.2}$$

where ϕ_β, V_β and $\dot{\varepsilon}_{\beta v}$ are the porosity, volume, and volumetric strain rate of the porous media β which is represented by f, p and t for the FC, PC and FPM, respectively.

3.2.3.1.1 Fractured continuum

The mass balance equation for the gas in the FC is expressed as (Rutqvist et al. 2001):

$$\frac{\partial\left(S_{fg}\rho_{fg}\phi_f\right)}{\partial t} + \nabla\cdot\left(S_{fg}\rho_{fg}\phi_f \boldsymbol{v}_{fg}\right) = 0 \tag{3.3}$$

where S_{fg} is the degree of saturation of gas, ρ_{fg} is the gas density in the FC, ϕ_f is the porosity of the FC, and $\boldsymbol{v}_{fg}$ is the absolute velocity of the gas phase.

The absolute velocity of the gas phase can be decomposed as:

$$\boldsymbol{v}_{fg} = \boldsymbol{v}_{rfg} + \boldsymbol{v}_s \tag{3.4}$$

where $\boldsymbol{v}_{rfg}$ is the relative velocity of the gas in fractures with respect to the solid phase, and $\boldsymbol{v}_s$ is the velocity of the solid phase.

By substituting Eq. (3.4) into Eq. (3.3), the mass balance equation for gas can be expressed as:

$$\frac{\partial\left(S_{fg}\rho_{fg}\phi_f\right)}{\partial t}+\nabla\cdot(\rho_{fg}\boldsymbol{v}_{fg}^{D})+S_{fg}\rho_{fg}\phi_f\nabla\cdot\boldsymbol{v}_s+\boldsymbol{v}_s\cdot\nabla\left(S_{fg}\rho_{fg}\phi_f\right)=0 \tag{3.5}$$

where $\boldsymbol{v}_{fg}^{D}=S_{fg}\phi_f\boldsymbol{v}_{rfg}$ is Darcy's velocity for the gas phase.

Due to the assumption of small deformation, the term $\boldsymbol{v}_s\cdot\nabla(\cdot)$ in Eq. (3.5) is negligible relative to the term $\partial(\cdot)/\partial t$, and the term $\nabla\cdot\boldsymbol{v}_s$ can be expressed as $\partial\varepsilon_v/\partial t$ (Cui and Fall 2015; Rutqvist et al. 2001). Then, Eq. (3.5) can be reformulated as:

$$S_{fg}\rho_{fg}\frac{\partial\phi_f}{\partial t}+\phi_f S_{fg}\frac{\partial\rho_{fg}}{\partial t}+\phi_f\rho_{fg}\frac{\partial S_{fg}}{\partial t}+\nabla\cdot(\rho_{fg}\boldsymbol{v}_{fg}^{D})+\phi_f S_{fg}\rho_{fg}\frac{\partial\varepsilon_v}{\partial t}=0 \tag{3.6}$$

Based on the definitions of porosity given by Eqs. (D.6) and (D.7) in Appendix D, the rate of change in the porosity of the FC and PC is respectively expressed as:

$$\frac{\partial\phi_f}{\partial t}=\frac{\partial\varepsilon_{fv}}{\partial t}-\phi_f\frac{\partial\varepsilon_v}{\partial t} \tag{3.7}$$

$$\frac{\partial\phi_p}{\partial t}=\frac{\partial\varepsilon_{pv}}{\partial t}-\phi_p\frac{\partial\varepsilon_v}{\partial t} \tag{3.8}$$

The porosity transformation between pores and fractures as illustrated in Section 3.2.2.3 is essentially achieved by using Eqs. (3.7) and (3.8).

Substituting Eq.(3.7) into Eq.(3.6) gives the mass balance equation for gas as:

$$S_{fg}\rho_{fg}\frac{\partial\varepsilon_{fv}}{\partial t}+\phi_f S_{fg}\frac{\partial\rho_{fg}}{\partial t}+\phi_f\rho_{fg}\frac{\partial S_{fg}}{\partial t}+\nabla\cdot(\rho_{fg}\boldsymbol{v}_{fg}^{D})=0 \tag{3.9}$$

By using a similar derivation procedure, the mass balance equation for water in the FC can be derived as:

$$S_{fw}\rho_{fw}\frac{\partial \varepsilon_{fv}}{\partial t}+\phi_f S_{fw}\frac{\partial \rho_{fw}}{\partial t}+\phi_f \rho_{fw}\frac{\partial S_{fw}}{\partial t}+\nabla\cdot(\rho_{fw}\boldsymbol{v}_{fw}^{D})=\Gamma_w \tag{3.10}$$

where $\boldsymbol{v}_{fw}^{D}=S_{fw}\phi_f\boldsymbol{v}_{rfw}$ is Darcy's velocity for water, S_{fw} is the degree of saturation of water, ρ_{fw} is the density of water in fractures, and Γ_w is a water exchange term.

To explicitly express the mass balance equations with respect to the field variables, i.e., gas pressure, p_{fg}, and water pressure, p_{fw}, some state equations are introduced as follows.

The rate of change in water density can be rewritten in terms of the water pressure by introducing the compressibility of water as:

$$\frac{\partial \rho_{\beta w}}{\partial t}=\rho_{\beta w}c_w\frac{\partial p_{\beta w}}{\partial t} \tag{3.11}$$

where β denotes p and f for the PC and the FC, respectively, and c_w is the compressibility of water.

By using the ideal gas law, the rate of change in gas density can be expressed as:

$$\frac{\partial \rho_{fg}}{\partial t}=\frac{M}{RT}\frac{\partial p_{fg}}{\partial t} \tag{3.12}$$

where M is the molar mass of the gas, R is a universal gas constant and T is the absolute temperature.

The residual degree of saturation in the FC is assumed to be 0 in this paper, and thus, the degree of saturation of water, S_{fw}, is equal to the effective degree of saturation, S_e. If the van Genuchten model (van Genuchten 1980) is adopted as the water retention curve, then

$$\frac{\partial S_{fg}}{\partial t}=-\frac{\partial S_{fw}}{\partial t}=-\frac{\partial S_e}{\partial t}=C_s\frac{\partial p_c}{\partial t} \tag{3.13}$$

$$C_s = -\frac{\partial S_e}{\partial p_c} = \frac{m}{p_{gev}(1-m)} S_e^{\frac{1}{m}} \left(1 - S_e^{\frac{1}{m}}\right)^m \tag{3.14}$$

where p_{gev} is the gas entry value, m is a shape parameter of the van Genuchten model, and $p_c = p_{fg} - p_{fw}$ is the capillary pressure in the FC.

Substituting Eqs. (3.11)-(3.14) into Eqs. (3.9) and (3.10) gives the final form of the mass balance equations for gas and water in the FC, respectively, as:

$$\rho_{fg}\left(\frac{\phi_f S_{fg} M}{\rho_{fg} RT} + \phi_f C_s\right)\frac{\partial p_{fg}}{\partial t} + \nabla\cdot(\rho_{fg}\boldsymbol{v}_{fg}^D) = \phi_f \rho_{fg} C_s \frac{\partial p_{fw}}{\partial t} - S_{fg}\rho_{fg}\frac{\partial \varepsilon_{fv}}{\partial t} \tag{3.15}$$

$$\rho_{fw}\left(\phi_f S_{fw} c_w + \phi_f C_s\right)\frac{\partial p_{fw}}{\partial t} + \nabla\cdot(\rho_{fw}\boldsymbol{v}_{fw}^D) = \phi_f \rho_{fw} C_s \frac{\partial p_{fg}}{\partial t} - S_{fw}\rho_{fw}\frac{\partial \varepsilon_{fv}}{\partial t} + \Gamma_w \tag{3.16}$$

As can be seen from the final form of the mass balance equations above, the storage terms (in the first parenthesis on the left side) and the equivalent mass source terms (on the right side) can be readily differentiated, which is helpful for better understanding the interaction between the water pressure and the gas pressure.

3.2.3.1.2 Porous continuum

As the pore size in the PC is extremely small, Darcy's flow of pore water is neglected in this study, but the water exchange between fractures and pores is allowed. Following a similar derivation procedure as in Section 3.2.3.1.1, the mass balance equation for water in the PC can be derived as:

$$\phi_p \frac{\partial \rho_{pw}}{\partial t} + \rho_{pw}\frac{\partial \phi_p}{\partial t} + \phi_p \rho_{pw}\frac{\partial \varepsilon_v}{\partial t} = -\Gamma_w \tag{3.17}$$

where ρ_{pw} is the density of the pore water, and ϕ_p is the porosity of the PC.

Substituting Eq. (3.8) into Eq.(3.17) gives the mass balance equation for the pore water as:

$$\phi_p \frac{\partial \rho_{pw}}{\partial t} + \rho_{pw} \frac{\partial \varepsilon_{pv}}{\partial t} = -\Gamma_w \tag{3.18}$$

Substituting Eq. (3.11) into Eq. (3.18) gives the mass balance equation for pore water with respect to the field variable, p_{pw}, as

$$\phi_p \rho_{pw} c_w \frac{\partial p_{pw}}{\partial t} = -\rho_{pw} \frac{\partial \varepsilon_{pv}}{\partial t} - \Gamma_w \tag{3.19}$$

It can be easily identified from Eqs. (3.15), (3.16) and (3.19) that the volumetric strain rates for both the FC and PC are explicitly incorporated into the mass balance equations. This will help to differentiate the mechanical contribution from each subcontinuum. The volumetric strain rate can be easily determined by using the concept of double effective stress and the corresponding mechanical constitutive models, which will be discussed later.

Similarly, the mass balance equation for the solid phase is derived as:

$$\frac{\partial \phi_f}{\partial t} + \frac{\partial \phi_p}{\partial t} = \frac{1-\phi_f-\phi_p}{\rho_s} \frac{\partial \rho_s}{\partial t} + \left(1-\phi_f-\phi_p\right) \frac{\partial \varepsilon_v}{\partial t} \tag{3.20}$$

where ρ_s is the density of the solid phase.

It is worth noting that summing Eqs. (3.7) and (3.8) yields Eq. (3.20) when the solid phase is assumed to be incompressible. This justifies the introduction of Eqs. (3.7) and (3.8) into the mass balance equations.

3.2.3.2 Momentum balance equation

Neglecting the inertial and viscous forces, the momentum balance equation for the FPM can be expressed as:

$$\nabla \cdot \boldsymbol{\sigma} + \rho \boldsymbol{g} = 0 \tag{3.21}$$

$$\rho = \left(1-\phi_f-\phi_p\right)\rho_s + \left(\phi_f S_{fw} + \phi_p\right)\rho_w + \left(\phi_f S_{fg}\right)\rho_g \tag{3.22}$$

where $\boldsymbol{\sigma}$ is the total stress tensor and $\boldsymbol{g}$ is the gravitational acceleration.

3.2.4 Constitutive Models

3.2.4.1 Mechanical constitutive models

The mechanical constitutive models are developed based on the double effective stress concept as derived from Eq. (D.1) to Eq. (D.19). The PC is assumed to present volumetrically elastoplastic behaviors, while the FC is assumed to present nonlinear elastic behaviors.

3.2.4.1.1 Porous continuum

Due to the extremely small pores in the clay matrix, the PC is assumed to maintain full saturation during the entire process. Thus, the well-known Terzaghi's effective stress concept which is given as Eq.(3.23) is used to govern the mechanical behaviors of the PC.

$$\boldsymbol{\sigma}'_p = \boldsymbol{\sigma} + p_{pw}\boldsymbol{I} \tag{3.23}$$

where $\boldsymbol{\sigma}'_p$ is the effective stress of the PC, and $\boldsymbol{I}$ is a second-order identity tensor.

Previous studies have concluded that the development of preferential pathways is accompanied by the consolidation of clay matrix adjacent to the developed fractures (Swift et al. 2001). The plastic behavior of clay matrix inhibits the complete closure of the developed fractures after the termination of gas injection. Börgesson et al. (1995) proposed a CLAY-TECH model to simulate the plastic behaviors of saturated clays. This model appears to be a good candidate to describe the mechanical behaviors of the PC but is mathematically complex. By contrast, Gens and Alonso (1992) and Sanchez et al. (2005) proposed a very simple model based on effective stress to govern the mechanical behaviors of the microstructure of unsaturated expansive soils. Although this simplified model only considers elastic volumetric behavior, it works very well for describing the interaction between macro-pores and micro-pores. For simplicity, this paper will extend this simplified model to describe the plastic volumetric behavior of the PC.

When the mean effective pressure in the PC is less than the pre-consolidation pressure, p_c' (which is defined as the maximum historical value of the mean effective pressure to which the PC was subjected), or the PC is unloaded, only elastic volumetric strain occurs, which is expressed as:

$$\dot{\varepsilon}_{pv}^{el} = -\frac{\dot{p}_p' \kappa_p}{(1+e_p) p_p'}, \quad p_p' < p_c' \text{ or } \dot{p}_p' < 0 \tag{3.24}$$

where $\dot{\varepsilon}_{pv}^{el}$ is the rate of change of the elastic volumetric strain of the PC, κ_p is the slope of swelling line, e_p is the void ratio of the PC, and p_p' and $\dot{p}_p'$ are the mean effective pressure and its corresponding rate of change, respectively.

When the mean effective pressure is greater than the pre-consolidation pressure, p_c', and the PC is loaded, the plastic volumetric strain would occur, which is determined by using:

$$\dot{\varepsilon}_{pv}^{pl} = -\frac{\dot{p}_p' (\lambda_p - \kappa_p)}{(1+e_p) p_p'}, \quad p_p' > p_c' \text{ and } \dot{p}_p' > 0 \tag{3.25}$$

where $\dot{\varepsilon}_{pv}^{pl}$ is the rate of change in plastic volumetric strain of the PC, and λ_p is the slope of the normal consolidation line.

To summarize, the elastoplastic volumetric strain, $\dot{\varepsilon}_{pv}$, of the PC can be expressed as:

$$\dot{\varepsilon}_{pv} = \begin{cases} -\dfrac{\dot{p}_p' \kappa_p}{(1+e_p) p_p'}, & p_p' < p_c' \text{ or } \dot{p}_p' < 0 \\ -\dfrac{\dot{p}_p' \lambda_p}{(1+e_p) p_p'}, & p_p' > p_c' \text{ and } \dot{p}_p' > 0 \end{cases} \tag{3.26}$$

3.2.4.1.2 Fractured continuum

As the FC is assumed to be unsaturated, Bishop-like effective stress is used here to formulate the mechanical constitutive model, which is expressed as:

$$\boldsymbol{\sigma}'_f = \boldsymbol{\sigma} + \left[S_{fw} p_{fw} + (1 - S_{fw}) p_{fg} \right] \boldsymbol{I} = \boldsymbol{\sigma} + \bar{p}_f \boldsymbol{I} \tag{3.27}$$

where $\boldsymbol{\sigma}'_f$ is the effective stress of the FC, and $\bar{p}_f$ is the average fluid pressure in fractures.

As gas injection is an unloading process for the FC and the HM properties are assumed to be isotropic and homogeneous, only elastic behaviors are considered in this study. However, more features can be incorporated into this constitutive model in the future, such as damage, plasticity or anisotropy, as done by (Arnedo et al. 2013; Fall et al. 2014; Qi and Vanapalli 2016).

As the PC only shows volumetric behavior, the volume dilation of the PC is like a thermal expansion process. Thus, the deviatoric strain rate of the FPM only stems from the FC, which can be expressed as:

$$\dot{\boldsymbol{\varepsilon}}_d = \dot{\boldsymbol{\varepsilon}}_{fd} \tag{3.28}$$

where $\dot{\boldsymbol{\varepsilon}}_d$ and $\dot{\boldsymbol{\varepsilon}}_{fd}$ are the deviatoric strain rate tensor of the FPM and the FC, respectively.

Multiplying Eq. (3.2) by 1/3 and adding the result to Eq.(3.28) gives

$$\dot{\boldsymbol{\varepsilon}}_d + \frac{1}{3}\dot{\varepsilon}_v \boldsymbol{I} = \dot{\boldsymbol{\varepsilon}}_{fd} + \frac{1}{3}\dot{\varepsilon}_{fv} \boldsymbol{I} + \frac{1}{3}\dot{\varepsilon}_{pv} \boldsymbol{I} \tag{3.29}$$

Then, Eq.(3.29) is rewritten with respect to the volumetric strain rate of the FC and PC as:

$$\dot{\boldsymbol{\varepsilon}} = \dot{\boldsymbol{\varepsilon}}_f + \frac{1}{3}\dot{\varepsilon}_{pv} \boldsymbol{I} \tag{3.30}$$

where $\dot{\boldsymbol{\varepsilon}}_f$ and $\dot{\boldsymbol{\varepsilon}}$ are the strain rate tensor of the FC and FPM, respectively; and $\dot{\varepsilon}_{pv}$ is the volumetric strain rate of the PC.

Thus, the mechanical constitutive model for the FC can be expressed as:

$$\dot{\boldsymbol{\sigma}}'_f = \mathbb{D}\dot{\boldsymbol{\varepsilon}}_f = \mathbb{D}\left[\dot{\boldsymbol{\varepsilon}} - (\dot{\varepsilon}_{pv} / 3) \boldsymbol{I} \right] \tag{3.31}$$

$$\dot{\boldsymbol{\varepsilon}} = \frac{1}{2}\left[\nabla\dot{\boldsymbol{u}} + \left(\nabla\dot{\boldsymbol{u}}\right)^{T}\right] \tag{3.32}$$

where $\mathbb{D}$ is a fourth-order elastic tensor determined by the bulk modulus, K, and shear modulus, G, and $\dot{\boldsymbol{u}}$ is the rate of displacement vector of the FPM.

The bulk modulus, K, and shear modulus, G, can be expressed as:

$$K = \frac{p'_f(1+e_f)}{\kappa_f} \tag{3.33}$$

$$G = \frac{3K(1-2\nu)}{2(1+\nu)} \tag{3.34}$$

where p'_f is the mean effective pressure of the FC, e_f is the void ratio of the FC, κ_f is the slope of the swelling line, and ν is the Poisson's ratio.

3.2.4.2 Hydraulic constitutive models

For the unsaturated FC, both gas and water flows are governed by a general Darcy's law, which is expressed as:

$$\boldsymbol{v}^{D}_{f\alpha} = -\frac{k_f k_{r\alpha}}{\mu_\alpha}(\nabla p_{f\alpha} - \rho_\alpha \boldsymbol{g}) \tag{3.35}$$

where k_f is the intrinsic permeability of the FC, α refers to w and g for water and gas respectively, $k_{r\alpha}$ is the relative permeability, μ_α is the fluid dynamic viscosity, $p_{f\alpha}$ is the fluid pressure, and ρ_α is the density of the fluid.

3.2.4.2.1 Intrinsic permeability

The well-known cubic law has been used to calculate the intrinsic permeability of the FC (Olivella and Alonso 2008), which can be expressed as:

$$k_f = \frac{b^3}{12a} \tag{3.36}$$

where b is the fracture aperture, and a is the average spacing between two adjacent fractures.

Based on the conceptual model, as shown in Figure 3.4(b), the porosity of a two-dimensional simplified FC can be expressed as

$$\phi_f = \frac{2b}{a} \tag{3.37}$$

By combining Eqs. (3.36) and (3.37), the intrinsic permeability of the FC after deformation can be derived as

$$k_f = k_{f0}\left(\frac{\phi_f}{\phi_{f0}}\right)^3\left(\frac{a}{a_0}\right)^2 \tag{3.38}$$

where notations with subscript '0' denote their corresponding initial values.

Similarly, Chen et al. (2016) derived an intrinsic permeability model with respect to aperture and spacing, but porosity was not explicitly included. Ma and Wang (2016) also proposed a model for intrinsic permeability, which is capable of reflecting the effects of changes in both volume and structure. As Eq.(3.38) shows, the porosity term represents the contribution from the dilation of the FPM and/or the consolidation of the PC, as shown in Figure 3.5(a) and (b), while the spacing term can be interpreted as a fracturing behavior which seems like fracture coalescence, as shown in Figure 3.5(c). However, it should be noted that the fracture coalescence in saturated bentonite has not been reported yet. The employment of this concept is just to interpret the effect of the spacing term on the intrinsic permeability from the viewpoint of the proposed conceptual model. From the original state, see Figure 3.5 (a), to the coalescence state, see Figure 3.5(c), the narrow fractures have merged into wide fractures, and the fracture spacing increases correspondingly. Based on Eq.(3.38), the increase of fracture spacing will induce growth in intrinsic permeability under the assumption of constant fracture porosity.

Meanwhile, the gas entry value for the FC will reduce as the fracture aperture increases. This will facilitate the desaturation process, and then increase the relative permeability of gas phase. Therefore, it can be seen that the concept of fracture coalescence is beneficial to achieving a significant increase of total permeability, and then to simulating the gas breakthrough behavior.

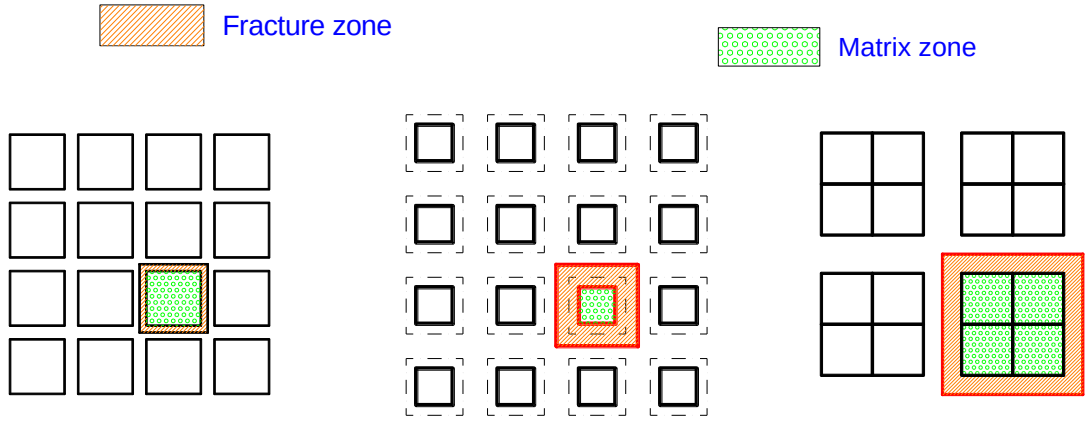

(a) Original state (b) Fracture dilation (c) Fracture coalescence

Figure 3.5 Schematic of the development of preferential pathways

As the spacing term in Eq. (3.38) is difficult to be quantified, an empirical transition function which is expressed as Eq. (3.39), is introduced to evaluate the effects of structure evolution:

$$f\left(\phi_f-\phi_{f0}\right)=\left(\frac{a}{a_0}\right)^2=\frac{A_t}{2}\left\{\tanh\left[B_t\left(\frac{\phi_f-\phi_{f0}}{\phi_{cr}}-1\right)\right]-\tanh\left(-B_t\right)\right\}+1 \tag{3.39}$$

where A_t, B_t and ϕ_{cr} are fitting parameters.

In order to provide a more intuitive understanding of the function above, it is plotted in Figure 3.6. The critical porosity is set to 0.015 at which the function value reaches half of the largest value and the slope at this point is the steepest. A_t is set to 5 to control the largest value of the function, and B_t is set to 3 which controls the slope of the transition function.

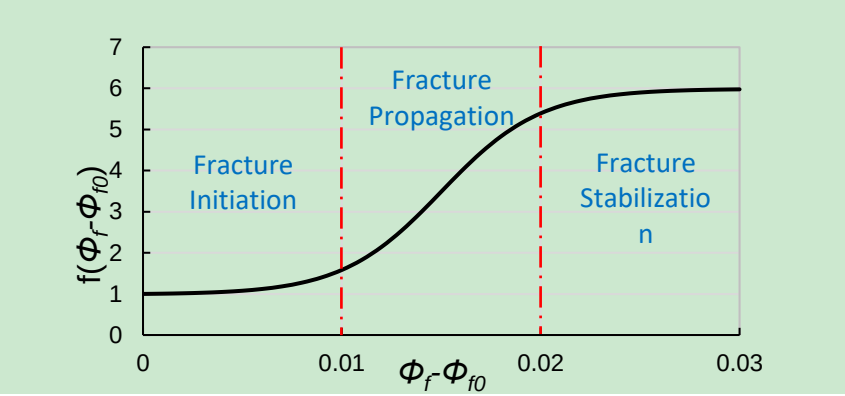

Figure 3.6 Shape of the transition function for permeability

The physical base for the proposed transition function is the development of preferential pathways during the period of gas breakthrough. Many experimental tests have proved the generation of micro-fractures within expansive clays after gas breakthrough (Graham et al. 2012; Horseman et al. 1999; Wiseall et al. 2015). The development of micro-fractures will induce a rapid increase in total permeability, and then give rise to the gas breakthrough behavior. In order to reflect this physical process, a transition function, Eq. (3.39), by using the hyperbolic tangent function is proposed to represent the spacing term in Eq. [38]. In addition, the transition function is also inspired by Chen et al. (2016) who proposed a logistic growth function to model the coal permeability in the post-failure state. As processed by Chen et al. (2016), the transition curve in this study can also be divided into three stages, i.e. fracture initiation, fracture propagation and fracture stabilization, see Figure 3.6.

Essentially, the basic idea of the new permeability model is originated from the well-known EFM, which can be identified from Eqs. (3.36)-(3.39). In order to incorporate the fracturing process, the EFM employed three empirical parameters, the fracture spacing (controlling the growth rate), the maximum aperture (controlling the maximum permeability), and the critical strain over which the cubic law is activated (Gerard et al. 2014; Olivella and Alonso 2008). Similarly, the new proposed model also introduced three empirical parameters which have similar functionalities to those in EFM. It should be noted that the introduced empirical parameters in both models have to be determined by fitting to the experimental curve due to the limitation of experimental data. Therefore, the EFM is equivalent to the proposed

permeability to some extent. However, the newly developed permeability model has an advantage over the EFM in that a smooth and continuous transition is allowed. This is beneficial to avoiding the convergence issues due to the discrete increase of intrinsic permeability when it is coupled with the gas entry value.

3.2.4.2.2 Water retention curve

The water retention curve (WRC) of the FC is given by the van Genuchten model (van Genuchten 1980) which is expressed as:

$$S_e = \left[1 + \left(\frac{p_c}{p_{gev}}\right)^n\right]^{-m} \tag{3.40}$$

where p_{gev} is the gas entry value, n is a fitting parameter and $m = 1 - 1/n$.

Fracture propagation accompanied by an increase in aperture can significantly reduce the gas entry value and then accelerate the desaturation process. The significance of this process in simulating gas breakthrough has been examined by Arnedo et al. (2013) who compared the numerical results with and without considering this process. In this study, the gas entry value of the FC is coupled with the intrinsic permeability by (Olivella and Alonso 2008) :

$$p_{gev} = p_{gev0}\left(k_{f0} / k_f\right)^{1/3} \tag{3.41}$$

3.2.4.2.3 Relative permeability

The widely used relative permeability model, i.e., the Mualem-van Genuchten model (Luckner et al. 1989; Mualem 1976; van Genuchten 1980), is used for the water flow within the FC, which is given as:

$$k_{rw}\left(S_e\right) = \sqrt{S_e}\left[1 - \left(1 - S_e^{1/m}\right)^m\right]^2 \tag{3.42}$$

where k_{rw} is the relative permeability of water in the FC.

The relative permeability of gas is somewhat more complex due to the gas entrapment. During the water imbibition process, a part of gas phase is trapped in the porous media as the form of blobs or ganglia (Juanes et al. 2006; Spiteri et al. 2008). As the trapped gas is immobile, both the relative permeability and the WRC present hysteresis behaviors when flow reversal occurs. Many models of this phenomenon have been proposed and applied in geotechnical engineering areas, such as oil and gas development and CO_2 geological storage (Doughty 2007; Juanes et al. 2006; Lenhard and Parker 1987; Parker and Lenhard 1987; Spiteri and Juanes 2006). However, hysteresis models have not yet been used to examine gas migration in bentonite. To gain a better understanding of the gas migration process, it is necessary to incorporate the hysteresis caused by gas entrapment into the coupled HM model. For simplicity, the hysteresis behavior in this study is assumed to only occur in the relative permeability of gas, as treated by Juanes et al. (2006).

The conceptual hysteresis model for the relative permeability of gas is shown in Figure 3.7. When gas saturation is on the bounding drainage curve, the relative permeability, k_{rg}^{d}, is calculated by using a power law, as shown in Eq. (3.43), which is widely used in the research topic at hand (Arnedo et al. 2013; Gerard et al. 2014; Gonzalez-Blanco et al. 2016):

$$k_{rg}^{d}\left(S_g\right) = A_k S_g^{n_k} + \delta \tag{3.43}$$

where A_k and n_k are fitting parameters, δ is a small constant (0.001) to ensure a minimum relative permeability, and S_g is the degree of saturation of gas.

When the water imbibition process takes place, the relative permeability of gas decreases along the scanning curve, as shown in Figure 3.7. Trapped gas saturation is calculated by using a trapping model given in Land (1968) and Juanes et al. (2006), which is expressed as:

$$S_{gt} = \frac{S_{gi}}{1 + C_L S_{gi}} \tag{3.44}$$

$$C_L = \frac{1}{S_{gtm}} - \frac{1}{S_{gim}} \tag{3.45}$$

where S_{gi} is the gas saturation at the reversal point, C_L is the Land trapping coefficient, S_{gim} is the maximum gas saturation, and S_{gtm} is the maximum trapped saturation on the bounding imbibition curve.

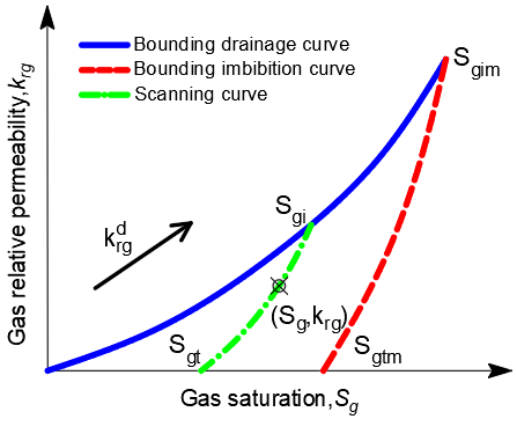

Figure 3.7 Hysteresis of relative permeability of gas phase (Modified from Juanes et al. (2006))

The relative permeability of gas on a scanning curve, k_{rg}, is calculated by using Killough's model (Killough 1976), which is expressed as:

$$k_{rg}(S_g) = k_{rg}^d\left(S_{gi}\right)\left(\frac{S_g - S_{gt}}{S_{gi} - S_{gt}}\right)^{n_h} \tag{3.46}$$

where k_{rg}^d is the relative permeability of gas on the bounding drainage curve, and n_h is a fitting parameter.

It should be noted that only the first-order scanning curve was considered for the hysteresis effects, which means that the drainage and imbibition process share the same scanning curve for a given gas saturation at the reversal point, S_{gi}.

3.2.4.2.4 Water exchange term

Once the gas infiltrates the saturated bentonite, the water in the PC may flow into the FC driven by the difference of water pressure between pores and fractures. The mass exchange model given by Warren and Root (1963) is adopted here, which is expressed as:

$$\Gamma_w = \xi_w \rho_{pw} \left(p_{pw} - p_{fw} \right) \tag{3.47}$$

where ξ_w is a fitting parameter controlling the water exchange rate between pores and fractures.

3.2.5 Model Validation and Simulation

In this section, the developed coupled HM model will be implemented into a FEM software called COMSOL Multiphysics, and then validated against experimental data. The field variables, i.e. the water and the gas pressure in the FC, the water pressure in the PC and the displacement components, are calculated by simultaneously solving the governing equations developed in previous sections. Then, the dependent variables are determined by their corresponding constitutive models. The developed coupled HM model is validated against three laboratory tests conducted under three types of boundary conditions, i.e., Mx80-4 test under a constant stress condition, Mx80-8 test under a constant volume condition, and Mx80-9 test under a K0 boundary condition.

3.2.5.1 Model parameters

Mx80 bentonite was used in all three tests but with different dry densities. Basic information on the bentonite samples is listed in Table 1, and readers can refer to (Harrington and Horseman 2003; Hoch et al. 2004) for more details.

Table 1 Basic information on the bentonite samples (Harrington and Horseman 2003)

Test No.	Dry density/g/cm^3	Void ratio	Diameter/mm	Length/mm
Mx80-4	1.670	0.659	49	49
Mx80-8	1.577	0.757	60	120
Mx80-9	1.568	0.767	51	51

The use of the concepts of double porosity and double effective stress has enhanced the capability of the coupled HM model to capture more experimentally observed behaviors. However, at the same time, the concepts have also generated many parameters to be determined. In this work, we determine the introduced parameters as reasonable as possible to run the simulation. A discussion about the determination of these parameters is given below. For clarity, the parameters are classified into two groups: one is the basic HM properties, and the other is the empirical parameters used in the proposed hydraulic constitutive models.

3.2.5.1.1 Basic hydro-mechanical properties

Values for the key HM properties are listed in Table 2.

Table 2 HM properties of saturated Mx80 bentonite

Test No.	Hydraulic properties			Mechanical properties			
	k_{f0}/m^2	p_{gev}/MPa	n	κ_f	κ_p	λ_p	υ
Mx80-4	5.79×10^{-21}	42.4					
Mx80-8	1.04×10^{-20}	30.3	1.5	0.07	0.05	0.15	0.3
Mx80-9	1.11×10^{-20}	29.5					

To determine the HM properties of the saturated bentonite as listed in Table 2, sophisticated experiments are needed to be conducted. Readers can refer to (Xu et al. 2017; Xu et al. 2016) for more details in measuring some important HM properties, such as the intrinsic permeability, the parameters for the WRC and the swelling pressure. The values of these parameters used in this paper are mainly extracted from the previous papers related to Mx80 bentonite.

The initial intrinsic permeability, k_{f0}, is determined based on an empirical model given in (Hoch et al. 2004), which is expressed as:

$$k_{f0} = \alpha_k e_v^{\gamma_k} \tag{3.48}$$

where e_v is the void ratio, α_k and γ_k are fitting parameters which are 3.45×10^{-20} m^2 and 4.28, respectively.

The gas entry value used in the van Genuchten model was estimated from the experimental data given by Villar (2005). The data showed that there is an approximately linear relationship between the parameter, α_{vG}, corresponding to the reciprocal of the gas entry value, and the dry density. This linear relationship will be adopted in this paper to determine the gas entry value for the three tests. However, it should be noted that this approximation is based on limited experimental data, and more experimental works are required to develop a stronger relationship between the two parameters. The shape parameter, *n*, was set as 1.6 for modelling gas migration in Mx80 bentonite by Gerard et al. (2010). However, it was found in the following simulations that the convergence rate is very sensitive to the shape parameter, and a smaller value gives a good convergence. Thus, the shape parameter for all three tests in this paper is set as 1.5. More future works are needed to tackle this convergence issue.

Determining the elastic and plastic constants, i.e. κ_f, κ_p and λ_p, for double porosity media is less easy compared with the case of single porosity media. Li et al. (2016) indicated that the elastic constant for the microstructure can be determined by using two types of approaches during wetting and drying processes, i.e., the MIP test and the consolidation test for highly over-consolidated soils. As for the elastic constant for the macrostructure, general unloading/reloading tests on saturated expansive soils can be used. Due to the lack of experimental data, the κ_p and λ_p values for the PC, and the Poisson's ratio are obtained from Abed et al. (2016) who also studied Mx80 bentonite. The compression index for the FC, κ_f, is set to 0.07 based on an assumption that the FC is somewhat softer than the PC. The current experimental data is not enough to estimate the porosity for both the FC and PC. In a report by Zheng et al. (2017), the residual degree of saturation was assumed to be 0.9 for saturated Mx-80 bentonite. Here, we consider the residual water as the water in the PC. Then, accounting for the different dry densities adopted in the three tests, the initial fraction of the porosity of the

FC to the total porosity is assumed to be 0.1, 0.15 and 0.15 for Mx80-4, Mx80-8, and Mx80-9 tests, respectively.

3.2.5.1.2 Empirical parameters

The empirical parameters for the hydraulic constitutive models are listed in Table 3.

Table 3 Parameters for hydraulic constitutive models

Test No.	Intrinsic permeability model			Relative permeability model				Water exchange term
	A_t	B_t	Φ_{cr}	A_k	n_k=n_h	S_{gim}	S_{gtm}	ξ_w / m*s/kg
Mx80-4	36	1.2	0.013	3	3	1	0.03	6.48×10^{-14}
Mx80-8	100	1.3	0.036	1	3	1	0.04	1.80×10^{-13}
Mx80-9	50	1.7	0.008	5	2	1	0.12	1.08×10^{-13}

It can be seen from Table 3 that the values of the empirical parameters vary from one test to another, although the used bentonite is the same. Several factors may lead to these variations.

(1) The dry density used in each test is different from each other. Dry density, as an important parameter for saturated bentonite-based materials, affects many HM properties, such as the intrinsic permeability, gas entry value, swelling ability (Xu et al. 2017). The differences in these HM properties may induce the variations of the empirical parameters.

(2) The heterogeneous distribution of HM properties may also be an important factor influencing the empirical parameters. Within the sample of different heterogeneous distribution, the developed preferential pathways may follow different trajectories, and therefore the developed pore structure may vary from one sample to another. As a result, the empirical parameters introduced in this paper, which are used to govern the dynamic process, may also be different for different samples, even though the used materials are the same.

(3) Boundary conditions may also affect the values of the empirical parameters. As stated by Graham et al. (2012), the number and location of the outflow sinks influence the gas pressure at breakthrough significantly. For the boundary having outlets of a small area, a denser fracture network is required to connect with the outlets. The developed pore

structures may vary with different boundary conditions, thus leading to different values for the empirical parameters.

In summary, the dilatancy-controlled flow is a dynamic process which is not only influenced by the test materials, but also depends on the developed pore structure during the fracturing process. More details about the characteristics of this dynamic process have been given by Graham et al. (2012). At present, both theoretical and experimental studies are still inadequate to evaluate the evolution of pore structure quantitatively. Therefore, the introduced empirical parameters have to be determined by fitting the experimental curve. To date, this is a widely used treatment for simulating the gas migration processes in low permeable porous media, for example, see (Gerard et al. 2014; Olivella and Alonso 2008; Tawara et al. 2014; Xu et al. 2013). To better determine these parameters, more experimental and theoretical efforts should be performed in the future.

3.2.5.2 Modelling of gas injection

The injection of gas into a bentonite sample has been experimentally carried out by compressing a certain amount of helium in a gas vessel by injecting water at a constant volume rate. Then, the gas pressure would increase in accordance with the ideal gas law if no gas flows out. In the previous literature, this process has been simulated by using the two phase flow model (Arnedo et al. 2008). This approach seems relatively complicated for such an auxiliary component. In this study, the gas vessel is also regarded as a porous medium where, however, only gas exists. Gas compression is carried out by reducing the porosity at a rate that corresponds to the water pumping rate, which can be expressed as:

$$\dot{\phi}_{gv} = -q_{wi} / V_{ac} \tag{3.49}$$

where $\dot{\phi}_{gv}$ is the reduction in the rate of porosity, q_{wi} is the water pumping rate, and V_{ac} is the actual volume of the gas vessel.

Compared with previous approaches, the approach used in this study has two advantages. First, the use of the two phase flow theory is avoided by introducing Eq. (3.49). This

substantially simplifies and stabilizes the gas injection model. Another advantage of this approach is that the volume of the simulated vessel can be much smaller than the real volume by increasing the porosity with a corresponding multiplier; see Eq. (3.50)

$$V_{gv} = \left(\frac{1}{\theta_{in}} V_{ac} \right) \cdot \left(\theta_{in} \phi_{gv} \right) = V_{si} \phi_{sgv} \tag{3.50}$$

where V_{ac}, V_{si} are the actual and the simulated volumes of the gas vessel, respectively, ϕ_{gv}, ϕ_{sgv} are the actual and the simulated porosities of the gas vessel, respectively, V_{gv} is the volume of gas in the vessel, and θ_{in} is a multiplier that controls the volume of geometry.

Eq.(3.50) shows that the initial simulated porosity could be larger than unity if the modelled volume is less than the real case, but mathematically, this treatment would not affect the simulated results. By applying Eq.(3.50), the dimensions of the simulated vessel can be very small, which reduces the number of meshing elements and increases computational efficiency.

3.2.5.3 Simulation results for Mx80-4 test

3.2.5.3.1 Initial and boundary conditions

Mx80-4 test was conducted under a constant stress condition. The meshed geometry for the simulated sample is shown in Figure 3.8. The boundary number is labelled alongside its corresponding boundary. Due to the axisymmetric condition, only half of the sample is modelled, and the left boundary (Boundary 4) represents the symmetrical axial.

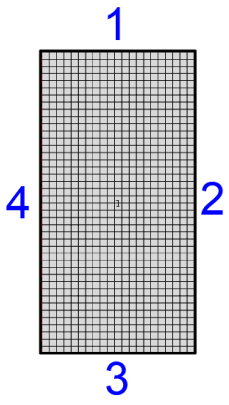

Figure 3.8 Geometry and meshing of sample in Mx80-4 test (1, 2, 3 and 4 are boundary numbers)

As discussed by Swift et al. (2001), the gas flow behavior at the bottom of the sample is still not physically clear, and the pathways may switch between closing state and opening state, thus inducing an intermittent flow behavior. Constant gas pressure is commonly used as the boundary condition on the outlet. However, this boundary condition may lead to an inertial area close to the boundary which responses marginally to the increase of the gas pressure in the vessel. Thus, it may not be appropriate to reflect real cases. In this model, a mass flux boundary condition is applied, which is expressed as:

$$Q=\begin{cases}\rho_{fg}\dfrac{k_{fg}k_{rg}}{\mu_g d_m}\left(p_{fg}-p_{cr}\right), & p_{fg}>p_{cr}\\ 0, & p_{fg}\le p_{cr}\end{cases} \tag{3.51}$$

where d_m is a characteristic length set to 1 mm for all of the simulations in this paper, p_{cr} is a critical pressure (slightly higher than the initial gas pressure to avoid convergence issue) above which the gas outflow is initiated.

Details on the HM boundary conditions are provided in Table 4.

Table 4 HM boundary conditions for Mx80-4 test

Boundary No.	Hydraulic Boundary			Mechanical Boundary
	Gas in FC	Water in FC	Water in PC	
1	Connect to gas vessel	No flow	No flow	Roller
2	No flow	No flow	No flow	16[MPa]
3	Mass flux Eq. (3.51)	1.01[MPa]	No flow	16[MPa]
4	Axisymmetric Boundary			

The initial water pressures in fractures and pores were 1.01 [MPa], and initial gas pressure in fractures was 1.06 [MPa] which was slightly higher than the initial water pressure to avoid convergence issues. However, the initial degree of saturation was still close to unity due to the high gas entry value. The initial effective stress was set to -14.99 [MPa] to achieve initial stress equilibrium. The pre-consolidation pressure was set to 15.1 [MPa] which was slightly higher than the absolute value of the initial effective stress to avoid convergence issues.

3.2.5.3.2 Results and discussion

(I) Changes of gas pressure and outflow rate

Figure 3.9 (a) and 9(b) show the comparisons between the simulated and the observed results with respect to the changes in gas pressure in the vessel and the outflow rate at a standard temperature and pressure (STP) condition, respectively. The entire injection test was divided into two injection cycles based on the water pumping rate; see Figure 3.9 (a). In general, the simulated results for both the gas pressure and the outflow rate are in good agreement with the observed results in the two injection cycles. Specifically, the gas breakthrough phenomenon is successfully captured in the first cycle of injection, which is characterized by a sharp decline in both the gas pressure and the outflow rate. Before gas breakthrough took place, the gas pressure gradually increased in accordance with the ideal gas law, and there was almost no gas that flowed out. Upon reaching the peak value, both the gas pressure and flow rate showed a rapid decline and then gradually approached an asymptotic value. During the transient stage in the termination of gas injection, the simulated gas pressure declined rapidly, and then gradually deviated from the observed value with time. Correspondingly, the simulated outflow rate did not decline as quickly as the measured rate after the termination of gas injection, as shown in Figure 3.9 (b). There appear to be two reasons for the discrepancies: (1) the simulated preferential pathways close more slowly than those in a real situation due to the possible overestimation of the plastic strain, and (2) the homogeneous HM properties adopted in the model cannot describe the local closure of developed fractures which may occur in real materials.

In the second injection cycle, the gas breakthrough is less intense than that in the first cycle of injection because (1) the gas pressure/outflow rate cannot reach a peak value that is as high as the peak value of the first cycle, and (2) the reduction in the gas pressure/outflow rate after the peak value is less obvious. Previous studies have stated that this behavior might result from plastic strain, creep strain as well as gas entrapment in the developed fractures (Hoch et al. 2004; Horseman et al. 1999; Swift et al. 2001). Specifically, the irreversible plastic strain prevents the complete closure of the developed fractures, and creep strain cannot recover

immediately when the gas pressure starts to decrease. The gas entrapped in the sample would lower the gas entry value and might be preferentially connected as a continuous phase once the gas injection is restarted. These three processes reduce the flow resistance of the sample, and therefore the peak value in the second gas breakthrough event is lower than that in the first breakthrough event. The simulated results for the subsequent reduction of the water pumping rate are also in good agreement with the observed results. After the termination of gas injection, the gas pressure gradually approached an asymptotic value which is known as the “shut-in” pressure (Horseman et al. 1999).

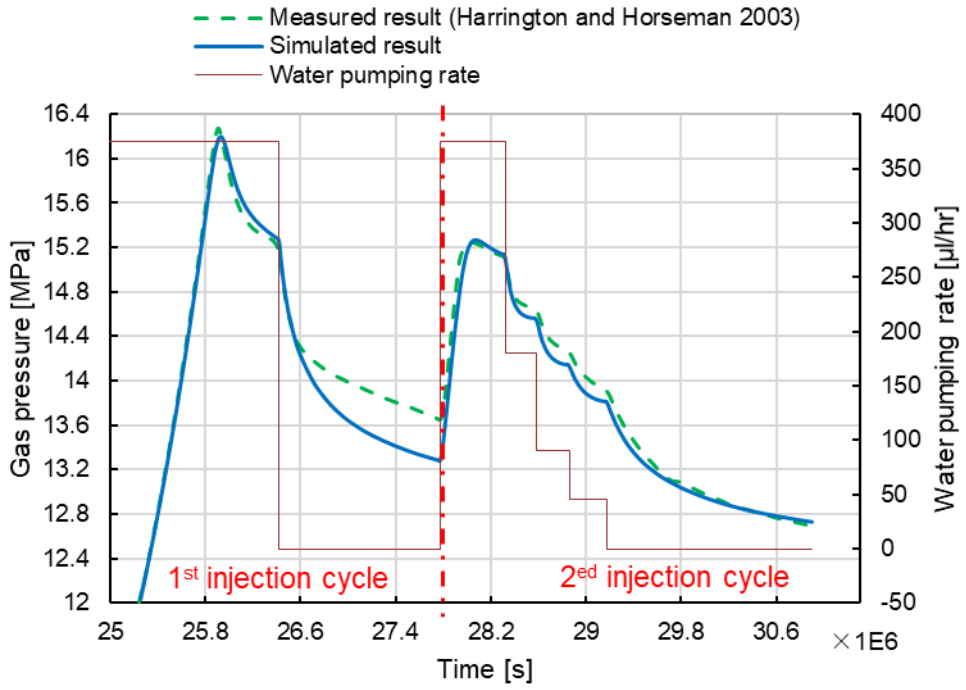

(a) Gas pressure in the gas vessel

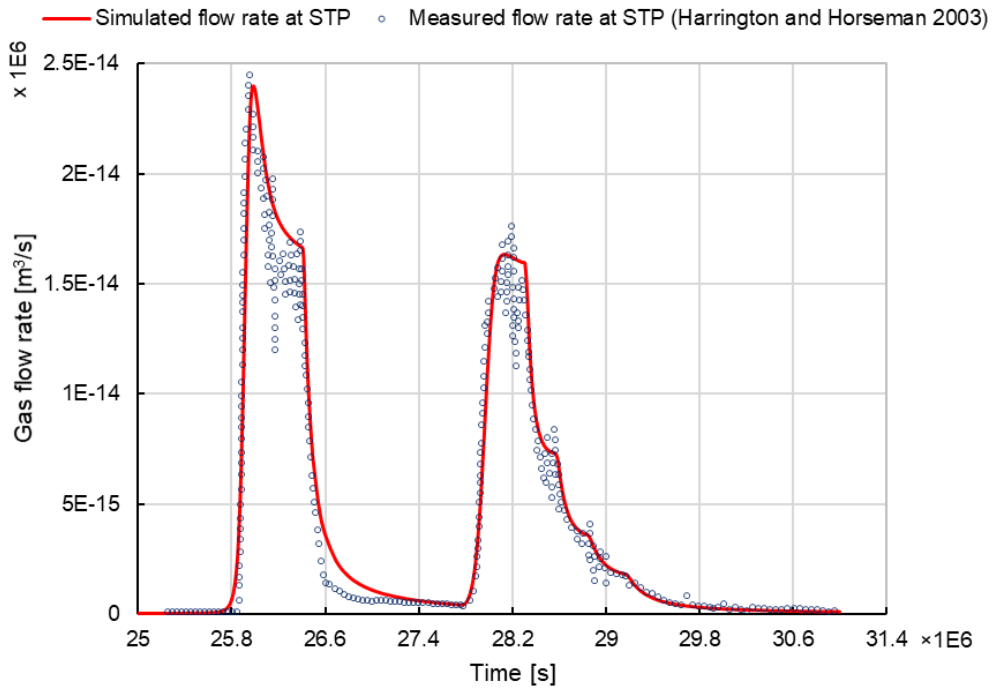

(b) Flow rate out of the sample

Figure 3.9 Comparison between the simulated and the measured results (STP: standard temperature and pressure)

(II) Changes of volumetric strain of PC, FC and FPM

Figure 3.10 presents the changes in the volumetric strain of the FC, PC and FPM. The opening/closure of the developed fractures is represented by the volumetric strain of the FC. According to Eq. (3.2), the volumetric strain rate of the FPM is equal to the sum of the volumetric strain rates of the FC and the PC. Therefore, both the dilation of the FPM and the consolidation of the PC would induce the opening of the developed fractures. This is successfully captured by the model, as seen in Figure 3.10. This simulated result is consistent with the conclusions of Swift et al. (2001) and Hoch et al. (2004) who claimed that the void space of developed pathways may result from the compression of water, the consolidation of clay matrix and the dilation of the sample volume. Although no experimental data are available to quantitatively validate the developed model in terms of the changes in volumetric strain, the physical processes represented by the simulation results can be qualitatively validated by other experimental results. For instance, the gas injection tests on different clay materials (Gonzalez-Blanco et al. 2016; Wiseall et al. 2015) have shown that volumetric dilation and consolidation indeed occur upon gas breakthrough.

Furthermore, the trend in the changes of the volumetric strain of the FC, PC and FPM is very similar to that of the gas pressure in Figure 3.9(a). During the period of gas breakthrough, both the dilation of the FPM and the compression of the PC underwent rapid changes, which led to a substantial increase in gas permeability. However, as the constant stress condition allows the sample to deform both radially and axially, the increase of total stress is not significant when high-pressure gas infiltrates the sample. Consequently, the consolidation of the PC only contributed marginally to the dilation of the developed fractures, compared with the predominant contribution from the dilation of the FPM. In addition, the plastic behavior of the PC was successfully captured by the developed elastoplastic model. During the whole simulation, the plastic strain only occurred in the first injection cycle. This may result from that the gas pressure in the second injection cycle could not reach the peak value as that in the first injection cycle, and therefore the pre-consolidation pressure could not be exceeded.

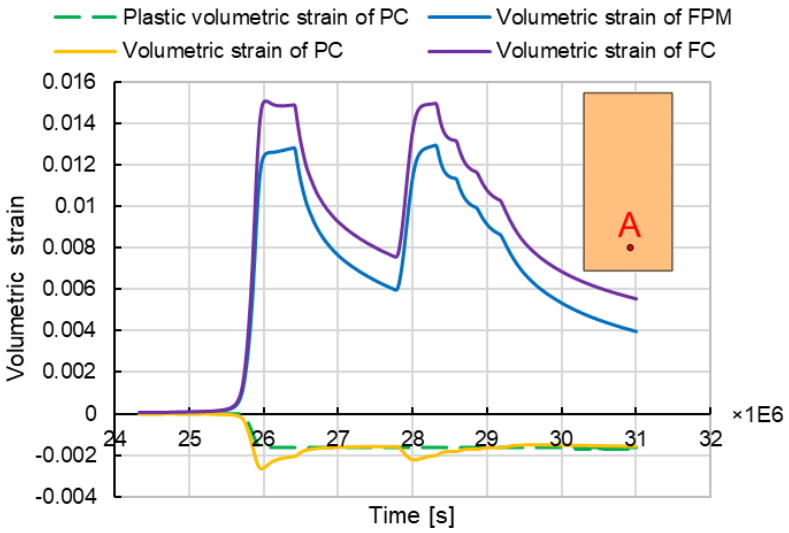

Figure 3.10 Changes in volumetric strain of PC, FC and FPM at Point A

3.2.5.4 Simulation of Mx80-8 test

3.2.5.4.1 Initial and boundary conditions

In the field, buffer materials are constrained by the surrounding rocks and the copper canister used in the EBS, and therefore all physicochemical processes are expected to proceed under a constant volume condition. Moreover, naturally occurring and excavation induced fractures around the wall of disposal boreholes serve as preferential pathways for gas migration. Thus, to realistically simulate field conditions, Mx80-8 test was conducted under a constant volume condition and the flow path was along the radial direction (Harrington and Horseman 2003). The geometry of the sample used in Mx80-8 test was a cylinder with a hole drilled along the center line. The geometry and meshing strategy are also illustrated see Figure 3.11. The simulation results with finer mesh are given in Appendix E. The boundary number is labelled alongside its corresponding boundary. Gas was injected into the bentonite sample at the center of the cylinder through a steel tube that was inserted into the drilled hole, and gas was only allowed to flow through three sets of sinks (four filters in each set) around the periphery of the sample (Harrington and Horseman 2003). It should be noted that the 3D geometry of the sample is simplified as an axisymmetric 2D geometry in this study. The locations of these three sets of sink filters are shown as Boundary 2 in Figure 3.11. The outer boundaries of the sample are

constrained by a stainless steel vessel. Therefore, the sample cannot dilate during the entire testing period. The HM boundary conditions are listed in Table 5.

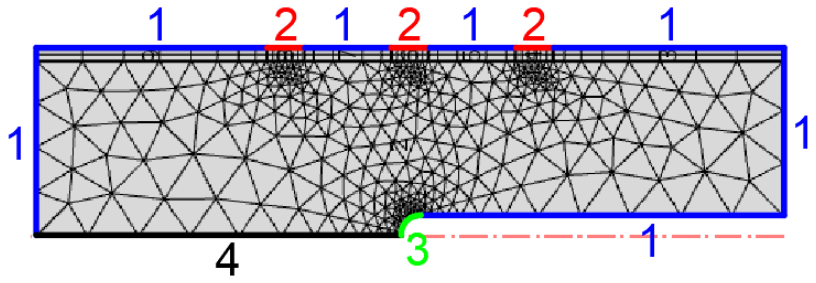

Figure 3.11 Geometry and meshing of sample in Mx80-8 test (1, 2, 3 and 4 are boundary numbers)

Table 5 HM boundary conditions for Mx80-8 test

Boundary No.	Hydraulic Boundary			Mechanical Boundary
	Gas in FC	Water in FC	Water in PC	
1	No flow	No flow	No flow	Roller
2	Mass flux Eq.(3.51)	1[MPa]	No flow	Roller
3	Connect to gas vessel	No flow	No flow	Roller
4	Axisymmetric Boundary			

As stated by Horseman et al. (1999), the swelling pressure can be interpreted as the effective stress for a high swelling clay. The swelling pressure for Mx80 bentonite can be determined by an empirical model given in (Hoch et al. 2004), which is expressed as:

$$p_{sw} = \frac{\alpha_s}{e_v^{\gamma_s}} \tag{3.52}$$

where e_v is the void ratio, the fitting parameters α_s and γ_s were determined to be 1.963 MPa and 4.85 respectively.

Then, the initial effective stress, i.e. the minus value of swelling pressure, was determined as -7.57 [MPa]. The pre-consolidation pressure was set to 7.67 [MPa]. The initial water pressures in fractures and pores were 1.0 [MPa], and initial gas pressure in fractures was 1.05 [MPa].

Compared with Mx80-4 test, the testing procedures of Mx80-8 test were more complex, as the gas volume was also increased during the testing period besides controlling the water pumping rate. As the initial amount of gas was not sufficient to complete the entire test, the gas amount in the injection vessel was increased for three times which naturally divided the test into four stages. The initial gas amount and the first increase of the gas amount were estimated by fitting the tested curve based on the ideal gas law. Information for the second and third increases of gas amount was obtained from Dr. Harrington (personal communication, Sep 14th, 2017). Details on these three increases of gas amount are provided in Table 6. For each increase event, while the gas pressure remained unchanged, the gas volume was increased based on the values given in Table 6.

Table 6 Increases in gas volume during Mx80-8 test

Event	Time/d	Pressure/MPa	Added volume of gas /mL
Initial state	0	1.05	306.9
1	28.1	5.84	56.0
2	38.3	14.2	139.7
3	121.24	8.54	99.8

3.2.5.4.2 Results and discussion

(I) Change of gas pressure

Figure 3.12 shows the changes in the gas pressure in the vessel, and Figure 3.13 presents the distribution of gas pressure in the FPM at different points of time. The red dashed lines in Figure 12 represent the three events of gas volume increase which separates the testing into four stages, i.e. Stages Ⅰ, Ⅱ, Ⅲ and Ⅳ. In Stages Ⅰ and Ⅱ, the simulated curve is in good agreement with the experimental curve. When the gas injection was initiated, the pressurized gas evenly infiltrated the sample from the inlet, as shown in Figure 3.13(a). During this period, the dilation of the developed fractures was not enough for the pressurized gas to reach the outlets. Therefore, the mass flux on the outlet boundary was very small according to Eq. (3.51), and the gas pressure in the vessel increased in accordance with the ideal gas law.

During the transient stage of the gas breakthrough, the preferential pathways developed rapidly, and then the high-pressure gas permeated most of the sample; see Figure 3.13(b). The gas pressure around the outlets reached about 14 [MPa], which would induce a significant gas outflow on the outlet boundary. Then, the significant gas breakthrough phenomenon was successfully captured by the developed model.

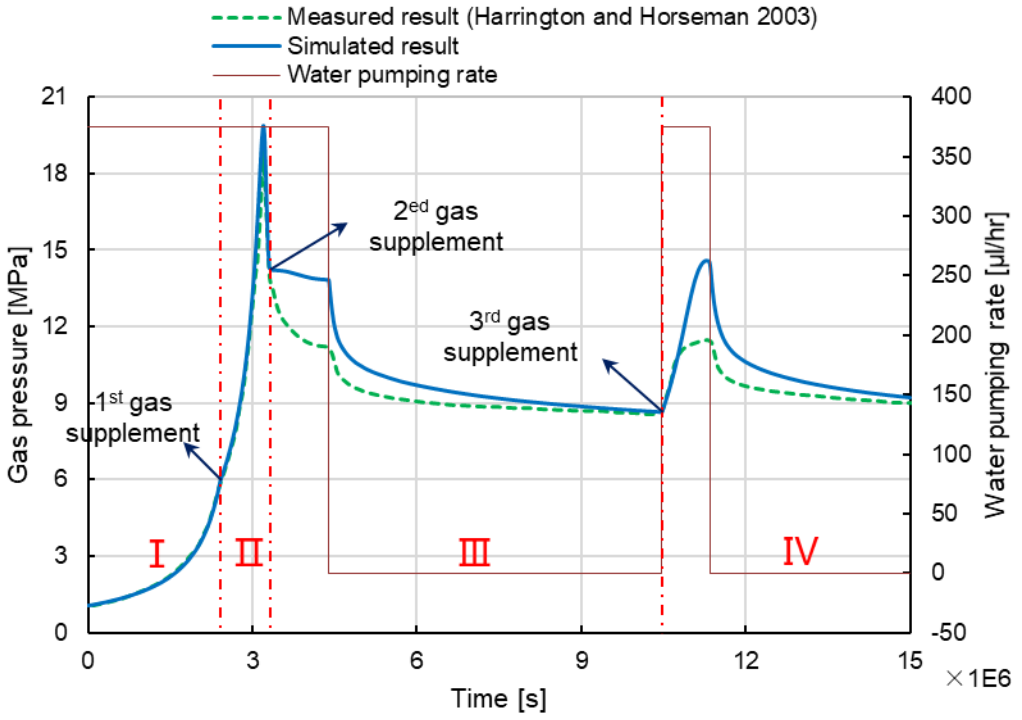

Figure 3.12 Changes in gas pressure in gas vessel

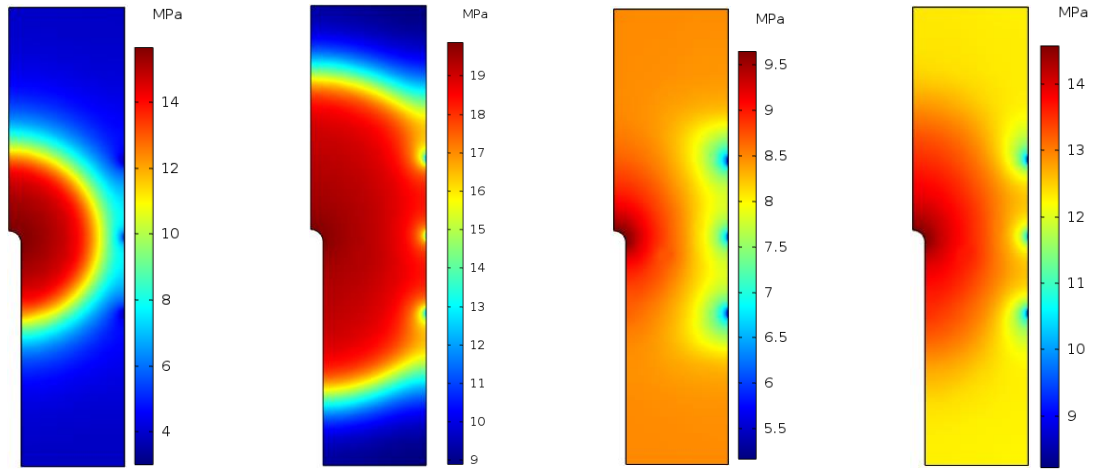

(a) t=3.080×10⁶[s] (b) t=3.2×10⁶[s] (c) t=6.100×10⁶[s] (d) t=1.130×10⁷[s]

Figure 3.13 Distribution of gas pressure in FPM

At the beginning of Stage Ⅲ, the gas volume in the vessel was increased for the second time. Based on the ideal gas law, the rate of reduction in gas pressure is expected to decrease. This was reflected by the simulated result, but the decreasing rate was much greater than that of real cases, thus leading to the overestimation of the gas pressure after the second gas supplement. After the termination of gas injection, the gas pressure consistently evolved with the experimental curve, and then approached the "shut-in" pressure (around 9.0 [MPa]). At the steady state, the gas pressure around the outlets decreased to about 6 [MPa]; see Figure 3.13(c). Again, this inhibited the gas outflow and the gas pressure in the vessel levelled off at the "shut-in" pressure.

At the beginning of Stage Ⅳ, the gas volume was increased for the third time and the gas injection rate (375 μL/hr) was also recovered. The simulated gas pressure increased to a peak value with the same slope as that of the experimental curve. However, the simulated peak value was higher than the experimental one, which may be caused by the overestimation in Stage Ⅲ. As shown in Figure 3.13(d), the relatively high gas pressure around the outlets recovered at the time of the second gas breakthrough. However, due to the damage caused by the first gas breakthrough, the gas pressure at the outlet boundaries could not reach a value that is as high as the value at the first gas breakthrough. Therefore, the second gas breakthrough was less significant than the first breakthrough in terms of the peak value and the rate of decrease in gas pressure after the peak value of gas pressure; see Figure 3.12. After the termination of gas injection, the gas pressure in the vessel again approached another asymptotic value.

In general, the simulated results show that the developed model is able to capture several important phenomena observed in Mx80-8 test: (1) the significant gas breakthrough in the first cycle of gas injection; (2) the less significant gas breakthrough in the second cycle of gas injection; and (3) the "shut-in" pressure after the termination of gas injection. However, the developed model was unable to detect some of the spatially and temporally dependent characteristics observed in experiments. The experimental results showed that the developed pathways are not stable during the gas flow process, and the gas flow in subsequent injection

cycles may not flow through the pathways created in previous cycles (Graham et al. 2012). In contrast, the simulated results show that the gas pressure is evenly and continuously distributed in the sample, which should result from the assumption of homogeneous HM properties in the current model.

(II) Changes of volumetric strain of PC, FC and FPM

Figure 3.14 presents the evolution of the volumetric strain of the FC, PC and FPM during the entire simulation period. The volumetric strains of both the FC and the PC followed a similar evolution trend as the gas pressure does in Figure 3.12. At each breakthrough event, the volumetric strain experienced a sharp change (i.e. dilation for the FC and compression for the PC). The change presented more significantly at the first breakthrough than that at the second one. This may be attributed to the fact that the damaged sample at the second breakthrough is not able to sustain a peak gas pressure as high as that at the first breakthrough.

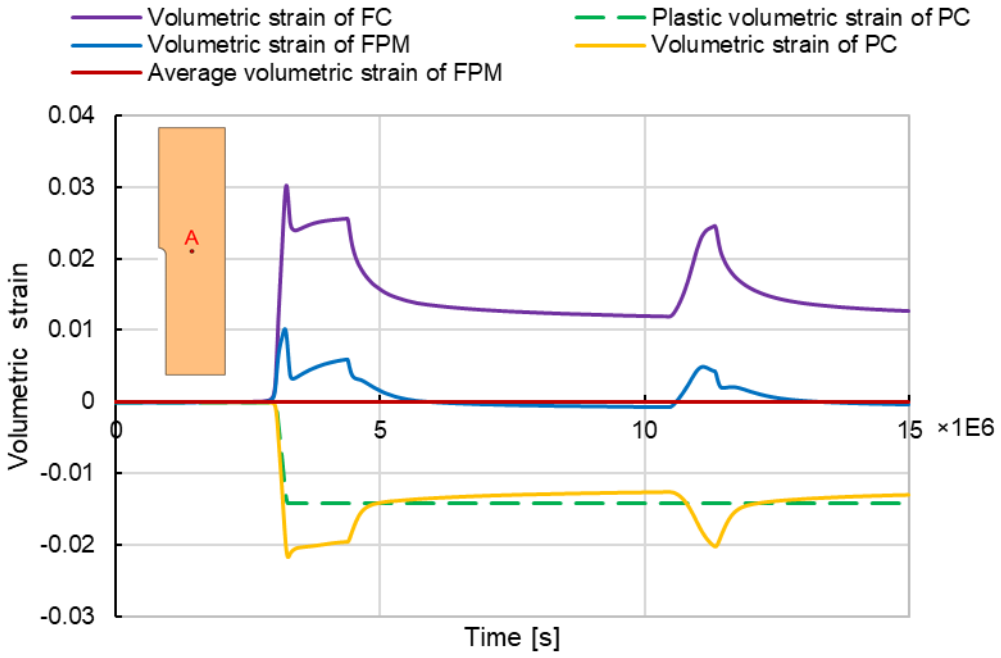

Figure 3.14 Changes in volumetric strain of PC, FC and FPM at Point A

The average volumetric strain over the entire volume of the FPM, as seen the red line in Figure 3.14, always remained at zero during the simulation. This validates the rationality of the boundary condition used in the simulation to represent the constant volume condition. In contrast, the volumetric strain of the FPM at a specific point A experienced an increasing trend

at each gas breakthrough event. This comparison reveals that the dilation and the compression of the FPM may simultaneously take place in the sample but distribute in different areas. As shown in Figure 3.15, the dilation mainly occurs around the inlet while the compression concentrates around the outlets. From a physical viewpoint, the dilation around the inlet inevitably compresses the material beside the boundary where the outlets are located. As the gas and the water within FPM are allowed to flow out through the outlets, the compression of the FPM will preferably take place around the three outlets. However, it is still not clear whether this result is consistent with real cases, as the hydraulic boundary conditions on the outlets are very complex to be numerically expressed (Swift et al. 2001).

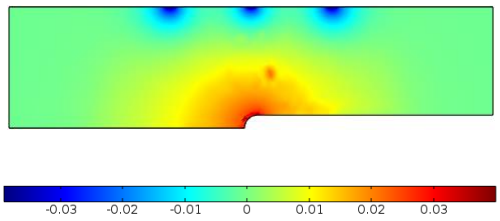

Figure 3.15 Distribution of volumetric strain of FPM

In comparison to the simulation results for Mx80-4 test, there are two distinctions that need to be addressed. First, both the FC and the PC undergo more abrupt changes in the volumetric strain at each breakthrough event for Mx80-8 test. This may be the cause that the gas breakthrough presents more prominently in Mx80-8 test. Another distinction is that the dilation of the developed micro-fractures (represented by the volumetric strain of the FC) mainly results from the consolidation of the PC in Mx80-8 test, rather than the dilation of the FPM as in Mx80-4 test. In particular, almost the entire dilation of the FC stems from the consolidation of the PC beyond the period of gas breakthrough. This simulation result indicates that the porosity transformation from pores to fractures plays a predominant role in the development of preferential pathways under constant volume condition. From the physical viewpoint, when the high-pressure gas infiltrates the sample, the total stress experiences a rapid increase due to the constraint from the constant volume condition. This could facilitate the consolidation process of the PC, and then, more pores are transformed into fractures.

In summary, the consolidation of the PC is a predominant process in realizing the development of preferential pathways under constant volume condition. Without considering this process, the fracture spaces are solely generated from the dilation of the FPM, which is not sufficient to trigger gas breakthrough. However, the heterogeneous distribution of the HM properties may enhance/inhibit the dilation of the FPM at some areas with low/high flow resistance, respectively. This would induce a random distribution of the developed pathways, and then contribute to a strong preferential gas flow. More future works would be conducted on the effects of soil heterogeneity on the development of preferential pathways.

(III) Changes of water pressure in fractures and pores

The build-up of pore water pressure during the period of gas breakthrough is an important behavior observed in Mx80-8 test (Harrington and Horseman 2003). However, previous models have not yet simulated the evolution of pore water pressure. As a supplement, the proposed coupled HM model presents a satisfactory capability to capture this behavior. As seen in Figure 3.16, water pressures in both pores and fractures experienced dramatically increasing trends during the first and the second period of gas breakthrough at point A. From a viewpoint of physics, the build-up of water pressure within pores and fractures is essentially caused by the infiltration of high-pressure gas into the sample through the developed pathways. In order to explain the simulation results from both the temporal and the spatial scale, the time evolution curves of the water pressure (as seen in Figure 3.16), will be analyzed together with the distributions of the difference of water pressure between pores and fractures, $p_{pw} - p_{fw}$, at four specific points of time (i.e. t_1, t_2, t_3 and t_4 in Figure 3.16(a)), as seen in Figure 3.17.

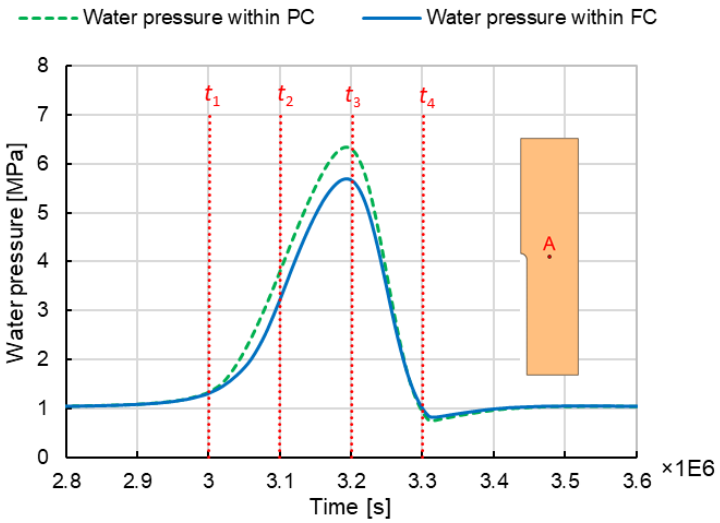

(a) During the period of the first gas breakthrough

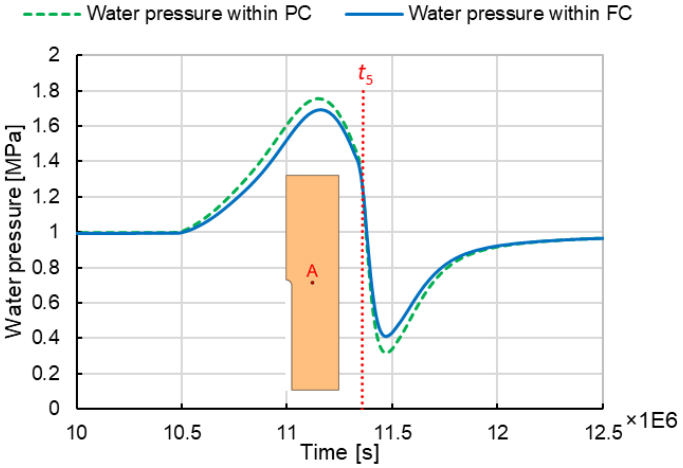

(b) During the period of the second gas breakthrough

Figure 3.16 Changes in water pressure in pores and fractures at Point A

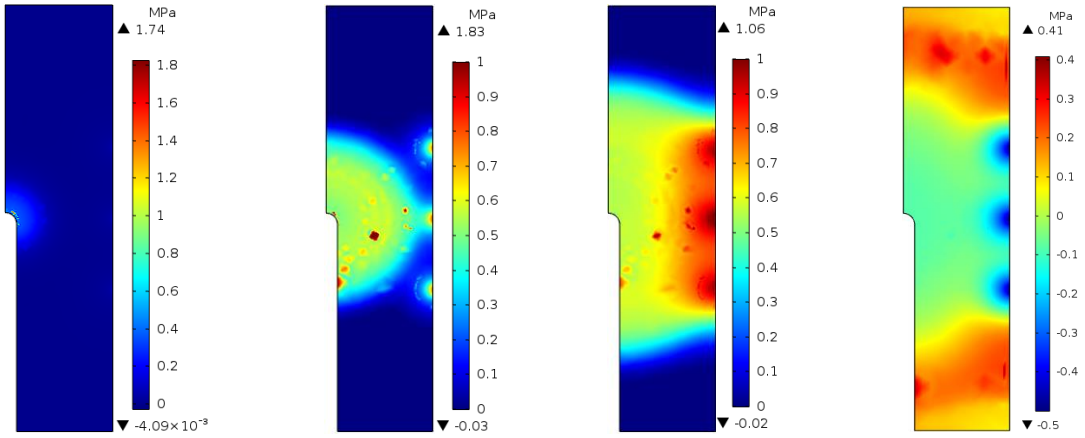

(a) $t=t_1$ (b) $t=t_2$ (c) $t=t_3$ (d) $t=t_4$

Figure 3.17 Distribution of the difference in water pressure between PC and FC

For $t \leq t_1$, the gas pressure was not high enough to induce preferential pathways, and the pressurized gas could hardly infiltrate the sample. Therefore, the water pressure was marginally affected by the pressurized gas, and remained almost at its initial value, as seen in Figure 3.16(a). At $t=t_1$, the water pressure in pores was almost identical to that in fractures for the most part of the sample, as seen in Figure 3.17 (a). This means that there was almost no water exchange and therefore no porosity transformation between pores and fractures.

From $t=t_1$ to $t=t_3$ (at which gas breakthrough took place), the gas pressure was sufficiently high to trigger the development of preferential pathways. The pressurized gas was able to infiltrate the sample through the developed pathways, and then the surrounding matrix was compressed. As the pore water could not be drained from the matrix immediately because of its small pore size, a part of load exerted by the gas pressure was sustained by the pore water, and then the water pressure within pores built up. Meanwhile, as the drainage of water in fractures was not sufficient, which may be caused by the high gas entry value, to counteract the effects of the rapid increase in gas pressure, a part of gas pressure transferred to the water, and then the water pressure in fractures also experienced an increasing trend. As seen in Figure 3.16(a), the increasing rate of the water pressure in pores was larger than that in fractures. The resultant difference of water pressure will act as a driving force for the water transfer from pores to fractures, as seen Eq. (3.47), thus inducing the porosity transformation according to the proposed conceptual model. In the spatial scale as seen in Figure 3.17 (a), (b) and (c), the area with a large value of the difference in water pressure extended from the inlet to the majority of the sample, and finally reached the outlets. It can be expected that the process of porosity transformation would also follow a similar evolution trend as that of the difference in water pressure.

For $t_3<t<t_4$, a great amount of gas flowed out of the sample, and the gas pressure declined abruptly, as seen in Figure 3.16(a). During this period, the water pressure in pores and fractures, following an evolution trend that is opposite to the trend before the gas breakthrough event, experienced a sharp decrease. At $t=t_4$, the difference of water pressure between pores and fractures recovered to almost zero in the middle part of the sample, as seen in Figure 3.17(d).

In addition, the difference in water pressure around the three filters was negative, which means that the water would transfer from fractures to pores. The negative value may result from the decrease of water pressure in pores, as the water pressure of the FC on the outlet boundary is set as a constant, i.e. 1[MPa]. The dilation of the matrix due to the rapid decrease in gas pressure may give rise to the reduction of water pressure in pores. However, it is still not fully clear whether this result is consistent with experiments, as the hydraulic boundary conditions on the outlet are very complex in real cases (Swift et al. 2001).

In the second cycle of gas injection (Stage Ⅳ), the damaged sample has a lower flow resistance compared with the intact one in the first cycle of injection (including Stage Ⅰ, Ⅱ and Ⅲ) due to the partially closed fractures. Therefore, the peak gas pressure sustained by the damaged sample cannot reach a value as high as that in the first cycle of injection. Correspondingly, the highest water pressure within pores and fractures is also lower at the second gas breakthrough event, as seen in Figure 3.16 (b).

It should be noted here that a rapid reduction in water pressure after the second termination of gas injection ($t=t_5$), as seen in Figure 3.16(b), was not observed in the previous experiments. This may be a numerical issue caused by the abrupt decrease of water pumping rate; see the brown line in Figure 3.12. With the time elapsing, the impact of the termination of gas injection diminished and the system returned to the original state, as seen in Figure 3.16 (b).

3.2.5.5 Simulation of Mx80-9 test

3.2.5.5.1 Initial and boundary conditions

Mx80-9 test was conducted under a K0 boundary condition which means that the sample was radially constrained and only deformation in the axial direction was allowed. The meshed geometry of the sample in Mx80-9 test is similar to that in Mx80-4 test, as shown in Figure 3.8. The HM boundary conditions are provided in Table 7.

Table 7 HM boundary conditions for Mx80-9 test

Boundary No.	Hydraulic Boundary			Mechanical Boundary
	Gas in FC	Water in FC	Water in PC	
1	Connect to gas vessel	No flow	No flow	Roller
2	No flow	No flow	No flow	Roller
3	Mass flux Eq. (3.51)	1.0[MPa]	No flow	10[MPa]
4	Axisymmetric Boundary			

The initial effective stress was set to -9 [MPa] to achieve an initial stress equilibrium. The pre-consolidation pressure was set to 9.1 [MPa]. The initial water pressures in fractures and pores are 1.0 [MPa], and initial gas pressure in fractures is 1.05 [MPa].

3.2.5.5.2 Results and discussion

(I) Change of gas pressure

Figure 3.18 shows the changes in gas pressure with time, as well as the water pumping rate in gas vessel in Mx80-9 test. In general, the developed model has satisfactorily captured two important phenomena observed in experiments: (1) the twice occurring gas breakthrough events, of which the second breakthrough is less significant than the first one, and (2) after the termination of gas injection, the gas pressure tends to approach an asymptotic value, i.e. the "shut-in" pressure.

However, the two overshoot events after the first gas breakthrough cannot be simulated by the developed model. To explain this limitation, overshoot events need to be examined from the perspective of physical processes. Once the gas pressure reaches a critical value, preferential pathways develop rapidly, and a great deal of gas flows into the sample. This would cause an abrupt reduction in gas pressure in the vessel, thus leading to a significant gas breakthrough phenomenon. However, the gas stored in the sample may not completely flow out due to the high flow resistance at the downstream side of the sample. Two possible factors might contribute to the high flow resistance: (1) the rate of the fracture propagation is reduced because of either a reduced gas pressure or high resistance to fracturing, and (2) the developed fractures close locally due to the heterogeneity of the HM properties of the real materials.

Inhibited by the high flow resistance ahead of the gas front, the gas stored in the sample preferably flows back into the gas vessel, thus inducing the overshoot events. To simulate the overshoot events, the abrupt breakthrough of gas should be first captured by the proposed model. However, after many numerical trials, it was found that the rapid increase in intrinsic permeability caused a serious convergence issue. It was found that the convergence is very sensitive to the changes in the gas entry value of WRC which is coupled with the intrinsic permeability. This is the main factor that limits the model from providing more accurate results. Future works should therefore be conducted to address this convergence problem.

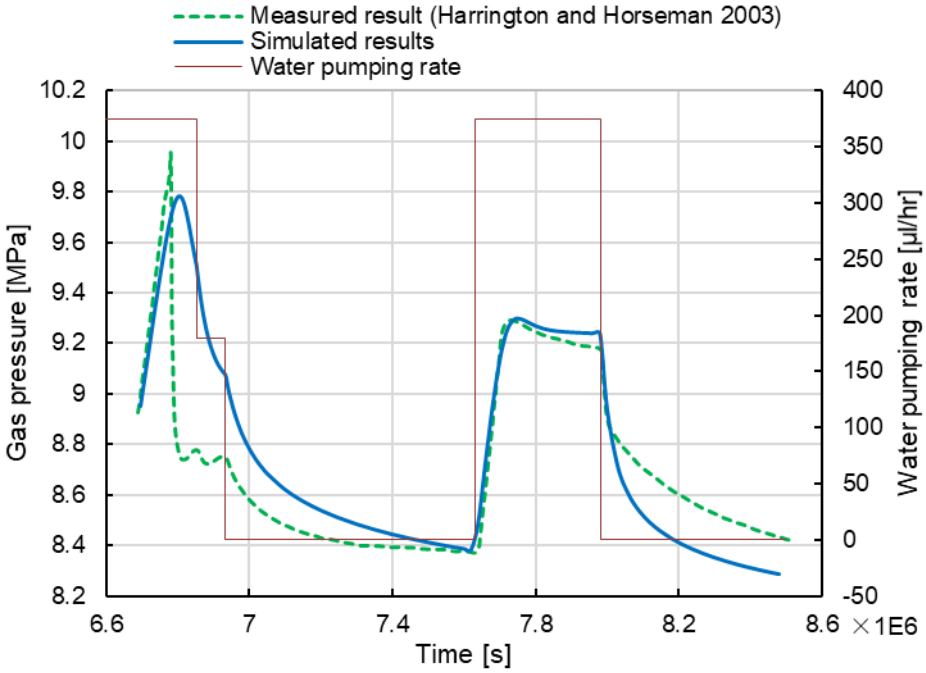

Figure 3.18 Evolution of gas pressure in gas vessel

(II) Changes of volumetric strain

Figure 3.19 shows the changes in the volumetric strain of the PC, FC, and FPM with time at a specific point in the sample. The trend of the changes is very similar to that in Mx80-4 test. The FPM showed volume dilation while the PC underwent volume shrinkage, both leading to the opening of the developed pathways denoted by the volumetric strain of the FC. However, in contrast to the simulated results of Mx80-4 test, the consolidation of the PC in this simulated test was comparable to the dilation of the FPM in terms of the contribution to the opening of

the developed fractures. This may be attributed to the increase of total stress caused by the K0 boundary condition which restricts the radial deformation.

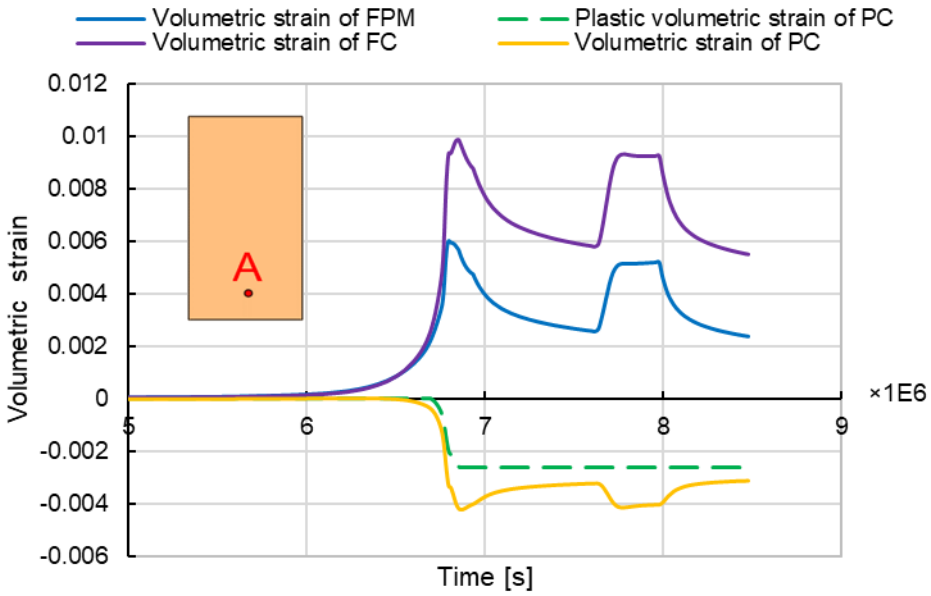

Figure 3.19 Changes in volumetric strain of FC, PC and FPM at Point A

(III) Effect of hysteresis of relative permeability

Gas entrapment during the imbibition process is considered to be an important process that affects the gas migration behaviors. However, models in previous studies have not yet estimated the effects of gas entrapment on the gas migration in buffer materials. In this study, by comparing the simulation results with and without considering the gas entrapment effects, as shown in Figure 3.20, the hysteresis of relative permeability induced by gas entrapment is identified as an important factor to achieve both the “shut-in” pressure and the less significant gas breakthrough in the second cycle of gas injection. Figure 3.7 shows that when the water imbibition process is initiated, the relative permeability of gas decreases along a steeper scanning curve, instead of the original one. Given a certain reduction in gas saturation, the decrease in relative permeability with considering gas entrapment is much more significant than that without considering. Alternatively, the gas saturation at a given relative permeability is greater for the case that considers the gas entrapment than the case that does not. This would inhibit the closure of the developed fractures, thus inducing a greater intrinsic permeability and

a lower gas entry value. Consequently, the second gas breakthrough is less significant for the case that considers the effects of gas entrapment, as shown in Figure 3.20.

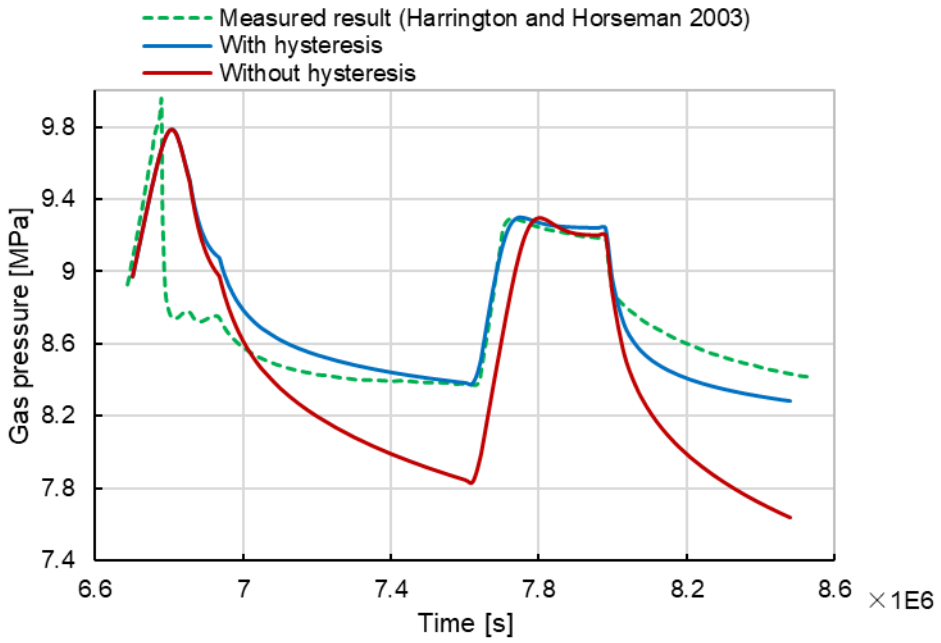

Figure 3.20 Effect of hysteresis on the evolution of gas pressure

3.2.6 Summary and Conclusions

A fully coupled HM model that uses the concepts of double porosity and double effective stress has been developed to simulate the gas migration process in saturated bentonite. The concept of double effective stress is derived based on the mixture theory and the first law of thermodynamics. This concept helps to give flexibility in describing the complex mechanical behaviors of the porous media with two levels of pore structure. The volumetric strain, which is work-conjugated to its corresponding effective stress, has been explicitly included in the governing equations. The thermodynamic analysis used in this paper consolidates the application of the concept of double effective stress in the double porosity media. While the FC is assumed to present nonlinear elastic behaviors, the PC presents volumetrically elastoplastic behaviors. The dilation/consolidation of the PC is able to induce the closure/open of the fractures in the FC according to the conceptual model which accounts for the porosity transformation and the water exchange between pores and fractures. The intrinsic permeability model derived from the well-known cubic law takes both volumetric dilation and structure

evolution into consideration. The rapid increase of intrinsic permeability is achieved through a transition function proposed for evaluating the effects of structure evolution. In addition, the hysteresis of the gas relative permeability is modelled by considering gas entrapment during the water imbibition process. The numerical results show that gas entrapment plays an important role in giving the "shut-in" pressure as well as a less significant gas breakthrough in the second cycle of gas injection.

The developed model is validated against three laboratory tests which are conducted under three types of boundary conditions, i.e. constant stress, constant volume, and K0 boundary conditions. The simulated results under a constant stress condition are in good agreement with the experimental data in terms of both the gas pressure in the vessel and the gas outflow rate. The opening of fractures in the FC mainly results from the expansion of the FPM, as the boundary condition allows the sample to dilate axially and radially. The simulated results for the constant volume condition also present a good agreement with the experimental data, although there are some overestimations after the second gas supplement and at the second gas breakthrough event. As the constant volume condition inhibits the dilation of the sample, the porosity transformation between pores and fractures is the main mechanism causing the opening of fractures in the FC. The build-up of the water pressure during the period of gas breakthrough is also captured by the proposed model. Under the K0 boundary condition, the developed model satisfactorily simulated two important observed behaviors, i.e., the two gas breakthrough events and the "shut-in" pressure. However, the model does not simulate the overshoot events well due to convergence issues caused by the attempts to achieve a sharper reduction in gas pressure after breakthrough. As only the radial deformation is restricted for the K0 condition, the porosity transformation is not as obvious as that for the constant volume condition, but more evident than that for the constant stress condition.

In summary, the developed model has satisfactorily simulated the main experimental observations, including the gas breakthrough phenomenon, the dilation of the sample, the consolidation of the clay matrix, the build-up of pore water pressure and the "shut-in" pressure. However, some of the spatially and temporally dependent characteristics under constant

volume condition cannot be captured by the model. This may result from the assumption of the homogeneity of the HM properties which prevents the model from simulating strong preferential flows. Thus, future studies need to be conducted on the effects of heterogeneous distribution of HM properties on the gas migration process. Another limitation is the inability of the model to simulate the overshoot behavior in Mx80-9 test. To properly simulate this behavior, the convergence issue caused by the rapid evolution of gas entry value need to be solved in the future. In addition, determining the parameters for the proposed double porosity model is still a challenging work, and more theoretical and experimental studies need to be performed in the future.

3.3 A Double Pore Structure Model for Gas Migration in Saturated Bentonite Accounting For Damaging Effects and Hysteresis of Permeability

(The full version of this Technical paper has been submitted for publication)

3.3.1 Introduction

The development of preferential pathways significantly influences the coupled HM behaviors during gas migration in saturated bentonite (Harrington et al. 2017b). Thus, it needs to be properly accounted for in the developed numerical models to realistically reproduce the coupled HM behaviors. Explicitly simulating the preferential pathways is mathematically challenging and computationally demanding. To avoid these issues, a damage model has been adopted in (Dagher et al. 2018; Fall et al. 2014) to implicitly simulate the development of preferential pathways. Owing to the introduction of damaging effect, the abrupt changes in both permeability and gas entry value can be well simulated. In this paper, the coupled HM framework based on double porosity concept in Section 3.2, will be enriched by a hybrid damage model to account for the fracturing process in saturated bentonite The saturated bentonite is considered as a composite porous media consisting of two subcontinua, i.e. MAcro-Continuum (MAC) and Micro-Continuum (MIC). The conceptual model and associated assumptions adopted in this paper are the same with those in Section 3.2. The independent stress state variables (net normal stress and suction) are applied on the MAC to construct the damage model, while the mean Terzaghi's effective stress is used to develop an isotropic elastoplastic model for the MIC. Compared with the Bishop-type effective stress, the independent stress state variables are more appropriate to simulate the tensile-induced damage, since the gas pressure fully contributes to the net normal stress. In addition, a novel permeability model accounting for hysteretic effects is proposed to describe the effect of unstable pathways on gas migration behavior.

This paper is organized as follows. In Section 3.3.2, governing equations, including the mass balance equations for gas and water, as well as the momentum balance equation, will be given. In Section 3.3.3, the mechanical models for MAC and MIC will be proposed. Moreover, a hysteretic model for intrinsic permeability will be developed and discussed. In Section 3.3.4,

the developed coupled HM model will be used to simulate the gas injection tests conducted by the British Geological Survey. In the last section, conclusions and recommendations for future works will be given.

3.3.2 Governing Equations

3.3.2.1 Mass balance equations

Following the derivation procedures in (Guo and Fall 2018)3.2.3, the mass balance equations for the fluid component α (denoting w and g for water and gas respectively) in the MAC are respectively derived as

$$\rho_{Mw}\left(\frac{\phi_M S_{Mw}}{K_w}-\phi_M C_s\right)\frac{\partial p_{Mw}}{\partial t}+\nabla\cdot(\rho_{Mw}\boldsymbol{v}_{Mw}^D)=-\phi_M\rho_{Mw}C_s\frac{\partial p_{Mg}}{\partial t}-S_{Mw}\rho_{Mw}\frac{\partial \varepsilon_{Mv}}{\partial t}+\Gamma_w \tag{3.53}$$

$$\rho_{Mg}\left(\frac{\phi_M S_{Mg}}{p_{Mg}}-\phi_M C_s\right)\frac{\partial p_{Mg}}{\partial t}+\nabla\cdot(\rho_{Mg}\boldsymbol{v}_{Mg}^D)=-\phi_M\rho_{Mg}C_s\frac{\partial p_{Mw}}{\partial t}-S_{Mg}\rho_{Mg}\frac{\partial \varepsilon_{Mv}}{\partial t} \tag{3.54}$$

where p_{Mw} is the water pressure in MAC, p_{Mg} is the gas pressure $S_{M\alpha}$ is the degree of saturation, $\rho_{M\alpha}$ is the fluid density, ϕ_M is the porosity, ε_{Mv} is the volumetric strain of MAC, Γ_w is the water exchange rate, K_w is the bulk modulus of water, $C_s=\frac{\partial S_e}{\partial p_c}$ is the storage coefficient, $\boldsymbol{v}_{M\alpha}^D=S_{M\alpha}\phi_M\left(\boldsymbol{v}_{M\alpha}-\boldsymbol{v}_s\right)$ is Darcy's velocity for fluid α, S_e is the effective degree of saturation and v_s is the velocity of solid grain. Note that the exchange term for gas in Eq. (3.54) is neglected, as the MIC is assumed fully saturated with water.

Due to the extremely small pore size and the high viscosity of water in the MIC, Darcy's flow of porewater is neglected. However, the local water transfer between the MAC and the MIC is allowed. Following the similar derivation procedures in (Guo and Fall 2018), the mass balance equation for water in the MIC is derived as:

$$\frac{\phi_m\rho_{mw}}{K_w}\frac{\partial p_{mw}}{\partial t}=-\rho_{mw}\frac{\partial \varepsilon_{mv}}{\partial t}-\Gamma_w \tag{3.55}$$

where ϕ_m is the porosity for MIC, ε_{mv} is the volumetric strain of MIC, p_{mw} is the porewater pressure and ρ_{mw} is the density of porewater.

The water exchange rate, Γ_w, is determined by a linear model proposed in (Warren and Root 1963):

$$\Gamma_w = \xi_w \rho_{mw} \left(p_{mw} - p_{Mw} \right) \tag{3.56}$$

where ξ_w is an exchange coefficient.

3.3.2.2 Momentum balance equation

By using the second Newton's law and neglecting the inertial and the viscous forces, the momentum balance equation for the porous media can be expressed as:

$$\nabla \cdot \boldsymbol{\sigma} + \rho \boldsymbol{g} = 0 \tag{3.57}$$

where $\boldsymbol{\sigma}$ is the total stress tensor, ρ is the averaged density of the mixture and $\boldsymbol{g}$ is the gravitational acceleration.

3.3.3 Constitutive Models

3.3.3.1 Mechanical constitutive models

In this section, the independent stress state variables, i.e. net normal stress and suction, are adopted to develop an elastic damage model for the MAC, while the mean effective stress is used to govern the elastoplastic behavior of the MIC.

3.3.3.1.1 Micro-Continuum

As the MIC is assumed fully saturated during the gas migration process, the Terzaghi's effective stress, as expressed Eq. (3.23), is adopted to develop the isotropic elastoplastic model.

$$\boldsymbol{\sigma}'_m = \boldsymbol{\sigma} + p_{mw} \boldsymbol{I} \tag{3.58}$$

where $\boldsymbol{\sigma}'_m$ is the effective stress tensor of the MIC.

As only the volumetric strain is considered for the MIC, the mean of Terzaghi's effective stress tensor, p'_m, is adopted:

$$p'_m = p_m + p_{mw} \tag{3.59}$$

where p_m is the mean total stress for the MIC.

The elastic and plastic strain can be determined by a nonlinear elastoplastic theory for clays, as given in (Qiao et al. 2019). However, as the focus of this paper is to examine the damaging effect on the gas migration behavior, the elastic and the plastic modulus are assumed as constant values in this paper for simplicity. Then, the constitutive model for the MIC is expressed as

$$p'_m = K_m^{el}\varepsilon_{mv}^{el} = K_m^{el}\left(\varepsilon_{mv} - \varepsilon_{mv}^{pl}\right) \tag{3.60}$$

where K_m^{el} is the elastic bulk modulus, ε_{mv}^{el} and ε_{mv}^{pl} are the elastic and the plastic volumetric strain of the MIC, respectively.

To evaluate the plastic volumetric strain, the yield function for the MIC is defined as (Qiao et al. 2019)

$$f_m\left(p'_m, \varepsilon_{mv}^{pl}\right) = p'_{my}\left(\varepsilon_{mv}^{pl}\right) - p'_m \tag{3.61}$$

where p'_{my} is the mean yielding effective stress at which the MIC starts yielding, . ε_{mv}^{pl} . is the hardening variable. It is noted here that the compressive stress is taken as a negative value.

If the mean effective stress is larger than the mean yielding effective stress, the MIC deforms elastically. The elastic volumetric strain is determined by

$$\dot{\varepsilon}_{mv}^{el} = \frac{\dot{p}'_m}{K_m^{el}} \tag{3.62}$$

If the mean effective stress is less than the mean yielding effective stress, the plastic volumetric strain occurs in the MIC. Then, the mean yielding effective stress is defined as a linear function of the hardening variable, which reads

$$p'_{my}\left(\varepsilon_{mv}^{pl}\right) = p'_{my0} + K_m^{pl}\varepsilon_{mv}^{pl} \tag{3.63}$$

where p'_{my0} is the initial mean yielding effective stress and K_m^{pl} is the plastic modulus.

The consistency condition for the plastic model reads

$$\dot{f}_m = K_m^{pl}\dot{\varepsilon}_{mv}^{pl} - \dot{p}'_m = 0 \tag{3.64}$$

Then, the plastic volumetric strain is determined as

$$\dot{\varepsilon}_{mv}^{pl} = \frac{\dot{p}'_m}{K_m^{pl}} \tag{3.65}$$

The summation of Eq. (3.62) and Eq. (3.65) gives the total volumetric strain of the MIC as

$$\dot{\varepsilon}_{mv} = \dot{\varepsilon}_{mv}^{el} + \dot{\varepsilon}_{mv}^{pl} = \frac{\dot{p}'_m}{K_m^{el}} + \frac{\dot{p}'_m}{K_m^{pl}} \tag{3.66}$$

3.3.3.1.2 Macro-Continuum

The mechanical constitutive model for the MAC is governed by independent stress state variables, i.e. net normal stress, σ'_n, and suction, s, which are expressed as

$$\boldsymbol{\sigma}'_n = \boldsymbol{\sigma} + p_{Mg}\boldsymbol{I} \tag{3.67}$$

$$s = p_{Mg} - p_{Mw} \tag{3.68}$$

Previous experimental studies showed that the gas pressure may be the primary driving force for the fracturing process (Graham et al. 2012; Harrington and Horseman 2003). In contrast, the effect of suction on the fracturing process is still unclear. For simplicity, it is assumed that the development of microfractures solely results from the evolution of net normal stress. In this paper, the fracturing process is implicitly simulated by a hybrid damage model. By adopting the hypothesis of strain equivalence, the net normal stress, $\boldsymbol{\sigma}_n'$, can be determined as

$$\boldsymbol{\sigma}_n' = (1-d)\,\mathbb{D} : \boldsymbol{\varepsilon}_n \tag{3.69}$$

where $\mathbb{D}$ is the fourth-order stiffness tensor, d is the damage variable, $\boldsymbol{\varepsilon}_n$ is the strain tensor corresponding to the net normal stress. Although the damage variable is isotropically applied to the stiffness tensor, the damage evolution law is only driven by the tensile strain, thus leading to a hybrid damage model (Chiarelli et al. 2003; Conil et al. 2004).

In this paper, an equivalent strain associated with the Rankine damage model is defined to drive the damaging process. This approach was widely used in previous studies, e.g. ones in (Gasch et al. 2016; Mobasher et al. 2017; Mobasher et al. 2018; Parisio and Laloui 2017; Parisio et al. 2015). Then, the Rankine-type equivalent strain, ε_{eq}, is defined as

$$\varepsilon_{eq} = \frac{\left\langle \sigma'_{Mp1} \right\rangle_+}{E_0} \tag{3.70}$$

where $\langle x \rangle_+ = (x + |x|)/2$ is the Macaulay bracket, σ'_{Mp1} is the first principal net normal stress in the intact MAC and E_0 is Young's modulus at intact state.

A local damage model, as defined by Eq. (3.69), may lead to the loss of ellipticity of the partial differential equations (PDE) and mesh dependency issues (Mobasher et al. 2017). To avoid these issues, a commonly used method is to define a damage evolution law with respect to a nonlocal equivalent strain that is derived from its local counterpart. The nonlocal equivalent strain can be determined by solving (de Borst and Verhoosel 2016)

$$\varepsilon_{nl} - c\nabla^2 \varepsilon_{nl} = \varepsilon_{eq} \tag{3.71}$$

where ε_{nl} is the nonlocal equivalent strain, $c = l_{\text{int}}^2 / (2n_d)$ controls the width of the localization band, l_{int} is the internal length scale and n_d is the geometric dimension.

The damage evolution law can be determined by the model proposed in (Mazars 1986):

$$d(\kappa) = \begin{cases} 1 - (1 - A_t)\frac{\varepsilon_0}{\kappa} - A_t \exp\left[-B_t(\kappa - \varepsilon_0)\right] & \kappa \geq \varepsilon_0 \\ 0 & \kappa < \varepsilon_0 \end{cases} \tag{3.72}$$

where κ is the historical maximum value of the nonlocal equivalent strain, $\varepsilon_0 = \sigma_t / E_0$ is a critical tensile strain at which the damage initiates, σ_t is the tensile strength, A_t and B_t are parameters controlling the shape of the evolution curve.

Due to the limited experimental data, the volumetric strain caused by the change in suction is determined by a simple elastic model:

$$s = -K_{sc}\varepsilon_{sv} \tag{3.73}$$

where s is the suction, ε_{sv} is the volumetric strain due to suction and K_{sc} is the bulk modulus associated with suction.

By far, the total strain tensor is decomposed into three parts, i.e. one from net normal stress, one from suction and the third one from MIC, which are expressed as

$$\boldsymbol{\varepsilon} = \boldsymbol{\varepsilon}_n + \frac{1}{3}\varepsilon_{sv}\boldsymbol{I} + \frac{1}{3}\varepsilon_{mv}\boldsymbol{I} \tag{3.74}$$

Then, by combining Eqs. (3.67), (3.69) and (3.74), the total stress tensor can be determined as

$$\boldsymbol{\sigma} = (1 - d)\mathbb{D} : \left(\boldsymbol{\varepsilon} - \frac{1}{3}\varepsilon_{sv}\boldsymbol{I} - \frac{1}{3}\varepsilon_{mv}\boldsymbol{I}\right) - \max\left(p_{Mg}, p_{Mw}\right)\boldsymbol{I} \tag{3.75}$$

$$\boldsymbol{\varepsilon} = \frac{1}{2}\left[\nabla \boldsymbol{u} + \left(\nabla \boldsymbol{u}\right)^{T}\right] \tag{3.76}$$

where $\boldsymbol{u}$ is the displacement vector of the porous media. It is noted here that the larger value between gas pressure and water pressure serves as the pore pressure in Eq. (3.75) to account for the saturated state.

3.3.3.2 Hydraulic constitutive models

The two-phase flow in bentonite is described by the generalized Darcy's law:

$$\boldsymbol{v}_{M\alpha}^{D} = -\frac{\boldsymbol{k}_{M} k_{r\alpha}}{\mu_{\alpha}}(\nabla p_{M\alpha} - \rho_{\alpha}\boldsymbol{g}) \tag{3.77}$$

where $\boldsymbol{k}_{M}$ is the intrinsic permeability tensor for the MAC, $k_{r\alpha}$ is the relative permeability, μ_{α} is the fluid dynamic viscosity, $p_{M\alpha}$ is the fluid pressure and ρ_{α} is the density.

This section focuses on the development of intrinsic permeability model that can account for the hysteretic effect caused by pore structure evolution. The water retention behavior is described by van Genuchten model (van Genuchten 1980) in which the gas entry value is coupled with the intrinsic permeability through a cubic root law, as seen in Section 3.2.4.2.2. The standard Mualem-van Genuchten model (Luckner et al. 1989; Mualem 1976; van Genuchten 1980) is used to simulate the relative permeability for gas and water.

The intrinsic permeability is one of the key hydraulic properties controlling the gas migration behavior. During the period of gas migration, the intrinsic permeability evolves with the changes of pore volume and pore structure. In previous numerical studies, various permeability models were proposed to simulate the gas breakthrough phenomenon. Among these models, the embedded fracture model, which is derived from the Poiseuille equation for two parallel smooth plates, was widely adopted, as it contains more geometrical features of the developed fractures. As analyzed in (Olivella and Alonso 2008), the intrinsic permeability for a finite element containing a series of embedded fractures is derived as

$$\boldsymbol{k}_{M} = \boldsymbol{k}_{mat} + \boldsymbol{k}_{ef} \tag{3.78}$$

$$\boldsymbol{k}_{mat} = k_{mat0}\left(\frac{\left(1-\phi_{M0}\right)^2}{\phi_{M0}^3}\right)\frac{\phi_M^3}{\left(1-\phi_M\right)^2}\boldsymbol{I} \tag{3.79}$$

$$\boldsymbol{k}_{ef} = \frac{\left(b_0+\Delta b\right)^3}{12a}\left(\boldsymbol{I}-\boldsymbol{n}_f\otimes\boldsymbol{n}_f\right) \tag{3.80}$$

where k_{mat0} and $\boldsymbol{k}_{mat}$ denote the initial and the transient intrinsic permeability for porous matrix in MAC, $\boldsymbol{k}_{ef}$ is the intrinsic permeability of embedded fracture, ϕ_{M0} and ϕ_M denote the initial and the transient porosity of MAC, respectively, b_0 is the initial fracture aperture, Δb is the incremental aperture due to deformation, a is the fracture spacing and $\boldsymbol{n}_f$ is the unit normal vector of the developed fracture.

Following the derivation procedures in (Levasseur et al. 2010), the intrinsic permeability of embedded fractures, i.e. Eq. (3.80), can be reformulated as

$$\boldsymbol{k}_{ef} = k_{ef0}\left(1+C_k\varepsilon_{nl}\right)^3\left(\boldsymbol{I}-\boldsymbol{n}_f\otimes\boldsymbol{n}_f\right) \tag{3.81}$$

where $k_{ef0}=b_0^3/(12a)$ is the initial intrinsic permeability and C_k is a calibrated coefficient controlling the evolution of the intrinsic permeability.

In previous papers (Gerard et al. 2014; Levasseur et al. 2010), the coefficient, C_k, in Eq. (3.81) was assumed as a constant value, which means that the evolution of the intrinsic permeability with the nonlocal strain is the same before and after the gas breakthrough event. In this paper, in order to highlight the effect of fracturing process on the evolution of intrinsic permeability, this coefficient is defined as an exponential function of the damage variable, as expressed by

$$C_k\left(d\right) = \exp\left(A_k + B_k d\right) \tag{3.82}$$

where A_k and B_k are calibrated parameters controlling the evolution of intrinsic permeability. It can be seen from Eq. (3.81) and Eq. (3.82) that with the increase of damage variable, the contribution of the nonlocal tensile strain to the intrinsic permeability is increased.

In addition, previous experiments showed that the permeability may experience a sharp decrease after the gas injection was stopped (Daniels and Harrington 2017; Graham et al. 2012). This phenomenon may be associated with the structural evolution of unstable pathways. The analysis of the unstable pathways can be found in (Graham et al. 2012; Harrington et al. 2017b; Harrington et al. 2019b). Explicitly simulating the transient evolution of unstable pathways is challenging work. As an alternative way, the effect of the unstable pathways on the intrinsic permeability may be indirectly described by a hysteretic model. Inspired by the hysteretic models in (Juanes et al. 2006; Killough 1976; Selvadurai and Głowacki 2008), a simple hysteretic model for the intrinsic permeability is then proposed as

$$\boldsymbol{k}_{ef} = \begin{cases} k_{ef0}\underbrace{\left[1+\exp\left(A_k+B_k d\right)\varepsilon_{nl}\right]^3}_{H_k}\left(\boldsymbol{I}-\boldsymbol{n}_f\otimes\boldsymbol{n}_f\right) & \varepsilon_{nl}\geq\varepsilon_{nl}^M, \\ k_{ef0}\underbrace{\left[1+\exp\left(A_k+B_k d\right)\varepsilon_{nl}^M\left(\varepsilon_{nl}/\varepsilon_{nl}^M\right)^h\right]^3}_{H_k}\left(\boldsymbol{I}-\boldsymbol{n}_f\otimes\boldsymbol{n}_f\right) & \varepsilon_{nl}<\varepsilon_{nl}^M. \end{cases} \tag{3.83}$$

where ε_{nl}^M is the maximum value ever reached by ε_{nl} and h is a calibrated parameter controlling the strength of the hysteretic effect, and H_k is an enhanced coefficient for the intrinsic permeability.

To have an intuitive understanding of the proposed hysteretic model, the evolution of the enhanced coefficient, H_k, with respect to the nonlocal tensile strain is illustrated in Figure 3.21. When $\varepsilon_{nl}\geq\varepsilon_{nl}^M$, the enhanced coefficient increases along the blue solid line. Once the nonlocal tensile strain decreases from the reversal point, as seen in Figure 3.21, the enhanced coefficient may decline along different paths depending on the specific value of h. When $h=1$, the hysteresis caused by the nonlocal tensile strain is not considered. However, the enhanced coefficient decreases along the red dashed line, rather than the original blue solid

line. This hysteresis is caused by the irreversible damage variable. As the value of the coefficient, $C_k(d)$, always keeps the maximum value ever reached, the enhanced coefficient, H_k, after decreasing from the reversal point is larger than its counterpart on the original blue curve. To compensate this damaged induced hysteresis, h could be set to a value larger than one. As seen in Figure 3.21, the dotted dashed line with $h=2$ is close to the original blue solid line. With a further increase of h, the enhanced coefficient drops more rapidly than the one along the original blue curve, see the dotted line with $h=5$ in Figure 3.21. This feature is suitable to describe the experimental behavior that the permeability drops rapidly when the tensile strain tends to decrease. In contrast, the enhanced coefficient declines more gently when $h<1$, see the circle-marked line in Figure 3.21. This feature can be used to model the rapid decrease of gas pressure after peaking, or the less significant gas breakthrough behavior in the subsequent injection cycles. As analysed above, the proposed permeability model is more flexible to fit the experimental results due to the introduction of the hysteretic effect. The parameter, h, can be determined through calibrating with the experimental data.

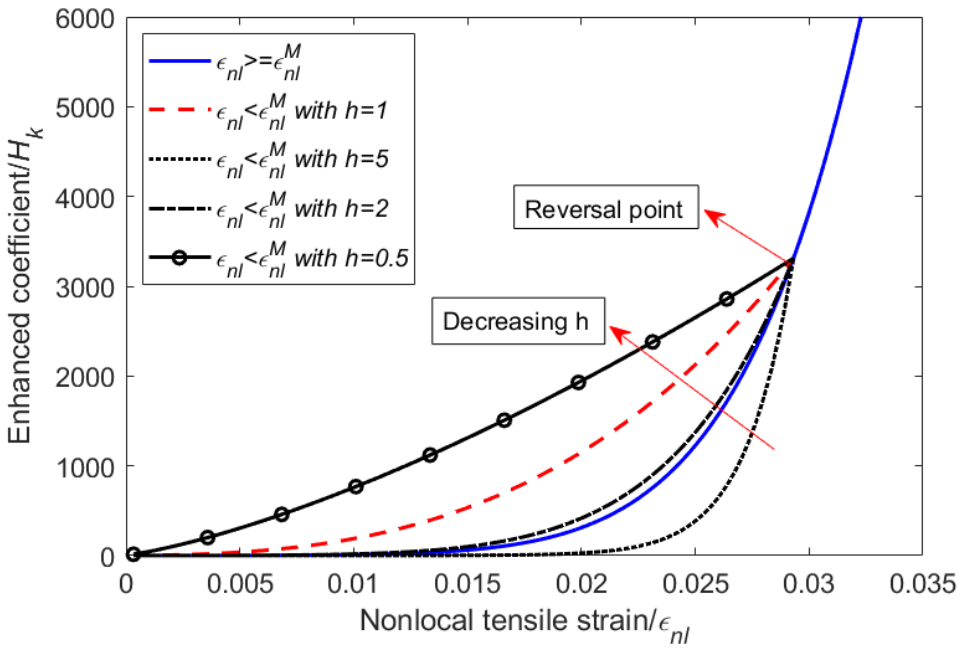

Figure 3.21 Hysteretic model for the intrinsic permeability

3.3.4 Model Implementation and Simulation

3.3.4.1 Implementation in COMSOL

The developed coupled HM model was implemented in a FEM based commercial software, COMSOL Multiphysics, to solve partial differential equations (PDEs). The primary variables are interpolated by the bilinear shape function that is beneficial to decreasing the degree of freedom and Gauss quadrature operations. However, a lower equal-order element, e.g. the Q4P4 element, for the coupled HM model may lead to the pore pressure oscillation. To avoid this issue, a stabilised term based on the Polynomial-Pressure-Projection technique is added to the mass balance equations for both water and gas in the MAC. More details about this stabilized method can be found in (Guo and Fall 2019; Song et al. 2017). As the developed coupled HM model is highly nonlinear, the segregated solver is used to alleviate the computational effort. The displacement vector, gas and water pressure in the MAC and the water pressure in the MIC are solved first. Then, the damage variable is calculated by using the outcomes in the previous segregated step. This segregated solver is iterated until the convergence criterion is satisfied.

3.3.4.2 Model parameters

The basic HM properties are extracted from (Tamayo-Mas et al. 2018) and listed in Table 8. In this paper, the initial permeability for both the matrix and the embedded fracture is assumed to equal to 3.4×10^{-21} m^2. The initial porosity of the MAC is assumed to occupy 10% of the initial total porosity, ϕ_0, as adopted in (Guo and Fall 2019; Zheng et al. 2017). As the mechanical properties for the MIC are still not available at present, the values of these properties are assumed to complete the simulation. The Young's modulus of the MIC is assumed 1.5 times that of the MAC. When the material yields, the overall bulk modulus is assumed 0.3 times the elastic bulk modulus. The bulk modulus for the suction, K_{sc}, is a calibrated parameter in (Tamayo-Mas et al. 2018), but it is assumed two times the elastic bulk modulus in this paper.

Table 8 Basic HM properties of the bentonite sample

Bentonite	Hydraulic properties			Mechanical properties			
	k_0/m^2	p_{gev}/MPa	m	E/MPa	υ	ϕ_0	σ_t/MPa
Mx80	3.4×10^{-21}	18	0.45	307	0.4	0.44	0.1

To account for the heterogeneous distribution of HM properties, some of the properties, i.e. intrinsic permeability, gas entry value, Young's modulus and tensile strength, are assumed to follow the lognormal distribution law. In reality, property at a particular position is more similar to the property nearby than that far away (Li et al. 2015). To capture this realistic feature, a spatially auto-correlated random field is generated by using the GSTools (Müller and Schüler 2019). In this paper, the mean values of these heterogeneous properties are equal to corresponding values listed in Table 8. The coefficient of variation, i.e. the ratio between the standard variation and the mean of a random field, is 0.1 for the gas entry value, Young's modulus and tensile strength, and 5 for the intrinsic permeability considering that it generally varies within several orders of magnitude. These parameters for the HM properties will be used for the following three simulation cases. For simplicity, only the heterogeneous distribution of Young's modulus is given in Figure 3.22. In the red (or blue, respectively) area, Young's modulus, gas entry value and tensile strength are larger (smaller), and the intrinsic permeability is smaller (larger). This means the red (or blue, respectively) area in the domain represents the area of high (or low) resistance to flow and fracturing.

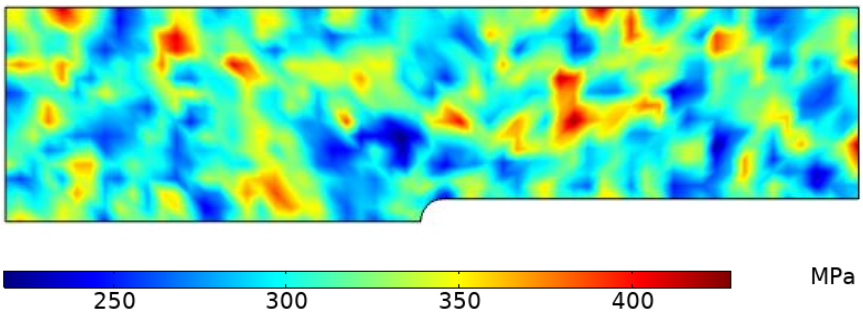

Figure 3.22 Heterogeneous distribution of Young's modulus

Except for the basic HM properties, the other parameters used for constructing the hydraulic model and the damage model are termed as empirical parameters. As the physical processes

involved during the gas migration process are very complex, determining these empirical parameters, either experimentally or theoretically, is challenging work. Currently, the calibration method is commonly used to determine the values of empirical parameters, as seen in (Gerard et al. 2014; Harrington et al. 2019a; Nguyen and Le 2014; Tamayo-Mas et al. 2018). In this paper, the values of the empirical parameters, as given in Table 9, are determined through model calibration.

Table 9 Calibrated parameters for hydraulic model and damage model

Test	Intrinsic permeability model			Damage model		Water exchange coefficient
	A_k	B_k	h	A_t	B_t	ξ_w / m*s/kg
Mx80-8 test	3	5	1	0.8	70	1.80×10^{-13}
1-D flow test	3	4.5	5	0.7	180	1.80×10^{-13}
Spherical flow test	3	5	1	0.7	170	1.80×10^{-13}

3.3.4.3 Mx80-8 test

Mx80-8 test was conducted by researchers from the British Geological Survey. Details about the experimental procedures were given in (Harrington and Horseman 2003). As the basic HM properties of the bentonite sample were not given in the original report, the values of these properties are assumed the same with those given in Table 8.

3.3.4.3.1 Initial and boundary conditions

Figure 3.11 shows the meshing strategy and boundary conditions for the Mx80-8 test. The height and the radius of the bentonite sample are 120 mm and 30 mm, respectively. The brown dashed line represents the axis of symmetry. Roller boundary is applied to all boundaries to simulate the constant volume condition. The helium gas was pressurized in a gas vessel by injecting water at a certain rate. The pressurized helium gas is then injected into the sample through the end of the drilled hole, i.e. the green boundary in Figure 3.11, and flows out through three sets of filters, i.e. red boundaries in Figure 3.11. The porewater is only allowed to flow out of the sample through the outflow boundaries (red boundaries in Figure 3.11) which are applied with a constant value, i.e. 1 [MPa]. A mass flux boundary (Neumann boundary) for gas field, as given by Eq. (3.51), is applied to the outflow boundary. The whole domain is meshed

by quadrilateral elements with a size of 2 mm, except for elements around the injection boundary that are finer to reasonably discretize the curved boundary. In Appendix E, the mesh around the outflow boundary is refined to examine the effect of the element size on the numerical result.

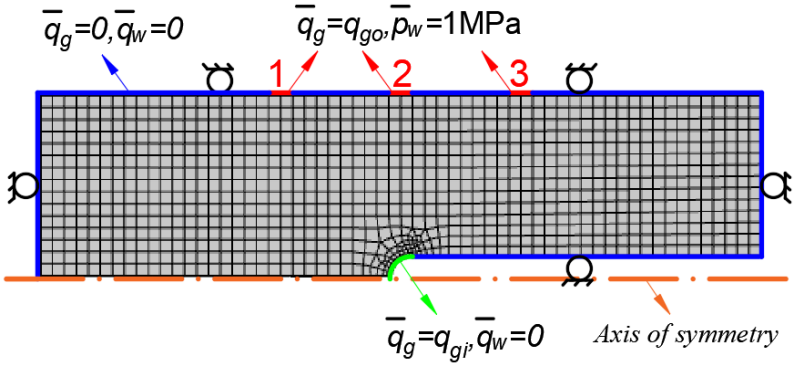

Figure 3.23 Boundary conditions and meshing strategy for Mx80-8 test (Green curve is the injection boundary which is connected with the gas vessel and red lines are the outflow boundaries)

As the initial amount of gas is not sufficient to complete the whole test, additional gas was added into the vessel three times during the test. More details about this technique can be found in (Guo and Fall 2018). The initial effective stress for the MAC is -7.57 [MPa] and the initial mean yielding effective stress for the MIC is assumed to be -7.67 [MPa]. The initial gas pressure in MAC is 1.05 [MPa], and the initial water pressure in both MAC and MIC is 1.0 [MPa]. The small gap between the water and the gas pressure is to avoid convergence issues.

3.3.4.3.2 Evolution of gas pressure

Figure 3.24 presents the evolution of gas pressure obtained from the numerical model and the experimental test. In the numerical study, the parameter, h, is equal to one, which means the hysteresis caused by the reversal of nonlocal tensile strain is not considered.

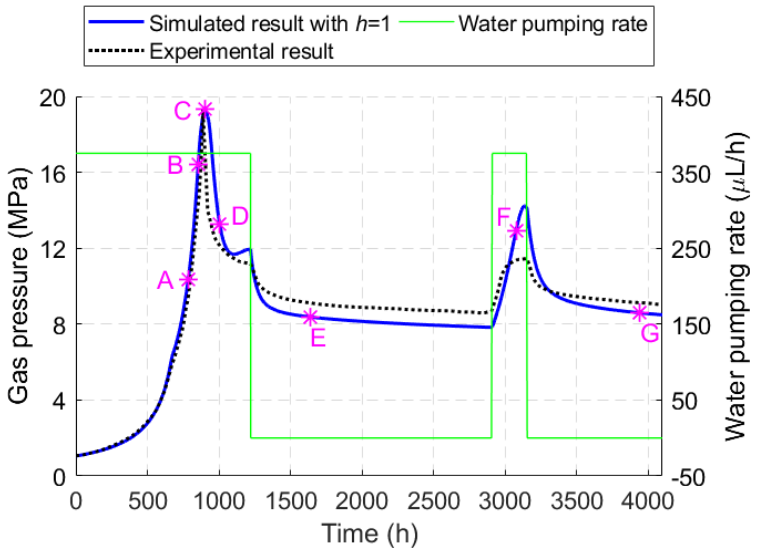

Figure 3.24 Comparison of gas pressure between simulated and experimental result

(Note: Marked points are some characteristic moments that will be analyzed in the following subsections; Experimental result is from (Harrington and Horseman 2003))

In general, the simulated result agrees well with the experimental one. Some key features of the experimental result are successfully captured by the coupled HM model, such as the two gas breakthrough events and the "shut-in" pressure after the cessation of gas injection. The "shut-in" pressure here denotes the asymptotic value to which the gas pressure approaches after the cessation of gas injection. Importantly, the phenomenon that the second gas breakthrough is less significant than the first one due to the development of microfractures, is also successfully captured by the developed model. There also exist small discrepancies between the simulated and the experimental result. For example, the peak value reached in the second gas injection is somewhat higher, while the "shut-in" pressure is slightly lower than the experimental one. However, considering that the involved physical process is very complex, such discrepancies are acceptable.

3.3.4.3.3 Evolution of damage field

Figure 3.25 presents the distribution of the damage field at five characteristic moments as marked in Figure 3.24.

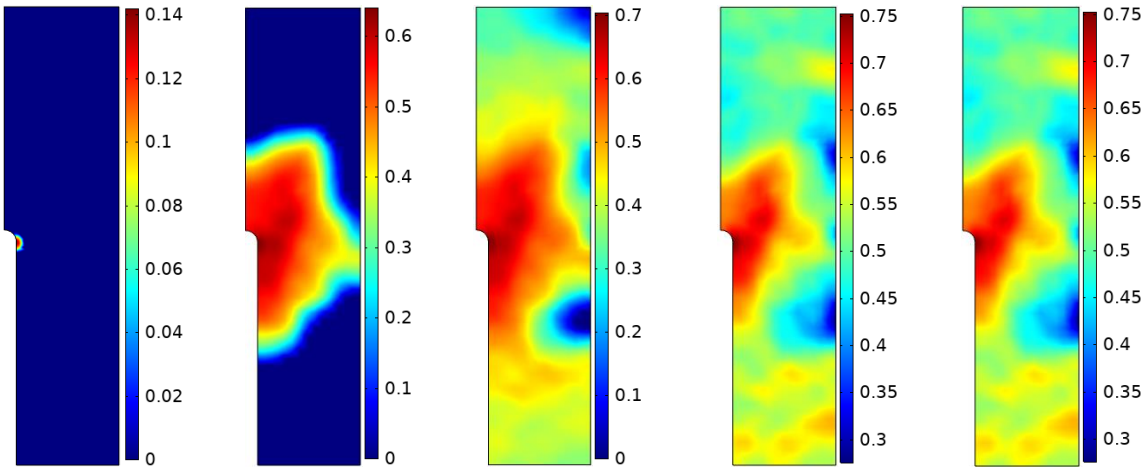

(a) Point A (b) Point B (c) Point C (d) Point D (e) Point G

Figure 3.25 Distribution of damage field at five characteristic moments (which are marked in Figure 3.24)

At point A, the damage just initiates around the injection boundary. Although the gas has entered the sample, the damage field has not yet connected with the outflow boundaries. Therefore, the gas can not flow out of the gas vessel, leading to a continuous increase in gas pressure, see Figure 3.24. At point B, the damage field has extended to a larger scale. As the area in the upright direction to the injection boundary has low resistance to flow and fracturing, see Figure 3.22, the damage field preferentially extends towards this direction, rather than expanding evenly from the injection boundary. At this moment, the damage field has extended to the middle outflow boundary, but the gas pressure still increases, see Figure 3.24. This may be due to that the developed damage field is not enough to induce a significant gas outflow. In contrast, at Point C when the damage field extends to a much larger scale, see Figure 3.25 (c), a large amount of gas is allowed to flow out of the sample, thus leading to a sharp decrease of gas pressure from the moment of Point C. This numerical result reflects the experimental finding that a sufficiently connected microfracture network is necessary to induce a gas breakthrough event (Graham et al. 2012; Harrington et al. 2019b).

As seen in Figure 3.25(c), the damage field around the bottom outflow boundary remains zero, due to the larger resistance to flow and fracturing, see Figure 3.22. Therefore, this boundary is much less permeable than the other two outflow boundaries. This numerical finding explains, to some extent, the experimental observation that the gas outflow may focus on certain outflow filters (Harrington and Horseman 2003; Harrington et al. 2017b; Harrington

et al. 2019b). At point D when the gas pressure is in a declining stage, the damage field still experiences a small increase in both scale and magnitude. This small increase may be caused by local high gas pressure. From point D to point G, the damage field remains the same, which demonstrates the damaging process only takes place in the first gas injection cycle. Therefore, in the second gas injection cycle, the damaged sample is unable to sustain a high gas pressure, yielding a less significant gas breakthrough phenomenon, see Figure 3.24.

3.3.4.3.4 Evolution of averaged degree of saturation

Figure 3.26 presents the distribution of averaged degree of saturation at five characteristic moments. The averaged degree of saturation, S_{ave}, is calculated as $S_{ave} = (S_M \phi_M + \phi_m) / (\phi_M + \phi_m)$, where S_M is the degree of saturation of the MAC. At point A, the bentonite sample is almost fully saturated due to the large gas entry value. At point C, with the increase of both damage variable and nonlocal tensile strain, the intrinsic permeability experiences a rapid increase, leading to a significant decrease of the gas entry value and a strong desaturation process in the MAC. As a result, the relative permeability of gas in the MAC also increase significantly, which further contributes to inducing a gas breakthrough event. Due to the heterogeneous distribution of HM properties, see Figure 3.22, the lower averaged degree of saturation preferentially expands to the upright side of the sample, while the area around the bottom outflow boundary keeps almost saturated. Therefore, the bottom boundary is almost nonpermeable to the gas phase. This further explains why the damage variable almost keeps zero around the bottom boundary, as seen in Figure 3.25 (c). At point E, the averaged degree of saturation has almost recovered to the saturated state, due to the wetting process caused by the decrease of gas pressure. As the sample returns to the saturated state, its sealing ability to gas phase is partially recovered. At point F, the reinjection of gas induces another round of desaturation process. Although the gas pressure at point F is far less than that at point C, the averaged degree of saturation at point F seems even less than that at point C. This is because the damaged sample in the second injection cycle has lower resistance to the

desaturation process than the intact sample in the first injection cycle. At point G, the sample again returns to an almost saturated state after the cessation of the gas injection.

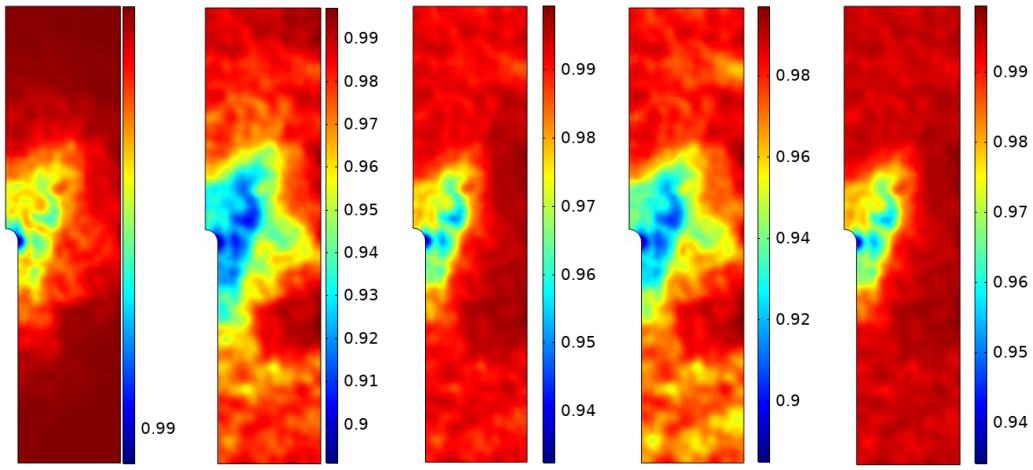

(a) Point A (b) Point C (c) Point E (d) Point F (e) Point G

Figure 3.26 Distribution of average degree of saturation at five characteristic moments

As seen from the distribution of averaged degree of saturation, the majority of the sample keeps saturated during the test. Even for the unsaturated state, the averaged degree of saturation also keeps at a high value, see Figure 3.26 (b) and (d). This simulation result is consistent with the experimental finding that the bentonite sample can keep almost saturated as the gas migrates in the bentonite (Graham et al. 2012; Harrington et al. 2017b; Horseman et al. 1999). As the desaturation is an essential feature of the two-phase flow mechanism, completely avoiding the desaturation process is not practical. However, owing to the differentiation of porosity in the MAC and in the MIC and the assumption that the MIC keeps fully saturated during the injection test, a very high degree of saturation can be achieved. In general, the developed model behaves well to simulate the evolution of degree of saturation.

3.3.4.3.5 Effect of hysteresis on gas flow process

Figure 3.27 presents the comparison of gas pressure between the experimental result and simulated results with different values of h. In general, the evolution trends of the simulated curves are similar to that of the experimentally obtained curve. The differences mainly occur in the "shut-in" pressure and the peak pressure in the second gas injection cycle. A higher value of the parameter, h, yields higher values in both the "shut-in" pressure and the peak pressure. As shown in Figure 3.21, when the nonlocal tensile strain decreases from the reversal point,

the intrinsic permeability decreases at a higher rate for a larger value of h. Therefore, for the current simulation, the intrinsic permeability corresponding to h=0.3, is higher than those with h=1 or h=5. According to Eq. (3.41), a higher intrinsic permeability implies a lower gas entry value that will facilitate the desaturation process and increase the relative permeability. As the analysis shows, both the intrinsic and the relative permeability are higher for a lower hysteretic parameter, h. That means a larger amount of gas can flow out of the gas vessel, which leads to lower values in both the "shut-in" pressure and the peak pressure in the second injection cycle. In conclusion, the hysteretic model has implicitly accounted for the effect of transient evolution of pore structure that may enhance or impede the gas outflow. In addition, the introduction of the parameter, h, makes the intrinsic permeability model more flexible to reproduce with the experimental result.

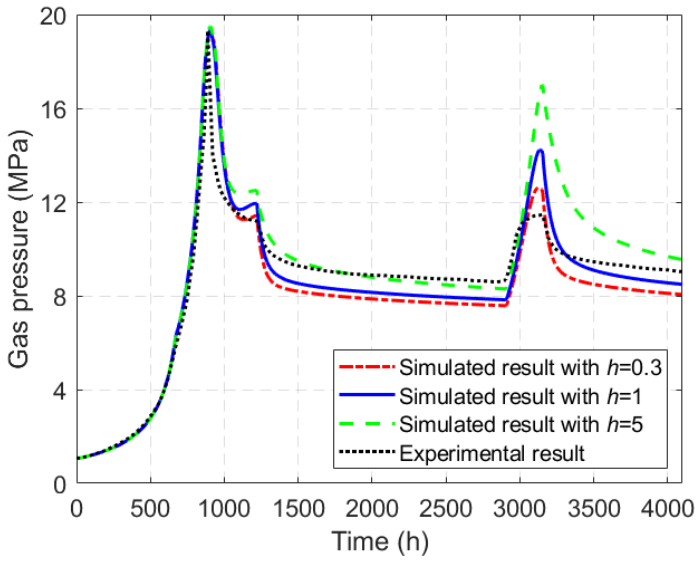

Figure 3.27 Evolution of gas pressure with different parameter, h

3.3.4.4 1-D gas flow test

The 1-D gas flow test, conducted by researchers in the British Geological Survey, is one part of Task A (i.e. Modelling gas injection experiments) of the DECOVALEX-2019 project. More details about the experimental procedures and data analysis were given in (Daniels and Harrington 2017).

3.3.4.4.1 Initial and boundary conditions

Figure 3.8 shows the meshed domain and the boundary conditions for the 1-D gas flow test. The brown dashed line represents the axis of symmetry. The radius and the height of the simulated domain are 30mm and 120mm respectively. It was found that applying roller boundary to all boundaries is too strict to simulate the constant volume condition for the 1-D flow test. In this simulation, the constant volume condition is weakly achieved through applying a constant load to balance the initial stress state and a spring boundary to constrain the further dilation of the sample, see Figure 3.8. The constant load is 6.55 [MPa] and the stiffness of the spring is 130 [GPa/m]. The pressurized helium gas is injected into the sample through the green boundary and flows out from the red boundary, as seen in Figure 3.8. The porewater pressure on the outflow boundary is 1MPa. The whole domain is meshed by using quadrilateral elements with a size of 2 mm. The initial gas pressure in MAC is 1.05 [MPa] and the initial water pressure in both MAC and MIC is 1.0 [MPa]. The initial mean yielding effective stress for the MIC is assumed to be -7.1 [MPa]. The initial effective stress in the axial and radial direction is -8.5 [MPa] and -5.5[MPa], respectively (Rutqvist et al. 2018).

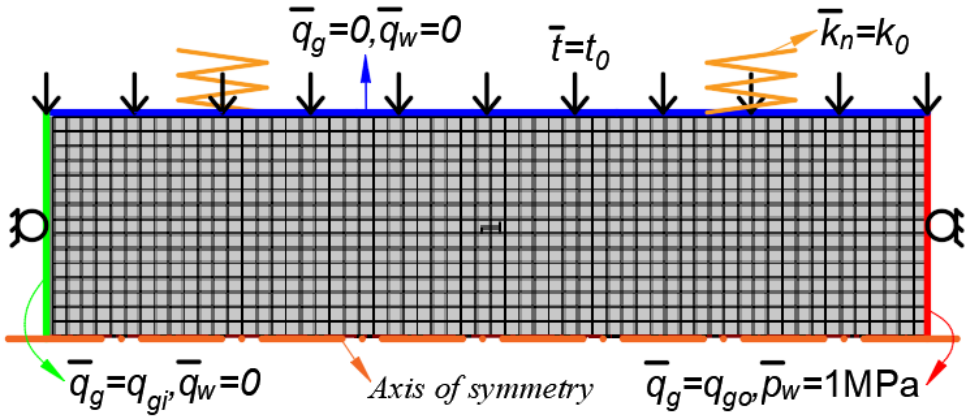

Figure 3.28 Boundary conditions and meshing strategy for 1-D gas flow test (Green line is the injection boundary which is connected with the gas vessel and red line is the outflow boundary)

3.3.4.4.2 Evolution of gas pressure and outflow rate

Figure 3.29 (a) presents the comparison between the simulated gas pressures with different hysteretic parameter, h, and the gas pressure obtained in experiment, while Figure 3.29 (b) shows the outflow rates from experiment and simulation, as well as the evolution of damage

variable at the injection and the outflow boundary. Instead of simulating the hydration process and series of gas injection procedures before the gas pressure reaches 3[MPa], a linear increase of gas pressure was applied in the gas vessel. Then the gas pressure was maintained for 7 days to achieve an equilibrium between the gas pressure and water pressure (Daniels and Harrington 2017). After the period for equilibrium, the gas injection was initiated by decreasing the porosity of gas vessel at a rate corresponding to the water pumping rate. As seen in Figure 3.29 (a), the simulated result agrees very well with the experimental one before reaching the peak value, even when the injection rate experiences a reduction. During this period, there is no gas flowing out of the sample, see Figure 3.29 (b). Although the damage has occurred on the injection boundary before the gas pressure reaches a peak value, see the solid pink line in Figure 3.29 (b), the gas is not able to flow out of the sample as the developed damage field has not yet connected with the outflow boundary, as analyzed in Section 3.3.4.3.3.

Immediately after the damage field reaches the outflow boundary, see the green solid line in Figure 3.29 (b), a large amount of gas starts flowing out of the sample. As seen in Figure 3.29 (b), the major gas outflow event is satisfactorily described by the numerical model in terms of both the starting moment and the magnitude. Corresponding to this major outflow event, the simulated gas pressure experiences a drop from the peak value. However, the gas pressure measured in the experiment showed a slight increase, which may indicate the increased permeability is not large enough to induce a sharp decrease in the gas pressure.

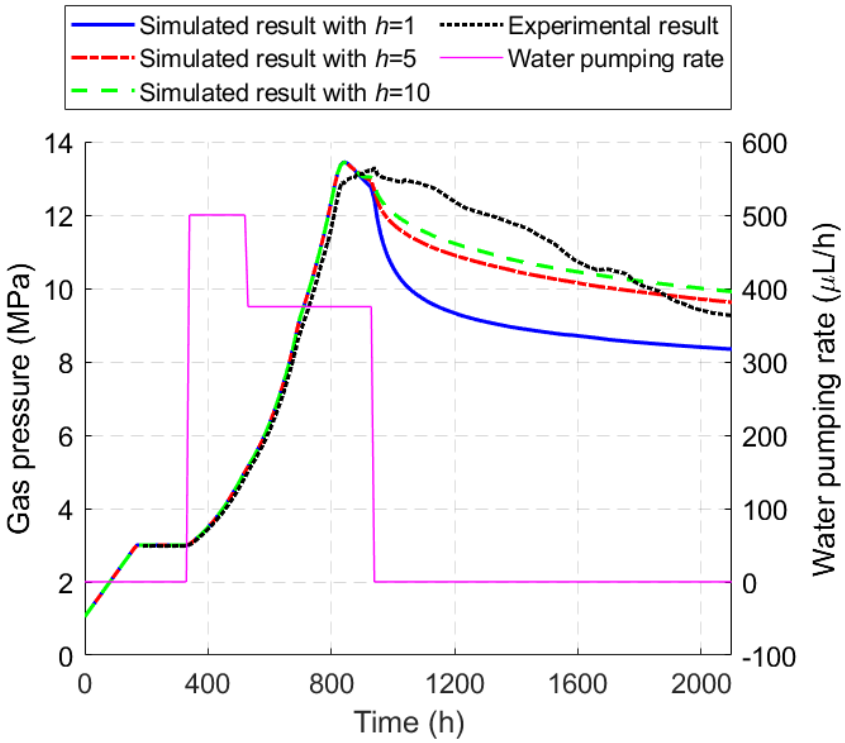

(a) Evolutions of gas pressures with different hysteretic parameters, h

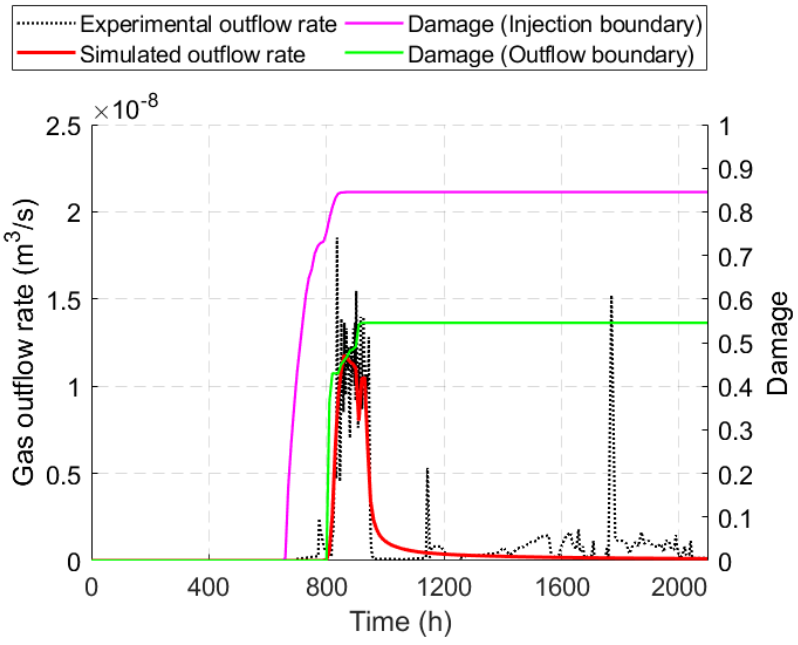

(b) Evolutions of gas outflow rates

Figure 3.29 Evolution of gas pressure and gas outflow rate (Experimental results from (Daniels and Harrington 2017))

After the cessation of gas injection, the outflow rate measured in experiment abruptly reduced to a value close to zero, see the black dotted line in Figure 3.29 (b). This may be caused by the abrupt collapse of the pore structure (or closure of the developed pathways). In contrast, the simulated outflow rate decreases in a much gradual manner, see the red solid line. As a result, a larger amount of gas for the simulation than the experiment will flow out of the sample. Thus, the simulated gas pressure, see the red dotted dash line in Figure 3.29 (a), decreases more rapidly than the experimental gas pressure does just after the cessation of gas injection. It is worth noting that increasing the hysteretic parameter from 1 to 5, has significantly improved the model to account for the abrupt collapse of pore structure, as compared between the blue solid line and the red dotted dash line. However, further increasing the hysteretic parameter from 5 to 10 has less influence on the simulated result. At this moment, the relative permeability may play a more important role in controlling the total permeability. However, this mechanism is beyond the scope of the current study. Interestingly, as time goes on, the decrease of the simulated gas pressure becomes gentler than its experimental counterpart. This may be explained by the evolution of the outflow rate. As seen in Figure 3.29 (b), as the simulated gas outflow rate gradually approaches zero, the measured outflow rate was sporadic with fluctuations and spikes, indicating the opening and closure of newly developed pathways (Daniels and Harrington 2017).

In conclusion, the developed model can well describe the general evolutions of both the gas pressure and the outflow rate. The abrupt decrease of outflow rate after the cessation of gas injection can be partially recovered by increasing the hysteretic parameter, but more mechanisms, such as the hysteresis of relative permeability and the pore structure evolution at a local scale, are necessary to be considered. As for the chaotic behavior of outflow rate at the declining stage, the current model is still incapable of achieving that, as the involved physical processes are very complex to be simulated.

3.3.4.4.3 Evolution of porewater pressure

Figure 3.30 shows the evolutions of porewater pressures at different positions of the tested sample. In general, the porewater pressures prior to the damage initiation only experience very

small increases but rise substantially once the damage occurs on the injection boundary. This qualitatively reflects the experimental observation. However, the simulated porewater pressures cannot reach values as high as those measured in the experiment. As shown in Figure 3.30, the maximum value of the simulated porewater pressure is almost half of its experimental counterpart which is comparable with the gas pressure. This phenomenon was also observed in other numerical studies, such as ones in (Tamayo-Mas et al. 2018). Furthermore, it is worth noting here that this phenomenon also occurred in previous experimental studies, such as Mx80-8 test and Mx80-10 test in (Harrington and Horseman 2003). For the current study, this discrepancy may be explained as follows. In this paper, the development of microfracture network is implicitly described by the evolution of damage field. The localized gas flow is simulated in a smeared way, which may lead to the desaturation of its surrounding areas that, in fact, should have been fully saturated. As the gas pressure serves as the pore pressure in the unsaturated condition, the desaturated areas may experience volume dilation. In such case, the porewater pressure may not reach a value as high as the value reached under saturated condition. To avoid this discrepancy, the localized gas flow is better to be modelled in an explicit way. After the cessation of gas injection, the simulated porewater pressure continuously decreases, following a similar evolution trend as the gas pressure. In contrast, the porewater pressure in experiment first experienced a decline and then increased to a value close to the gas pressure. This may be caused by the development of new pathways (Daniels and Harrington 2017). This behavior is closely related to the transient evolution of unstable pathways at a local scale. The current model is still incapable of simulating such complex coupled HM behaviors. Therefore, more efficient models that can explicitly account for the localized gas flow and transient evolution of unstable pathways are necessary to be developed to well describe the evolution of porewater pressure.

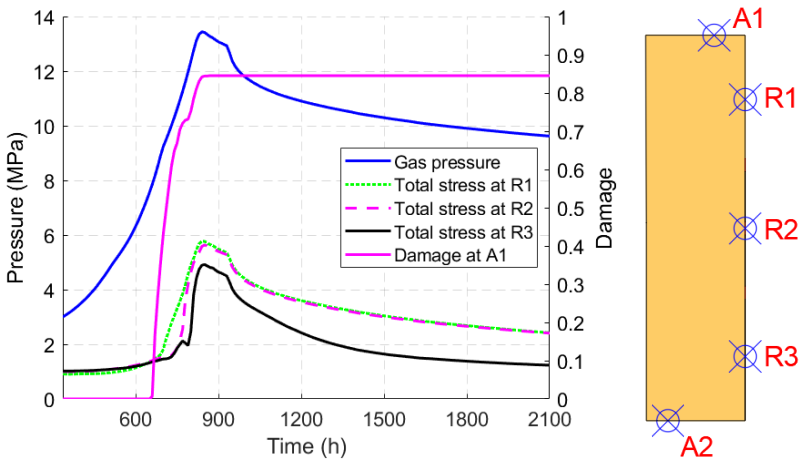

(a) Evolutions of simulated porewater pressures

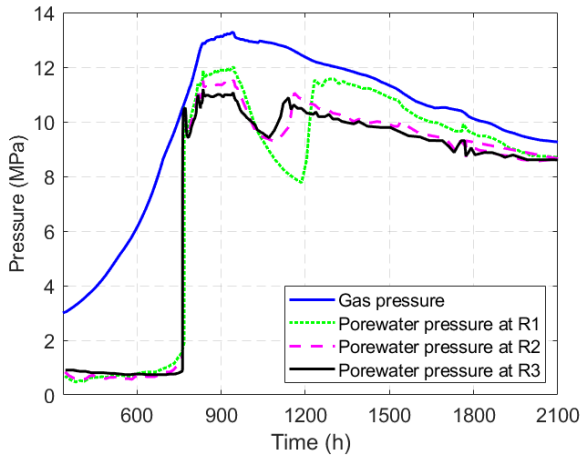

(b) Evolutions of experimental porewater pressures ((Daniels and Harrington 2017))

Figure 3.30 Evolutions of porewater pressures at different positions

3.3.4.4.4 Evolution of total stress

Figure 3.31 (a) and Figure 3.31 (b) respectively present the evolutions of the simulated and the experimentally observed total stresses in different positions of the sample. The simulated total stresses increase slowly prior to the damage initiation but turn to rapid increases when the damage occurs at the injection boundary, see Figure 3.31 (a). In general, this simulated result reflects the experimental finding that the measured total stresses experienced sharp increases once microfractures started to develop in the sample (Daniels and Harrington 2017; Harrington et al. 2017b), as seen in Figure 3.31 (b). Then, the simulated total stresses evolve in a similar manner as the gas pressure, which is also observed in the experimental results, see Figure 3.31 (b).

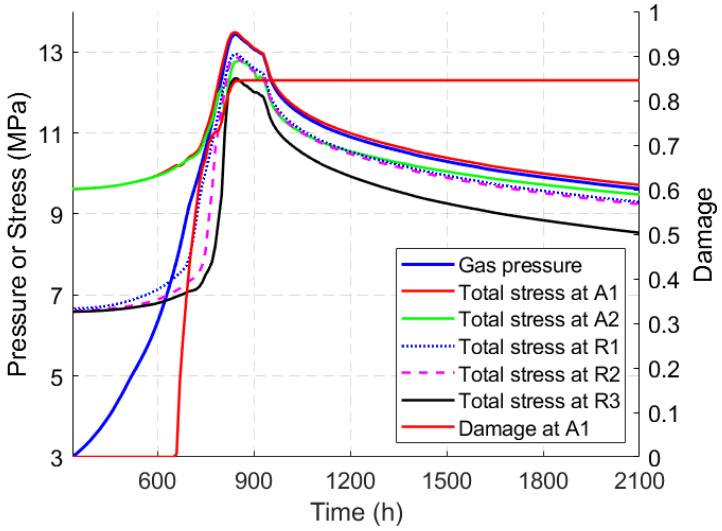

(a) Evolutions of simulated total stresses

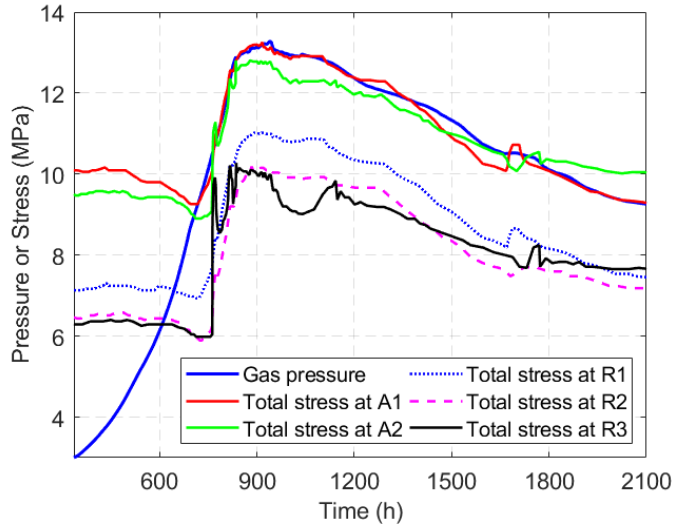

(b) Evolutions of experimental total stresses (Daniels and Harrington 2017)

Figure 3.31 Evolutions of total stresses at different positions of the sample

However, the developed model is still inadequate to describe some specific details. As Figure 3.31 (b) shows, the total stresses experience significant fluctuations which are associated with the evolutions of the aperture size and the orientation of unstable pathways. This behavior is very sensitive to the local stress state. Although the heterogeneous distribution of HM properties has been considered by the current model, the scale at which the heterogeneity has effects is still much larger than the scale where the concerned physical processes take place. Therefore, a much smaller scale needs to be introduced into the model to capture the related physical process. In addition, the simulated radial total stresses can reach

higher values than their experimental counterparts, as compared between Figure 3.31 (a) and Figure 3.31 (b). This may result from the overestimation of the contribution of gas pressure to the pore pressure. As analyzed in the previous section, when the areas that should have been saturated become unsaturated due to the smeared way to treat the localized gas flow, the gas pressure serves as pore pressure, which may lead to larger total stress.

3.3.4.5 Spherical gas flow test

Spherical gas flow test is another part of Task A of the DECOVALEX-2019 project. Experimental details and data analysis were given in (Harrington et al. 2017b).

3.3.4.5.1 Initial and boundary conditions

The meshed domain and boundary conditions for simulating the spherical gas flow test are the same with those in Mx80-8 test, see Figure 3.11, but the specific operations for gas injection are different. As the initial amount of gas is not sufficient to complete the whole test, additional gas was injected into the gas vessel three times during the test. Table 10 lists the three gas supplement events, including the moment and the increased volume of each event. This data was given by Dr. Harrington (personal communication, Oct 1st, 2019). As the hydration process is not considered in the current model, the time as listed in Table 10 has been modified to be consistent with the numerical study.

Table 10 Gas supplement events during the test

Event	Time/h	Added volume of gas /mL
1	2235.426	92.44
2	2977.746	27.68
3	3173.826	61.27

The initial pressure for water and gas in the MAC is 1 [MPa] and 1.05[MPa], respectively, and the initial water pressure in the MIC is 1 [MPa]. The swelling pressure at the initial state is 5.8[MPa] (Harrington et al. 2017b). As the absolute value of effective stress is equal to the swelling pressure for a high swelling clay (Horseman et al. 1999), the initial effective stress for

the MAC is set to -5.8[MPa]. The initial mean yielding effective stress for the MIC is assumed to be -5.9[MPa].

3.3.4.5.2 Evolution of gas pressure

Figure 3.32 presents the simulated gas pressure (the blue solid line) and the measured gas pressure in the experiment (the black dotted line). The pink solid line represents the evolution of water pumping rate in the gas injection system. The experimental result presents significant fluctuations because of the strong coupling between the gas pressure and the local stress state (Harrington et al. 2017b).

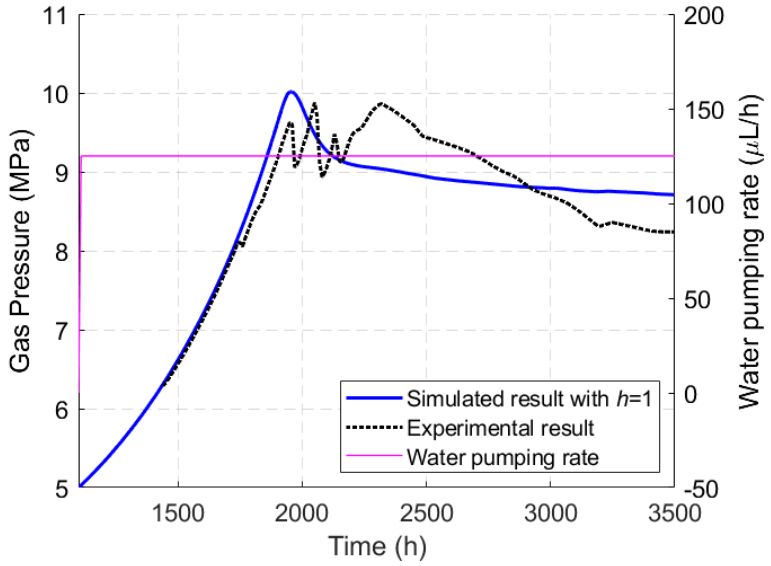

Figure 3.32 Evolution of gas pressure in the gas vessel (Experimental result from (Harrington et al. 2017b))

When the gas pressure exceeds the local tensile strength, microfractures are expected to propagate. Due to the heterogeneous distribution of HM properties and stress state, the generated fractures are unstable in terms of both the aperture size and the orientation (Harrington et al. 2017b). The developed fractures may open or close in a rapid manner in response to small variations of stress state, thus leading to strong fluctuations of gas pressure. In contrast, the simulated result experiences a relatively smooth transition from the increasing stage to the declining stage. Currently, the developed model is incapable of describing the strong fluctuations which are associated with physical processes at a local scale, as discussed

above. Although the double pore structure has been considered by the current model, the local HM behaviors can hardly be described, as the localised gas flow is treated in a smeared way. Therefore, to describe the strong fluctuations, a more advanced multiscale model that can explicitly account for local HM behaviors, is necessary to be developed.

3.3.4.5.3 Evolution of total stress

Figure 3.33 (a) shows the simulated gas pressure, the total stress and the damage variable at the injection boundary at different positions of the sample, while Figure 3.33 (b) presents the measured gas pressure and total stresses in the experiment. Some general behaviors have been successfully captured by the numerical model. In both the experimental and the simulated results, the evolution trends of the total stresses are consistent with that of the gas pressure. This demonstrates that the strong coupling between the gas pressure and the stress state has been successfully achieved by the developed HM model. In addition, the experimental finding that the build-up of total stress is closely related to the development of microfractures (Harrington et al. 2017b; Harrington et al. 2019b), is also reflected by the numerical results. As shown in Figure 3.33 (a), the total stresses at all monitoring points increase with small rates prior to the damage initiation. When the damage initiates on the injection boundary, the total stresses experience significant increases until reaching peak values, seen Figure 3.33 (a). However, as analyzed in the previous section, the developed model is incapable of describing local HM behaviors. Therefore, the significant fluctuations of the total stress are not observed in the numerical results.

It is worth noting that the discrepancy between the numerical and the experimental results may also result from the simplification of the dimension from a 3D domain to an axisymmetric 2D domain. The preferential pathways in a 3D domain may have more possible directions to propagate than those in the axisymmetric domain. This part is beyond the scope of the current paper but will be explored in the future.

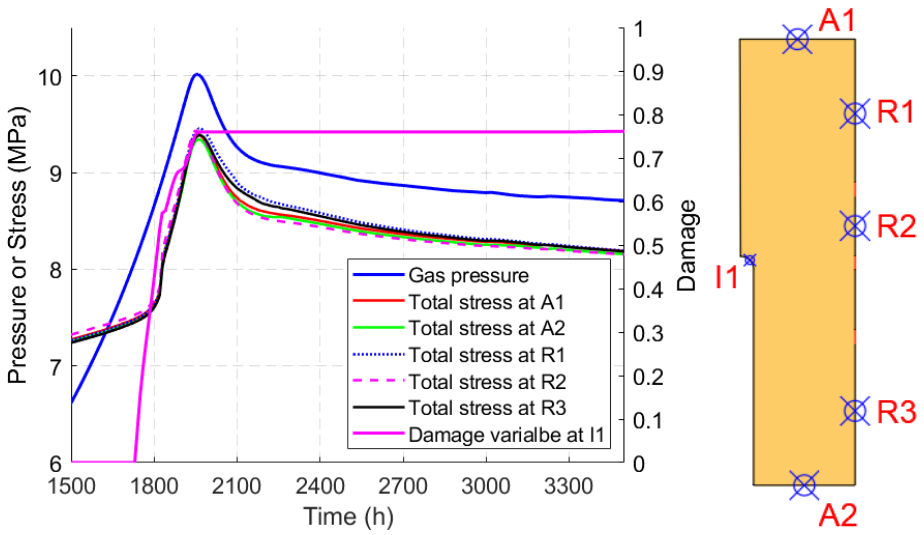

(a) Total stresses simulated by the current model at different positions (as marked on the sample)

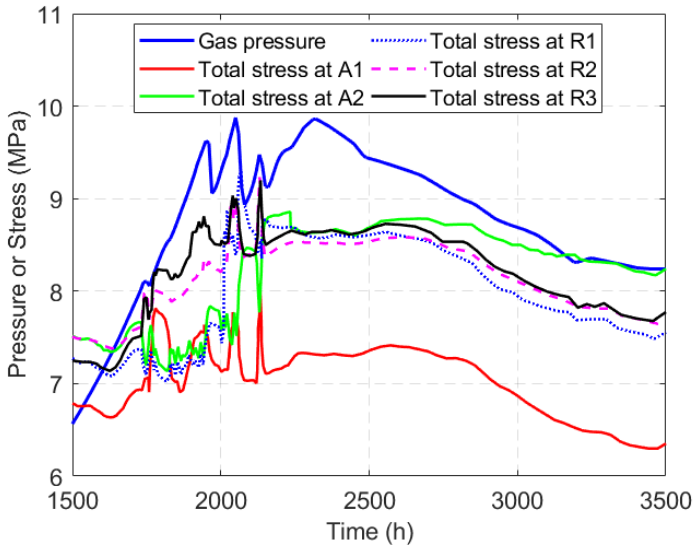

(b) Total stresses measured in the experiment (Harrington et al. 2017b)

(Note that the original time in this figure has been modified to be consistent with the numerical results)

Figure 3.33 Evolution of total stress at different positions of the sample

3.3.5 Conclusions

A coupled HM model, accounting for double pore structure, damaging effects and hysteresis of permeability, has been developed in this paper to simulate gas migration in saturated bentonite. According to the numerical results, several main conclusions can be drawn as follows.

(1) Owing to the differentiation of porosity between the MAC and the MIC and the assumption that the MIC remains fully saturated, the simulated sample is able to keep a high degree of saturation during the whole simulation.

(2) The damage model helps to implicitly simulate the development of microfracture network which is closely related to the evolution of total stress, porewater pressure and outflow rate. Specifically, the total stress and the porewater pressure present substantial increase once the damage initiates from the injection boundary. The major gas outflow event only occurs after the damage field reaches the outflow boundary. In addition, the damage model is beneficial to achieving the less significant gas breakthrough event in the second injection cycle.

(3) The hysteresis of intrinsic permeability results from two mechanisms. Firstly, as the damage variable is irreversible, the intrinsic permeability can keep a larger value when the tensile strain returns from the reversal point. Another mechanism of the hysteresis is from the tensile strain itself. When the tensile strain returns from the reversal point, the reduction rate of the intrinsic permeability is controlled by the hysteretic parameter. Numerical results showed that considering the hysteresis of intrinsic permeability makes the developed model more flexible to fit the experiment.

In general, the developed HM model can well describe some main experimental findings. However, there are still some limitations that need to be resolved in the future. Firstly, the strong fluctuations during the development of microfracture network are associated with the transient evolution of aperture size and orientation of unstable pathways. To numerically capture these features is still a challenging work, as the involved physical processes are very sensitive to the local stress state and local HM properties. The heterogeneous distribution of HM properties considered in this paper is beneficial to simulating the preferential development of microfracture network to some extent. However, the effective scale of the heterogeneity is much larger than the scale where the concerned physical processes take place. In addition, the smeared way to treat the localised gas flow may desaturate the areas that should have been saturated. This may lead to the overestimation of the contribution of gas pressure, thus

influencing the capability to predict the evolution of total stress and porewater pressure. To resolve these limitations, more advanced models that can capture the multiscale effects and the localised gas flow are necessary to be developed in the future.

Chapter 4 Phase Field Modelling of Preferential Gas Flow in Saturated Bentonite

4.1 Introduction

The development of preferential pathways is an important characteristic of gas migration in saturated bentonite. Previous experimental studies, like those in (Harrington and Horseman 2003; Harrington et al. 2017b; Harrington et al. 2019b), indicated that the development of preferential pathways directly controlled the evolutions of total stress, porewater pressure and permeability. The chaotic behavior in stress field is closely associated with the changes in the aperture and orientation of the developed fractures (Harrington et al. 2017b). Therefore, the development of preferential pathways needs to be considered in the coupled HM model to realistically simulate the gas migration process. By far, numerical models that can explicitly simulate the development of preferential pathways in saturated bentonite are less reported. In recent years, phase filed (PF) method has been widely used to simulate hydraulic fracturing and desiccation cracking. In this chapter, the PF method is incorporated into the coupled HM model to simulate the development of preferential pathways, thus forming a coupled HM-PF framework. The framework is rigorously developed based on Coussy's thermodynamic theory for unsaturated porous media and microforce balance law. It is further enriched by considering the effects of swelling pressure and heterogeneity of HM properties on the fracturing process.

4.2 Modelling of Preferential Gas Flow in Heterogeneous and Saturated Bentonite Based on Phase Field Method

Published in Computers and Geotechnics Volume 116, December 2019, 103206

Guanlong Guo, Mamadou Fall

Abstract:

Phase field (PF) method is incorporated into the coupled hydromechanical (HM) model in this paper to simulate the preferential gas flow in saturated bentonite. In order to account for the effect of the heterogeneous distribution of HM properties on the development of preferential pathways, a spatially auto-correlated random field is generated and applied to the coupled HM-PF model. A stabilized technique for equal low-order finite element is adopted in this paper to avoid the pore pressure oscillation and to increase the computational efficiency. The simulated results showed that the developed coupled HM-PF model is able to explicitly describe the preferential gas flow in saturated bentonite. Meanwhile, some of the commonly observed behaviors in experiments, such as the nearly saturated state after gas injection, the heterogeneous distribution of water pressure and the build-up of both water pressure and total stress during fracturing process, are successfully captured by the developed model. In addition, four factors, including the Gaussian random field, the coefficient of variation, the boundary condition and the injection rate, have been examined in terms of their effects on the fracturing process. The numerical results showed that these four factors have significant influences on both the fracture pattern and the evolution of gas pressure.

Keywords: Phase field; Preferential pathways; Deep geological repository; Bentonite; Hydro-mechanical model; Nuclear wastes

4.2.1 Introduction

Bentonite-based geomaterials are regarded as ideal barrier materials to seal nuclear waste in deep geological repositories (DGRs) because they have desirable properties, such as low permeability, low molecular diffusion, high retention capacity of radionuclides and self-sealing ability (Cuss et al. 2014a; Harrington et al. 2017a; Hoch et al. 2004; Liu et al. 2015; Wang et al. 2013b; Ye et al. 2014). During the lifespan of DGRs, a large volume of gas is expected to be produced as a result of three basic physicochemical processes, i.e. metal corrosion, water radiolysis and bio-degradation (Graham et al. 2012; Guo and Fall 2018; Harrington et al. 2017a; Marschall et al. 2005; Ye et al. 2014). The migration of the produced gas in buffer materials may, however, have detrimental effects on the desirable properties of bentonite-based geomaterials. It is widely accepted that there are four basic types of gas transport mechanisms in porous media of low permeability, i.e., advection/diffusion of dissolved gas, visco-capillary two-phase flow, dilatancy-controlled flow (DCF) and macro-fracture flow (Liu et al. 2016; Marschall et al. 2005; Nagra 2008; Xu et al. 2015; Ye et al. 2014; Yu and Weetjens 2009).

At the beginning of gas generation, the generated gas can dissolve into pore water, as the rate of gas production is less than that of gas dissolution (Ye et al. 2014). The dissolved gas is transported under the gradient of gas concentration or along with the advective flow of pore water. This transport mechanism is less efficient although it may exist during the whole period of gas migration (Nagra 2008). Visco-capillary two-phase flow is a transport process where pore water is displaced by gas when the capillary pressure exceeds the gas entry value of porous media (Bear 1972). Due to the extremely small size of pores in saturated bentonite, the gas pressure required to entry the bentonite may even exceed the total stress. Under such a condition, the mechanical process plays an important role in gas migration behavior. Previous experiments conducted under constant volume condition showed that the gas migration in bentonite is generally accompanied by the development of preferential pathways (Graham et al. 2012; Harrington and Horseman 2003; Horseman et al. 1999), which characterizes the so-called dilatancy-controlled flow. The macro-fracture flow also involves the development of preferential pathways that, however, occurs at a macroscale sense (Ye et al. 2014).

The preferential pathways are considered to be a series of fractures developed under the high gas pressure (Horseman et al. 1999) (Graham et al. 2012). When the gas pressure reaches a value close to the total stress, a strong coupling between gas pressure, water pressure and total stress occurs, which indicates the propagation of fractures (Graham et al. 2012). Moreover, some direct evidence for the formation of fractures were observed in experiments (Cuss et al. 2012; Horseman et al. 1999; Wiseall et al. 2015). These developed fractures were found unstable and varied spatially and temporally during the gas migration test (Graham et al. 2012; Harrington et al. 2017b; Harrington et al. 2019b). For example, the major outflow flux may switch between different sink filters and the gas in the subsequent injection cycle may not use the preferential pathways created in the previous injection cycle (Harrington and Horseman 2003; Horseman et al. 1999). As the gas preferentially flows through the developed fractures, the surrounding porous matrix is left at an almost fully saturated state (Hoch et al. 2004; Horseman et al. 1999; Pusch and Hökmark 1990). Moreover, the self-sealing behavior of the saturated bentonite was also commonly observed in experiments. For example, after the gas injection is halted, the decreased gas pressure is not large enough to support the opening of the developed fracture, thus leading to the fracture closure (Harrington and Horseman 2003). In addition, the rehydration of the tested specimen may lead to a certain recovery of the original tensile strength (Graham et al. 2012; Horseman et al. 1999). As a summary, the evolution of preferential pathways significantly controls the gas migration behavior in saturated bentonite. Thus, physically simulating the development of preferential pathways is crucial to obtain an in-depth understanding of the gas migration behavior.

Most of the current numerical models mainly considered the developed preferential pathways in an implicit manner. For example, some of the nonlinear mechanical models, such as plasticity (Alonso et al. 2012; Nguyen and Le 2014; Xu et al. 2013) and damage (Fall et al. 2014; Mahjoub et al. 2017), are used to incorporate the effects of preferential pathways on the gas migration behavior in saturated bentonite or porous media. These models have presented decent capabilities of capturing the effects of material degradation on the hydraulic properties, such as the gas entry value, the intrinsic and the relative permeability. To simulate the

development of preferential pathways in a more physical sense, some advanced conceptual models, such as the embedded fracture model and the double porosity model, have been incorporated into the conventional coupled hydromechanical (HM) framework. The former, which is a strain-controlled permeability model, is a widely used conceptual model to simulate gas preferential flow in low permeable media (Arnedo et al. 2013; Delahaye and Alonso 2002; Gerard et al. 2014; Olivella and Alonso 2008). However, these embedded fractures are a series of imaginary fractures that only change the hydraulic properties and have no effects on the mechanical properties. In addition, the volume of these fractures has not been independently incorporated into governing equations, which means that the coupling between the embedded fracture and the porous matrix is indirect (Guo and Fall 2018; Rutqvist and Stephansson 2003). In order to account for the direct coupling process, double porosity and double effective stress concepts were introduced into the coupled HM framework by Guo and Fall (2018). In that model, a double effective stress concept was derived based on the mixture theory and the first law of thermodynamics. The mechanical behavior of each subcontinuum (i.e. fractured continuum or porous continuum) is governed by its own effective stress. The direct coupling between the fractured and the porous continuum is achieved through total strain, total porosity and a water exchange term. This treatment is able to simultaneously capture the consolidation of porous matrix and the dilation of fracture, which is necessary to be considered when simulating the dilatancy-controlled flow under constant volume condition (Harrington et al. 2017b). However, the double porosity model is unable to explicitly simulate the preferential pathways.

At present, both the finite element method (FEM) and the discrete element method (DEM) have been used to model the process of fracture propagation in an explicit manner. To capture sharp discontinuities by using FEM, the common method is to insert interface elements between standard solid elements to represent potential fractures that may initiate and then propagate when the defined fracturing criterion is fulfilled. This FEM-based model has been used in (Sanchez et al. 2014) and (Vo et al. 2017) to model desiccation cracking, and in (Nguyen et al. 2017) for hydraulic fracturing. In addition, the extended finite element method

(XFEM), by defining a new shape function, can model the propagation of fractures without introducing interface elements or remeshing strategy. This approach has also been adopted to simulate both desiccation cracking and hydraulic fracturing (Mohammadnejad and Khoei 2013a, b; Salimzadeh and Khalili 2015c). Compared to FEM, using DEM to model fracture propagation is more straightforward, as sharp discontinuities are essentially constructed in DEM. This method has also been used to model desiccation cracking in soils (Amarasiri and Kodikara 2011; Amarisiri et al. 2013; Gui et al. 2017; Gui et al. 2016; Kodikara and Costa 2013). Although these models can explicitly capture the fracture trajectory, they not only require high computational efforts, but also have limitations in simulating the kinking and branching of cracks, especially in three-dimensional condition (Miehe et al. 2015b; Miehe et al. 2010b; Santillán et al. 2018).

In contrast, the phase field (PF) method provides a continuous approach to explicitly model the fracturing process in the framework of the standard FEM. In this approach, sharp discontinuities are regularized as diffusive crack zones by using a scalar auxiliary variable called PF (Miehe et al. 2010b). Compared to the discontinuous approaches where either an interface element or new shape function is introduced, the PF method can be implemented in a straightforward manner by using the standard FEM (Miehe et al. 2010a). This is due to the fact that the PF method describes the initiation, propagation and branching of cracks by using a governing equation which is derived from the principle of minimum potential energy or the thermodynamics theory (De Lorenzis et al. 2016; Miehe et al. 2010a; Miehe et al. 2010b). To date, the PF method, combined with conventional coupled HM frameworks (e.g. Biot's consolidation theory (Lee et al. 2017; Xia et al. 2017; Zhou et al. 2018), mixture theory (Choo and Sun 2018b; Wilson and Landis 2016) or the theory of porous media (Ehlers and Luo 2017)), has been a popular means of simulating hydraulic fracturing in fully saturated poroelastic media. By contrast, the use of the PF approach in unsaturated porous media has not been reported often. Cajuhi et al. (2018) extended a coupled HM-PF model to the unsaturated condition for modelling desiccation cracking in clays. In addition, Lee et al. (2017) proposed a PF model for fracturing process that involves immiscible two-phase flow. The model

considered non-zero capillary pressure and derived the absolute and the relative permeability in the induced fractures.

As stated earlier, the coupled HM-PF model might be a good candidate for simulating gas-driven fracturing in initially saturated porous media, as its extension to the unsaturated state is more straightforward. Moreover, the application of the phase field approach to model desiccation cracking in clays (Cajuhi et al. 2018) provides a general numerical framework for simulating the gas-driven fracturing in initially saturated bentonite. However, different constitutive models or coupling relationships should be used in the general framework to describe the physical processes that are specific to the gas-driven fracturing behavior. To examine the effects of heterogeneous distribution of HM properties on the development of preferential pathways, a spatially auto-correlated random field is generated by using the Cholesky decomposition technique. In addition, a stabilized technique, which was originally proposed by White and Borja (2008) and then extended by Song et al. (2017) to the unsaturated state, is adopted in this paper to reduce computational efforts and avoid pore pressure oscillation. It is worth noting that the aim of this paper is to explicitly simulate the development of preferential pathways in initially saturated bentonite, and then provide a qualitative reproduction of some commonly observed behaviors in experiments. The quantitative reproduction of the experimental results is beyond the scope of this paper but will be explored in the future.

4.2.2 Conceptual Coupled HM-PF Model

Before developing the coupled HM-PF model, a conceptual model is first proposed based on the commonly observed experimental behaviors as discussed in the Introduction. The traditional coupled HM models that are based on Biot's consolidation theory or mixture theory are inadequate to explicitly describe the localized gas flow. To address this research gap, the PF method is incorporated into the conventional coupled HM framework, which is illustrated as Figure 4.1.

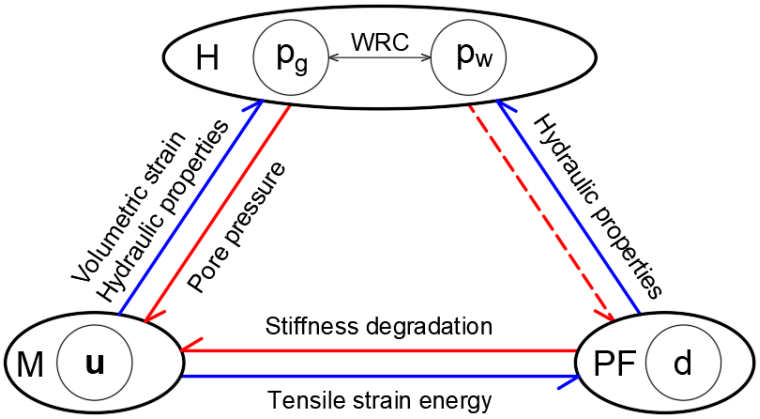

Figure 4.1 Coupling processes between different primary variables

Notes: H: Hydraulic process; M: Mechanical process; PF: Phase field; p_g and p_w are gas pressure and water pressure respectively; $\boldsymbol{u}$ is displacement vector; d is the phase field variable; WRC: water retention curve

As Figure 4.1 shows, the coupled HM-PF model consists of four primary variables, i.e. gas pressure, water pressure, displacement vector, and PF variable. The interactions between any two of these primary variables are discussed as follows.

4.2.2.1 Phase field approach

The Griffith fracture theory states that a critical energy release rate needs to be reached to initiate the propagation of fractures (Miehe et al. 2010b). As the critical energy release rate is defined at a lower-dimensional order, special treatments, such as node splitting, remeshing, adding interface elements or introducing a new shape function, need to be carried out to simulate sharp discontinuities. In order to bypass such complexities, a regularized crack surface functional with respect to the PF variable, see Eqs. (4.1) and (4.2), is developed by Miehe et al. (2010b) to convert an areal integral to a volume integral. As a result, the sharp discontinuities are smeared over a certain transition zone, and then the standard FEM can be used to model fracture propagation. This smeared approach is illustrated in Figure 4.2, where $d=0$, $0<d<1$, and $d=1$ denote the intact, transitional and fully fractured zones, respectively.

$$A_\Gamma = \int_\Gamma dA \approx \int_\Omega \Gamma_d(d,\nabla d)dV \tag{4.1}$$

$$\Gamma_d(d,\nabla d)=\frac{d^2}{2l}+\frac{l}{2}|\nabla d|^2 \tag{4.2}$$

where Γ and Γ_d denote a set of sharp and smeared fractures in the domain Ω, respectively, l is a characteristic length that controls the width of the transition zone and d is the PF variable.

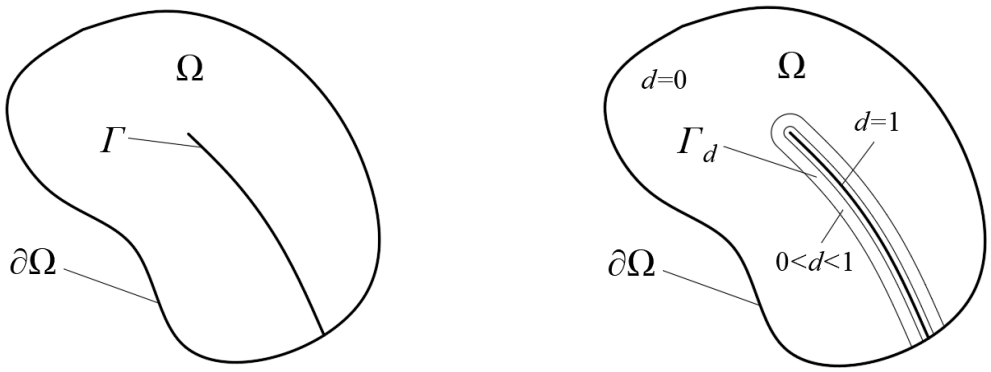

(a) Sharp fracture Γ (b) Smeared fracture Γ_d

Figure 4.2 Sharp fracture and smeared fracture with a phase field

(Notes: (a) A sharp fracture Γ in the domain Ω with boundary $\partial\Omega$ (b) A smeared fracture Γ_d in the domain Ω where $d=0$, $0<d<1$, and $d=1$ denote the intact, transition and fully fractured zones, respectively)

As shown in Figure 4.1, the evolution of the PF variable is driven by the tensile elastic strain energy. While the water content in the porous medium may influence the fracture energy release rate (Cajuhi et al. 2018; Wang et al. 2007; Yin and Vanapalli 2018), this coupling process is not considered in this study due to the limitations of experimental data.

4.2.2.2 Mechanical process

The mechanical process is interactively coupled with the hydraulic process and the PF, as indicated by the solid blue and red lines in Figure 4.1. The effect of pore pressure on the mechanical behaviors is reflected by the selected stress state variable. Typically, there are three types of stress state variables that are used for the current topic of interest, i.e., the effective stress with respect to average pore pressure (Fall et al. 2014; Guo and Fall 2018; Xu et al.

2013), independent stress state variables (i.e. net normal stress and suction) (Alonso et al. 2006; Arnedo et al. 2008; Olivella and Alonso 2008), and the effective stress with the pore pressure represented by the larger one between the gas and water pressure (Mahjoub et al. 2017; Nguyen and Le 2014; Vilarrasa et al. 2010). A large volume of literature has discussed the pros and cons of the effective stress and the independent stress state variables, such as (Khalili et al. 2004; Nuth and Laloui 2008). Currently, both stress state variables are used to model the elastoplastic behaviors of unsaturated expansive soils. The third effective stress concept is specifically used for gas migration in low permeable media in order to enhance the effect of gas pressure on the mechanical behavior. Note that selecting an appropriate stress state variable for modelling gas migration in low permeable media is still a topic under discussion. For simplicity, the effective stress concept with respect to average pore pressure, as expressed by Eq. (4.3), is used here to construct the coupled HM-PF model. The sign convention of continuum mechanics (i.e. the direction of the tensile stress and the compressive pressure is taken as positive) is used in this paper.

$$\boldsymbol{\sigma}' = \boldsymbol{\sigma} + \alpha_B \bar{p}\boldsymbol{I} = \boldsymbol{\sigma} + \alpha_B \left(S_w p_w + S_g p_g \right) \boldsymbol{I} \tag{4.3}$$

where $\boldsymbol{\sigma}$ is the total stress, $\boldsymbol{\sigma}'$ is the effective stress tensor, $\bar{p}$ is the average pore pressure, p_α and S_α are the pressure and the degree of saturation of fluid α (which denotes w and g for water and gas), respectively, α_B is the Biot's coefficient and $\boldsymbol{I}$ is a second-order identity tensor.

After the average pore pressure reaches the applied total stress (Biot's coefficient is assumed 1 for bentonite in this paper), the porous medium is subjected to a tensile effective stress. Driven by the tensile elastic strain energy, the fracture represented by the PF develops. As the phase field evolves from 0 to 1, the studied material gradually loses its ability to sustain the tensile stress, thus presenting a degradation of elastic stiffness, see Figure 4.1. As a result, the aperture of the developed fracture increases, which leads to an increase in intrinsic permeability

and a decrease of gas entry value. For an unsaturated porous medium, Young's modulus is generally enhanced by suction (Qi and Vanapalli 2018). However, due to the limited experimental data, this effect will not be discussed here but explored in the future.

4.2.2.3 Hydraulic process

The fluid flow is described by the generalised Darcy's law where relative permeability is introduced to differentiate between gas flow and water flow. The interaction between gas and water is described by using a water retention curve. In this paper, the same set of governing equations is used for fluid flow in both fractures and porous matrix, but the hydraulic properties used in Darcy's law are different from each other. Therefore, the flow in fractures and in a porous matrix is indirectly coupled based on the discussion in (Rutqvist and Stephansson 2003). This indirect coupling can be extended to a direct coupling by introducing an additional set of governing equations for fluid flow in fractures, as in (Santillán et al. 2018). In this paper, a smooth transition function with respect to the PF variable is proposed to differentiate the hydraulic properties of fractures and porous matrix. By applying a hyperbolic tangent function, the transition function can be expressed as:

$$T(d)=\frac{1}{2}\left\{\tanh\left[\theta_t\left(d-d_{cr}\right)\right]-\tanh\left(-d_{cr}\theta_t\right)\right\}, \tag{4.4}$$

where θ_t is a shape parameter that controls the slope of the transition function, and d_{cr} is a critical value of the PF at which the transition function is 0.5. To obtain a more intuitive understanding of the effects of the two parameters on the profile of the transition function, four different sets of parameters are plotted in Figure 4.3. It can be observed that d_{cr} controls the position where the transition takes place, while a larger θ_t leads to a more rapid transition.

Then, the hydraulic properties for the transition zone are expressed as:

$$H_t=T(d)H_f+\left[1-T(d)\right]H_p \tag{4.5}$$

where H_t stands for a specific hydraulic property in the transition zone, such as intrinsic permeability, relative permeability and degree of saturation, H_f and H_p are the corresponding hydraulic properties in fractures and porous matrix, respectively. The specific form of each hydraulic property listed above will be given in Section 4.2.4.2.

The deformation of the solid phase affects the two-phase flow in direct and indirect ways, see Figure 4.1. Direct coupling is reflected by the rate of volumetric strain that influences the source term in the governing equations for water and gas. In contrast, changes in the hydraulic properties (e.g. intrinsic permeability, storage coefficient, and gas entry value) caused by the deformation of the solid skeleton characterise the indirect couplings.

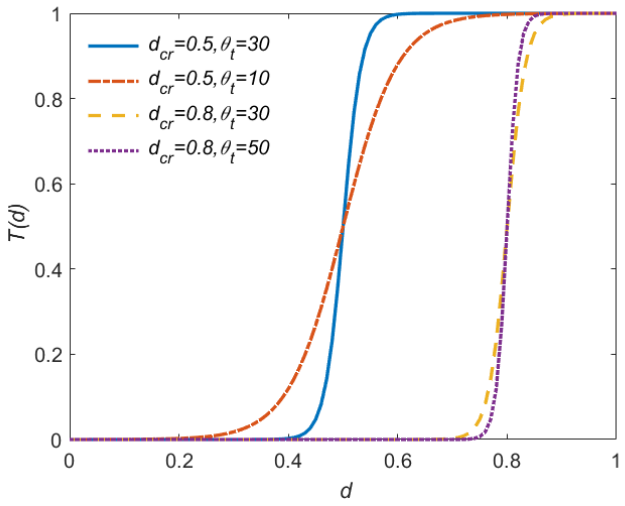

Figure 4.3 Transition function for hydraulic properties in fractures and porous matrix

4.2.3 Governing Equations

4.2.3.1 Mass balance equations

Based on the mixture theory and the assumption of small deformation (Hu et al. 2011; Rutqvist et al. 2001), the mass balance equations for gas and water can be respectively derived as

$$\rho_g\left[\left(S_g^2 - S_g p_c \frac{\partial S_e}{\partial p_c}\right)\frac{\alpha-\phi}{K_s} + \phi\left(\frac{S_g}{K_g} - \frac{\partial S_e}{\partial p_c}\right)\right]\frac{\partial p_g}{\partial t} + \rho_g\left[\left(S_g S_w + S_g p_c \frac{\partial S_e}{\partial p_c}\right)\frac{\alpha-\phi}{K_s} + \phi\frac{\partial S_e}{\partial p_c}\right]\frac{\partial p_w}{\partial t} + \nabla\cdot(\rho_g \boldsymbol{v}_g^D) = -\alpha_B S_g \rho_g \frac{\partial \varepsilon_v}{\partial t} \tag{4.6}$$

$$\rho_w\left[\left(S_w^2 + S_w p_c \frac{\partial S_e}{\partial p_c}\right)\frac{\alpha-\phi}{K_s} + \phi\left(\frac{S_w}{K_w} - \frac{\partial S_e}{\partial p_c}\right)\right]\frac{\partial p_w}{\partial t} + \rho_w\left[\left(S_g S_w - S_w p_c \frac{\partial S_e}{\partial p_c}\right)\frac{\alpha-\phi}{K_s} + \phi\frac{\partial S_e}{\partial p_c}\right]\frac{\partial p_g}{\partial t} + \nabla\cdot(\rho_w \boldsymbol{v}_w^D) = -\alpha_B S_w \rho_w \frac{\partial \varepsilon_v}{\partial t} \tag{4.7}$$

where S_e is the effective degree of saturation of water, $p_c = p_g - p_w$ is the capillary pressure, K_α is the bulk modulus of fluid α, K_s is the bulk modulus of solid grain, ε_v is the volumetric strain, ρ_α is the fluid density, ϕ is the porosity and $\boldsymbol{v}_\alpha^D$ is Darcy's velocity of the fluid α.

The rate of porosity change can be derived as (Hu et al. 2011; Rutqvist et al. 2001)

$$\frac{\partial \phi}{\partial t} = (\alpha_B - \phi)\left(\frac{1}{K_s}\frac{\partial \overline{p}}{\partial t} + \frac{\partial \varepsilon_v}{\partial t}\right) \tag{4.8}$$

4.2.3.2 Momentum balance equations

In this paper, the PF and its gradient constitute a microscopic force system, while the traditional forces, i.e. body and surface forces, are regarded as the components of a macroscopic force system. Therefore, two sets of momentum balance equations are presented in this section for the macroscopic and the microscopic force systems.

4.2.3.2.1 Macroscopic force system

Based on the mixture theory and neglecting the inertial and viscous forces, the momentum balance law for the macroscopic force system is derived as (Borja 2006; Rutqvist et al. 2001):

$$\nabla\cdot\boldsymbol{\sigma} + \rho\boldsymbol{g} = \boldsymbol{0} \tag{4.9}$$

where $\rho = (1-\phi)\rho_s + \phi(S_w\rho_w + S_g\rho_g)$ is the average density of the mixtures and $\boldsymbol{g}$ is the gravitational acceleration vector.

4.2.3.2.2 Microscopic force system

Currently, there are two commonly used ways to derive the governing equation for the PF, i.e., the variational principle of free energy minimization (Lee et al. 2018; Nguyen et al. 2016; Santillán et al. 2018; Xia et al. 2017) and microscopic force balance law (Choo and Sun 2018b; De Lorenzis et al. 2016; Na and Sun 2018; Wilson and Landis 2016). The former method is based on the pioneering work of Francfort and Marigo (1998), while the latter, which will be used in this paper, was originally developed by Gurtin (1996). Here, the momentum balance equation for the microscopic force system is derived from the principle of virtual work. For an arbitrary domain Ω, the internal power for the microscopic force system can be expressed as (De Lorenzis et al. 2016):

$$I = \int_\Omega \boldsymbol{\xi} \cdot \nabla \dot{d} \, \mathrm{d}\Omega + \int_\Omega \pi \dot{d} \, \mathrm{d}\Omega \tag{4.10}$$

where $\boldsymbol{\xi}$ is an internal microscopic stress that is work-conjugated to $\nabla \dot{d}$, and π is an internal microscopic body force that is work-conjugated to $\dot{d}$.

The external power for the microscopic force system over the domain Ω is expressed as:

$$W = \int_{\partial\Omega} \gamma(\boldsymbol{n}) \dot{d} \, \mathrm{d}\partial\Omega + \int_\Omega \varsigma \dot{d} \, \mathrm{d}\Omega \tag{4.11}$$

where $\gamma(\boldsymbol{n})$ and ς are an external microscopic traction force and an external body force, respectively.

If the virtual field is denoted by $\tilde{d}$, the principle of virtual work for the microscopic force system can be expressed as:

$$\int_\Omega \boldsymbol{\xi} \cdot \nabla \tilde{d} \, \mathrm{d}\Omega + \int_\Omega \pi \tilde{d} \, \mathrm{d}\Omega = \int_{\partial\Omega} \gamma(\boldsymbol{n}) \tilde{d} \, \mathrm{d}\partial\Omega + \int_\Omega \varsigma \tilde{d} \, \mathrm{d}\Omega \tag{4.12}$$

Following the procedures given by (De Lorenzis et al. 2016; Gurtin et al. 2010; Na and Sun 2018), the governing equations for the microscopic force system can be derived as:

$$\nabla \cdot \boldsymbol{\xi} - \pi + \varsigma = 0 \tag{4.13}$$

$$\gamma(\boldsymbol{n}) = \boldsymbol{\xi} \cdot \boldsymbol{n} \tag{4.14}$$

The specific forms of the above governing equations will be provided in the following section.

4.2.4 Constitutive Models

In this section, the mechanical constitutive models are derived from the thermodynamic approach, while the hydraulic constitutive models are directly given in a conventional way. A similar treatment is also proposed by Choo and Sun (2018b).

4.2.4.1 Mechanical constitutive models

4.2.4.1.1 Thermodynamic laws

To describe the evolution of PF variable, the contribution of the microscopic force system (as discussed in Section 4.2.3.2) to the change in the internal energy should be considered. Following the approach in (De Lorenzis et al. 2016), the rate of the internal energy per unit volume can be expressed as:

$$\dot{e} = \boldsymbol{\sigma}' : \dot{\boldsymbol{\varepsilon}} + \boldsymbol{\xi} \cdot \nabla \dot{d} + \pi \dot{d} - \nabla \cdot \boldsymbol{q} + r_T \tag{4.15}$$

where $\boldsymbol{\varepsilon}$ is the total strain tensor, $\boldsymbol{q}$ is the heat flux vector and r_T is the heat source term.

The second law of thermodynamics is generally described by the Clausius-Duhem inequality (Gurtin et al. 2010; Na and Sun 2018), which is written as:

$$D_{\text{int}} = \dot{\eta} + \nabla \cdot \left(\frac{\boldsymbol{q}}{T} \right) - \frac{r_T}{T} \geq 0 \tag{4.16}$$

where η is the entropy and T is the absolute temperature.

Helmholtz free energy, ψ, is defined with respect to the internal energy and the entropy as

$$\psi = e - T\eta . \tag{4.17}$$

By combining Eqs. (4.15)-(4.17) and assuming an isothermal condition, the Clausius-Duhem inequality is then rewritten as:

$$D_{\text{int}} = \boldsymbol{\sigma}' : \dot{\boldsymbol{\varepsilon}} + \boldsymbol{\xi} \cdot \nabla \dot{d} + \pi \dot{d} - \dot{\psi} \geq 0 \tag{4.18}$$

The general form of the Helmholtz free energy can be expressed as:

$$\psi = \psi\left(\boldsymbol{\varepsilon}, d, \nabla d\right) \ . \tag{4.19}$$

Substituting Eq. (4.19) into Eq. (4.18), and assuming that there is no plastic strain (i.e. $\boldsymbol{\varepsilon} = \boldsymbol{\varepsilon}^{el}$, ε^{el} is the elastic strain tensor), the second law of thermodynamics is rewritten as:

$$D_{\text{int}} = \left(\boldsymbol{\sigma}' - \frac{\partial \psi}{\partial \boldsymbol{\varepsilon}^{el}}\right) : \dot{\boldsymbol{\varepsilon}}^{el} + \left(\boldsymbol{\xi} - \frac{\partial \psi}{\partial \nabla d}\right) \cdot \nabla \dot{d} + \left(\pi - \frac{\partial \psi}{\partial d}\right) \dot{d} \geq 0 \tag{4.20}$$

Based on the Coleman-Noll procedure, the dissipation inequality given above results in the constitutive relations for the effective stress, σ', the internal microscopic stress, $\boldsymbol{\xi}$, and the internal microscopic body force, π, respectively as (De Lorenzis et al. 2016; Na and Sun 2018):

$$\boldsymbol{\sigma}' = \frac{\partial \psi}{\partial \boldsymbol{\varepsilon}^{el}} , \tag{4.21}$$

$$\boldsymbol{\xi} = \frac{\partial \psi}{\partial \nabla d} , \tag{4.22}$$

$$\pi = \frac{\partial \psi}{\partial d}. \tag{4.23}$$

Substituting Eqs. (4.22) and (4.23) into Eq. (4.13) and assuming there is no microscopic body force ($\varsigma = 0$) give the governing equation for the microscopic force system as:

$$\nabla \cdot \left(\frac{\partial \psi}{\partial \nabla d} \right) - \frac{\partial \psi}{\partial d} = 0. \tag{4.24}$$

4.2.4.1.2 Helmholtz free energy

As discussed in the previous section, the constitutive models of the macroscopic force and the microscopic force system depend on the specific form of the Helmholtz free energy functional. A general form of the Helmholtz free energy functional consists of a part due to elastic strain, ψ^e, and a part from the fracture surface energy, ψ^c, which is written as (Santillán et al. 2017a, 2018):

$$\psi = \psi^e(\boldsymbol{\varepsilon}, d) + \psi^c(d, \nabla d) \tag{4.25}$$

The fractures driven by the highly pressurized gas mainly belong to the Mode I fracture which is a fracture type that is caused by the tensile stress. To numerically describe the unilateral behavior, the elastic strain energy, ψ^e, is generally decomposed into a positive (tensile) part and a negative (compressive) part, in which only the positive part serves as the driving force for the fracturing process. Therefore, the degradation function $g(d)$ is only applied to the positive part (Miehe et al. 2010b). Then, the elastic part of the Helmholtz free energy can be expressed as

$$\psi^e(\boldsymbol{\varepsilon}, d) = g(d)\psi_0^{e+}(\boldsymbol{\varepsilon}) + \psi_0^{e-}(\boldsymbol{\varepsilon}) \tag{4.26}$$

where $\psi_0^{e\pm}(\boldsymbol{\varepsilon})$ is the positive or negative undamaged elastic strain energy.

Furthermore, to avoid the fracturing process caused by compressive load, the spectral decomposition technique is used to derive the positive part and the negative part in Eq. (4.26) , which are expressed as (Miehe et al. 2010b)

$$\psi_0^{e\pm}(\boldsymbol{\varepsilon}) = \frac{\lambda}{2}\langle tr(\boldsymbol{\varepsilon})\rangle_{\pm}^2 + \mu\sum_{a=1}^{\delta}\langle \varepsilon_a\rangle_{\pm}^2 \tag{4.27}$$

where $\langle x\rangle_{\pm} = (x \pm |x|)/2$ is the Macaulay bracket, $tr(\boldsymbol{\varepsilon})$ is the trace of the strain tensor, $\{\varepsilon_a\}_{a=1,2,3}$ are the principal strains, δ is the dimension of the model, λ and μ are the Lamé parameters.

The quadratic degradation function in Eq. (4.28) is used in this paper because it is capable of L convergence (Santillán et al. 2017b):

$$g(d) = (1-k)(1-d)^2 + k \tag{4.28}$$

where k is a small positive parameter introduced to avoid singularity of the stiffness matrix due to fully fractured components (Bourdin et al. 2000).

Combining Eqs. (4.21) and (4.25)-(4.27), the effective stress tensor is derived as:

$$\boldsymbol{\sigma}'(\boldsymbol{\varepsilon}, d) = g(d)\boldsymbol{\sigma}'^{+}(\boldsymbol{\varepsilon}) + \boldsymbol{\sigma}'^{-}(\boldsymbol{\varepsilon}) \tag{4.29}$$

$$\boldsymbol{\sigma}'^{\pm}(\boldsymbol{\varepsilon}) = \sum_{a=1}^{\delta}\left[\lambda\langle tr(\boldsymbol{\varepsilon})\rangle_{\pm} + 2\mu\langle \varepsilon_a\rangle_{\pm}\right]\boldsymbol{n}_a \otimes \boldsymbol{n}_a \tag{4.30}$$

$$\boldsymbol{\varepsilon} = \frac{1}{2}\left[\nabla\boldsymbol{u} + (\nabla\boldsymbol{u})^T\right] \tag{4.31}$$

where $\boldsymbol{\sigma}'^{\pm}$ are the positive and negative part of the effective stress tensor, $\{\boldsymbol{n}_a\}_{a=1,2,3}$ are the directional vectors of the principal strains and $\boldsymbol{u}$ is the displacement vector.

Then, substituting Eqs. (4.3) and (4.29) into Eq. (4.9) leads to a more specific momentum balance equation for the macroscopic force system, which is expressed as

$$\nabla \cdot \left[g\left(d\right)\boldsymbol{\sigma}'^{+}\left(\boldsymbol{\varepsilon}\right)+\boldsymbol{\sigma}'^{-}\left(\boldsymbol{\varepsilon}\right)-\bar{p}\boldsymbol{I} \right]+\rho \boldsymbol{g}=\boldsymbol{0}\,. \tag{4.32}$$

As seen in Eq. (4.32), when the degradation function, $g\left(d\right)$, reduces to 0, the contribution of the positive effective stress to the total stress becomes negligible. This means that the fully damaged zone has totally lost the capability to transfer stress, thus leading to a fracture zone.

By using the PF approach, i.e. Eqs. (4.1) and (4.2), the fracture surface energy is expressed as (Miehe et al. 2010b):

$$\psi^{c}\left(d,\nabla d\right)=G_{c}\left(\frac{1}{2l}d^{2}+\frac{l}{2}\left|\nabla d\right|^{2}\right) \tag{4.33}$$

where G_c is the critical fracture energy release rate.

Combining Eqs. (4.24)-(4.26) and (4.33) gives the governing equation of the PF as:

$$\left(1-d\right)H^{+}-\left(d-l^{2}\nabla^{2}d\right)=0 \tag{4.34}$$

$$H^{+}=\frac{2\psi_{0}^{e+}}{G_{c}/l} \tag{4.35}$$

where H^{+} is the fracture driving force.

After the gas injection is terminated, the developed fractures are unstable and may self-seal with time. However, the fracturing process is assumed irreversible for simplicity in this paper. Therefore, the fracture driving force H^{+} in Eq. (4.34) is replaced by its historical maximum value, H_{M}^{+} (Miehe et al. 2010b), which is defined as:

$$H_{M}^{+}=\max_{\tau\in[0,t]}\left\{\frac{2\psi_{0}^{e+}}{G_{c}/l}\right\} \tag{4.36}$$

4.2.4.2 Hydraulic constitutive models

At present, Darcy's law is a widely used constitutive model to describe the hydraulic process in expansive soils, as seen in (Gens 2010; Olivella and Alonso 2008; Sánchez et al. 2016). However, some scholars stated that the traditional Darcy's law may not be sufficient to account for the interactions between the fluid and the clay matrix and then proposed an improved Darcy's law (Achanta et al. 1994; Bennethum et al. 1997). In addition, when the mean free path of the gas molecules is comparable to the pore size, the molecules may slide along the pore wall, thus leading to a higher gas permeability (Coussy 2004). This physical process, which is called "Klinkenberg effect", generally occurs in porous media with low permeability or at low gas pressure (Rodwell et al. 1999). Due to the limited experimental data, the interaction between the fluid and the clay matrix as well as the "Klinkenberg effect" will not be considered in the current paper. Therefore, the generalized Darcy's law, as expressed by Eq. (4.37), is used to govern the fluid flow in both the porous matrix and the developed fracture.

$$\boldsymbol{v}_{\alpha}^{D} = -\frac{\boldsymbol{k}_{in} k_{r\alpha}}{\mu_{\alpha}} (\nabla p_{\alpha} - \rho_{\alpha} \boldsymbol{g}) \tag{4.37}$$

where $\boldsymbol{k}_{in}$ is the intrinsic permeability tensor, $k_{r\alpha}$ is the relative permeability and μ_{α} is the fluid dynamic viscosity.

Due to the development of preferential pathways in saturated bentonite under high gas pressure, the intrinsic and the relative permeability vary with the changes in both pore volume and pore structure. The formation of preferential pathways leads to a significant increase of intrinsic permeability and a decrease of gas entry value (which indirectly increases the relative permeability). The specific models to describe these couplings are given as follows.

4.2.4.2.1 Intrinsic permeability

The evolution of intrinsic permeability of the porous matrix is assumed associated with the change in porosity, which is simulated by using the Kozeny-Carman model (Chapuis and Aubertin 2003) as follows:

$$k_p = k_{p0}\left(\frac{(1-\phi_0)^2}{\phi_0^3}\right)\frac{\phi^3}{(1-\phi)^2} \tag{4.38}$$

where k_p and ϕ denote the current intrinsic permeability and porosity, respectively, k_{p0} and ϕ_0 represent the corresponding initial values.

The fracture here is idealized as two parallel plates, and then the intrinsic permeability can be expressed as (Choo and Sun 2018b; Miehe and Mauthe 2016):

$$\boldsymbol{k}_f = \frac{w^2}{12}\left(\boldsymbol{I} - \boldsymbol{n}_f \otimes \boldsymbol{n}_f\right) \tag{4.39}$$

$$w = h_e\left(\boldsymbol{n}_f \cdot \boldsymbol{\varepsilon} \cdot \boldsymbol{n}_f\right) \tag{4.40}$$

where $\boldsymbol{n}_f = \nabla d / |\nabla d|$ is the unit normal vector perpendicular to the developed fracture, h_e is the element size and w is the fracture aperture.

4.2.4.2.2 Relative permeability

The relative permeability of water and gas in porous media is commonly determined by using the Mualem-van Genuchten model (Luckner et al. 1989; Mualem 1976; van Genuchten 1980). The relative permeability of water, k_{prw}, and gas, k_{prg}, are, respectively, expressed as:

$$k_{prw} = \sqrt{S_e}\left[1-\left(1-S_e^{1/m}\right)^m\right]^2 \tag{4.41}$$

$$k_{prg} = \sqrt{1-S_e}\left(1-S_e^{1/m}\right)^{2m} \tag{4.42}$$

where m is a shape parameter of the van Genuchten model.

The relative permeability for fluid component, α, in the developed fracture differs from that in the porous media. Based on the assumption that there is a Stokes flow in smooth

fractures, the relative permeability of water and gas in fractures is derived respectively as (Cueto-Felgueroso and Juanes 2014):

$$k_{frw} = \frac{1}{2} S_w^2 \left(3 - S_w\right) \tag{4.43}$$

$$k_{frg} = S_g^3 + \frac{3}{2M_v} S_g \left(1 - S_g^2\right) \tag{4.44}$$

where μ_g is the dynamic viscosity of gas and M_v is the viscosity ratio, $M_v = \frac{\mu_w}{\mu_g}$.

4.2.4.2.3 Water retention curve

The water retention behavior of both the porous matrix and the developed fracture is described by the van Genuchten model (van Genuchten 1980) which is written as:

$$S_{\beta e} = \left[1 + \left(\frac{p_c}{p_{\beta gev}}\right)^n\right]^{-m} \tag{4.45}$$

where β denotes the f and p for the fractures and porous matrix, respectively; $p_{\beta gev}$ is the gas entry value, n is a shape parameter and $n = 1/\left(1-m\right)$.

In this paper, the degree of saturation, Eq. (3.40), the intrinsic permeability, Eq. (3.79)-(4.40), and the relative permeability, Eq. (3.42)-(4.44), are substituted into Eq. (4.5) to calculate the corresponding values in the transitional zone.

4.2.5 Model Implementation and Validation

4.2.5.1 Model implementation in COMSOL

4.2.5.1.1 Weak forms

The studied mixture is assumed to occupy a domain, Ω, with a boundary of $\partial\Omega$. The entire boundary, $\partial\Omega$, consists of Dirichlet boundary, $\partial\Omega_D$ (D denotes u, p_w, p_g and d for displacement, pore water pressure, pore gas pressure and PF, respectively), and Neumann

boundary, $\partial\Omega_N$ (N denotes t, q_w, q_g and q_d for traction, pore water flux, pore gas flux and the flux for PF, respectively). The Dirichlet and the Neumann boundaries are subjected to the restrictions as follows:

$$\partial\Omega = \partial\Omega_u \cup \partial\Omega_t = \partial\Omega_{p_w} \cup \partial\Omega_{q_w} = \partial\Omega_{p_g} \cup \partial\Omega_{q_g} = \partial\Omega_d \cup \partial\Omega_{q_d} \tag{4.46}$$

$$\varnothing = \partial\Omega_u \cap \partial\Omega_t = \partial\Omega_{p_w} \cap \partial\Omega_{q_w} = \partial\Omega_{p_g} \cap \partial\Omega_{q_g} = \partial\Omega_d \cap \partial\Omega_{q_d} \tag{4.47}$$

The Dirichlet and Neumann boundaries are prescribed as:

$$\boldsymbol{u} = \bar{\boldsymbol{u}} \quad \text{on} \quad \partial\Omega_u, \text{ and } \boldsymbol{n}\cdot\boldsymbol{\sigma}' = \bar{\boldsymbol{t}} \quad \text{on} \quad \partial\Omega_t, \tag{4.48}$$

$$p_w = \bar{p}_w \quad \text{on} \quad \partial\Omega_{p_w}, \text{ and } -\boldsymbol{n}\cdot\boldsymbol{v}_w^D = \bar{q}_w \quad \text{on} \quad \partial\Omega_{q_w}, \tag{4.49}$$

$$p_g = \bar{p}_g \quad \text{on} \quad \partial\Omega_{p_g}, \text{ and } -\boldsymbol{n}\cdot\boldsymbol{v}_g^D = \bar{q}_g \quad \text{on} \quad \partial\Omega_{q_g}, \tag{4.50}$$

$$-\boldsymbol{n}\cdot\nabla d = 0 \quad \text{on} \quad \partial\Omega_d. \tag{4.51}$$

where $\boldsymbol{n}$ is the unit normal to the boundary and the letters with bars denote the prescribed values on boundaries.

To construct the weak forms of the governing equations, the spaces of the weighting functions are defined as:

$$\mathcal{V}_u := \left\{ \boldsymbol{\eta} : \Omega \to \mathcal{R}^2 \mid \boldsymbol{\eta} \in \boldsymbol{H}^1, \boldsymbol{\eta} = \boldsymbol{0} \ \text{ on } \ \partial\Omega_u \right\} \tag{4.52}$$

$$\mathcal{V}_{p_w} := \left\{ \theta_w : \Omega \to \mathcal{R} \mid \theta_w \in H^1, \theta_w = 0 \ \text{ on } \ \partial\Omega_{p_w} \right\} \tag{4.53}$$

$$\mathcal{V}_{p_g} := \left\{ \theta_g : \Omega \to \mathcal{R} \mid \theta_g \in H^1, \theta_g = 0 \ \text{ on } \ \partial\Omega_{p_g} \right\} \tag{4.54}$$

$$\mathcal{V}_d := \left\{ \varphi : \Omega \to \mathcal{R} \,|\, \varphi \in H^1 \right\} \tag{4.55}$$

where H^1 is the Sobolev space of order one.

The weak forms of the developed coupled HM-PF model can be derived by integrating the product of the strong forms, i.e. Eqs. (4.6), (4.7), (4.32) and (4.34), with their corresponding weighting functions, i.e. Eqs. (4.52)-(4.55), over the domain Ω. Then, rearranging the resultant functions by using the integration by parts, the Gaussian integral theorem and the boundary conditions, Eqs. (4.48)-(4.51), yields the final weak forms as follows:

$$\mathcal{G} = \int_\Omega \nabla^s \boldsymbol{\eta} : \boldsymbol{\sigma}' d\Omega - \int_\Omega \bar{p} \nabla \cdot \boldsymbol{\eta} d\Omega - \int_\Omega \boldsymbol{\eta} \cdot \rho \mathbf{g} d\Omega - \int_{\partial\Omega} \boldsymbol{\eta} \cdot \bar{\mathbf{t}} d\partial\Omega = 0 \tag{4.56}$$

$$\mathcal{F}_w = \int_\Omega \theta_w \left[S_w \nabla \cdot \dot{\mathbf{u}} + C_{ww} \dot{p}_w + C_{wg} \dot{p}_g \right] d\Omega - \int_\Omega \nabla \theta_w \cdot \mathbf{v}_w^D d\Omega - \int_{\partial\Omega} \theta_w \bar{q}_w d\partial\Omega = 0 \tag{4.57}$$

$$\mathcal{F}_g = \int_\Omega \theta_g \left[S_g \nabla \cdot \dot{\mathbf{u}} + C_{gg} \dot{p}_g + C_{gw} \dot{p}_w \right] d\Omega - \int_\Omega \nabla \theta_g \cdot \mathbf{v}_g^D d\Omega - \int_{\partial\Omega} \theta_g \bar{q}_g d\partial\Omega = 0 \tag{4.58}$$

$$\mathcal{P} = \int_\Omega \varphi H_M^+ (1-d) d\Omega - \int_\Omega \left[\varphi d + l^2 (\nabla \varphi \cdot \nabla d) \right] d\Omega = 0 \tag{4.59}$$

where $C_{gg} = \phi \left(\frac{S_g}{K_g} - \frac{\partial S_e}{\partial p_c} \right)$, $C_{gw} = C_{wg} = \phi \frac{\partial S_e}{\partial p_c}$ and $C_{ww} = \phi \left(\frac{S_w}{K_w} - \frac{\partial S_e}{\partial p_c} \right)$. Note that the solid grains are assumed incompressible and the Biot's coefficient is equal to 1 in the above equations.

4.2.5.1.2 Implementation in COMSOL

The weak forms of the governing equations, as given in Eqs. (4.56) to (4.59), were implemented in a FEM-based commercial software, COMSOL MULTIPHYSICS. The numerical manipulations of the weak forms, including temporal and spatial discretization and consistent linearization, can be automatically achieved by COMSOL. For more details about these manipulations, readers can refer to (Choo and Sun 2018b; Song et al. 2017). A bilinear Lagrange shape function is adopted to interpolate all of the primary variables. The time

integration approach is based on the backward differentiation formulas (a fully implicit and adaptive integration method).

At present, most of the coupled HM-PF models, e.g., those in (Choo and Sun 2018b; Mauthe and Miehe 2017; Xia et al. 2017), used a staggered approach to solve the coupled equations because it is computationally efficient and shows good convergent features. Therefore, the segregated time-dependent solver is also used in this paper to solve the developed coupled HM-PF model. There are five primary steps involved in this solver at a time step [t_n, t_{n+1}] to solve the model, which are detailed as follows.

(1) The initial values of the primary variables for iteration at time step t_{n+1} are set as the values of the converged solutions in the previous time step t_n.

(2) The linearized matrix form of the coupled HM model, as expressed by Eq. (4.60), is solved first by using the Newton-Raphson iteration based on the values of primary variables in the previous iterative step.

$$\begin{bmatrix} \boldsymbol{J}_{uu} & \boldsymbol{J}_{uw} & \boldsymbol{J}_{ug} \\ \boldsymbol{J}_{wu} & \boldsymbol{J}_{ww} & \boldsymbol{J}_{wg} \\ \boldsymbol{J}_{gu} & \boldsymbol{J}_{gw} & \boldsymbol{J}_{gg} \end{bmatrix} \begin{Bmatrix} \delta \boldsymbol{u} \\ \delta \boldsymbol{p}_w \\ \delta \boldsymbol{p}_g \end{Bmatrix} = - \begin{Bmatrix} \mathcal{R}_u^h \\ \mathcal{R}_{p_w}^h \\ \mathcal{R}_{p_g}^h \end{Bmatrix} \tag{4.60}$$

where $\delta \boldsymbol{u}$, $\delta \boldsymbol{p}_w$, and $\delta \boldsymbol{p}_g$ are the nodal incremental vectors over a given time interval for displacement, pore water pressure and pore gas pressure, respectively; $\mathcal{R}_u^h$, $\mathcal{R}_{p_w}^h$ and $\mathcal{R}_{p_g}^h$ are the residual vectors for the balance of the linear momentum, water content and gas content. Readers can refer to (Song et al. 2017) for more details of the components of the Jacobian matrix, $\boldsymbol{J}$.

(3) The maximum historical value of the positive elastic strain energy is evaluated.

(4) The PF is updated by using Eq. (4.61), with the maximum historical value obtained in step (3).

$$\left[\boldsymbol{J}_{dd}\right]\left\{\delta \boldsymbol{d}\right\} = -\left\{\mathcal{R}_d^h\right\} \tag{4.61}$$

where $\boldsymbol{J}_{dd}$ is the Jacobian matrix that is the partial derivative of $\mathcal{R}_d^h$ with respect to the PF, d.

(5) If the convergence criterion is satisfied, the solution is updated in time step t^{n+1}, i.e. $\left\{\boldsymbol{u}_{n+1}, p_{w,n+1}, p_{g,n+1}, d_{n+1}\right\} = \left\{\boldsymbol{u}_{n+1}^{(i+1)}, p_{w,n+1}^{(i+1)}, p_{g,n+1}^{(i+1)}, d_{n+1}^{(i+1)}\right\}$. Otherwise, Step (2) is carried out again for the next iteration until the convergence criterion is satisfied.

4.2.5.1.3 Stabilization technique

To model the coupled HM process in porous media with low permeability, the Taylor-Hood element (where the shape function for displacement is one-order higher than that for pore pressure) is widely adopted to ensure stabilized mixed finite elements (Hu et al. 2016). However, using a Taylor-Hood element, e.g. the Q9P4 element, to discretize the studied domain leads to more degrees of freedom and Gauss quadrature operations than using a lower equal-order element, e.g. the Q4P4 element (White and Borja 2008). As the PF method requires a very fine mesh to capture the trajectories of the developed fractures, it is more computationally efficient to use a lower equal-order element. However, the equal-order shape function for interpolating pore pressure and displacement violates the well-known Ladyzhenskaya-Babuška-Brezzi condition, which causes an unstable mixed finite element (White and Borja 2008). To resolve this issue, a stabilized term is developed based on the Polynomial-Pressure-Projection technique, and then added to the mass balance equation for the water phase (White and Borja 2008). For coupled HM models that involve a two-phase flow, the stabilized term is directly applied to the gas phase as in (Song et al. 2017). In this paper, this simple approach is adopted to stabilize the mixed finite elements. It should be noted that stabilized terms with more rigour for twofold saddle point problems have been developed by (Choo and Borja 2015; Sun et al. 2013). Their performance on the current issue is beyond the scope of this paper but will be explored in the future. The stabilized weak forms of the mass

balance equations for water and gas, $\mathcal{F}_\alpha^S$, can be expressed as (Song et al. 2017; White and Borja 2008):

$$\mathcal{F}_\alpha^S = \mathcal{F}_\alpha + \mathcal{F}_\alpha^{stab} \tag{4.62}$$

$$\mathcal{F}_\alpha^{stab} = \int_\Omega \frac{\tau}{2G}(\theta_\alpha - \Pi\theta_\alpha)(\dot{p}_\alpha - \Pi\dot{p}_\alpha) \tag{4.63}$$

where $\mathcal{F}_\alpha^{stab}$ is the weak form of the stabilized term, G is the shear modulus, and τ is a constant multiplier. Note that a more rigorous model for τ has been derived by (Li and Wei 2018). For simplicity, the value of τ is equal to 1 in this paper as in (White and Borja 2008).

The projection operator, Π, for the water or the gas as shown in Eq. (4.63), is defined as (Song et al. 2017; White and Borja 2008):

$$\Pi p_\alpha|_{\Omega^e} = \frac{1}{V^e}\int_{\Omega^e} p_\alpha d\Omega \tag{4.64}$$

where V^e and Ω^e are the volume and the domain occupied by a single element.

Thus, it can be seen that the projection operator results in the element average of the pressure of the fluid α.

Following the numerical manipulations in (Song et al. 2017), the contribution of the proposed stabilized term to the Jacobian matrix for Newton-Raphson iteration in Eq. (4.60) is expressed as:

$$\boldsymbol{J}_{\alpha\alpha}^{stab} = \int_\Omega \frac{\tau}{2G}\left(\boldsymbol{N}^T - \Pi\boldsymbol{N}^T\right)\left(\boldsymbol{N} - \Pi\boldsymbol{N}\right)d\Omega \tag{4.65}$$

where $\boldsymbol{N}$ is a bilinear shape function.

Then, the diagonal components of the Jacobian matrix in Eq. (4.60) for water pressure and gas pressure are replaced by the stabilized ones, $\boldsymbol{J}_{\alpha\alpha}^S$, as expressed by:

$$\boldsymbol{J}_{\alpha\alpha}^{S} = \boldsymbol{J}_{\alpha\alpha} + \boldsymbol{J}_{\alpha\alpha}^{stab} \tag{4.66}$$

4.2.5.2 Basic validation tests

The proposed coupled HM-PF model consists of two basic models, i.e. a fracture model based on the PF method and a conventional coupled HM model for porous media. Before applying the coupled HM-PF model to simulate the preferential gas flow in saturated bentonite, the two basic models will be first validated against previous numerical and theoretical results, respectively. Meanwhile, the stabilized term introduced to avoid spurious pore pressure oscillation and reduce computational efforts will also be examined.

4.2.5.2.1 Pure shear test

The simulated domain is a square-shaped domain with dimensions of 1 mm. An initial fracture with a length of 0.5mm is prescribed at the center of the domain, as seen in Figure 4.4. In order to save the computational time, the domain where the fracture is expected to propagate is meshed by using fine quadrilateral elements, while the remainder is meshed by coarser triangular elements, see Figure 4.4.

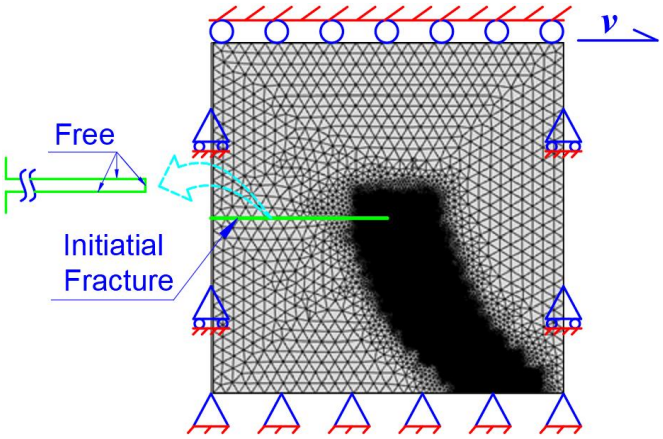

Figure 4.4 Meshing strategy and boundary conditions of pure shear test

The dimension of the quadrilateral element is 0.002 mm × 0.002 mm which was used by Miehe et al. (2010a). The elastic bulk modulus, K, and the shear modulus, G, were set to be 121.15 kN/mm^2 and 80.77 kN/mm^2, respectively. The critical energy release rate, G_c, is 2.7×10^{-3} kN/mm. The internal length scale, l, is 0.0075 mm. These parameters are used in Miehe et al. (2010a). The displacement increment of the top boundary is 1×10^{-4} mm per step

for the initial 85 steps, and then decreased to 1×10^{-5} mm per step for the remaining 600 steps to accurately depict the load-displacement curve. The bottom boundary is fixed in both the vertical and the horizontal directions, while the lateral boundaries were fixed in the vertical direction and free in the horizontal direction. The boundary conditions for the initial fracture are set as free, see Figure 4.4.

Figure 4.5(a) shows the load-displacement curves obtained by the current model and the model in (Miehe et al. 2010a), while Figure 4.5(b) presents the fracture (phase field) profiles at three specific shear displacements which correspond to Points A, B and C in Figure 4.5(a).

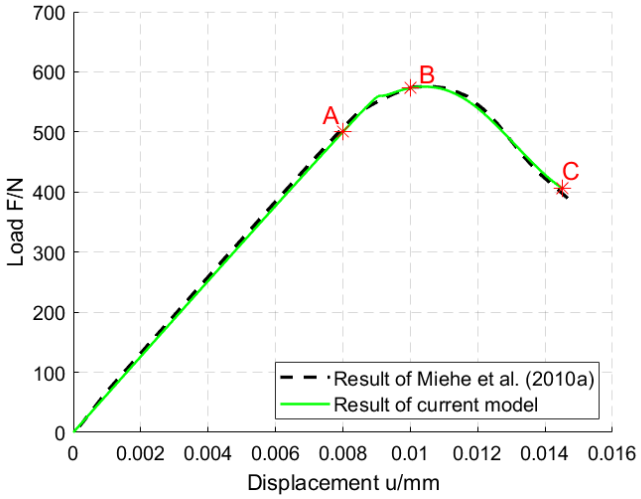

(a) Comparison of load-displacement curves

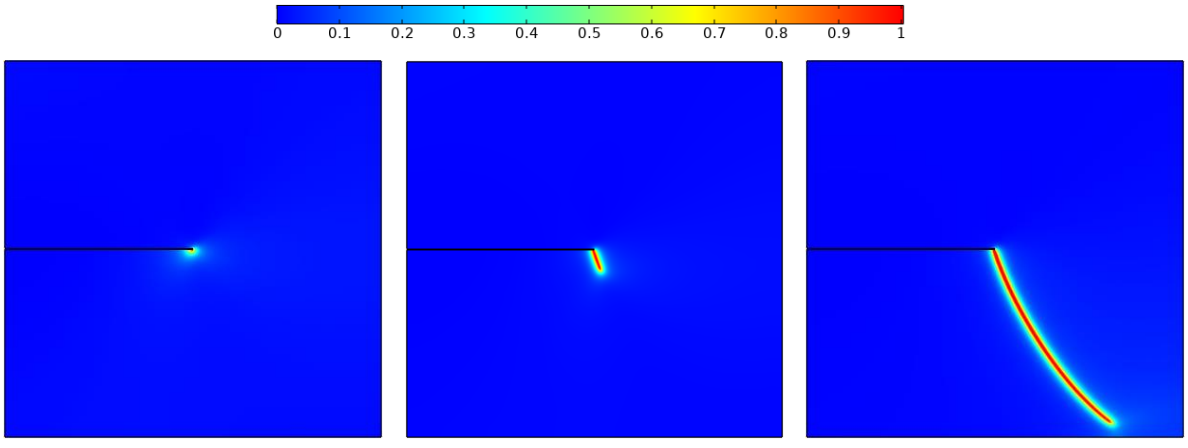

(1) Point A (2) Point B (3) Point C

(b) Fracture (phase field) profiles at three shear displacements

Figure 4.5 Load-displacement curves and fracture profiles during the fracturing process

It can be seen that the curve obtained by the current model agrees very well with the curve in (Miehe et al. 2010a). At point A, the fracture has not yet propagated in the domain, see Figure 4.5(b1), which leads to a linear increase of load with the shear displacement. At point B that is close to the peak value, the load increases nonlinearly with the shear displacement and the fracture has started to propagate, see Figure 4.5(b2). After the peak value, the load-displacement curve enters a softening stage and the fracture rapidly propagates towards the bottom of the domain, see Figure 4.5(b3). The obtained fracture profile in this study is very similar to that in (Miehe et al. 2010a). Therefore, the comparisons and discussions above demonstrate the capability of the proposed PF model to explicitly simulate the fracturing process.

4.2.5.2.2 One-dimensional Terzaghi's consolidation problem

In this section, the stabilization technique proposed in Section 4.2.5.1.3 will be examined by modelling a one-dimensional Terzaghi's consolidation problem. The numerical results which are based on three types of elements, i.e. Q9P4, Q4P4, and Q4P4S (S means the element is stabilized), are compared with the analytical results to demonstrate the capability of the proposed stabilization technique.

The domain to model the one-dimensional Terzaghi's consolidation problem is shown in Figure 4.6. The height of the soil column, h_s, is equal to 1m. The water pressure at the top boundary is set to zero, while the other boundaries are impermeable. The displacement at the bottom boundary is fixed in both directions, while the lateral boundaries are constrained in the horizontal direction. A constant compressive load, i.e. $\bar{t}$ = 10 kPa, is immediately applied on the top boundary at the beginning of the simulation. A plane strain condition is assumed. Material properties are assigned as follows (Li and Wei 2018): Young's modulus E = 10 MPa, Poisson's ratio ν = 0.2, initial porosity ϕ_0 = 0.3, intrinsic permeability k_{in} = 1×10^{-13} m^2, and fluid viscosity μ_w = 1×10^{-3} Pa·s. The analytical solution to Terzaghi's consolidation problem is given in Appendix F.

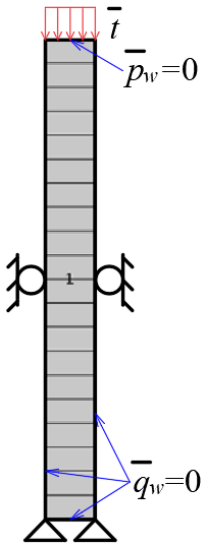

Figure 4.6 Geometry of soil column and HM boundary conditions

The analytical solution of the pore pressure at time t=0.001 s is represented by the black dashed line in Figure 4.7. The numerical solutions with three types of element s are also presented in Figure 4.7. Clearly, the solution of the lower equal-order elements, i.e. Q4P4, presents serious pore pressure oscillation, while the solutions for Q4P4S and Q9P4 elements are much more stable although slight oscillations occur close to the drainage boundary which is also observed in (Li and Wei 2018; White and Borja 2008).

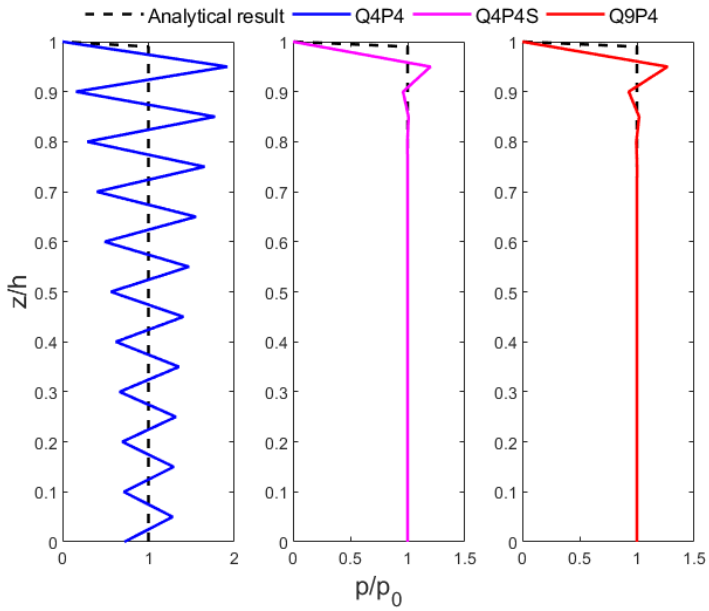

Figure 4.7 Pressure profile of different element types at t=0.001 s

The profile of the pore pressure at different times calculated by using the Q4P4S element is given in Figure 4.8. It can be seen that the numerical solutions agree quite well with the analytical solutions, which demonstrates that the stabilization technique is successfully implemented in the commercial software. Therefore, this technique will be used for the models in the following sections to stabilize the numerical solution and reduce computational efforts.

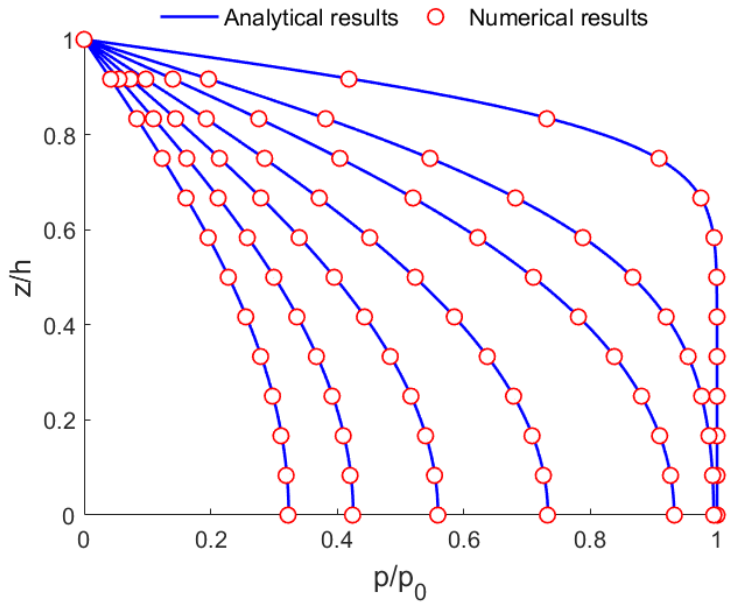

Figure 4.8 Profile of pore pressure at different times calculated by using Q4P4S element

4.2.5.3 Hydraulic fracturing test

In this section, the proposed HM-PF model is used to simulate the hydraulic fracturing process. The porous medium is assumed saturated with water. Thus, the governing equation for water, i.e. Eq. (4.7), is simplified by setting the degree of saturation of water as 1.

4.2.5.3.1 Initial and boundary conditions

The simulation is conducted on a square-shaped domain with dimensions of 20 m × 20 m. However, to reduce the computational efforts, only a quarter of the entire domain is simulated; see Figure 4.9. An initial fracture with a length of 1 m is prescribed at the bottom left boundary by setting the PF variable to 1. To precisely capture the fracture trajectory, a banded domain at the bottom where the fracture is expected to propagate is finely meshed by using quadrilateral

elements with a size of 5 cm, while the remainder of the square is meshed by using coarse elements. The meshing strategy and boundary conditions are presented in Figure 4.9.

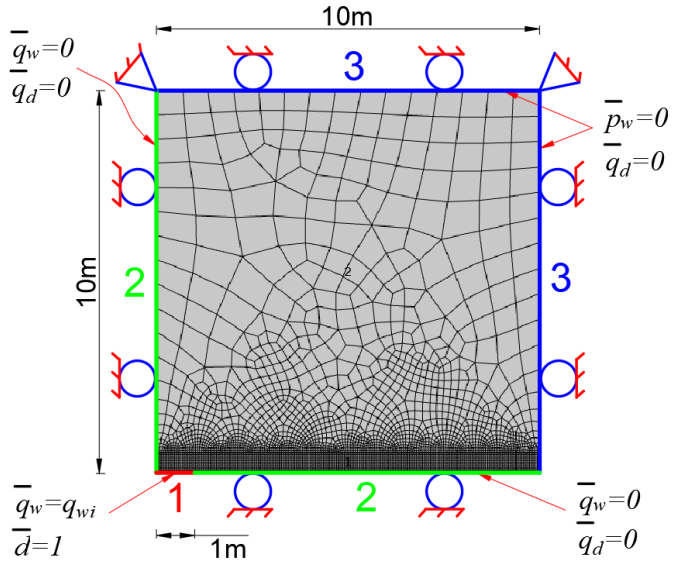

Figure 4.9 Meshing strategy and boundary conditions of the simulated domain ($\bar{q}_w$, $\bar{q}_d$ are the flux boundaries for water and phase field; q_{wi} is the value of mass flux of water at injection boundary; 1, 2 and 3 are boundary numbers)

Here, it should be noted that the governing equation for the PF, i.e. Eq. (4.35), may not be appropriate to model fluid-induced fracturing, as the fracture will propagate immediately once the tensile principal strain occurs, which means that the damage may even occur at a low-stress level. To avoid this issue, an alternative functional of the fracture driving force (proposed by Miehe and Mauthe (2016)) which includes a threshold value will be used in the current and the subsequent simulations. The functional for the fracture driving force is expressed as:

$$H_M^+ = \max_{\tau\in[0,t]}\left\{\left\langle \frac{\psi_0^{e+}}{\psi_{cr}} - 1 \right\rangle_+\right\}, \tag{4.67}$$

where ψ_{cr} is the critical fracture energy over which the fracture starts to propagate.

By using the Legendre transformation (Mauthe and Miehe 2017), the critical fracture energy can be expressed as:

$$\psi_{cr} = \frac{1}{2E}\sigma_{cr}^2 \quad , \tag{4.68}$$

where σ_{cr} is the critical tensile stress.

The HM properties of the porous medium are listed in Table 11. Both the initial fluid pressure and initial stress within the porous medium are 0 [MPa]. The initial PF in the domain is 0. The boundary conditions for the coupled HM-PF model are present in Figure 4.9 and listed in Table 12. The constant flux applied at the initial fracture is 0.01 kg/(m^2▪s).

Table 11 Basic HM properties of simulated porous medium (Xia et al. 2017)

Hydraulic properties		Mechanical properties			Phase field	
k_{in}/m^2	ϕ_0	E/GPa	ν	α_B	σ_{cr}/MPa	l/cm
5×10^{-15}	0.3	15.96	0.2	0.79	0.5	10

Table 12 HM boundary conditions for hydraulic fracturing test

Boundary No.	Phase field	Hydraulic Boundary	Mechanical Boundary
1	1	Constant flux (0.01 kg/(m^2▪s))	Symmetric
3	0	0[MPa]	Roller
2	Symmetric Boundary		

4.2.5.3.2 Results and discussion

Figure 4.10(a) presents the changes in water pressure at the injection boundary, while Figure 4.10(b) gives the profiles of the fracture aperture along the bottom boundary which correspond to Points A, B, C, and D in Figure 4.10(a). Note that water injection is initiated at t=5 s. The water pressure increases linearly to around 140 kPa at which the rate of increase shows a slight decline which should be caused by the slight dilation of the initial fracture. This can be observed in Figure 4.10(b) in which the fracture aperture gradually increases with almost no extension. When the water pressure reaches a peak value at point B, the fracture dilates vertically and propagates horizontally, which leads to a significant increase of volume of the developed fracture; see Figure 4.10(b). Initially, the rate of the increased volume caused by fracturing is larger than the rate of the injected volume of water, thus leading to a decline in water pressure, see Figure 4.10(a). Then, the fracturing process slows down as the water pressure decreases. When the rate of the increased volume of fracture reaches a balance with

the rate of the injected volume of water, the water pressure is stabilized at a constant value, see Figure 4.10(a). The changes in water pressure as discussed above are commonly observed in both numerical and experimental studies on hydraulic fracturing (Wilson and Landis 2016; Xia et al. 2017). The "V-shape" drop in Figure 4.10 (b) may result from a slight inconsistency between the prescribed PF variable ($d = 1$) on the initial fracture boundary and the developed PF variable on the remaining part of the bottom boundary.

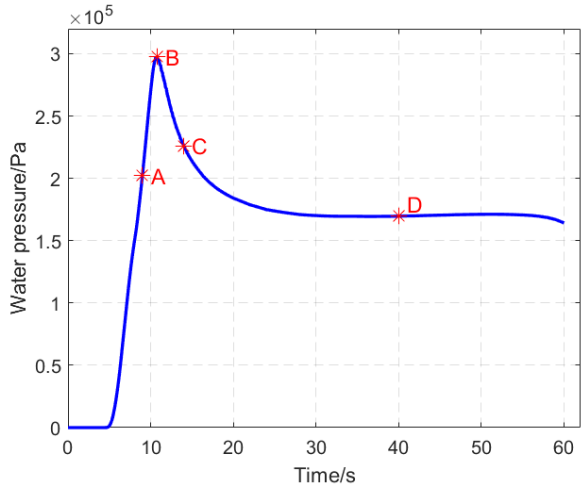

(a) Water pressure at injection boundary

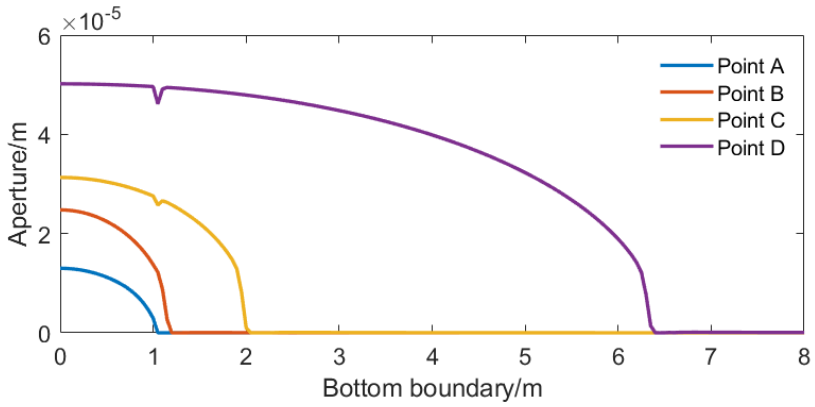

(b) Profile of fracture aperture at four different points of time

Figure 4.10 Evolution of water pressure and aperture profile during hydraulic fracturing period

Figure 4.11 shows the distribution of the water pressure at Points C and D. High water pressure is localized in the developed fracture, as the permeability of the developed fracture is several orders of magnitude greater than that of the porous matrix. Behind the fracture tip, the

high pressure in the fracture is gradually distributed to the surrounding areas, thus leading to a bullet-shaped profile. In contrast, a small area with negative water pressure is observed ahead of the fracture tip. This is also commonly observed in previous numerical studies (Miehe et al. 2015a; Santillán et al. 2018; Xia et al. 2017). Physically, the negative water pressure may originate from the dilation of the fracture process zone ahead of the fracture tip (Kumar et al. 2017). Based on the analysis given above, the developed HM-PF model can well describe the primary characteristics of the hydraulic fracturing process.

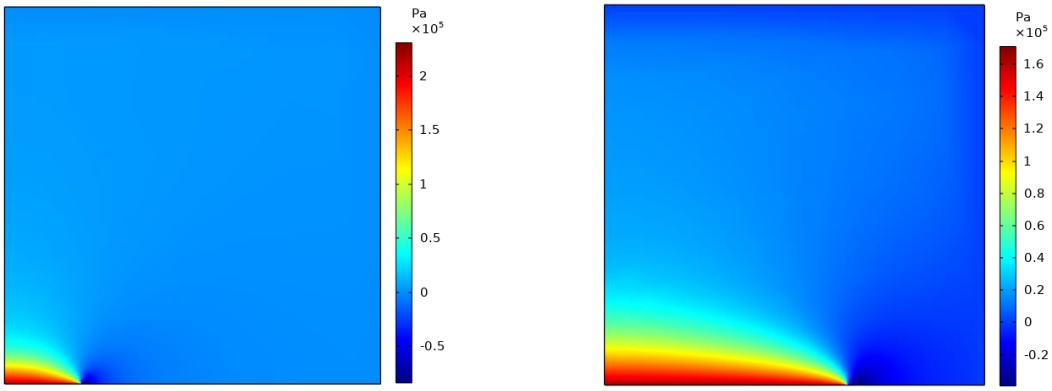

(a) At Point C (b) At Point D

Figure 4.11 Distribution of water pressure at Points C and D

4.2.6 Model Simulation and Sensitivity Analysis

4.2.6.1 Preferential gas flow in saturated and heterogeneous bentonite

4.2.6.1.1 Initial and boundary conditions

The studied domain is a square with dimensions of 50 mm × 50 mm. An initial fracture with a length of 2 mm is prescribed by setting the PF variable as 1 on Boundary 5 in Figure 4.12. In the field, the natural rock surrounding the buffer materials is much harder than the bentonite, which significantly inhibits the volume expansion of the buffer material. Therefore, constant volume condition was generally considered in previous experimental studies (Daniels and Harrington 2017; Harrington and Horseman 2003; Harrington et al. 2017b; Xu et al. 2017). However, a fully constrained boundary may induce convergence issues. In order to avoid the issue, a larger rectangular domain with dimensions of 300 mm × 150 mm was added to the outside of the studied domain, see Figure 4.12. It should be noted here that only the mechanical model is applied to the outer domain. Both the size and the mechanical properties (i.e. Young's

modulus and Poisson's ratio) of the outer domain may control the boundary rigidity of the studied domain. In this paper, the effect of the mechanical properties will be analyzed in section 4.2.6.2.3, while the size effect of the outer domain will be examined in the future. The Young's modulus and Poisson's ratio of the outer domain are set as 3 GPa and 0.4, respectively. In order to capture the fracture trajectory accurately, the studied domain is finely discretized by using Q4P4S elements with an element size of 0.25 mm, while the outer domain is meshed by using coarse triangular elements. The meshing strategy and boundary conditions are shown in Figure 4.12.

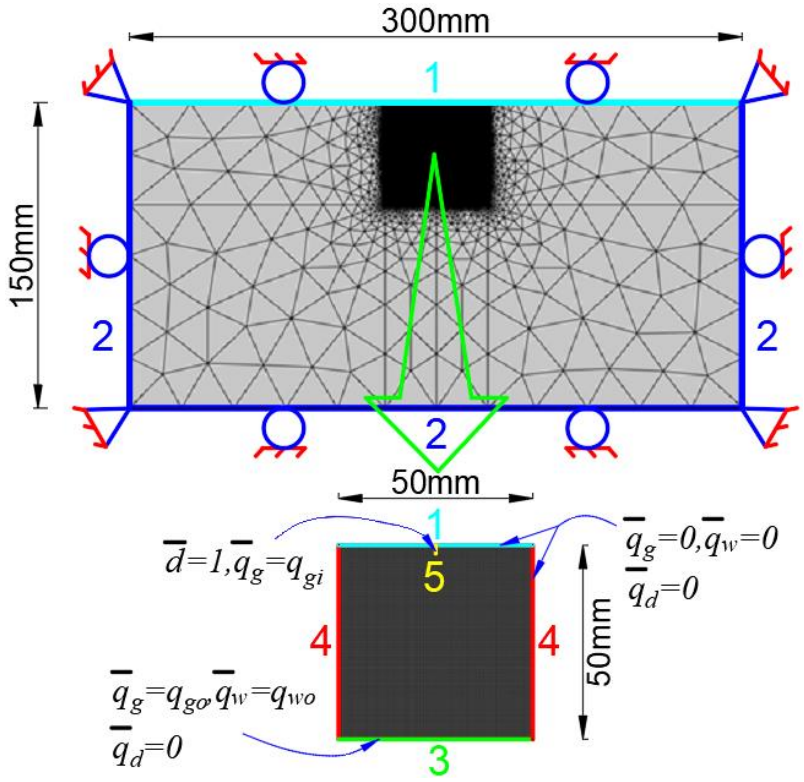

Figure 4.12 Meshing strategy and boundary conditions of the whole domain

($\bar{q}_g$, $\bar{q}_w$, $\bar{q}_d$ are the flux boundaries for gas, water and phase field; q_{gi} and q_{go} are the values of mass flux of gas at injection and outflow boundaries, respectively; q_{wo} is the value of mass flux of water at outflow boundary; 1, 2, 3, 4 and 5 are boundary numbers)

The initial gas and water pressure in the porous medium are 0.02 MPa and 0 MPa, respectively. The gas pressure is slightly higher than the water pressure to avoid the convergence issue. For simplicity, the swelling pressure is not considered for the current model, but it will be considered in future work. In addition, the intrinsic permeability of the developed

fracture in the following sections is assumed 1×10^{8} times the permeability of the porous matrix in order to reduce computational efforts. This simplified treatment is also adopted by (Yoshioka and Bourdin 2016; Zhou et al. 2018). However, a more robust and computationally efficient permeability model will be explored in the future. The hydro-mechanical properties of the porous medium (Mx80 bentonite) are listed in Table 13 (Zheng et al. 2017). Due to the limited experimental data for the tensile strength of the saturated bentonite, the critical stress in the phase field model is assumed 0.5 MPa. A more exact value will be used once the experimental data is available in the future. To estimate the characteristic length of the phase field, Choo and Sun (2018b) proposed a model based on the relationship between tensile strength and mode I fracture toughness. However, due to the limited experimental data, the characteristic length, l, is set as twice the size of a single meshing element, which is suggested in (Miehe et al. 2010a; Miehe et al. 2010b).

The boundary conditions for the coupled HM-PF model are present in Figure 4.12 and listed in Table 14. The constant mass flux of gas applied at the initial fracture is 15×10^{-9} kg/(m^2▪s). For Boundary No. 3 (drainage boundary), a type of mass flux rather than a constant pressure is used as the boundary condition for the pressure field of water and gas, as expressed by Eq. (4.69). This is because a constant pressure condition is too rigid to describe the outflow behavior in real cases (Guo and Fall 2018).

$$q_{\alpha o}=\begin{cases}\rho_{\alpha}\dfrac{k_{in}k_{r\alpha}}{\mu_{\alpha}l_{q}}\left(p_{\alpha}-p_{\alpha cr}\right), & p_{\alpha}>p_{\alpha cr}\\ 0, & p_{\alpha}\le p_{\alpha cr}\end{cases} \tag{4.69}$$

where l_q is a characteristic length set as 1 mm for all simulations in this paper, and $p_{\alpha cr}$ is a critical pressure (slightly higher than the initial fluid pressure) over which fluid outflow is initiated.

Table 13 Basic HM-PF properties of simulated material (Mx80 bentonite)

Material	Hydraulic properties				Mechanical properties		Phase field	
	k_{in}[m^2]	ϕ_0	p_{gev}[MPa]	m	E[MPa]	ν	σ_{cr}[MPa]	l[mm]
Mx80	3.4×10^{-21}	0.44	18	0.45	307	0.4	0.5	0.5

Table 14 HM-PF boundary conditions of fracturing in saturated porous medium

Boundary No.	Phase field	Hydraulic Boundary		Mechanical Boundary
		Water	Gas	
2	/	/	/	Roller
3	0	Mass flux q_{wo}	Mass flux q_{go}	/
4	0	No flow	No flow	/
5	1	/	Mass flux q_{gi}	/
1	Symmetric Boundary			

The heterogeneous distribution of the hydro-mechanical properties of soils or rocks has a significant influence on the fracture patterns (Santillán et al. 2017b). Previous studies have shown that both the hydraulic properties (e.g. permeability, fluid storage and pore size)(Kosugi 1994, 1996), and mechanical properties (e.g. elastic modulus, strength, and fracture energy), can be assumed to follow the lognormal distribution law (Santillán et al. 2017b). This assumption will also be adopted in this paper to construct the random field for both the hydraulic and mechanical properties. For a heterogeneous material, the properties at a particular position are more closely related to those in adjacent positions than those far away (Li et al. 2015). To account for this characteristic, a spatially auto-correlated random field will be created and used to conduct the heterogeneous analysis in this paper. More details on the formulas and techniques to create such a spatially auto-correlated random field are provided in Appendix G. It should be noted that the cross correlation between different properties and changes of random field caused by the on-going HM processes are not considered in this paper.

In this study, the mechanical properties, i.e. Young's modulus and critical tensile stress, and the hydraulic properties, i.e. intrinsic permeability and gas entry value, are assumed governed by the lognormal distribution law. As the standard variance and the correlation length for these

HM properties of bentonite are still unavailable, these parameters will be estimated within an appropriate range of values. The mean values for these properties are assumed the same as those listed in Table 13. The coefficient of variation, which is defined as the ratio of the standard deviation and the mean of a lognormal random field, for these properties is assumed 0.2, except for the intrinsic permeability which is C_v=10. The reason why the coefficient of variation for intrinsic permeability is larger is due to the fact that the intrinsic permeability in real cases may vary within several orders of magnitude. The two parameters for the transition function, i.e. θ_t and d_{cr} are set as 30 and 0.9, respectively. The correlation length is assumed 3 mm in both the horizontal and vertical directions.

4.2.6.1.2 Evolution of gas pressure and fracture patterns

In Figure 4.13, the blue solid line shows the evolution of gas pressure at the injection boundary, while the brown dashed line represents the growth of the fracture area (which is calculated through conducting an areal integral over the domain where the value of the PF is greater than 0.9) during the fracturing process.

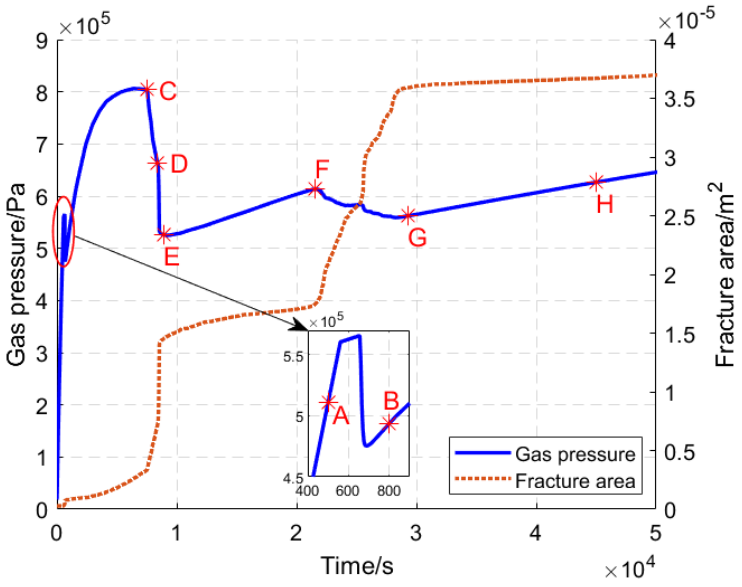

Figure 4.13 Changes in gas pressure and fracture area during the fracturing process

Points A to H are some of the critical moments that characterize pressure evolution. The fracture trajectories associated with these eight points are presented in Figure 4.14. The spatially auto-correlated random field is represented by contour lines where the lighter (darker)

lines give larger (smaller) values of the Gaussian random field, $Z(\boldsymbol{x})$. In the areas with dark (or light) lines, Young's modulus, critical tensile strength and gas entry value have lower (or higher) values, while the permeability is higher (or lower, respectively). As a result, the dark areas are relatively less resistant to both the fluid flow and the fracture propagation compared with the light areas. Meanwhile, the PF is represented by the grey area in Figure 4.14.

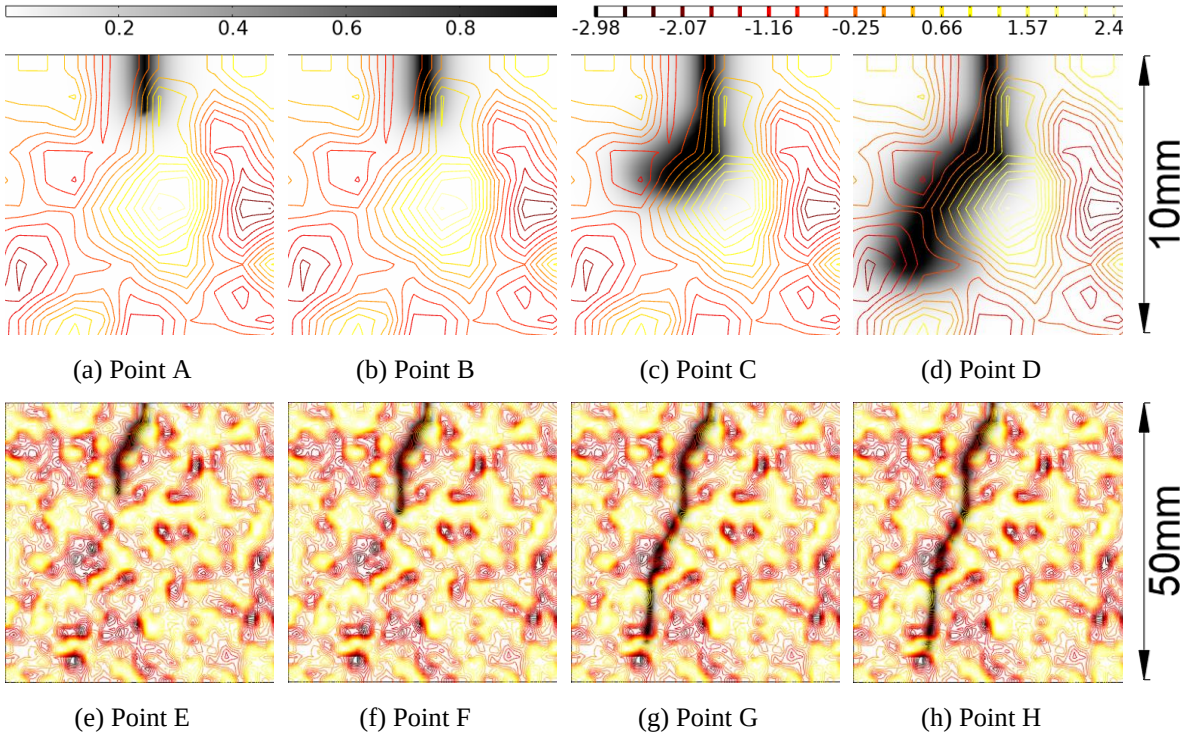

(a) Point A (b) Point B (c) Point C (d) Point D

(e) Point E (f) Point F (g) Point G (h) Point H

Figure 4.14 Evolution of fracture trajectory during the fracturing process (Note that Figs (a)-(d) are areas around the initial fracture that are magnified by five times in length to highlight the details of fracture propagation; the grey area represents the developed fracture; the contour represents the Gaussian random field)

Figure 4.13 shows that each drop of gas pressure at the injection boundary is associated with an increase in the fracture area. This result is consistent with the ideal gas law in that the rate of gas pressure is controlled by the rate of fracture volume when the injection rate is kept constant. As seen from Figure 4.13 and Figure 4.14 (a-c), the fracture experiences a very slight dilation and extension, thus leading to an increasing trend in general from Point A to Point C. This may be due to the light area ahead of the tip of initial fracture that inhibits the fracture propagation. In contrast, the fracture tip has reached the dark area at Point D, see Figure 4.14 (d), where the resistance to both the fluid flow and the fracture propagation is lower. As a result,

the fracture propagates rapidly along with the dark areas until the moment at Point E when the fracture tip encounters another light area, see Figure 4.14 (e) and the brown dashed line in Figure 4.13. This is accompanied by a sharp drop of gas pressure from Point D to E, see Figure 4.13. Due to the high resistance of the light area at point E, the fracture propagation is inhibited, thus leading to an almost linear increase of gas pressure from Point E to Point F, see Figure 4.13. It can be identified from Figure 4.13 and Figure 4.14 that the evolutions of gas pressure and fracture area from Point F to Point H are very similar to those from Point D to Point F.

The analysis given above shows that the profiles of gas pressure and fracture area are very sensitive to the distribution of the random field. Spatially, the fracture preferentially propagates through areas of low resistance, see Figure 4.14. Temporally, the rate of fracture propagation in areas of low resistance is much larger than that in areas of high resistance, see the brown dashed line in Figure 4.13. In addition, the simulated fluctuations of gas pressure during fracturing process may be able to explain the experimentally observed fluctuations before gas breakthrough as detailed in (Harrington and Horseman 2003; Harrington et al. 2017b; Harrington et al. 2019b). Therefore, the developed HM-PF model which incorporates a spatially auto-correlated random field is capable of describing arbitrary fracture propagation and preferential gas flow in saturated bentonite.

4.2.6.1.3 Distribution of fluid pressure

Figure 4.15 shows that the distribution of the degree of saturation exactly follows the fracture trajectory (as seen in Figure 4.14) at the three characteristic moments. The degree of saturation in the developed fracture is close to 0 and almost 1 in the surrounding porous matrix. This distinct contrast is due to that the gas entry value for the fracture is set to a very low value, i.e. 2 kPa, in this paper. This is based on the fact that the developed fractures can hardly retain the capillary water due to the large aperture (Vo et al. 2017). Therefore, the gas will preferentially flow through the developed fractures, while leaving the surrounding matrix in a fully saturated state. This numerical result is qualitatively consistent with the experimental results obtained by (Graham et al. 2012; Harrington and Horseman 2003; Horseman et al. 1997), in that the sample remains almost saturated after gas injection.

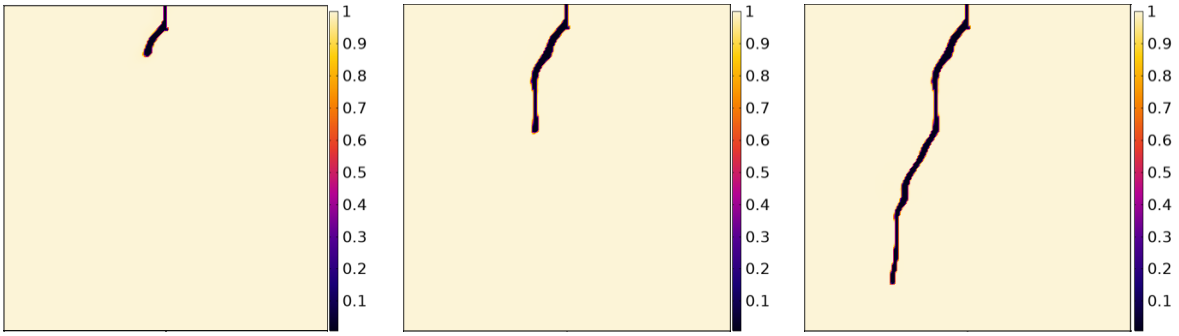

(a) Point D (b) Point F (c) Point G

Figure 4.15 Distribution of degree of saturation in the studied domain

Figure 4.16 and Figure 4.17 present the distributions of the gas pressure and the water pressure, respectively, at the three characteristic moments. As the fracture propagates towards the outflow boundary, the fluid (gas or water) pressure in the surrounding porous matrix increases. This may primarily result from the compressive load exerted by the highly pressurized gas in the developed fracture. As the fracture solely propagates in the left side of the studied domain, the fluid pressure generated in the left side is generally higher than that on the right side. Due to the random distribution of HM properties, the fluid pressure developed during the fracturing process also distributes heterogeneously, see Figure 4.16 and Figure 4.17. It should be noted here that the degree of saturation of gas in the surrounding porous media has a very small positive value, instead of exact zero, to avoid the convergence issue. Therefore, the gas pressure in the surrounding porous media also increases under the compressive load, although the amount of gas is very small. In Figure 4.17 (a), the water pressure in the developed fracture reaches a negative value as low as -0.47MPa. This may be caused by the rapid extension of fracture at the moment of point D, see the brown dashed line in Figure 4.14. In addition, the water pressure ahead of the fracture tip also reaches a negative value due to the dilation of the fracture process zone. This is also captured in the numerical simulation for hydraulic fracturing test, see Figure 4.11. To physically describe this behavior, a more robust permeability model that can capture the evolution of fracture aperture needs to be developed in the future.

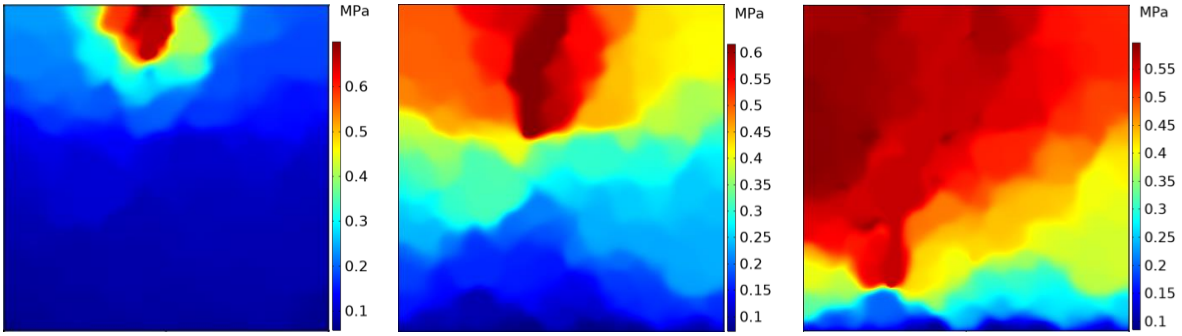

(a) Point D (b) Point F (c) Point G

Figure 4.16 Distribution of gas pressure in the studied domain

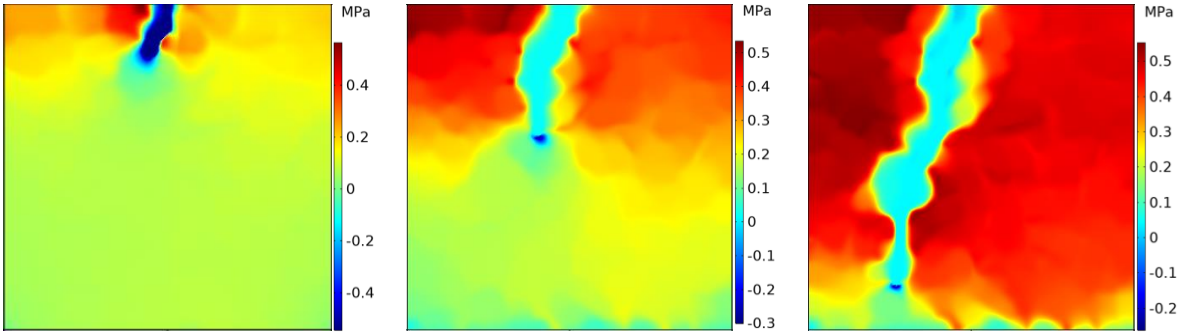

(a) Point D (b) Point F (c) Point G

Figure 4.17 Distribution of water pressure in the studied domain

4.2.6.1.4 Evolution of water pressure and mean total stress

The build-up of water pressure and total stress during the gas migration process is commonly observed in experiments (Graham et al. 2012; Harrington et al. 2017b). To examine the evolution of the water pressure and the mean total stress, six monitoring points are set on the lateral boundaries of the studied domain, i.e. top left (TL), center left (CL), bottom left (BL), top right (TR), center right (CR) and bottom right (BR), as seen in Figure 4.18.

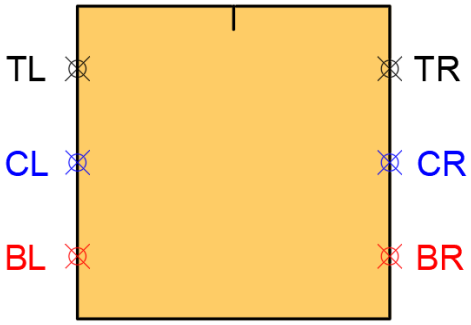

Figure 4.18 Monitoring points on the studied domain (Note: Top left (TL), center left (CL), bottom left (BL), top right (TR), center right (CR) and bottom right (BR), respectively)

The evolutions of the water pressure and the mean total pressure (the absolute value of mean total stress) are present in Figure 4.19(a) and Figure 4.19(b), respectively. Clearly, the increase of either the water pressure or the mean total pressure is closely associated with the growth of fracture area. As analyzed in section 4.2.6.1.3, this is due to the dilation of the fracture that exerts a compressive load on the surrounding porous media. As the fracture only propagates in the left side of the domain, the water pressure in this side is generally larger than that in the right side. However, this general conclusion may not be applicable at some specific points. For instance, while the water pressure at TL is always lager than that at TR (see the black line in Figure 4.19(a)), the pressure at BL is less than that at BR (see the red line in Figure 4.19(a)). This inconsistency may result from the heterogeneous distribution of the HM properties. In addition, the difference between the water pressure at CL and that at CR (see the line in Figure 4.19(a)) switches from negative sign to positive sign. This switch may be controlled by the fracturing process. A further comparison between Figure 4.19(a) and Figure 4.19(b) indicates that the value of the mean total pressure is very close to that of the water pressure at any given moment. This means that the build-up of the mean total pressure primarily results from an increase in water pressure, while the increase of effective stress has only a minor contribution due to the rigid boundary condition.

The analysis given above shows that the developed HM-PF model is able to qualitatively simulate the build-up of water pressure and total stress during the gas migration process. This is a commonly observed behavior in experimental studies (Graham et al. 2012; Harrington et al. 2017b). Furthermore, the experimental finding that the pore pressure is distributed heterogeneously in clay-rich materials (Cuss et al. 2012) is also reflected by the model to some extent.

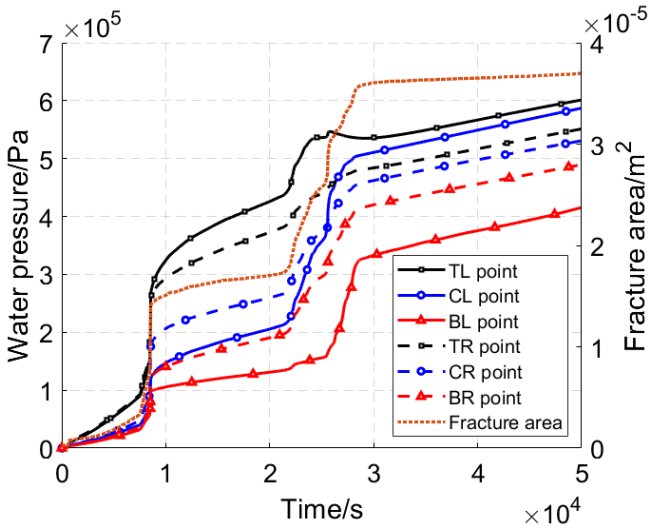

(a) Evolution of water pressure

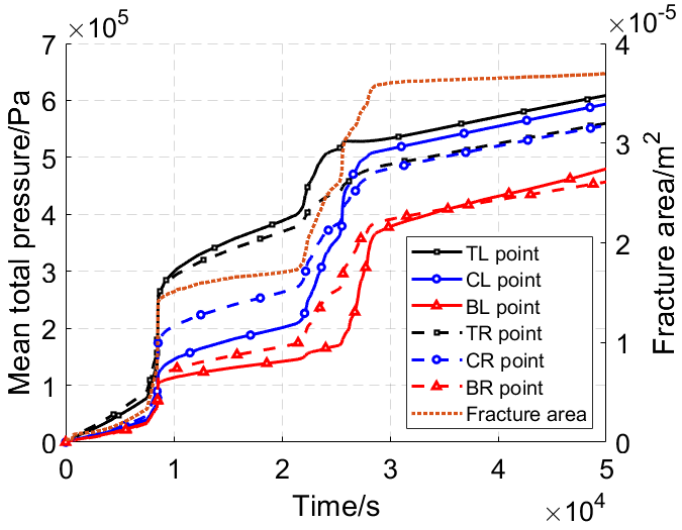

(b) Evolution of mean total pressure

Figure 4.19 Evolutions of water pressure and mean total pressure at six monitoring points

4.2.6.2 Fracture patterns under different factors

In this section, four factors that may influence the fracture patterns, including the Gaussian random field, the coefficient of variation, the boundary condition and the gas injection rate, will be examined. To make reasonable comparisons among these factors, a basic model with controlled parameters is proposed as follows. The basic parameters for the model are listed in Table 13. The two parameters for the transition function, i.e. θ_t and d_{cr} are set as 30 and 0.8. The gas injection rate is 2×10^{-8} kg/(m^2•s). The other necessary parameters are the same to those

of the model in section 4.2.6.1. As the comparison study in this section involves many simulations, the size of the quadrilateral element used to discretize the domain is set to 0.5 mm in order to reduce computational efforts.

4.2.6.2.1 Gaussian random field

Four spatially auto-correlated Gaussian random fields, i.e. $Z_1(\boldsymbol{x})$, $Z_2(\boldsymbol{x})$, $Z_3(\boldsymbol{x})$ and $Z_4(\boldsymbol{x})$, are generated by using four different random seeds, as seen in Figure 4.20.

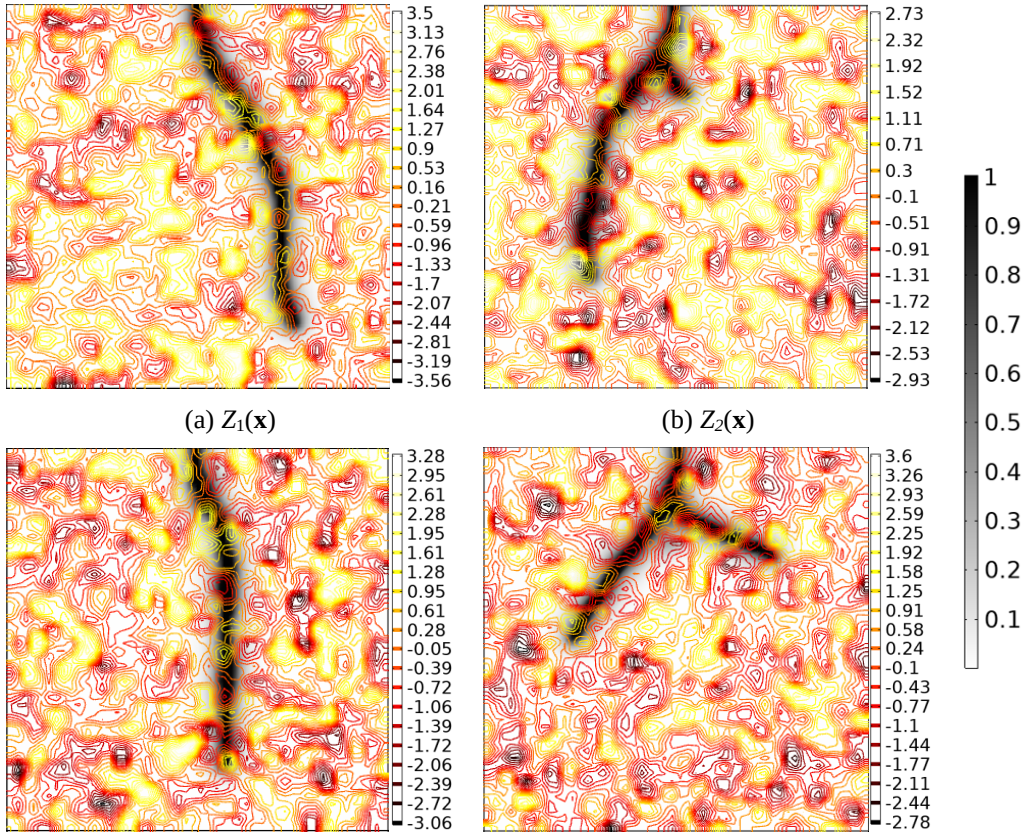

(a) $Z_1(\mathbf{x})$ (b) $Z_2(\mathbf{x})$

(c) $Z_3(\mathbf{x})$ (d) $Z_4(\mathbf{x})$

Figure 4.20 Fracture patterns in the studied domain with different Gaussian random fields ($Z(\mathbf{x})$)

It can be observed that the fracture pattern is very sensitive to the Gaussian random field. A single fracture is developed in random fields $Z_1(\boldsymbol{x})$ and $Z_3(\boldsymbol{x})$, while the branching of fracture is observed in random fields $Z_2(\boldsymbol{x})$ and $Z_4(\boldsymbol{x})$. In general, the developed fracture preferentially propagates through the areas of low resistance (the dark areas), thus leading to either the deviation of fracture from the centerline or the branching of fracture. The evolutions of gas pressure for the four random fields are presented in Figure 4.21. The curves for random fields, $Z_2(\boldsymbol{x})$ and $Z_3(\boldsymbol{x})$, present distinct peak values, while the other two experience a gentle

evolution. As analyzed in section 4.2.6.1.2, these differences in the pressure profiles should result from the heterogeneous distribution of HM properties. This result demonstrates the heterogeneity may be a contributor to the very different evolutions of gas pressure in the tests given by (Harrington and Horseman 2003) and (Harrington et al. 2017b), which, although, were conducted under similar experimental conditions.

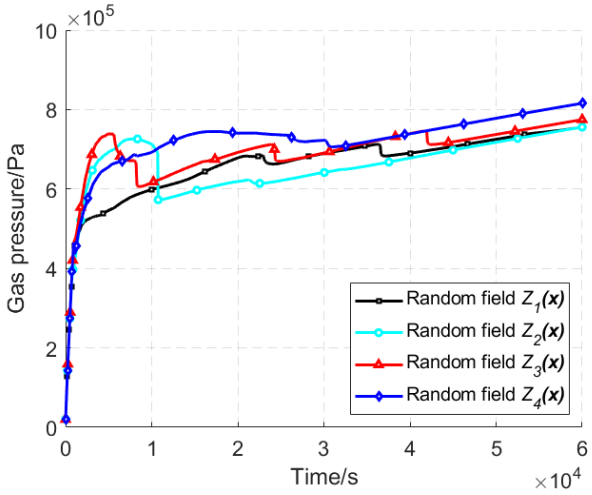

Figure 4.21 Evolution of gas pressure at injection boundary for different Gaussian random fields ($Z(\mathbf{x})$)

4.2.6.2.2 Coefficient of variation

In this section, the effect of the coefficient of variation on the fracture pattern is examined by comparing the results obtained from the numerical tests with different coefficient of variations. Four groups of coefficients of variation are applied to the developed HM-PF model, i.e. C_{v1}(0.05, 5), C_{v2}(0.2,10), C_{v3}(0.3,20) and C_{v4}(0.4,30), where the first value in each group is for Young's modulus (critical tensile strength or gas entry value) and the second is for the intrinsic permeability.

Figure 4.22 shows that the coefficient of variation significantly affects the fracture patterns in the studied domain. With an increase in the coefficient of variation, the distribution of the random field becomes more heterogeneous. Therefore, the fracture can more easily propagate through the areas of low resistance (i.e. the dark areas), which leads to a more tortuous fracture trajectory, see Figure 4.22(a) and Figure 4.22(d). For the case of C_{v1}, the fracture is less affected by the random field and mainly propagates along the center line of the studied domain, see

Figure 4.22(a). In contrast, the fracture can precisely propagate through the areas of low resistance for the case of C_{v4}, see Figure 4.22(d).

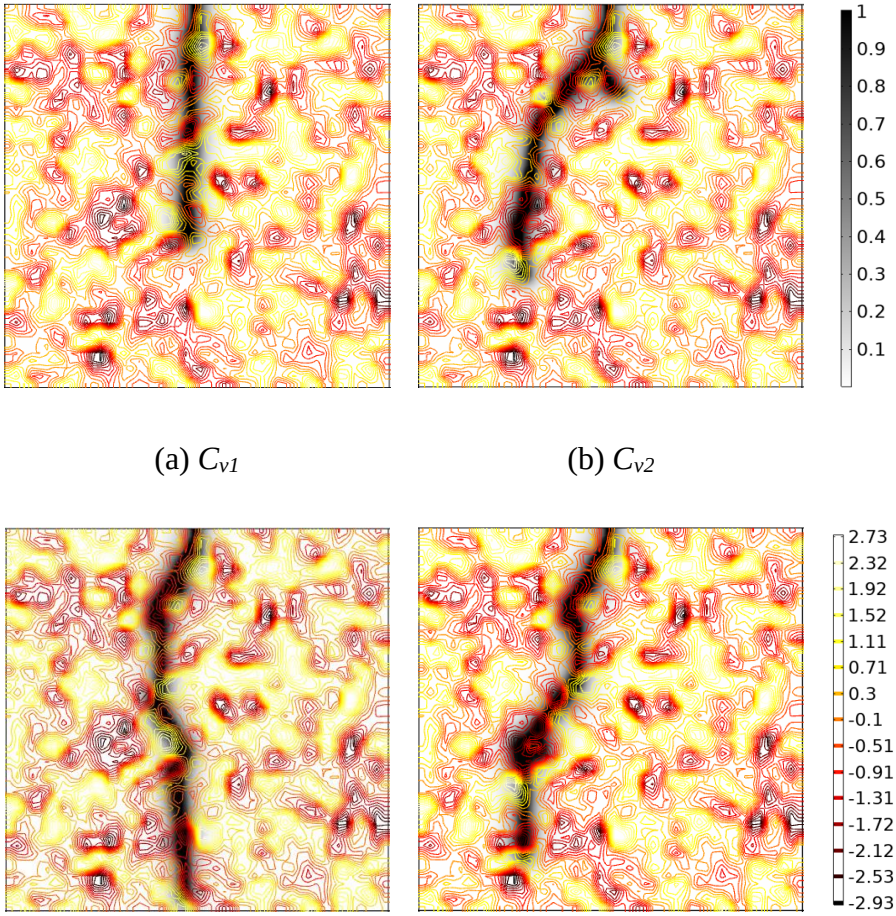

(a) C_{v1} (b) C_{v2}

(c) C_{v3} (d) C_{v4}

Figure 4.22 Fracture patterns in the studied domain with different coefficients of variation (C_v)

Figure 4.23 shows the evolutions of gas pressure for different coefficients of variation are similar to each other. The curve first experiences a peak value and then a gradually increasing trend. There does not seem to be a proportional relationship between the peak value and the coefficient of variation. Specifically, the lowest peak value is observed for the case of C_{v4}, while the highest is observed for C_{v3}. The scattered peak value with the coefficient of variation may imply that the fracturing process is sensitive to small changes in the HM properties.

Based on the analysis above, it can be seen that with the increase of the coefficient of variation, the developed fracture is more capable of bypassing the light areas where the resistance to the flow and fracturing is higher.

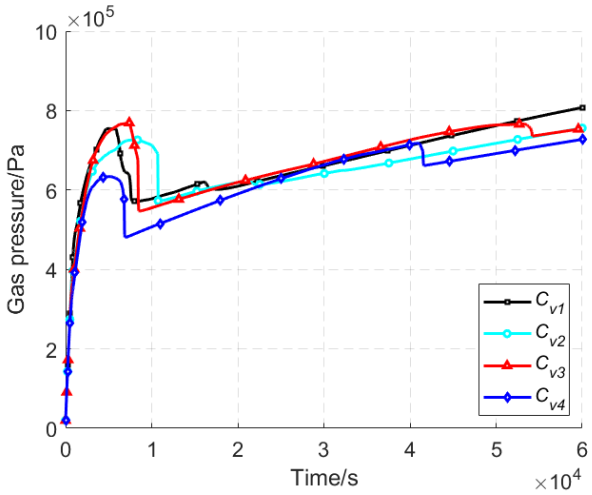

Figure 4.23 Evolution of gas pressure at the injection boundary with different coefficients of variation (C_v)

4.2.6.2.3 Boundary conditions

Previous experimental studies (Harrington and Horseman 2003; Xu et al. 2017; Xu and Zhao 2018) have shown that the mechanical boundary condition has a significant influence on the gas migration behaviors in saturated bentonite. In this section, the transition from a flexible boundary to a rigid boundary is achieved through increasing Young's modulus of the outer domain, E_b. The Young's modulus in this study is set as 0.5 GPa, 1 GPa, 3 GPa and 10 GPa.

Figure 4.24 presents the developed fracture patterns under different boundary conditions. It can be seen that the fracture pattern is highly dependent on the mechanical boundary condition. The fracture patterns in Figure 4.24 are obtained at the end of simulation, except for the one in Figure 4.24(a) which occurs at a much earlier time, i.e. t=8400 s. Clearly, with an increase of the rigidity of mechanical boundary, the fracturing process is increasingly inhibited. For example, the fracture almost propagates to the bottom boundary for E_b=1 GPa (see Figure 4.24(b)), but only to the center of the domain for E_b=10 GPa (see Figure 4.24(d)). This obtained result is essentially due to the constraint from the mechanical boundary. Under the rigid boundary condition, the dilation of the studied domain is inhibited and consequently, the total stress builds up. Under the environment of high total stress, the fracturing process is hard to proceed, thus leading to a lower rate of fracturing. In addition, the branching of fracture is gradually inhibited with the increase in the rigidity of mechanical boundary, see Figure 4.24(b-d). It appears that the branching of fractures under the rigid boundary condition is less sensitive

to the heterogeneous distribution of the HM properties. This may also result from the build-up of total stress that changes the original stress distribution in the studied domain.

Figure 4.25 shows that the gas pressure under the rigid boundary condition can reach a higher value after the peak point. This is because the created volume of fracture per unit time under the rigid boundary condition is less than that under the flexible boundary, see Figure 4.24. This numerical result seems able to qualitatively explain the experimental finding that the gas breakthrough pressure under constant volume condition is higher than that under constant stress condition (Harrington and Horseman 2003).

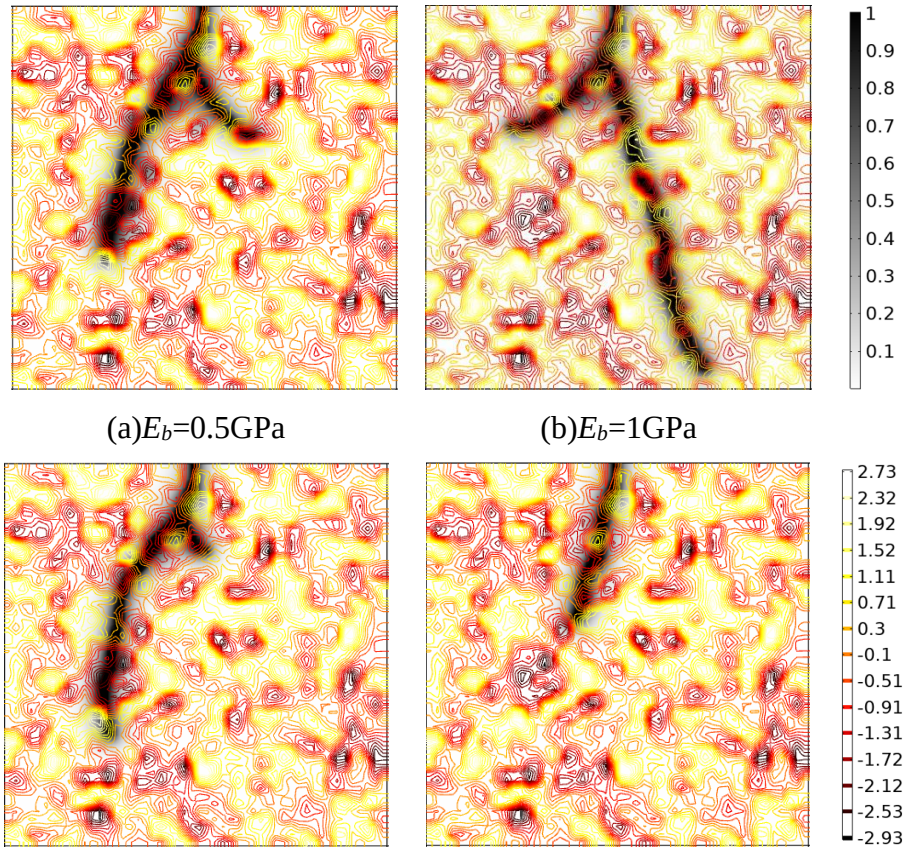

(a)E_b=0.5GPa (b)E_b=1GPa

(c)E_b=3GPa (d)E_b=10GPa

Figure 4.24 Fracture patterns with different mechanical boundaries (E_b: Young's modulus of outer material)

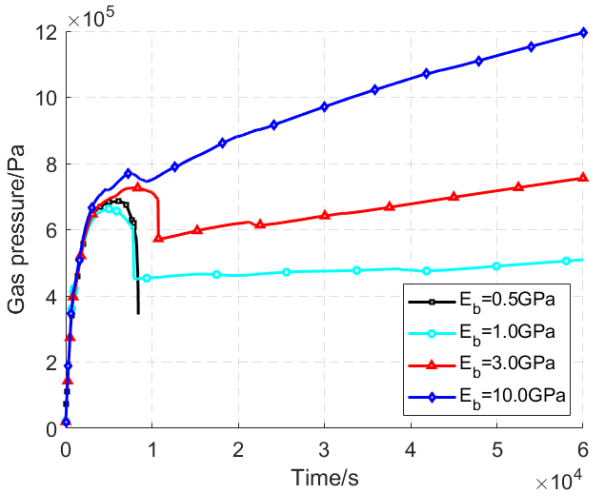

Figure 4.25 Evolution of gas pressure at injection boundary for different boundary conditions (E_b: Young's modulus of outer material)

4.2.6.2.4 Effects of injection rate

The rate of gas generation influences the gas migration process in barrier materials (Marschall et al. 2005; Ye et al. 2014). In this section, the effect of the gas injection rate on the developed fracture pattern is examined by conducting a contrastive analysis. To do that, four injection rates are applied at the injection boundary, i.e. 1×10^{-8} kg/(m^2•s), 2×10^{-8} kg/(m^2•s), 4×10^{-8} kg/(m^2•s), and 8×10^{-8} kg/(m^2•s). Figure 4.26 shows the fracture patterns developed in the studied domain under four different injection rates. Interestingly, the lowest injection rate results in the most obvious branching of fracture, while higher injection rates only give rise to slight branching behavior. This result appears to be inconsistent with our expectation that a higher injection rate should cause more obvious branching behaviors. However, as the fracture pattern generally depends on many factors, it is difficult to make a conclusion solely based on a single factor. In this case, the numerical result could be explained as follows. With a low injection rate, there is more time for the gas in the developed fracture to flow into the surrounding porous matrix before the next fracturing event occurs. Therefore, the highly pressurised gas has more chances to find the potential pathways to flow through, which results in a high level of branching. In contrast, with a high gas injection rate, the fracture is more likely to propagate along the weakest area of the studied domain, as there is not enough time for the gas flow into other possible pathways.

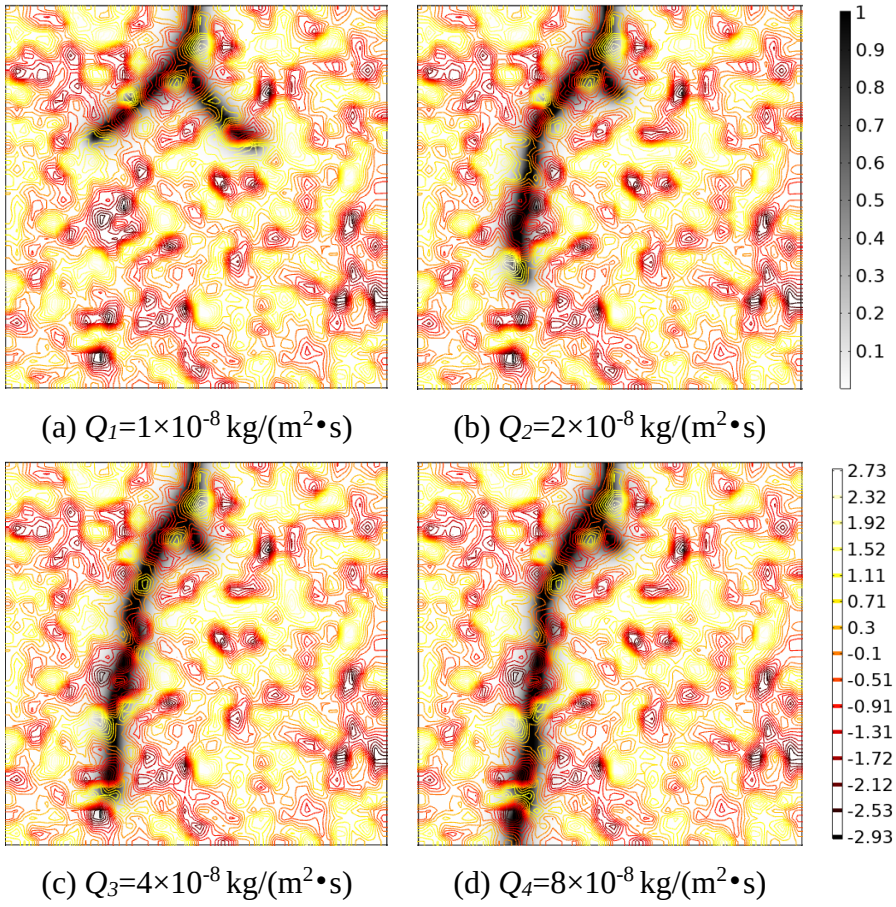

(a) Q_1=1×10^{-8} kg/(m^2•s) (b) Q_2=2×10^{-8} kg/(m^2•s)

(c) Q_3=4×10^{-8} kg/(m^2•s) (d) Q_4=8×10^{-8} kg/(m^2•s)

Figure 4.26 Fracture patterns in the studied domain with different injection rates (Q)

Figure 4.27 shows the changes in gas pressure at the injection boundary under different injection rates. It can be seen that the peak value that the gas pressure can reach increases with the injection rate. According to the ideal gas law, the rate of gas pressure is controlled by the rate of gas injection and the rate of volume created by the fracturing process. To induce a drop in gas pressure, the rate of the created volume should be larger enough to counteract the effect of the gas injection rate. For a low gas injection rate, the required rate of volume to trigger the drop of gas pressure is low. Correspondingly, the peak value that the gas pressure can reach should be small for the low gas injection rate. In addition, the leakage of gas from the developed fracture to the surrounding porous media will reduce the net injection rate and then further reduce the peak value of gas pressure.

As seen in Figure 26(d), the fracture has propagated to the bottom boundary of the studied domain for the case of the highest injection rate. As a result, the gas pressure rapidly declines,

see the blue line in Figure 4.27. This simulated result does not appear to be consistent with the experimental observation in which the gas pressure at the injection boundary approaches an asymptotic value after gas breakthrough occurs (Graham et al. 2012; Harrington and Horseman 2003). This inconsistency is due to the assumption of an irreversible fracturing process and the simplified permeability model adopted in this paper. Therefore, the self-sealing process and a more rigorous permeability model that can capture the changes in fracture aperture will be left to future studies.

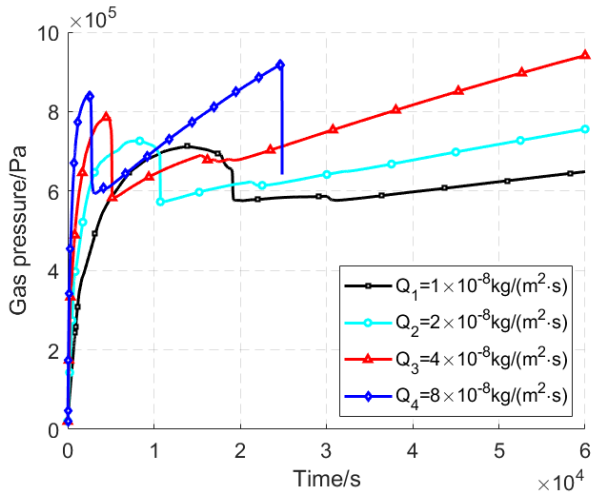

Figure 4.27 Evolution of gas pressure at injection boundary for different injection rates (Q)

4.2.7 Conclusions

A coupled HM-PF model that incorporates a spatially auto-correlated random field is developed in this paper to simulate the preferential gas flow in saturated bentonite. To avoid the pore pressure oscillation and alleviate computational efforts, a stabilization technique for the low equal-order finite elements is adopted.

The coupled HM-PF model demonstrates its capability to explicitly describe the development of preferential pathways in heterogeneous and saturated bentonite. Meanwhile, the developed model has qualitatively reproduced some of the key behaviors commonly observed in experiments, e.g. the nearly saturated sate after the injection test, the heterogeneous distribution of water pressure and the increases of both water pressure and total stress during the fracturing process. The effects of some critical factors, i.e. the Gaussian random field, the coefficient of variation, the boundary condition and the injection rate, on the fracturing process

have also been examined. It has been found that both the fracture pattern and the evolution of gas pressure at injection boundary are highly dependent on these factors. Specifically, as the distribution of HM properties varies with the seed used to generate the Gaussian random field, the developed fracture distributes differently in the studied domain with different random fields. With the increase of the coefficient of variation, the developed fracture can bypass the areas of high resistance more easily, thus leading to a more tortuous trajectory. The increase of boundary rigidity can significantly inhibit both the fracturing process and branching behavior. In terms of the effects of the injection rate, the fracturing at high injection rates is more rapid than that at low injection rates.

As an initial work, this paper still has some limitations that need to be addressed in the future. The intrinsic permeability of the developed fracture is assumed constant in this paper to alleviate computational efforts. A more robust and computationally efficient model for the intrinsic permeability is necessary to be developed to describe the fracturing process physically. As the main objective of the paper is to explicitly describe the preferential pathway, the swelling pressure has not yet been considered in this paper. A more physical based model would be developed in the future for describing the effect of swelling pressure on the gas migration process. Last but not least, the developed fracture is assumed irreversible once created. However, previous experimental studies have shown that the fracture may self-seal after gas breakthrough occurs. Therefore, the self-sealing of fractures in saturated bentonite should be further explored and modelled in the future.

4.3 A Thermodynamically Consistent Phase Field Model for Gas Migration in Saturated Bentonite Accounting For Initial Stress State

(The full version of this Technical paper has been submitted for publication)

4.3.1 Introduction

A thermodynamically consistent HM-PF framework is derived from the theory of thermodynamics proposed by Coussy (2004) for unsaturated porous media and the microforce balance law. The coupled HM-PF model in Section 4.2 can well describe the experimentally observed behaviors during gas migration in a qualitative way, such as the preferential gas flow, the build-up of water pressure and total stress and the fully saturated state around the developed fracture. However, the swelling pressure, an important factor controlling the fracturing process, has not yet been considered by the framework. As stated in (Horseman et al. 1999), the effective stress is equivalent to the swelling pressure for a high swelling clay. In the current coupled HM-PF framework, the effect of initial stress on the fracturing process is accounted for by introducing a modified strain tensor, i.e. the sum of the strain tensor due to deformation and a fictitious strain tensor corresponding to initial stress, into the phase field method. The simulated results show that the effect of the initial stress on the fracture initiation has been well described by the proposed method. Specifically, the effect of either isotropic or anisotropic stress state on the fracturing process can be well reflected by the phase field approach based on Rankine-type fracture criterion. In contrast, the phase field approach based on Griffith fracture criterion is more appropriate for the isotropic stress state than the anisotropic stress state because of the Poisson's effect.

This paper is organized as follows. In Section 4.3.2, governing equations for the stress equilibrium and the microforce balance law are provided. The mechanical constitutive models are developed in the framework of Coussy's thermodynamic theory for unsaturated porous media. In Section 4.3.3, the mass balance equations and constitutive models for the hydraulic process are given. Model validation and simulations of gas migration in initially saturated bentonite are presented in Section 4.3.4. Finally, conclusions and recommendations for future works will be given in Section 4.3.5.

4.3.2 Mechanical Model

4.3.2.1 Governing equations

By using the second Newton's law and neglecting the inertial and the viscous forces, the macroforce balance law for the porous media can be expressed as:

$$\nabla \cdot \boldsymbol{\sigma} + \rho \boldsymbol{g} = 0 \tag{4.70}$$

where $\boldsymbol{\sigma}$ is the total stress tensor, ρ is the averaged density of the mixture and $\boldsymbol{g}$ is the gravitational acceleration.

As done by Gurtin (1996), a set of microforces, including the surface microscopic force, γ, the internal microscopic stress, $\boldsymbol{\xi}$, and the internal microscopic body force, π, are introduced to construct a microforce balance law. The microforce balance law can be derived as (Wilson et al. 2013):

$$\nabla \cdot \boldsymbol{\xi} + \pi = 0 \tag{4.71}$$

$$\gamma = \boldsymbol{\xi} \cdot \boldsymbol{n} \tag{4.72}$$

where $\boldsymbol{n}$ is the outwards unit normal vector.

4.3.2.2 Coussy's thermodynamic theory

By using the mixture theory, Coussy (2004) developed a thermodynamically consistent framework for describing the coupled thermo-hydro-mechanical (THM) behaviors of unsaturated porous media. The detailed derivation processes can be found in (Coussy 2004). Based on the first law and the second law of thermodynamics, the final form of the Clausius-Duhem inequality is derived as

$$\Phi = \Phi_{\text{int}} + \varphi_f + \varphi_{th} \geq 0 \tag{4.73}$$

where Φ_{int} is the dissipation associated with the skeleton (including the solid matrix and the interfaces between different phases), φ_f and φ_{th} are the dissipations associated with the fluid flow and the heat transfer, respectively.

To satisfy the above Clausius-Duhem inequality, a sufficient but unnecessary condition is generally assumed that each dissipation component is nonnegative. As the thermal effect on the hydromechanical process is not considered in the current study, the dissipation related to heat transfer, φ_{th}, will not be discussed in the following. The dissipation due to fluid flow, φ_f, will be discussed in Section 4.3.3. Here, the dissipation related to the skeleton under isothermal condition can be expressed as (Coussy 2004)

$$\Phi_{\text{int}} = \boldsymbol{\sigma} : \dot{\boldsymbol{\varepsilon}} + p_w \dot{\phi}_w + p_g \dot{\phi}_g - \dot{\Psi}_s \geq 0 \tag{4.74}$$

where Ψ_s is the skeleton free energy, $\boldsymbol{\varepsilon}$ is the strain tensor, $\phi_w = \phi S_w$ and $\phi_g = \phi S_g$ are volume percentages occupied by water phase and gas phase respectively, ϕ is porosity and S_w and S_g are the degree of saturations for water and gas respectively.

4.3.2.3 Clausius-Duhem inequality

By using the microforce balance law, i.e. Eq. (4.71), the mechanical power from the microforce system, P_{mic}, can be derived as (Choo and Sun 2018b)

$$P_{mic} = \int_{\partial\Omega} (\boldsymbol{\xi} \cdot \boldsymbol{n}) \dot{d} \mathrm{d}\partial\Omega = \int_{\Omega} \left(\boldsymbol{\xi} \cdot \nabla \dot{d} - \pi \dot{d} \right) \mathrm{d}\Omega \tag{4.75}$$

This mechanical power needs to be incorporated into the Clausius-Duhem inequality for unsaturated porous media, Eq. (4.74), to account for the contribution from the fracturing process. This will result in an enriched Clausius-Duhem inequality as:

$$\Phi_{\text{int}} = \boldsymbol{\sigma} : \dot{\boldsymbol{\varepsilon}} + p_w \dot{\phi}_w + p_g \dot{\phi}_g + \boldsymbol{\xi} \cdot \nabla \dot{d} - \pi \dot{d} - \dot{\Psi}_s \geq 0 \tag{4.76}$$

Reformulating Eq. (4.18) with respect to suction, i.e., $p_c = p_g - p_w$, yields

$$\Phi_{\text{int}} = \boldsymbol{\sigma} : \dot{\boldsymbol{\varepsilon}} + \bar{p} \dot{\phi} - \phi p_c \dot{S}_w + \boldsymbol{\xi} \cdot \nabla \dot{d} - \pi \dot{d} - \dot{\Psi}_s \geq 0 \tag{4.77}$$

where $\bar{p} = S_w p_w + (1 - S_w) p_g$ is the average pore pressure.

In analogy to Coussy (2004), a general form for the skeleton free energy, Ψ_s, that considers the evolution of phase field can be defined as

$$\Psi_s = \psi_s(\boldsymbol{\varepsilon}, d) + \phi U(S_w, d) \tag{4.78}$$

where ψ_s is the free energy of solid matrix and U is the free energy of interfaces per unit volume of void space. Note that only elastic strain tensor is considered in the current study.

In previous studies, such as (Na and Sun 2018; Wilson et al. 2013), the free energy due to the fracturing process is also included in the free energy of the solid matrix, i.e., ψ_s. This definition may not be appropriate to describe the fracturing as a fully dissipative and irreversible process (Choo and Sun 2018a, b). To remedy this issue, Choo and Sun (2018a) developed a novel approach based on the maximum energy dissipation principle to derive the constitutive model for the phase field evolution. This approach will be briefly introduced in the following analysis. In addition, as seen in Eq. (4.78), the free energy of interfaces, i.e., U, not only depends on the degree of saturation but also on the phase field variable. This reflects the influence of the evolution of pore structure on the free energy of interfaces.

Substituting Eq. (4.78) into Eq. (4.77), yields

$$\Phi_{\text{int}} = \boldsymbol{\sigma} : \dot{\boldsymbol{\varepsilon}} + \pi_{eq}\dot{\phi} - \phi\left(p_c + \frac{\partial U}{\partial S_w}\right)\dot{S}_w + \boldsymbol{\xi}\cdot\nabla\dot{d} - \left(\pi + \phi\frac{\partial U}{\partial d}\right)\dot{d} - \dot{\psi}_s \geq 0 \tag{4.79}$$

where $\pi_{eq} = \bar{p} - U$ is the equivalent pore pressure as originally proposed in (Coussy 2004).

Compared with the relatively large compressibility of the porous skeleton as considered in the current study, the solid grain can be assumed incompressible, which leads to $\dot{\phi} = \boldsymbol{\delta} : \dot{\boldsymbol{\varepsilon}}$ (Coussy 2007). Substituting this equality into Eq. (4.79), gives

$$\Phi_{\text{int}} = \boldsymbol{\sigma}' : \dot{\boldsymbol{\varepsilon}} - \phi\left(p_c + \frac{\partial U}{\partial S_w} \right)\dot{S}_w + \boldsymbol{\xi} \cdot \nabla \dot{d} - \left(\pi + \phi \frac{\partial U}{\partial d} \right)\dot{d} - \dot{\psi}_s \geq 0 \tag{4.80}$$

$$\boldsymbol{\sigma}' = \boldsymbol{\sigma} + \pi_{eq}\boldsymbol{\delta} \tag{4.81}$$

where $\boldsymbol{\sigma}'$ is the effective stress tensor.

Substituting Eq. (4.78) into Eq. (4.79) and reformulating the resultant inequality lead to

$$\Phi_{\text{int}} = \left(\boldsymbol{\sigma}' - \frac{\partial \psi_s}{\partial \boldsymbol{\varepsilon}} \right) : \dot{\boldsymbol{\varepsilon}} - \phi\left(p_c + \frac{\partial U}{\partial S_w} \right)\dot{S}_w + \boldsymbol{\xi} \cdot \nabla \dot{d} - \left(\pi + \phi \frac{\partial U}{\partial d} + \frac{\partial \psi_s}{\partial d} \right)\dot{d} \geq 0 \tag{4.82}$$

By applying the standard Coleman-Noll argument to the inequality above, the constitutive relations for the effective stress tensor, $\boldsymbol{\sigma}$, the capillary pressure, p_c, can be derived as (De Lorenzis et al. 2016; Na and Sun 2018)

$$\boldsymbol{\sigma}' = \frac{\partial \psi_s}{\partial \boldsymbol{\varepsilon}}, \tag{4.83}$$

$$p_c = -\frac{\partial U}{\partial S_w}. \tag{4.84}$$

In the last term of Eq. (4.82), the internal microforce can be decomposed into an energetic part, π^{en} and a dissipative part, π^{dis}, which is expressed as (Choo and Sun 2018a, b)

$$\pi = \pi^{en} + \pi^{dis} \tag{4.85}$$

Following the standard Coleman-Noll statement, the energetic part of the internal microforce can be determined as

$$\pi^{en} = -\frac{\partial \psi_s}{\partial d} - \phi \frac{\partial U}{\partial d} \tag{4.86}$$

At this moment, the final form of the Clausius-Duhem inequality has been simplified as

$$\Phi_{\text{int}} = \boldsymbol{\xi} \cdot \nabla \dot{d} - \pi^{dis} \dot{d} \geq 0 \tag{4.87}$$

The specific forms for the microforces, i.e., $\boldsymbol{\xi}$ and π^{dis}, will be given in the following section.

4.3.2.4 Constitutive models

The gas-driven fracturing in bentonite is mainly caused by the tensile load exerted by the highly pressurized gas. To avoid the compression-induced fracturing, the free energy of the solid matrix is decomposed into a tensile part, $\psi_{s0}^{e+}(\boldsymbol{\varepsilon})$ and a compressive part, $\psi_{s0}^{e-}(\boldsymbol{\varepsilon})$, where only the tensile part serves as the driving force for the fracturing process, which is expressed as

$$\psi_s^e(\boldsymbol{\varepsilon}^e, d) = g(d)\psi_{s0}^{e+}(\boldsymbol{\varepsilon}) + \psi_{s0}^{e-}(\boldsymbol{\varepsilon}) \tag{4.88}$$

where $g(d)$ is a degradation function.

In this paper, the tensile part of the free energy is degraded by the widely used quadratic degradation function:

$$g(d) = (1-k)(1-d)^2 + k \tag{4.89}$$

where k is a small positive value to avoid the singularity of stiffness matrix (Bourdin et al. 2000).

By using the spectral decomposition technique, as done in (Miehe et al. 2010b), the tensile part and the compressive part of the free energy of solid matrix can be expressed as

$$\psi_{s0}^{e\pm}(\boldsymbol{\varepsilon}) = \lambda \langle \varepsilon_1 + \varepsilon_2 + \varepsilon_3 \rangle_{\pm}^2 / 2 + \mu \left(\langle \varepsilon_1 \rangle_{\pm}^2 + \langle \varepsilon_2 \rangle_{\pm}^2 + \langle \varepsilon_3 \rangle_{\pm}^2 \right) \tag{4.90}$$

where λ and μ are the Lamé parameters, $\langle x\rangle_{\pm}=\left(x\pm|x|\right)/2$ is the Macaulay bracket, and $\{\varepsilon_a\}_{a=1,2,3}$ are the principal components of the strain tensor.

The effective stress tensor can be derived by substituting Eqs. (4.88)-(4.90) into Eq. (4.21) as

$$\boldsymbol{\sigma}'\left(\boldsymbol{\varepsilon},d\right)=g\left(d\right)\boldsymbol{\sigma}'^{+}\left(\boldsymbol{\varepsilon}\right)+\boldsymbol{\sigma}'^{-}\left(\boldsymbol{\varepsilon}\right) \tag{4.91}$$

$$\boldsymbol{\sigma}'^{\pm}\left(\boldsymbol{\varepsilon}\right)=\sum_{a=1}^{3}\left[\lambda\left\langle\varepsilon_1+\varepsilon_2+\varepsilon_3\right\rangle_{\pm}+2\mu\left\langle\varepsilon_a\right\rangle_{\pm}\right]\boldsymbol{n}_a\otimes\boldsymbol{n}_a \tag{4.92}$$

where $\boldsymbol{\varepsilon}=\frac{1}{2}\left[\nabla\boldsymbol{u}+\left(\nabla\boldsymbol{u}\right)^{T}\right]$, $\boldsymbol{u}$ is the displacement vector, $\boldsymbol{\sigma}'^{\pm}$ are the tensile and compressive parts of the effective stress tensor, and $\{\boldsymbol{n}_a\}_{a=1,2,3}$ is the principal vector corresponding each principal strain.

Substituting Eqs. (4.81) and (4.91) into Eq. (4.70) gives the specific momentum balance law of the macroforce system as

$$\nabla\cdot\left[g\left(d\right)\boldsymbol{\sigma}'^{+}\left(\boldsymbol{\varepsilon}\right)+\boldsymbol{\sigma}'^{-}\left(\boldsymbol{\varepsilon}\right)-\pi_{eq}\boldsymbol{\delta}\right]+\rho\boldsymbol{g}=\boldsymbol{0}\,. \tag{4.93}$$

The specific forms for the internal microforces, i.e., $\boldsymbol{\xi}$ and π^{dis}, can be determined by using the approach proposed by Choo and Sun (2018a). This approach is briefly introduced here for completeness. More details and discussions on it can be found in (Choo and Sun 2018a, b). The approach is essentially developed on the postulate that the evolution of the phase field variable can maximize the energy dissipation, i.e., Eq. (4.87). To this end, the negative of the fracture dissipation functional should be minimized with the following constraint:

$$\left(\frac{d}{l}\right)\dot{d}+l\nabla d\left(\nabla\dot{d}\right)=\dot{\Gamma}_d \tag{4.94}$$

where l is a characteristic length controlling the width of the phase field and Γ_d is the crack density functional that is used to regularize the sharp discontinuity.

To solve this constrained minimization problem, a Lagrangian can be constructed as

$$\mathcal{L}\left(\dot{d},\nabla\dot{d},\Lambda\right)=-\boldsymbol{\xi}\cdot\nabla\dot{d}+\pi^{dis}\dot{d}+\Lambda\left[\left(\frac{d}{l}\right)\dot{d}+l\nabla d\left(\nabla\dot{d}\right)-\dot{\Gamma}_d\right] \tag{4.95}$$

where Λ is the Lagrangian multiplier.

By applying the stationary condition for the proposed Lagrangian, i.e., Eq. (4.95), the internal microforce $\boldsymbol{\xi}$ and π^{dis} can be determined as (Choo and Sun 2018a)

$$\boldsymbol{\xi}=\Lambda l\nabla d \tag{4.96}$$

$$\pi^{dis}=-\Lambda d/l \tag{4.97}$$

As analyzed in (Choo and Sun 2018a), the Lagrangian multiplier can be interpolated as the critical fracture energy, i.e., $\Lambda=G_c$. Then, substituting Eqs. (4.96), (4.97) and (4.23) into Eq. (4.71) yields the microforce balance law as

$$G_c l\nabla^2 d-g'(d)\psi_{s0}^{e+}-G_c d/l-\phi\frac{\partial U\left(S_{\mathrm{w}},d\right)}{\partial d}=0 \tag{4.98}$$

The interfacial energy in intact porous media, $U\left(S_w\right)$, is defined with respect to the capillary pressure, p_c, as (Coussy 2004):

$$U\left(S_w\right)=\int_{S_w}^{1}p_c\left(S\right)\mathrm{d}S \tag{4.99}$$

In Eq. (4.99), the capillary pressure is defined as a function of the degree of saturation, which leads to the water retention model. The water retention capability of the developed

fractures is inferior to that of the porous matrix, since the size of the fractures is much larger than that of the porous matrix. Therefore, at a given degree of saturation, the interfacial energy of the fractures is less than that of the porous matrix. In order to account for the fracturing effect, the interfacial energy should also be defined with respect to the phase field variable. In analogy to the degradation of the free energy of solid matrix, i.e., Eq. (4.88), the interfacial energy can be defined as

$$U(S_w, d) = (1-d)^{n_U} U(S_w) \tag{4.100}$$

where n_U is a positive value controlling the degradation of the interfacial energy. With the increase of n_U, the degradation of the interfacial energy will be more sensitive to the change of the phase field variable. The value of n_U may depend on the specific material in which the fracturing takes place. If n_U takes 2, substituting Eq. (4.100) into Eq. (4.98) yields a standard governing equation for the phase field, as derived in (Mauthe and Miehe 2017):

$$(1-d)H^+ - \left(d - l^2\nabla^2 d\right) = 0 \tag{4.101}$$

$$H^+ = \frac{2\left(\psi_{s0}^{e+} + \phi U(S_w)\right)}{G_c / l} \tag{4.102}$$

where H^+ is the fracture driving force functional. It is worth noting that the standard governing equation for phase field, i.e., Eq. (4.101), may not be obtained if the interfacial energy took other forms than the one in Eq. (4.100). More theoretical and experimental works need to be conducted to determine a specific form for the degraded interfacial energy. However, this is beyond the scope of the current study.

As seen in Eq. (4.102), the interfacial energy between wetting and nonwetting fluids has been analytically added to the fracture driving force functional based on the theory of thermodynamics. However, the real contribution of the interfacial energy to the fracturing

process in porous media is still under discussion. The experimental and numerical studies in (Shin and Santamarina 2011) highlighted the effect of air-water interfaces on the desiccation cracking. Moreover, the grain-scale model in (Jain and Juanes 2009) indicated that the capillary effects may influence the gas pressure required for fracturing in saturated porous media. In contrast, Espinoza and Santamarina (2012) stated that capillary-driven fractures may not likely occur in porous media of low porosity that is subjected to high effective stress. This statement may be applied to the current research topic, as the saturated bentonite sample can be considered as a low porosity media (if the adsorbed water is regarded as a part of the solid grain) that has a larger swelling pressure at the beginning of gas injection. Importantly, the previous experimental studies on gas migration in saturated bentonite rarely, if ever, examined the capillary effect on the fracturing process. Instead, these experimental studies mainly concluded that the gas entry mainly occurs when gas pressure reaches the sum of swelling pressure and porewater pressure (Graham et al. 2012; Harrington and Horseman 2003; Harrington et al. 2019b). As analyzed above, the free energy of interfaces will not be examined in the current study but may be considered in the future when enough experimental findings are available.

In addition, previous experimental studies, such as (Graham et al. 2012) and (Harrington et al. 2019b), showed that the developed fractures may self-heal after the gas breakthrough phenomenon. This self-sealing behavior may involve complex interactions between fluids (water/gas) and clay minerals. For simplicity, the gas-driven fracturing is assumed as an irreversible process in this study, while the self-sealing behavior is left for the future study. To achieve this irreversibility, the driving force H^+ in Eq. (4.34) without considering the free energy of interfaces is replaced by its maximum value during the loading history, H_M^+, as adopted in (Choo and Sun 2018a; Miehe et al. 2010b):

$$H_M^+ = \max_{\tau\in[0,t]}\left\{\frac{2\psi_{s0}^{e+}}{G_c / l}\right\} \tag{4.103}$$

4.3.2.5 Effect of initial stress state

Previous experimental studies showed that major gas entry occurs when gas pressure reaches the sum of the swelling pressure and the porewater pressure (Cuss et al. 2014b; Graham et al. 2012; Horseman et al. 1999). The swelling pressure can be considered as the effective stress to which the saturated bentonite is initially subjected for a high swelling clay (Horseman et al. 1999). Previous phase field models rarely considered the effect of initial stress state, except for the one in (Zhou et al. 2020). In that model, the initial stress state is accounted for by incorporating the strain energy caused by the initial stress state (i.e., the product of the initial stress tensor and the strain tensor) into the historical maximum driving force, i.e., Eq. (4.103) . The model was able to capture some desirable features during the hydraulic fracturing process. However, the proposed approach seems not sufficient to identify the effective component of an anisotropic stress state that drives the fracturing process. It is worth noting that the anisotropy concerned in this section is associated with the stress state, rather than the material properties. In this paper, a new approach will be proposed to reasonably describe the effect of the initial stress state on the fracturing process.

Prior to developing a general approach in two dimensions or three dimensions, a one-dimensional tensile test on a bar that is initially in the compressive state, as seen in Figure 4.28(a), is analyzed. Figure 4.28(b) shows the stress-strain relationship of this tensile test. With the increase of the tensile strain, the stress within the bar increases from the initial compressive stress, σ_0, to zero, i.e., the stress-free state (corresponding to the dashed configuration in Figure 4.28(a)). At this point, the corresponding tensile strain, ε_{t1}, can be easily determined as

$$\varepsilon_{t1} = -\frac{\sigma_0}{E} \tag{4.104}$$

As the tensile strain further increases, the bar begins to be subjected to the tensile stress, see Figure 4.28(b). Clearly, it is the elastic tensile strain energy under tensile stress state that provides the driving force for the fracturing process. The elastic tensile strain energy, ψ_{ten}, is represented by the area of the grey triangle in Figure 4.28(b), which can be easily calculated as

$$\psi_{ten} = \frac{1}{2} E \left(\varepsilon_{t2} - \varepsilon_{t1} \right)^2 \tag{4.105}$$

Alternatively, the above strain energy can be determined by subtracting the elastic compressive strain energy, ψ_{comp} (represented by the trapezoid BCFD), from the total elastic strain energy, ψ_{tot} (represented by the triangle ADF), which is formulated as

$$\psi_{ten} = \psi_{tot} - \psi_{comp} \tag{4.106}$$

Here, we can introduce a theoretical or a fictitious initial strain that corresponds to the initial compressive stress as

$$\varepsilon_0 = \frac{\sigma_0}{E} \tag{4.107}$$

Combining Eqs. (4.104)-(4.107), the elastic tensile strain energy can be reformulated as

$$\psi_{ten} = \frac{1}{2} E \left(\varepsilon_{t2} + \varepsilon_0 \right)^2 \tag{4.108}$$

It can be seen from Eq. (4.108) that the initial stress state has been accounted for in the elastic tensile strain energy functional by transforming the initial stress into its corresponding strain. Therefore, we can assume that the tensile test on the pre-stressed bar can be decomposed into two loading steps, i.e., a stress-free bar is loaded to a compressive state (i.e., the bar configuration transforms from the dashed line to the dotted dashed line in Figure 4.28(a)) and then a tensile load is applied on the bar (i.e., the right end of the bar extends from the dotted dashed line to the solid line in Figure 4.28(a)) until fracturing occurs. Clearly, the first step is a fictitious process, while the second one is the real loading process. It is the overall strain, i.e., the sum of strains in the first and in the second step, that determines the elastic tensile strain energy for the fracturing process, see Eq. (4.108).

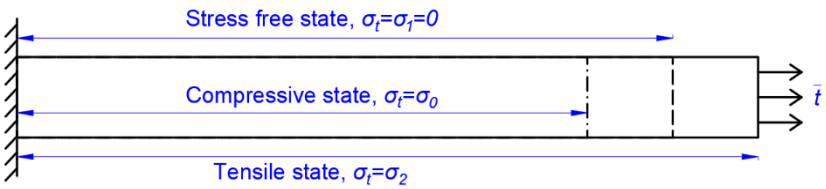

(a) 1-D bar under tensile load

(The dotted dashed line represents the bar under the compressive state, the dashed line corresponds to the stress-free state, and the solid line to the tensile state)

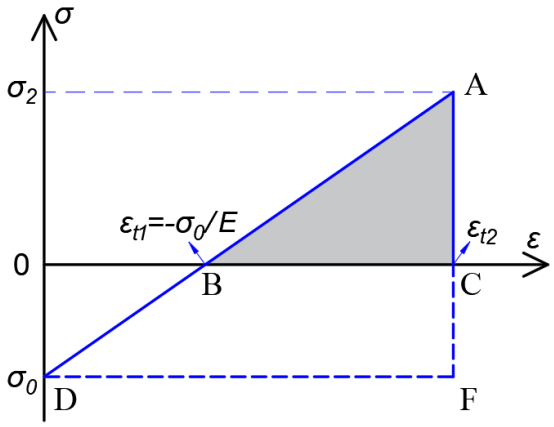

(b) Stress-strain relationship of the 1-D bar (E is Young's modulus of the bar)

Figure 4.28 A 1-D bar under tensile load and its stress-strain relationship

The 1-D bar analysis given above can be easily extended to either the 2-D or 3-D case. For a general dimensional condition, the fictitious initial strain tensor can be determined as

$$\boldsymbol{\varepsilon}_0 = \mathbb{C} : \boldsymbol{\sigma}_0 \tag{4.109}$$

where $\mathbb{C}$ is the elastic compliance tensor, $\boldsymbol{\varepsilon}_0$ is the fictitious initial strain tensor corresponding to the initial stress tensor, $\boldsymbol{\sigma}_0$. It is worth noting that $\boldsymbol{\sigma}_0$ here represents the initial stress tensor for pure mechanical problems, while it is interpreted as the initial effective stress tensor for poromechanical problems.

Then, the modified strain tensor, $\tilde{\boldsymbol{\varepsilon}}$, can be determined as

$$\tilde{\boldsymbol{\varepsilon}} = \boldsymbol{\varepsilon}_0 + \boldsymbol{\varepsilon} \tag{4.110}$$

Therefore, the initial stress state can be naturally accounted for in the phase field model by replacing the strain tensor $\boldsymbol{\varepsilon}$, in Eqs. (4.88), (4.90), (4.29), (4.92) and (4.32) by the modified strain tensor, $\tilde{\boldsymbol{\varepsilon}}$. As seen from Eqs. (4.90) and (4.92), it is the positive principal strains of the modified strain tensor, $\tilde{\boldsymbol{\varepsilon}}$, that provide the driving force for the fracturing process. Clearly, the different contributions of the three principal components of an anisotropic stress state can be easily identified in this proposed approach.

For a plane strain problem, the specific components of the fictitious strain tensor in Eq. (4.109) can be expressed as

$$\begin{cases} \varepsilon_{0xx} = \dfrac{1+\nu}{E}\left[(1-\nu)\sigma_{0xx} - \nu\sigma_{0yy}\right] \\ \varepsilon_{0yy} = \dfrac{1+\nu}{E}\left[(1-\nu)\sigma_{0yy} - \nu\sigma_{0xx}\right] \\ \varepsilon_{0xy} = \dfrac{1+\nu}{E}\sigma_{0xy} \end{cases} \tag{4.111}$$

where σ_{0xx}, σ_{0yy}, ε_{0xx}, ε_{0yy} are the normal stress and strain in the x and y direction, respectively, σ_{0xy} and ε_{0xy} are shear stress and strain components, E is Young's modulus and ν is the Poisson's ratio.

As seen in Eq. (4.111), for a strong anisotropic stress tensor, the normal strain components may become positive even when both the normal stress components are negative. Then, the tensile elastic strain energy, i.e., ψ_{s0}^{e+} in Eq. (4.90), becomes positive, and the phase field variable increases according to the fracture driven force functional, i.e., Eq. (4.103). Note that the contribution of the interface energy is not considered here. This means that the fracture can develop even though the material is subject to fully compressive stress. Clearly, this result is not consistent with reality. To avoid this issue caused by the Poisson's effect, a stress-based fracture driving force functional, originally proposed in (Miehe et al. 2015b), can be used to govern the fracturing process. This driving force functional is expressed as

$$H_M^+ = \max_{\tau\in[0,t]}\left\{\zeta\left\langle\sum_{a=1}^{3}\left(\frac{\langle\sigma'_a\rangle_+}{\sigma_{cr}}\right)^2-1\right\rangle_+\right\} \tag{4.112}$$

where $\{\sigma'_a\}_{a=1,2,3}$ is the principal effective stress, σ_{cr} is a critical tensile stress and ζ is a dimensionless parameter that controls the evolution of phase field after the critical tensile stress is reached. As seen in Eq. (4.112), the driving force functional is proportional to the ζ after the critical stress is exceeded. Thus, with the increase of ζ, the fracturing process will be accelerated. As presented in (Miehe et al. 2015b), a larger value of ζ can lead to a more rapid increase of the phase field variable.

Hereafter, the energy-based fracture driving force functional, i.e., Eq. (4.103), is termed as a Griffith Fracture Criterion (GFC), while the stress-based functional, i.e., Eq. (4.112), is called a Rankine-type Fracture Criterion (RFC). Both fracture criteria will be examined in terms of their performances in controlling the fracturing process in Section 4.3.4.

4.3.3 Hydraulic Model

4.3.3.1 Mass balance equations

Based on the assumption of small deformation and incompressible solid grain, the mass balance equations for gas and water can be expressed as (Guo and Fall 2019)

$$\rho_g\phi\left(\frac{S_g}{K_g}-\frac{\partial S_e}{\partial p_c}\right)\frac{\partial p_g}{\partial t}+\nabla\cdot(\rho_g\boldsymbol{v}_g^D)=-\rho_g\phi\frac{\partial S_e}{\partial p_c}\frac{\partial p_w}{\partial t}-S_g\rho_g\frac{\partial\varepsilon_v}{\partial t} \tag{4.113}$$

$$\rho_w\phi\left(\frac{S_w}{K_w}-\frac{\partial S_e}{\partial p_c}\right)\frac{\partial p_w}{\partial t}+\nabla\cdot(\rho_w\boldsymbol{v}_w^D)=-\rho_w\phi\frac{\partial S_e}{\partial p_c}\frac{\partial p_g}{\partial t}-S_w\rho_w\frac{\partial\varepsilon_v}{\partial t} \tag{4.114}$$

where K_α is the bulk modulus of fluid α, S_e is the effective degree of saturation, ε_v is the volumetric strain and $\boldsymbol{v}_\alpha^D$ is Darcy's velocity.

4.3.3.2 Constitutive models

The dissipation due to the viscous fluid flow in porous space is expressed as

$$\varphi_f = \left(-\nabla p_w + \rho_w \boldsymbol{g}\right)\cdot \boldsymbol{v}_w^D + \left(-\nabla p_g + \rho_g \boldsymbol{g}\right)\cdot \boldsymbol{v}_g^D \geq 0 \tag{4.115}$$

To ensure the positiveness of the dissipation due to the viscous fluid flow, the fluid flux can be described by a generalized Darcy's law,

$$\boldsymbol{v}_\alpha^D = -\frac{\boldsymbol{k}_{in} k_{r\alpha}}{\mu_\alpha}(\nabla p_\alpha - \rho_\alpha \boldsymbol{g}) \tag{4.116}$$

where $\boldsymbol{k}_{in}$ is the intrinsic permeability tensor, $k_{r\alpha}$ is the relative permeability, and μ_α is the fluid dynamic viscosity.

Two sets of hydraulic properties, including the intrinsic permeability, relative permeability and gas entry value, are proposed for the developed fractures and the porous matrix, respectively, as done in (Guo and Fall 2019). The two sets of hydraulic properties are connected by a transitional function to describe the corresponding properties in the transition zone between fractures and porous matrix. The intrinsic permeability model, water retention model and relative permeability model for both the developed fractures and the porous matrix can be referred to Section 4.2.4.2. This section mainly discusses the Mualem-van Genuchten model and power law model for the relative permeability of gas.

In the intact porous matrix, the relative permeabilities for gas and water (k_{prw} and k_{prg}, respectively) are generally described by the Mualem-van Genuchten model (Luckner et al. 1989; Mualem 1976; van Genuchten 1980), which are expressed as

$$k_{prw} = \sqrt{S_e}\left[1-\left(1-S_e^{1/m}\right)^m\right]^2 \tag{4.117}$$

$$k_{prg} = \sqrt{1-S_e}\left(1-S_e^{1/m}\right)^{2m} \tag{4.118}$$

Alternatively, the relative permeability of gas is commonly described by a power law, as seen in (Arnedo et al. 2013; Gerard et al. 2014; Olivella and Alonso 2008), which is expressed as

$$k_{prg} = \left(1 - S_e\right)^{n_r} \tag{4.119}$$

where n_r is a model parameter which is taken as 3 in this study.

Figure 4.29 presents the curves for the Mualem-van Genuchten model, i.e., Eq. (4.118) with m taken as 0.45, and the power law, i.e., Eq. (4.119). The two models perform rather differently to describe the relative permeability of gas evolving with the effective degree of saturation. In general, the power law with order of 3 predicts a lower relative permeability of gas than that predicted by the Mualem-van Genuchten model. In particular, the relative permeability of gas given by the power law is close to 0 when the effective degree of saturation ranges between 0.8 and 1. In contrast, the relative permeability of gas given by the Mualem-van Genuchten model has reached approximately 0.2 when the effective degree of saturation is 0.8. Therefore, the power law with order of 3 is more suitable to simulate the low permeable feature of the porous matrix adjacent to the developed fracture. In the following sections, the power law model will be used to describe the relative permeability of gas, unless otherwise stated.

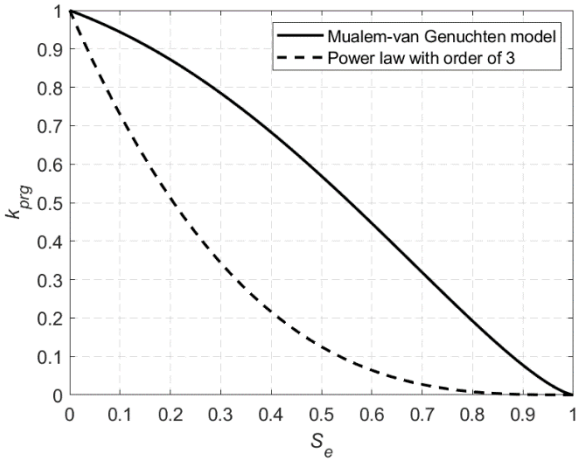

Figure 4.29 Curves of relative permeability of gas

4.3.4 Model Validation and Simulations

The developed coupled HM-PF model is implemented in COMSOL. Details about the implementation can be found in Section 4.2.5.1. The effect of initial stress state on the fracture initiation and propagation is validated in Section 4.3.4.1. The gas-driven fracturing in saturated bentonite is simulated in Section 4.3.4.2 where the effects of initial stress state and boundary conditions on the fracturing process have been examined. It is worth noting that the sign of compressive stress is taken as positive when analyzing the simulated results.

4.3.4.1 Model validation

Some basic validations for the proposed coupled HM-PF model have been conducted in Section 4.2, including the pure shear test, the one-dimensional consolidation test and the hydraulic fracturing test. In this section, the main goal of the simulations is to validate that the effect of initial stress state can be well described by the proposed modified strain tensor. Both the isotropic and the anisotropic initial stress state will be examined.

Figure 4.30 shows the simulated domain and boundary conditions. The dimension of the domain is 25mm in width and 50mm in height. The center part of the domain is discretized by fine square elements with a size of 0.25mm, while the other part is discretized by coarser quadrilateral elements to alleviate computational effort. The initial porewater pressure and water pressure on the boundary are 1MPa. The initial stress state will be given in the following subsections. The tractions in the vertical and horizontal direction, i.e., t_v and t_h, are set as values that can achieve an initial stress equilibrium at the boundary. The left boundary is an axis of symmetry and the point at the left corner is fixed to ensure convergency. The Young's modulus is 307 MPa and the Poisson's ratio is 0.4 (Tamayo-Mas et al. 2018). Here both the RFC and the GFC will be examined in terms of their performance in controlling the fracturing process. The tensile strength is set as 0.5 MPa for the RFC, while the fracture energy is set as 1.0 J/m^2 for the GFC. The initial porosity is 0.044, by assuming that the adsorbed water that accounts for 90% of the total water content is a part of the solid particle (Zheng et al. 2017). The initial permeability of the porous media is assumed to be 3.4×10^{-21} m^2. As adopted in (Guo and Fall 2019; Miehe et al. 2010b), the internal length scale, l, is set as twice the element size

for all simulations in this paper. An additional mass source, i.e., 0.3 kg/m^3, is applied to the red injection zone, as seen in Figure 4.30, to simulate the water injection operation. The size of the red zone is 0.25mm × 3mm in height and width respectively.

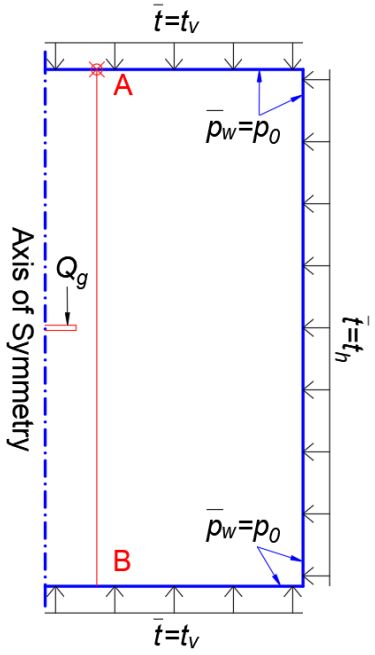

Figure 4.30 Simulated domain and applied boundary conditions (Note: Point A is a monitoring point and Line AB is a monitoring line that will be used in Section 4.3.4.2.3)

4.3.4.1.1 Isotropic initial stress state

In this section, the simulated domain is subjected to isotropic initial stress that is selected as 3MPa, 5MPa and 7MPa in each respective case. Both the GFC and the RFC will be examined in terms of their performances of controlling the fracturing process.

Figure 4.31 (a) presents the simulated water pressure at the injection zone based on the GFC. For each specific initial stress, the water pressure mainly experiences two peaks. As the water is injected into the injection zone, the water pressure increases rapidly until reaching the first peak at which the GFC is fulfilled, as seen in Figure 4.31 (a). Then, a tensile failure occurs in the injection zone. This leads to a rapid volume dilation, and as a result, a drop of water pressure in the injection zone. In contrast, the second peak is associated with the fracture propagation towards the right boundary. The extension of the fracture has increased the volume of the fracture space at a higher rate than the water injection rate, thus leading to the continuous drop of water pressure after the second peak, as seen in Figure 4.31 (a).

For each case of initial stress, the water pressure at the first peak has exceeded the total stress (the sum of the initial porewater pressure and the initial stress) by a certain small value that corresponds to the fracture energy required by the GFC. In addition, corresponding to each increasing step, i.e., 2MPa, in the initial stress, the water pressure required to trigger the fracturing process increases in a comparable step. As seen in Figure 4.31 (a), the curves after the second peak are almost parallel to each other with a difference of approximately 2MPa. When the fracture reaches the right boundary, the water flows out of the domain rapidly, thus leading to an abrupt decrease of water pressure. As seen in Figure 4.31 (a), the fracture that is developed under lower initial stress firstly reaches the right boundary, since less water content is required to induce the fracture propagation. This is also observed in Figure 4.31 (b) where the phase field profiles with lower initial stress at *t*=5000s are closer to the right boundary.

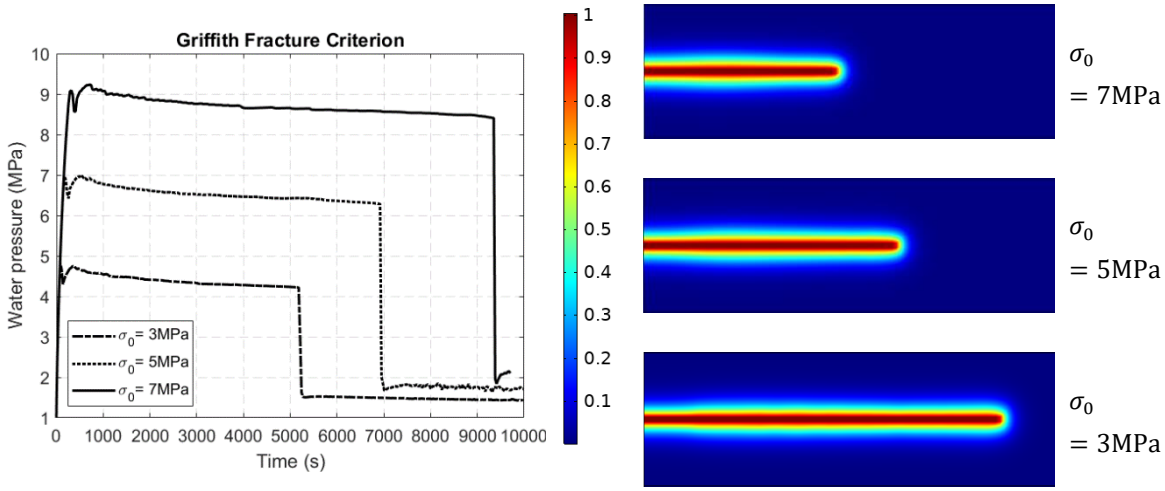

(a) Water pressure at injection zone

(b) Profiles of phase field at t=5000s

Figure 4.31 Simulated water pressure and phase field based on GFC (Note that only the center part of the domain is presented in Figure (b))

Figure 4.32(a) presents the simulated water pressure at the injection zone based on the RFC. In general, the evolution curves of water pressure are very similar to those determined by using the GFC. With the increase of the initial stress, the water pressure at peak increases by an approximately equal value. The peak value of the water pressure is just above a critical value, i.e., the sum of the total stress and the tensile strength (i.e., 0.5 MPa). As the fracture propagates towards the right boundary, the water pressure at the injection zone is maintained around the critical value. In addition, the fracture propagates faster under lower initial stress than under

higher initial pressure, see Figure 4.32(a) and (b). This is consistent with the numerical results based on the GFC.

As analyzed above, the effect of initial stress state can be well described by adopting the modified strain tensor, i.e., Eq. (4.110), in the phase field model. Both the GFC and the RFC can realistically simulate the fracture propagation under isotropic initial stress state. Here, it is worth noting that the coupled HM-PF models based on the GFC are more computationally efficient than those based on the RFC, which needs an additional spectral decomposition on the stress tensor, see Eq. (4.112).

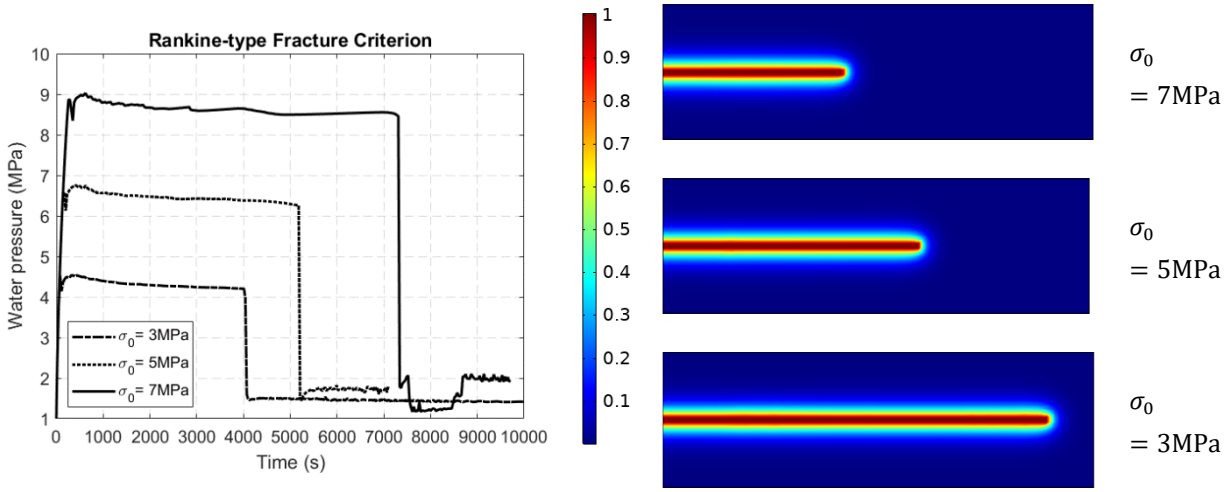

(a) Water pressure at injection zone (b) Phase field profiles at t=4000s

Figure 4.32 Simulated water pressure and phase field based on RFC

4.3.4.1.2 Anisotropic initial stress state

As discussed in Section 4.3.2.5, the phase field model based on GFC is not appropriate to simulate the fracture propagation in anisotropic initial stress field because of the Poisson's effect. In this section, therefore, only the RFC will be examined in terms of its performance of simulating the fracturing process under anisotropic initial stress state. Five groups of vertical and horizontal initial stress, i.e., (3MPa, 5MPa), (4MPa, 5MPa), (5MPa, 6MPa), (5MPa, 7MPa) and (7MPa, 5MPa), are used to conduct the sensitivity analysis. Figure 4.33 presents the profiles of the phase field under different anisotropic initial stress states. For the first four groups of stress combination as given above (where the horizontal stress is larger than the vertical one), the fractures propagate along the horizontal direction, see Figure 4.33(a-d). In

contrast, for the last group of stress combination (where the horizontal stress is less than the vertical one), the fracture propagates vertically, although the initial injection zone is predefined horizontally, see Figure 4.33(e). This numerical result is consistent with the fracturing theory that the fracture propagates along the direction that is perpendicular to the minimum principal stress.

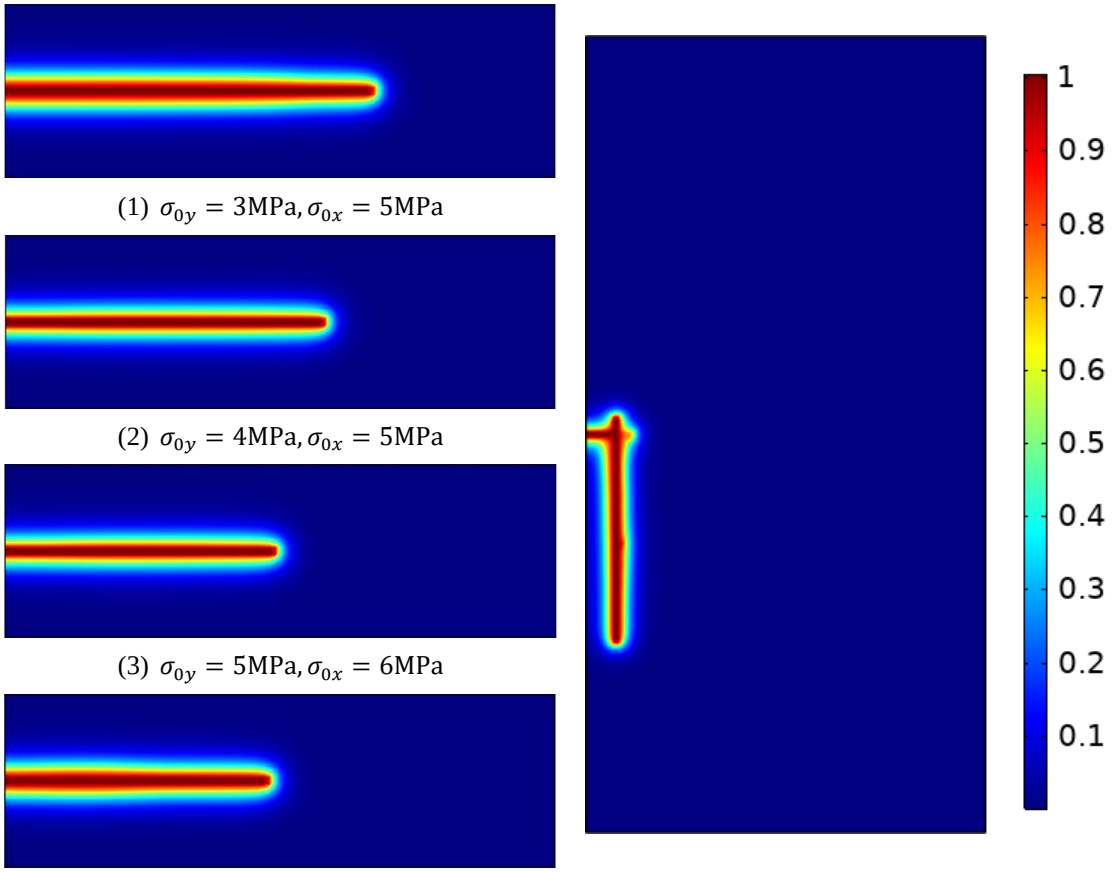

(1) $\sigma_{0y} = 3\text{MPa}, \sigma_{0x} = 5\text{MPa}$

(2) $\sigma_{0y} = 4\text{MPa}, \sigma_{0x} = 5\text{MPa}$

(3) $\sigma_{0y} = 5\text{MPa}, \sigma_{0x} = 6\text{MPa}$

(4) $\sigma_{0y} = 5\text{MPa}, \sigma_{0x} = 7\text{MPa}$

(5) $\sigma_{0y} = 7\text{MPa}, \sigma_{0x} = 5\text{MPa}$

Figure 4.33 Profiles of phase field under anisotropic initial stress state at t=4000s

Figure 4.34 shows the evolutions of water pressure in the injection zone under different anisotropic initial stress states. For the first four groups of stress combination, the water pressure required to trigger the fracture propagation is approximately equal to the sum of the initial vertical stress, the porewater pressure and the tensile strength. When the vertical stress is fixed at 5MPa, the variation in the horizontal stress has little influence on the evolution of water pressure, as indicated by comparing the dotted green line and the dotted black in Figure 4.34. For the last group of stress combination, i.e., (σ_{y0}=7MPa and σ_{x0}=5MPa), the water

pressure reaches as high as 8.5MPa and then declines rapidly, leading to a more distinct peaking stage compared with other cases. The occurrence of the peak value is associated with the predefined horizontal direction of the red injection zone, as seen in Figure 4.30. As the horizontal stress is less than the vertical one, the propagation direction switches from the horizontal to the vertical, which leads to the rapid drop of the water pressure, see in Figure 4.34.

In general, the numerical results as analyzed above prove that the RFC can satisfactorily describe the fracture propagation under an anisotropic initial stress state.

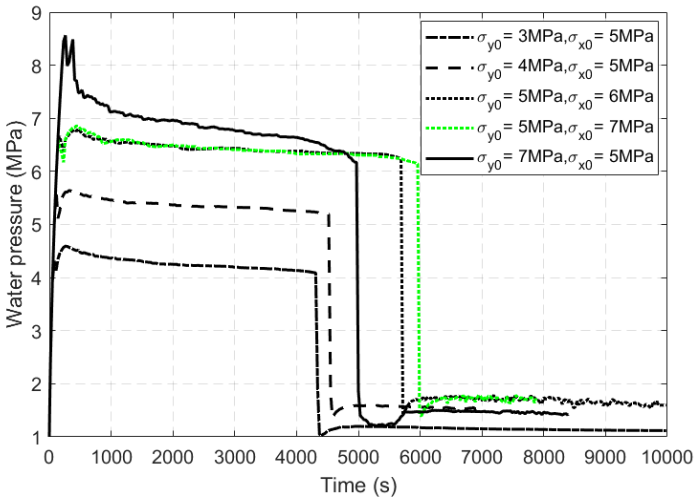

Figure 4.34 Evolutions of water pressure at injection zone with different initial stress states

Here, it is worth noting that for the stress combinations in which there is a larger difference between the horizontal and the vertical stress, such as (3MPa, 5MPa) and (5MPa, 7MPa), the width of the phase field profile is relatively larger, see Figure 4.33 (a) and (d). This means that the developed fracture tends to expand towards the direction of lower principal stress. As the difference between the horizontal and the vertical stress increases, the profiles of phase field become more sensitive in the direction of the lower stress component. Through controlling the coefficient, ζ, in Eq. (4.112), the sensitivity may be alleviated. Figure 4.35 shows the profiles of phase field for the initial stress combinations, i.e., (3MPa, 5MPa) and (5MPa, 7MPa), with the coefficient ζ decreased from 1 to 0.1. Clearly, with the decrease of the coefficient, ζ, both the width of the phase field profile and the rate of fracture propagation have decreased.

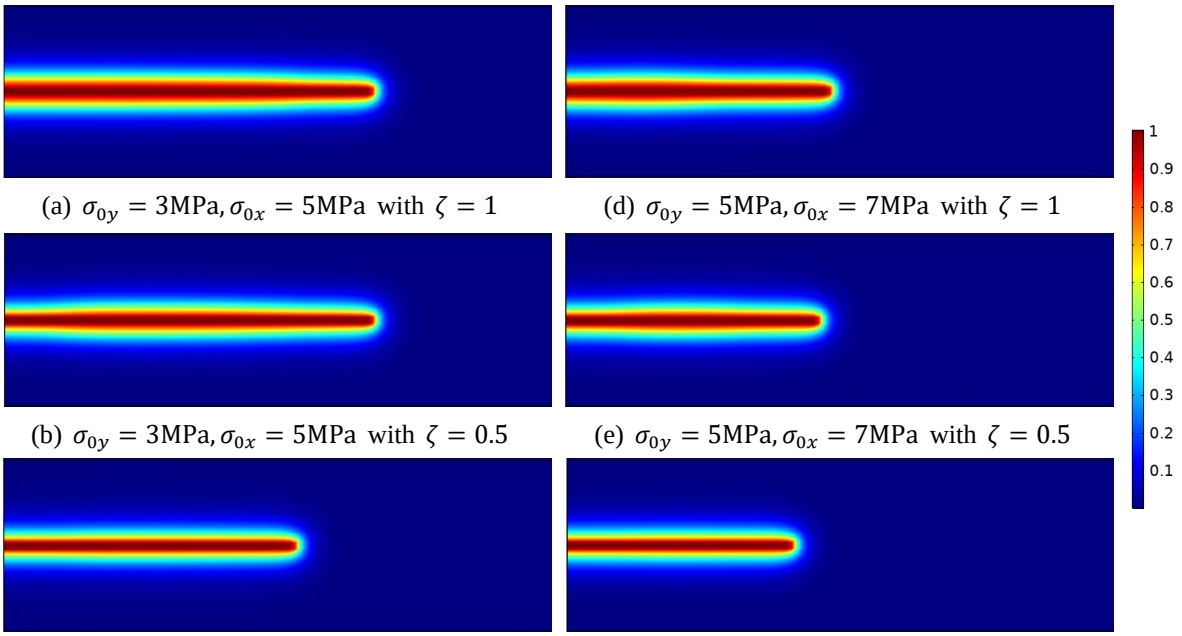

(a) $\sigma_{0y} = 3\text{MPa}, \sigma_{0x} = 5\text{MPa}$ with $\zeta = 1$ (d) $\sigma_{0y} = 5\text{MPa}, \sigma_{0x} = 7\text{MPa}$ with $\zeta = 1$

(b) $\sigma_{0y} = 3\text{MPa}, \sigma_{0x} = 5\text{MPa}$ with $\zeta = 0.5$ (e) $\sigma_{0y} = 5\text{MPa}, \sigma_{0x} = 7\text{MPa}$ with $\zeta = 0.5$

(c) $\sigma_{0y} = 3\text{MPa}, \sigma_{0x} = 5\text{MPa}$ with $\zeta = 0.1$ (f) $\sigma_{0y} = 5\text{MPa}, \sigma_{0x} = 7\text{MPa}$ with $\zeta = 0.1$

Figure 4.35 Profiles of phase field with different values of ζ at t=4000s

4.3.4.2 Gas-driven fracturing in saturated bentonite

The simulated domain in Section 4.3.4.1 is adopted in the following simulations. The initial gas pressure and the initial water pressure for the entire domain are set as 1.05MPa and 1.0MPa, respectively. The gas entry value for the injection zone is set as an extremely small value, i.e., 10Pa, to ensure the injection zone is saturated with the gas phase. The gas entry value for the remaining domain is set as 18MPa (Tamayo-Mas et al. 2018). Therefore, the gas pressure in the injection zone fully contributes to the pore pressure, which makes tensile failure possible in the injection zone. The gas entry value for the developed fractures is set as 5Pa. The shape parameter, *m*, in the van Genuchten model is 0.45 (Tamayo-Mas et al. 2018). The other hydromechanical properties are the same as those in Section 4.3.4.1. The mass injection rate applied on the injection zone is 0.001kg/(m^3·s). The top and bottom boundaries are impermeable to water and gas. A mass flux, as given by Eq. (4.69), is applied on the right boundary for both gas and water. The other boundary conditions are the same as those in Section 4.3.4.1.1, unless otherwise stated.

As the swelling pressure for expansive soils is generally considered as an isotropic value, both the GFC and the RFC can be used to describe the fracturing process. In this section, the GFC is used, as it is more computationally efficient. According to the experimental result in

(Wang et al. 2007), the fracture toughness of the used clay is between 7.10 and 31.43 kPa·m$^{0.5}$. Then, the fracture energy of the clay can be determined as

$$G_c = \frac{K_{IC}^2}{E'} \tag{4.120}$$

where K_{IC} is the fracture toughness and E' is Young's modulus under the plane strain condition.

Then, the fracture energy ranges from 0.14 J/m^2 to 2.70J/m^2. For simplicity, the fracture energy for the current bentonite material is assumed to be 1 J/m^2, as it has not yet been reported in previous studies. To realistically simulate the fracturing process in bentonite, more experimental studies on the fracturing energy need to be conducted in the future.

4.3.4.2.1 Effect of initial stress state

In this section, the simulated domain is subjected to constant stress on the outside boundaries. Three different isotropic initial stress states, i.e., 4.8MPa, 5.8MPa and 6.8MPa, are examined in terms of their effects on the fracturing behavior. Figure 4.36(a) presents the evolutions of gas pressure at the injection zone under the three initial stress states. For each case of the initial stress, the gas pressure mainly experiences two peaks and a series of fluctuations. As mentioned in Section 4.3.4.1.1, the first peak is associated with the failure of the injection zone, while the second one represents the value required to trigger the fracture propagation. The second peak value, in general, exceeds the sum of the initial stress and the initial porewater pressure by a certain value that corresponds to the fracture energy. As a larger amount of gas is required to trigger the fracturing process under higher initial stress, the length of the developed fracture at a specific moment is smaller than its counterpart under lower initial stress, see Figure 4.36(b). In addition, corresponding to the increase step, i.e., 1MPa, in the initial stress state, the first and the second peak value also have a similar increase step with their respective values in the adjacent evolution curve. In general, the three evolution curves are almost parallel to each other with a similar increase step during the whole period of gas injection. Therefore, this numerical result validates that the effect of the swelling pressure

(regarded as the initial stress in this paper) has been appropriately accounted for by using the modified strain tensor and the GFC.

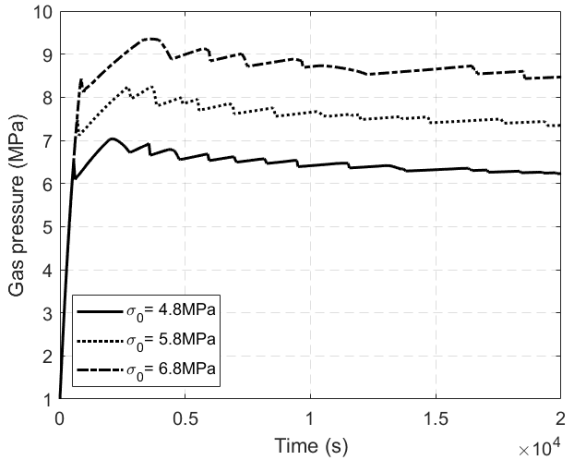

(a) Evolutions of gas pressure at the injection zone

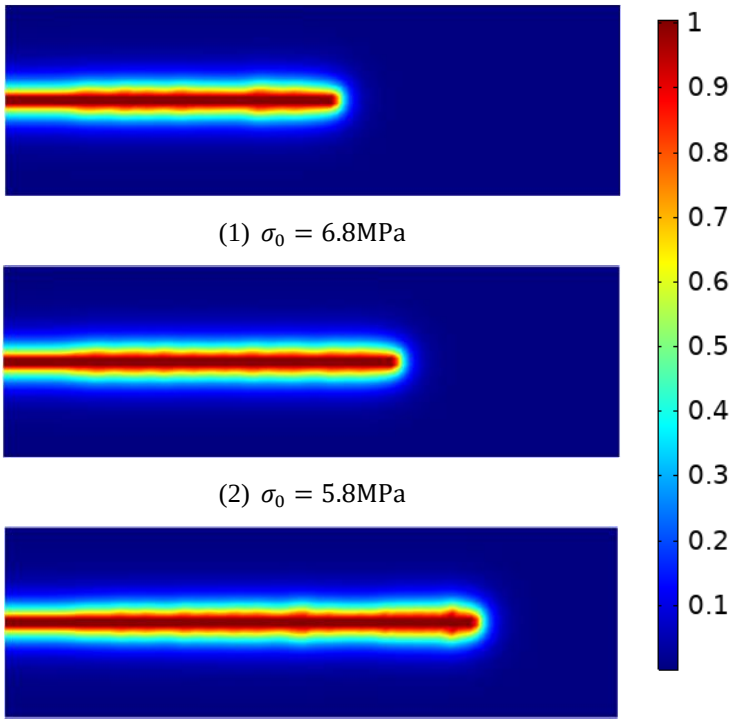

(1) $\sigma_0 = 6.8\text{MPa}$

(2) $\sigma_0 = 5.8\text{MPa}$

(3) $\sigma_0 = 4.8\text{MPa}$

(b) Profiles of phase field at time t=20000s

Figure 4.36 Evolutions of gas pressure and profiles of phase field under different initial stress states

4.3.4.2.2 Effect of boundary condition

In this section, the effect of boundary condition on the hydromechanical behaviors, including gas pressure, water pressure, total stress and boundary displacement, is examined.

To simulate different boundary stiffnesses, a spring-type boundary condition is added to the outside boundaries. As the domain expands outwards under high gas pressure, the spring-type boundary provides an additional compressive load to restrain the expansion tendency. The normal stiffness, k_n, of the spring varies from 0 GPa/m, 60 GPa/m, 120 GPa/m, 240 GPa/m, 480 GPa/m to +∞ GPa/m. Clearly, the normal stiffnesses, 0 GPa/m and +∞ GPa/m, represent the CSC and the CVC, respectively. The shear stiffness of the boundary is assumed to be zero in the current study. Here it is noted that the constant pressure on the outside boundaries is maintained to achieve the initial stress equilibrium. The initial stress of the domain is set as 5.8MPa.

Figure 4.37 (a) presents the evolutions of water pressure at a monitoring point A, as marked in Figure 4.30. A higher boundary stiffness leads to higher water pressure at the monitoring point, since the water under a more rigid boundary condition is compressed more significantly by the highly pressurized gas. This can be observed in Figure 4.37 (b) where the vertical displacement at the monitoring point decreases with the increase of boundary stiffness. Under the CVC, the dilation is totally prohibited on the boundary, see the red line in Figure 4.37 (b), which leads to high sensitivity of water pressure to the deformation within the simulated domain. As shown by the red line in Figure 4.37(a), the water pressure presents a rapid increase at the very beginning of gas injection. Similar to the evolution of water pressure, the total stress can reach a higher value under the boundary condition with larger stiffness, seen in Figure 4.37 (c). At the monitoring point A, the degree of saturation remains almost one during the period of gas injection (as will be discussed in the next subsection), and therefore, the porewater pressure fully contributes to the total stress. Then, Terzaghi's effective stress is recovered. By comparing Figure 4.37(a) and Figure 4.37(c), it can be found that the change of total stress mainly results from the change of water pressure, while the contribution of effective stress is less for any levels of boundary stiffness. This means that the deformation at the monitoring point is less even under boundary condition with lower stiffness. The dilation of the boundary under CSC mainly results from the opening of the developed fracture.

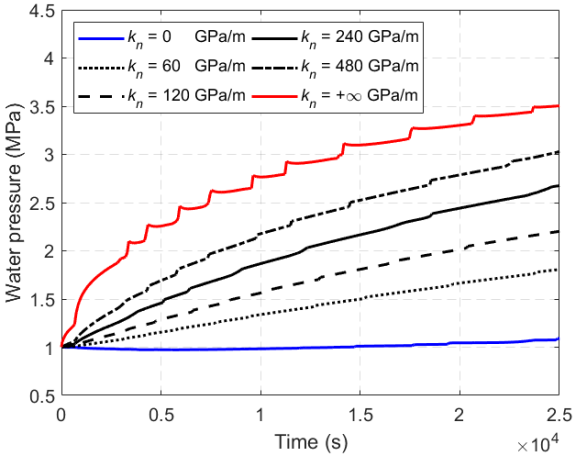

(a) Water pressure at monitoring point A

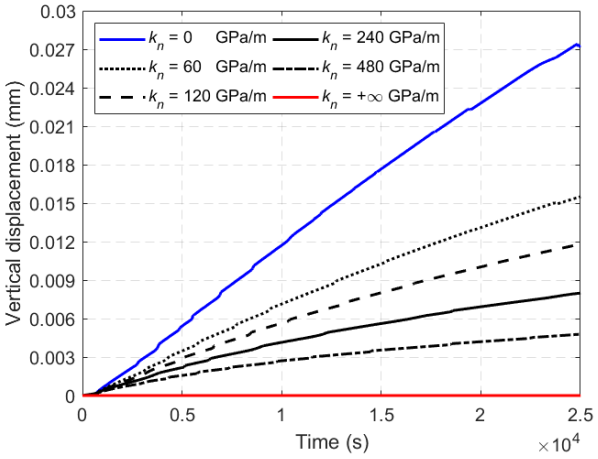

(b) Vertical displacement at monitoring point A

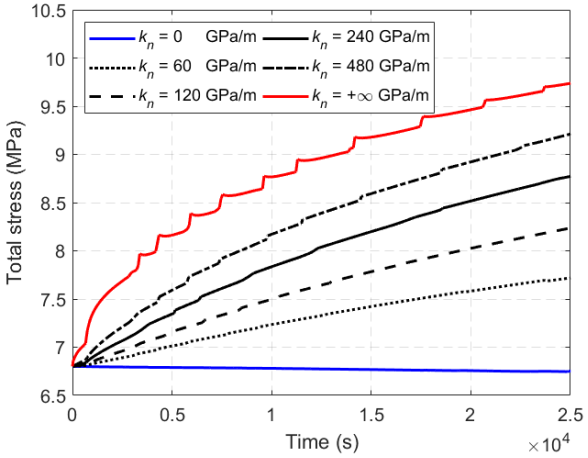

(c) Total stress at monitoring point A

Figure 4.37 Evolutions of water pressure, vertical displacement and total stress under different boundary conditions

Figure 4.38(a) shows the evolutions of gas pressure at the injection zone with different boundary stiffnesses.

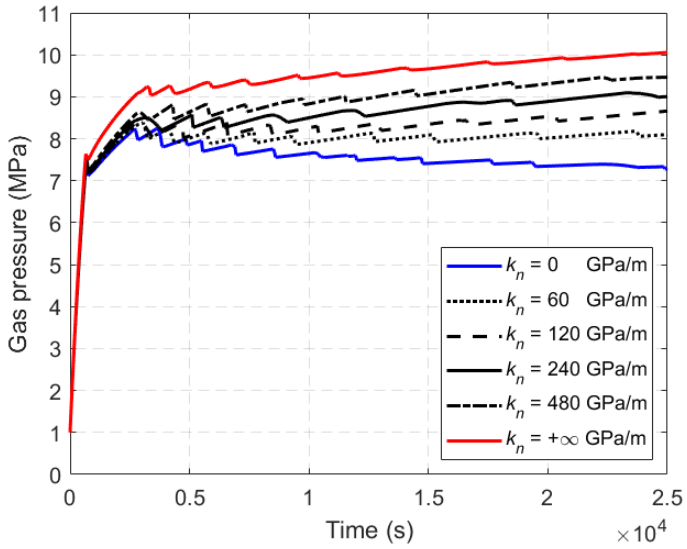

(a) Evolutions of gas pressure at the injection zone

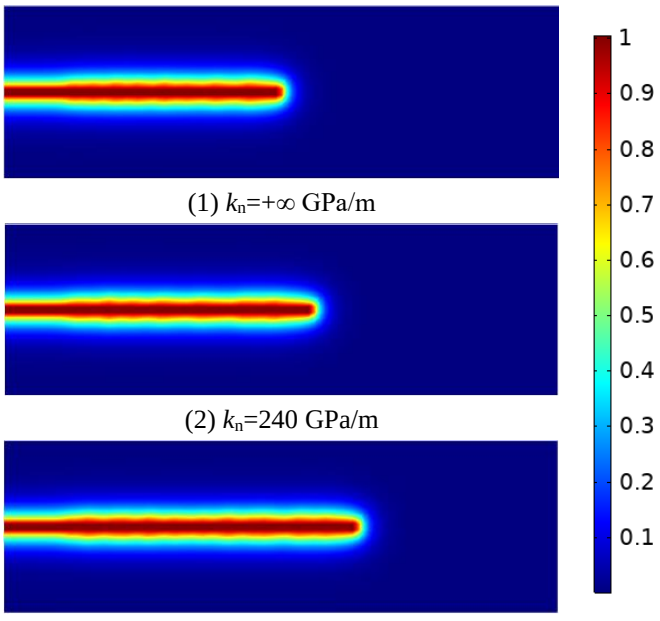

(b) Profiles of phase field at time t=20000s

Figure 4.38 Evolution of gas pressure and profiles of phase field under different boundary conditions

The gas pressure required to maintain the fracturing process is higher for the case of larger boundary stiffness. In specific, the gas pressure at the second peak under the CVC exceeds its counterpart under the CSC by almost 1MPa, see the red and blue lines in Figure 4.38 (a). This

difference essentially results from the restraint of the rigid boundary, as previously discussed. This is qualitatively consistent with the experimental finding in (Graham et al. 2012; Harrington and Horseman 2003) that shows the gas pressure for the breakthrough phenomenon is higher for the CVC than that for the CSC. In addition, after the second peak, the gas pressure under CVC experiences an increasing trend, while the pressure under CSC shows a decreasing trend. This is essentially caused by the different rates of fracture propagation controlled by the boundary stiffness. With the increase of the normal stiffness, the capability of the spring to restrain the dilation of the domain is enhanced. In other words, at a given dilation amount, the spring with larger normal stiffness provides a larger compressive load to the domain. Therefore, the fracture propagation is more difficult to take place under the boundary condition with higher stiffness. This is reflected in Figure 4.38(b) where the length of the developed fracture is smaller for the case of higher stiffness at a specific moment. As analyzed above, the fracture propagates more rapidly under the CSC, see Figure 4.38(b3), than that under the CVC, see Figure 4.38(b1). If the rate of fracture propagation is large enough to counteract the rate of gas injection, the gas pressure will present a decreasing trend, see the blue line in Figure 4.38 (a). Otherwise, the gas pressure experiences an increasing trend, see the red line in Figure 4.38 (a).

As analyzed above, the numerical results are qualitatively consistent with the experimental results as discussed in (Daniels and Harrington 2017; Graham et al. 2012; Harrington and Horseman 2003). Therefore, the proposed coupled HM-PF model can well describe the evolutions of the fluid pressure, the displacement and the total stress under different boundary conditions.

4.3.4.2.3 Hydromechanical behaviors under CVC

Previous experimental studies were mainly conducted under the CVC, since this boundary condition is close to the condition in the field. Therefore, the hydromechanical behaviors of the sample under the CVC will be analyzed in detail in this section.

Figure 4.39 presents the profiles of the degree of saturation and the distribution of gas pressure at time t=20000s. The profile of the degree of saturation is similar to that of the phase field, as compared between Figure 4.38 (b1) and Figure 4.39 (a). The degree of saturation in

the developed fracture is close to zero, while the remaining of the domain is almost fully saturated. This result is qualitatively consistent with the experimental finding that the sample can remain in an almost saturated state after the gas injection test (Graham et al. 2012; Harrington and Horseman 2003; Harrington et al. 2017b; Horseman et al. 1999).

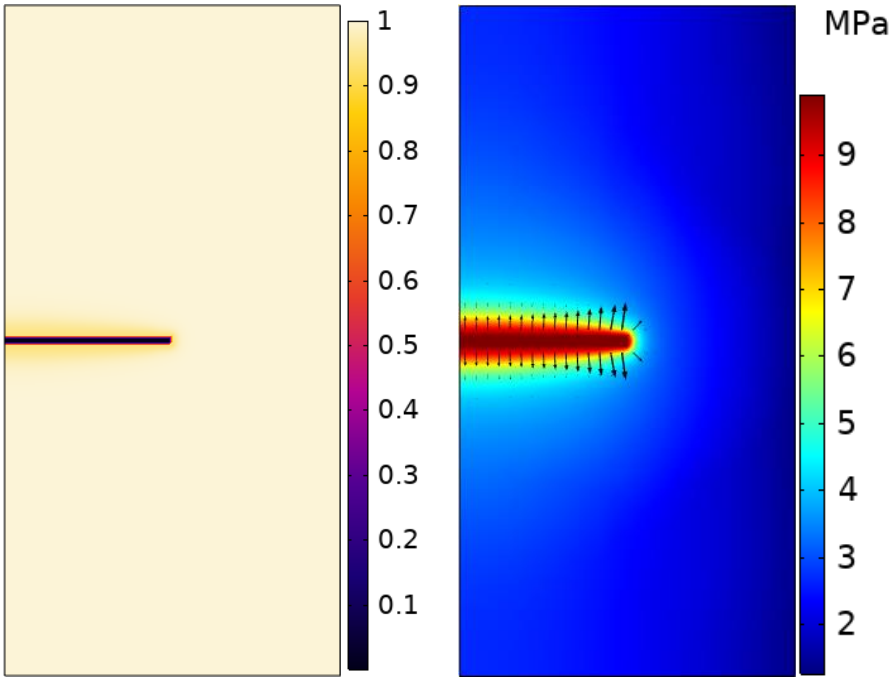

(a) Profile of degree of saturation (b) Distribution of gas pressure

Figure 4.39 Profiles of degree of saturation and distribution of gas pressure at time t=20000s (Note: Black arrows in the figure represent the gas flux. The length of the arrow is proportional to the magnitude of the flux)

Corresponding to the distribution of the degree of saturation, the high gas pressure is localized around the developed fracture, as seen in Figure 4.39(b). As the gas entry value in the intact porous media is very high, i.e., 18MPa, the area adjacent to the fracture is slightly desaturated, see Figure 4.39(a). According to the power law model, i.e., Eq. (4.119), the relative permeability of gas is very low when the effective degree of saturation is over 0.8, as seen in Figure 4.29. Therefore, the highly pressurized gas can hardly transport from the fracture to the surrounding porous matrix, thus leading to a preferential gas flow in the developed fracture. On the other hand, the primary gas transport within the simulated domain mainly occurs around the developed fracture, as shown by the black arrows in Figure 4.39(b), since the pressure gradient is larger there compared with other parts of the domain. In general, the

developed coupled HM model has qualitatively captured the preferential gas flow which is commonly observed in experiments (Graham et al. 2012; Harrington et al. 2017b; Harrington et al. 2019b).

Figure 4.40(a) presents the distribution of water pressure within the simulated domain at time t=20000s. The water pressure in the porous matrix at the two sides of the developed fracture has significantly built up. This is caused by the compressive load exerted by the highly pressurized gas. As the CVC does not allow any dilations, the porewater in the porous matrix is significantly compressed, thus leading to the increase in porewater pressure. As seen in Figure 4.40(a), the water pressure and the volumetric strain along the cut line A-B, as marked in Figure 4.30, are presented. At the center of the line where the fracture is located, the porous media is subjected to a significant tensile volumetric strain due to the high gas pressure, see the blue dashed line in Figure 4.40(b). As the distance to the fracture increases, the volumetric strain rapidly drops to a negative value (i.e., compressive strain), forming two minimum values besides the fracture. This means the porous matrix adjacent to the developed fracture has experienced a consolidation process during the fracturing period. This numerical result is consistent with the statement in (Graham et al. 2012; Harrington et al. 2017b) that the generation of microfractures can result in a localized consolidation. As the distance to the fracture further increases, the volumetric strain gradually increases, but it remains less than zero. Corresponding to the evolution of volumetric strain along the cut line A-B, the water pressure reaches a maximum value beside the developed fracture, and then gradually decreases with the increase of the distance to the fracture. This numerical result indicates that water pressure is closely associated with the volumetric strain. Due to the build-up of the water pressure along the developed fracture, the water flows out of the sample under the formed pressure gradient. However, it is worth noting that the sample, except for the fracture zone, is still in almost full saturation, as seen in Figure 4.39(a), due to the low intrinsic permeability and the high gas entry value in the porous matrix.

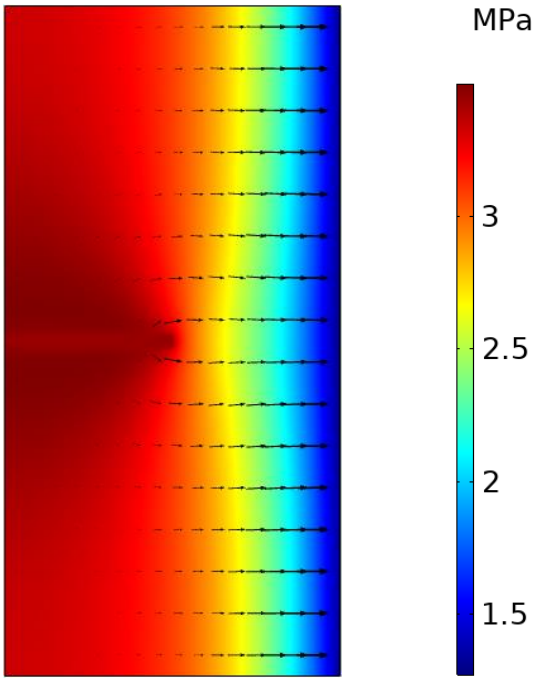

(a) Distribution of water pressure

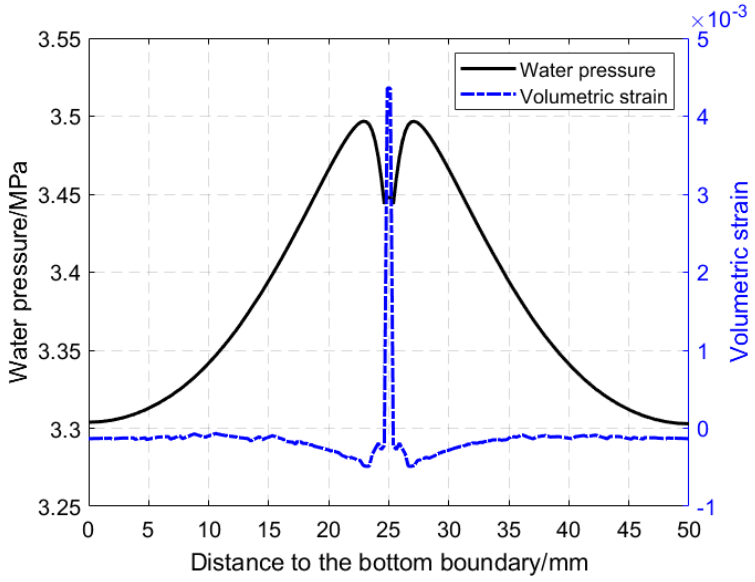

(b) Water pressure and volumetric strain along the cut line A-B

Figure 4.40 Distributions of water pressure and volumetric strain at time t=20000s

As analyzed above, some key experimental findings, such as the preferential gas flow, the build-up of porewater pressure, the almost fully saturated state after the gas injection test and the localized consolidation, have been qualitatively captured by the developed coupled HM-PF model.

4.3.5 Conclusions

A coupled HM-PF model is rigorously developed in this paper based on Coussy's thermodynamic theory for unsaturated soils and the microforce balance law. The possible contribution of interfaces between different phases to the fracturing process has been analytically accounted for in the proposed framework. However, due to the limited experimental studies, the effect of interfaces on the fracturing process has not been considered when simulating the gas-driven fracturing process in saturated bentonite.

The swelling pressure is an important factor controlling the gas entry into the saturated bentonite. In this paper, the swelling pressure is regarded as initial stress. A fictitious strain tensor is calculated from this initial stress tensor based on the linear elastic theory. A modified strain tensor, which is used to construct the phase field model, is obtained by adding the fictitious strain tensor to the strain tensor due to deformation. The validation simulations showed that the proposed HM-PF model can satisfactorily capture the effect of initial stress state on the fracturing process. Specifically, both the GFC and the RFC can be used to describe the fracturing under the isotropic initial stress state, while the RFC is more appropriate than the GFC to govern the fracturing process under the anisotropic initial stress state. In addition, the proposed coupled HM-PF model is able to qualitatively reproduce some of the experimental behaviors during gas migration in saturation bentonite. For example, the gas pressure required for triggering the fracturing process in bentonite should exceed the sum of the swelling pressure and the porewater pressure. Due to the strong constraint of the CVC, the gas pressure in the developed fracture, and the water pressure in the porous matrix are higher than those under the CSC. In addition, the preferential gas flow, the build-up of porewater pressure, the almost fully saturated state and the localized consolidation, have also been captured by the proposed model.

This paper mainly focuses on the thermodynamic consistency of the coupled HM-PF model and the effect of initial stress state on the fracturing process. The other commonly observed behaviors in experiments, such as the gas breakthrough phenomenon, the "shut-in" pressure and the fracture self-sealing process, have not yet been captured by the proposed model. Reproducing these experimentally observed behaviors may need more advanced permeability

model and mechanical model that can describe both the damaging and sealing process. These works may be left for future studies.

Chapter 5 Results Synthesis and Discussion

5.1 Introduction

In this thesis, two new coupled HM frameworks, i.e., one based on the double porosity (DP) concept and the other on the phase field (PF) method, are developed to simulate the key experimentally observed behaviors. For convenience, the DP-based framework is referred to as coupled HM-DP framework, whereas the PF-based framework is termed as coupled HM-PF framework. The coupled HM-DP framework has been used to simulate several laboratory tests, including Mx80-4 test, Mx80-8 test, Mx80-9 test, 1-D gas flow test and spherical gas flow test. In contrast, the coupled HM-PF framework has been adopted to conduct qualitative analysis for the fracture propagation process in saturated bentonite. The numerical results obtained from these two numerical frameworks are synthesized and discussed as follows. Based on the discussion, the original contributions of this Ph.D thesis are highlighted at the end of this chapter.

5.2 Numerical Results of the Coupled HM-DP Framework

Within the coupled HM-DP framework, a new coupled HM model is developed based on a double effective stress (DES) concept. This model is referred to as coupled HM-DES model. The MAC is governed by Bishop-type effective stress, whereas the MIC by Terzaghi's effective stress. It is noted here that the abbreviations, i.e., 'FC' and 'PC' used in Section 3.2 are replaced by 'MAC' and 'MIC' as used in Section 3.3 respectively in the following discussion for convenience. To account for the development of preferential pathways, a damage model is introduced into the HM-DP framework to describe the mechanical behavior of MAC, thus leading to a coupled HM-DAM model. In this damage-enhanced model, the Bishop-type effective stress is replaced by the independent stress state variables, i.e., net normal stress and suction, since the net normal stress can ease the tensile failure.

5.2.1 Evolutions of Gas Pressure and Gas Outflow Rate

The coupled HM-DES model performs well to simulate the evolutions of gas pressure and

gas outflow rate. In general, the simulated curves agree well with the experimental ones both qualitatively and quantitatively. The starting moment of gas outflow and the magnitude of outflow rate in Mx80-4 test have been accurately simulated. Moreover, the two gas breakthrough events as observed in experiments have been reproduced. In particular, the phenomenon that the second gas breakthrough is less significant than the first one is captured by the model. This may be attributed to the plastic strain of MIC that inhibits the complete closure of the developed fracture. The hysteretic model for relative permeability of gas contributes to simulating the "shut-in" pressure, since the relative permeability decreases more rapidly on the scanning curve when gas saturation decreases. On the other hand, this model is incapable of capturing the overshoot events observed in Mx80-9 test. The overshoot events may involve complex local HM behaviors that are hard to be described by the developed model.

The coupled HM-DAM model is more flexible to fit the evolution curve of gas pressure due to the introduction of a hysteretic model for intrinsic permeability. The hysteretic model reflects the effect of transient evolution of pore structure on the gas transport behavior. Through calibrating the hysteretic parameter, the possible enhancing or inhibiting effect due to transient changes in pore structure on the intrinsic permeability can be accounted for. In the 1-D gas flow simulation, the gas outflow rate is highly associated with the evolution of the damage field. It is found that the major gas outflow initiates until the damage field has connected with the outflow boundary. This numerical result is qualitatively consistent with the experimental finding in (Harrington et al. 2017b) that an effective flow network is required to be formed before a major gas outflow. Thus, the damage model is beneficial to describing the effect of preferential pathways to some extent. Nevertheless, the coupled HM-DAM is still unable to simulate the strong fluctuations in the evolution curves for gas pressure and gas outflow rate.

5.2.2 Evolutions of Water Pressure and Total Stress

In the coupled HM-DES model, the build-up of water pressure has been qualitatively captured. At low gas pressure, the gas cannot infiltrate the saturated bentonite and the porewater pressure almost remains at the initial value. When the gas pressure increases to a certain value that is close to the peak pressure, the porewater pressure experiences a rapid increase. The gas

pressure at which porewater pressure rapidly increases is associated with a critical porosity of the MAC that needs to be calibrated based on experimental data. It is found that the highest porewater pressure in the second gas injection cycle is less than that in the first cycle. This is consistent with the evolution of gas pressure in the two gas injection cycles. However, this simple method is not strong enough to account for the effect of preferential pathways.

In contrast, the coupled HM-DAM model has adopted a damage model to implicitly describe the development of preferential pathways. The numerical results showed that the significant increase of porewater pressure occurs when the damage just initiates on the injection boundary. This is qualitatively consistent with the experimental result. However, the simulated porewater pressure is much lower than its experimental counterpart. In the experiment, the location where the porewater pressure was monitored may be saturated. Once the discrete pathways develop within the bentonite, the infiltrated gas will immediately exert a compressive load on the location, thus leading to the sharp increase of porewater pressure. By contrast, the monitored location in the simulation cannot keep fully saturated as the developed fracture network is simulated in a smeared way. As a result, the compression-induced increase of porewater pressure may not be captured by the developed model.

The simulated total stress follows a similar evolution trend as the simulated gas pressure. Prior to the damage initiation, the simulated total stresses experience tiny increases. Once the damage occurs on the injection boundary, the total stresses increase dramatically. This numerical result can qualitatively reflect the corresponding experimental findings.

5.2.3 Evolution of Damage Field and Degree of Saturation

Due to the introduction of heterogeneity, the damage field preferentially propagates through the areas that are less resistant to flow and failure, while leaving the areas of high resistance at a much lower damaging level. The damaging process takes place prior to the gas breakthrough event, as an effective fracture network is required for triggering a major gas outflow. It is worth noting that the damage model cannot explicitly capture the discrete pathways even with the heterogeneity introduced. This is attributed to that the scale at which the heterogeneity plays a role is much larger than the scale where the fracturing process really

takes place.

The simulated degree of saturation can keep a very high value during the whole gas injection test. The major part of the simulated domain remains an almost saturated state. The significant desaturation process mainly occurs in the areas with lower gas entry value, while the degree of saturation in these areas can remain a high value. This numerical result reflects the experimental finding that the tested sample can remain an almost saturated state during the gas migration process. Essentially, the high degree of saturation during gas injection test is attributed to the differentiation of two types of pores in which the pores of the MIC can keep a fully saturated state during gas injection test.

5.2.4 Pore Transformation and Water Exchange

During the period of gas breakthrough, the dilation of the whole composite porous media (the superposition of MIC and MAC) and the consolidation of the MIC are successfully captured within the coupled HM-DP framework. Once the highly pressurized gas infiltrates the MAC, the total stress to which the composite porous media is subjected shows an increasing trend. As a result, the MIC is compressed and the porewater is squeezed out from the MIC. This will lead to the consolidation of the MIC. It is found that the contribution of consolidation of the MIC to the opening of the developed fractures (represented by volume change in the MAC) is highly dependent of the boundary condition. Under constant confining stress, the composite porous media can deform freely in both radial and axial directions when the highly pressurized gas migrates through the media. Thus, the total stress cannot reach a higher value. Moreover, the contribution of the consolidation of the MIC to the dilation of MAC (reflecting the opening of the developed fractures) is less significant than that of expansion of the whole porous media. In contrast, the opening of the developed fractures mainly results from the consolidation of the MIC under the constant volume condition, as the rigid boundary condition inhibits the expansion of whole porous media. This numerical result is consistent with the conclusions in (Harrington et al. 2017b; Hoch et al. 2004; Swift et al. 2001; Wiseall et al. 2015) that the opening of the preferential pathways is originated from compression of water, consolidation of clay matrix and dilation of the whole porous media. When a large amount of

gas flows out of the porous media, the gas pressure shows a dramatical decrease. As responses to that, the consolidated MIC partially recovers its original volume, whereas the MAC shrinks, both of which lead to the closure of the developed pathways.

5.2.5 Effects of Hysteresis of Permeability

A hysteretic model for relative permeability of gas is adopted in the coupled HM-DES model to describe the effect of gas entrapment on the gas flow behaviors. In the hysteretic model, once the gas saturation decreases from a reversal point, the relative permeability of gas drops more rapidly along a scanning curve than along the bounding drainage curve. Thus, for a given reduction of gas saturation, the relative permeability of gas can reach a lower value in the scanning curve. The numerical results showed that considering the hysteresis is beneficial to achieving the "shut-in" pressure and the less significant gas breakthrough in the second injection cycle.

In the coupled HM-DAM model, a hysteretic model for intrinsic permeability is proposed. The hysteresis of intrinsic permeability results from the damaging process and the evolution of equivalent tensile strain. After the cessation of gas injection, the intrinsic permeability may be enhanced or inhibited due to the transient evolution of the unstable pathways. Directly modelling the evolution of the unstable pathways is challenging, as it involves complex coupled HM behaviors at a local scale. The possible enhancing or inhibiting effect due to the unstable pathways is implicitly considered in the hysteretic model. Numerical results showed that considering the hysteresis of intrinsic permeability can make the developed model more flexible to reproduce the experimental results.

5.3 Numerical Results of the Coupled HM-PF Framework

5.3.1 Evolutions of Preferential Pathways and Degree of Saturation

The discrete feature of preferential pathways has been successfully captured by the coupled HM-PF model. In order to consider the heterogeneity of soil properties, a spatially autocorrelated random field is applied to construct the HM properties of bentonite, including intrinsic permeability, gas entry value, Young's modulus and tensile strength. It is found that

the fracture preferentially propagates through the areas that are less resistant to flow and fracturing. The gas pressure in the injection point is highly dependent of the fracturing rate. A rapid fracture growth is companied by a significant drop of gas pressure at the injection point.

Four factors, including the Gaussian random field, the coefficient of variation, the boundary condition and the gas injection rate, have been examined in terms of their influences on the fracture trajectory. In different Gaussian random fields, the fracture trajectory can be rather different from each other. Both the single fracture propagation and the fracture branching have been achieved in these random fields. The coefficient of variation plays a critical role in controlling the tortuosity of the developed fracture. With the increase of the coefficient of variation, the fluctuations in the HM properties become more significant, thus leading to a more tortuous fracture trajectory. The boundary condition influences both the fracture length and the fracture trajectory. With the increase of the boundary stiffness, the fracturing process is increasingly suppressed. Consequently, higher gas pressure is required for the fracture to propagate through the sample. Under a rigid boundary condition, the fracture branching is also suppressed, which may be associated with the build-up of total stress under rigid boundary condition. Gas injection rate directly controls the fracturing rate. Higher gas injection rate leads to a more rapid fracture propagation process.

As the gas entry value in the developed fracture is very low, the degree of saturation in the fracture is close to zero. By contrast, the remaining part of the domain where the gas entry value is very high, remains almost saturated. Thus, the profile of the zero degree of saturation coincides with the profile of phase field.

5.3.2 Evolutions of Fluid Pressure and Total Stress

Numerical results showed that the high gas pressure was highly localized in the developed fracture. It is found that the power law model for relative permeability is superior to the Mualem-van Genuchten model in terms of simulating the localized gas flow. The build-up of porewater pressure and the localized consolidation are numerically captured in the clay matrix surrounding the developed fracture. The boundary stiffness has significant influences on the evolutions of water pressure and total stress. When the boundary stiffness is zero, the sample

can expand freely. As a result, the porewater pressure and the total stress only experience slight changes. With the increase of boundary stiffness, changes in porewater pressure and total stress become more distinct. Under constant volume condition, the porewater within clay matrix is significantly compressed by the highly pressurized gas, thus leading to significant increases in both porewater pressure and total stress.

5.3.3 Effects of Initial Stress

Previous experimental studies showed that swelling pressure plays an important role in gas entry behavior. For saturated bentonite, the swelling pressure is equivalent to effective stress (Horseman et al. 1999). The effect of swelling pressure on the gas-driven fracturing has been considered in the PF model by using a modified strain tensor that is the sum of the strain tensor due to deformation and the strain tensor calculated from the initial effective stress. Numerical results showed that when the swelling pressure has increased by a certain value, the gas pressure at which the fracture starts to propagate will increase by an equivalent value. Therefore, the effect of swelling pressure on the gas-driven fracturing has been well considered in the developed coupled HM-PF framework.

5.4 Original Contributions of This Ph.D Thesis

The original contributions of this Ph.D thesis are listed as follows.

A new coupled HM framework that incorporates both double porosity concept and double effective stress concept has been developed to simulate the gas migration in saturated bentonite. The double effective stress concept is derived from a new theoretical approach based on the mixture theory and the first law of thermodynamics. Owing to the differentiation of two types of pores in saturated bentonite, the developed framework can concurrently capture the localized consolidation of clay matrix and the expansion of the whole porous media during the gas migration process.

The developed coupled HM-DP framework is enhanced by applying a damage model on the MAC to implicitly account for the development of preferential pathways. The damage-enhanced model is more capable of describing the key HM behaviors associated with the

development of preferential pathways. This extended model has captured the experimental finding that an effective microfracture network is a necessity to trigger a major gas outflow. Moreover, the experimental behavior that the significant increase of either total stress or porewater pressure occurs once the microfractures initiate in the sample is also qualitatively described by the developed model.

The hysteresis in relative permeability and in intrinsic permeability is incorporated into the coupled HM framework for the first time, to respectively account for the effects of gas entrapment and the evolution of unstable pathways on the gas migration in saturated bentonite. The consideration of the hysteresis makes the coupled HM framework more flexible to simulate the experimentally observed behaviors.

A coupled HM-PF framework for simulating the gas-driven fracturing in saturated bentonite is originally developed based on Coussy's thermodynamic theory for unsaturated porous media and microforce balance law. A stabilized technique is adopted in the framework to avoid the oscillation of pore pressure and enhance the computational efficiency. In addition, a new approach for considering the effect of swelling pressure (initial stress) on the fracturing process has been proposed by introducing a modified strain tensor in the phase field model. The heterogeneous distributions of HM properties have been introduced in the HM-PF framework to examine their effects on the fracture trajectory.

Chapter 6 Conclusions and Recommendations

6.1 Conclusions

Gas migration in saturated bentonite is accompanied by several key experimentally observed behaviors, such as gas breakthrough event, development of preferential pathways, build-up of water pressure and total stress, almost saturated state after gas injection test, water exchange between clay matrix and developed fractures, localized consolidation and self-sealing process. These behaviors involve complex couplings between the hydraulic process and the mechanical process. In this thesis, two coupled HM frameworks are developed, based on the thermodynamic theory and mixture theory, to simulate the gas migration in saturated bentonite as well as the accompanied HM behaviors.

The first coupled HM framework is based on the double porosity concept, leading to a so-called coupled HM-DP framework. The bentonite is assumed as a composite porous medium consisting of two subcontinua, i.e., MAC and MIC. The mechanical behavior of the MAC is controlled by either Bishop-type effective stress or independent stress states (net normal stress and suction), whereas the MIC is governed by the mean of Terzaghi's effective stress. This coupled HM framework can concurrently capture the expansion of the composite medium and the consolidation of the MIC, both of which induce the dilation of the MAC. Thus, this framework is beneficial to describing the dilation of the developed pathways under constant volume condition. To account for the effect of the development of preferential pathways on the gas flow behavior, a tensile-controlled damage model is incorporated into the framework. This damage-enhanced framework can well describe the coupled HM behaviors that are related to the development of preferential pathways. In this coupled HM framework, the hysteresis of either intrinsic or relative permeability has been considered. It was found that the hysteretic models can make the developed coupled HM model more flexible to simulate the experimental results. In general, the coupled HM framework based on the double porosity concept can well describe some key HM behaviors either quantitatively or qualitatively, including gas breakthrough phenomenon, build-up of the water pressure and total stress, consolidation of

clay matrix and almost saturated state of the tested sample.

In the coupled HM-PF framework, the phase field method is adopted to simulate the preferential pathways. This framework is developed based on Coussy's thermodynamic theory for unsaturated porous media and the microforce balance law. The phase field variable, ranging between 0 and 1, degrades both the mechanical stiffness and the hydraulic resistance to gas flow. The effect of swelling pressure on the gas flow behavior has been accounted for by introducing a modified strain tensor in the phase field model. It was found that the coupled HM-PF framework can explicitly simulate the discrete pathways and the localized gas flow. In addition, some other HM behaviors, such as the build-up of water pressure and total stress, the nearly saturated state during gas migration and the localized consolidation, can be qualitatively described. The possible heterogeneities in the HM properties have been examined in terms of their effects on the gas flow behavior and the fracturing process. It was found that the fracture preferentially propagates through the areas of low resistance to gas flow, leading to an arbitrary fracture propagation in the heterogeneous field.

6.2 Recommendations for Future Works

In response to the research gaps of the current research topic and the limitations of the models proposed in this thesis, recommendations for future works are made as follows.

The heterogeneity of swelling pressure needs to be considered in the coupled HM frameworks as proposed in this thesis. The swelling pressure prior to gas injection can be regarded as the initial effective stress to which the sample is subjected. In previous models, the initial stress state was assumed to distribute homogeneously in the bentonite sample. However, the swelling pressure may differ from place to place due to the heterogeneous distribution of dry density. As discussed previously, swelling pressure is a significant factor that controls the gas entry and breakthrough event. The highly pressurized gas should preferentially flow through the areas where swelling pressure is low. Thus, considering the heterogeneity of swelling pressure can enhance the capability of the coupled HM model to simulate the preferential gas flow.

A more advanced damage model that accounts for the effects of fracture size and fracture

orientation need to be developed to realistically simulate the development of microfracture network. Due to the heterogeneous distribution of stress state and HM properties, the size and orientation of the developed microfractures may vary significantly within the sample. The damage model as proposed in this thesis is rather simple to capture these features, since the scalar damage variable only predicts an isotropic damage field. An advanced damage tensor defined with respect to the aperture size and fracture orientation could be beneficial to reproducing the response of stress field to the gas migration process.

The coupled HM-PF framework needs to be further improved to quantitatively simulate the experimentally observed behaviors. The phase field model proposed in this thesis can only be used to do qualitative analysis for the gas migration process in bentonite. To quantitatively reproduce the HM behaviors, an advanced intrinsic permeability model that can properly account for the evolutions of fracture aperture and orientation needs to be developed. In addition, the fracturing process in saturated bentonite may be accompanied by plastic behavior or micro-fracturing process ahead of the fracture tip. Thus, plastic models or cohesive zone model can be incorporated into the phase field model to simulate the ductile fracture. Moreover, the capillary effect on both the fracturing process and mechanical properties needs to be further examined in future experimental and numerical studies.

Self-sealing process of the developed microfractures needs to be systematically studied in future. Self-sealing is a desirable ability of bentonite to serve as the barrier material for DGRs. The self-sealing process has been indirectly observed in previous experimental studies. Nevertheless, the fundamental mechanisms that may affect the self-sealing are still not clear. It may involve complex couplings between clay minerals, adsorbed water, capillary water and gas phase. Developing a reliable numerical model that can properly account for these couplings is critical to do a meaningful performance assessment for the buffer material.

The development of preferential pathways needs to be properly treated in numerical models. Previous experimental studies showed that the strong couplings between total stress, water pressure, gas pressure and gas outflow are closely associated with the development of preferential pathways. The orientation and aperture of the developed pathways control the

magnitude and direction of stress in the bentonite. As the developed pathways are highly unstable, they may evolve spatially and temporally during the gas transport process. In addition, it has been found that the developed pathways may not be utilized as conduits for gas flow in subsequent gas injection cycles. It can be seen that the development of preferential pathways significantly influences the HM behavior, and further affects the sealing ability of the buffer material. Current numerical models are still inadequate to capture these characteristics of the developed pathways. More advanced numerical models that can simulate the spatial and temporal evolutions of the developed pathways are necessary to be developed to evaluate the sealing ability of the bentonite.

An advanced coupled HM model that can account for multiscale effects needs to be developed to simulate the gas migration process. This research topic may involve several scales, including nanoscale, microscale, lab-scale and field scale. Specifically, the swelling behavior or self-sealing behavior is fundamentally governed by water adsorption at the nanoscale. The dilation of preferential pathways mainly occurs at the microscale. The gas breakthrough and responses of total stress and fluid pressure are observed at lab scale. The overall performance of the buffer material is associated with the HM processes at the field scale. Most of previous numerical models on this topic are phenomenologically based and therefore, incapable of capturing the multiscale effects. However, the performance of the buffer material fundamentally depends on the coupled HM processes at microscale or nanoscale. Therefore, an advanced and effective multiscale model is necessary to be developed to conduct a reliable performance assessment for the buffer material.

References

Abed, A.A., Laitinen, M., Lämsä, J., Harjupatana, T., Sołowski, W.T., and Kataja, M. 2016. Hydro-mechanical modelling of MX-80 bentonite: one dimensional study. In E3S Web of Conferences. EDP Sciences. p. 18005.

Achanta, S., Cushman, J.H., and Okos, M.R. 1994. On multicomponent, multiphase thermomechanics with interfaces, International Journal of Engineering Science 32(11): 1717-1738.

Alkan, H., and Muller, W. 2008. Approaches for modelling gas flow in clay formations as repository systems, Physics and Chemistry of the Earth 33: S260-S268.

Alonso, E.E., Olivella, S., and Arnedo, D. 2006. Mechanisms of gas transport in clay barriers, Journal of Iberian Geology 32(2).

Alonso, E.E., Vaunat, J., and Gens, A. 1999. Modelling the mechanical behaviour of expansive clays, Engineering Geology 54(1-2): 173-183.

Alonso, J., Navarro, V., and Calvo, B. 2012. Flow path development in different CO2 storage reservoir scenarios A critical state approach, Engineering Geology 127: 54-64.

Amarasiri, A.L., and Kodikara, J.K. 2011. Numerical modeling of desiccation cracking using the cohesive crack method, International Journal of Geomechanics 13(3): 213-221.

Amarisiri, A., Shannon, B., and Kodikara, J. 2013. Numerical modelling of desiccation cracking in a restrained ring test, Canadian Geotechnical Journal 51(1): 67-76.

Arnedo, D., Alonso, E.E., and Olivella, S. 2013. Gas flow in anisotropic claystone: Modelling triaxial experiments, International Journal for Numerical and Analytical Methods in Geomechanics 37(14): 2239-2256.

Arnedo, D., Alonso, E.E., Olivella, S., and Romero, E. 2008. Gas injection tests on sand/bentonite mixtures in the laboratory. Experimental results and numerical modelling, Physics and Chemistry of the Earth 33: S237-S247.

Bear, J. 1972. Dynamics of fluids in porous media. American Elsevier Pub. Co., New York.

Bennethum, L.S., Murad, M.A., and Cushman, J.H. 1997. Modified Darcy's law, Terzaghi's effective stress principle and Fick's law for swelling clay soils, Computers and Geotechnics 20(3-4): 245-266.

Börgesson, L., Johannesson, L., Sandén, T., and Hernelind, J. 1995. Modelling of the physical behaviour of water saturated clay barriers. Laboratory tests, material models and finite element application. Swedish Nuclear Fuel and Waste Management Co.

Borja, R.I. 2006. On the mechanical energy and effective stress in saturated and unsaturated porous continua, International Journal of Solids and Structures 43(6): 1764-1786.

Borja, R.I., and Koliji, A. 2009. On the effective stress in unsaturated porous continua with double porosity, Journal of the Mechanics and Physics of Solids 57(8): 1182-1193.

Bourdin, B., Francfort, G.A., and Marigo, J.J. 2000. Numerical experiments in revisited brittle fracture, Journal of the Mechanics and Physics of Solids 48(4): 797-826.

Brown, R.C. 1999. A multiple front propagation model for gas migration through clay, Engineering Geology 54(1-2): 151-158.

Cajuhi, T., Sanavia, L., and De Lorenzis, L. 2018. Phase-field modeling of fracture in variably

saturated porous media, Computational Mechanics 61(3): 299-318.
Carrier, B., and Granet, S. 2012. Numerical modeling of hydraulic fracture problem in permeable medium using cohesive zone model, Engineering Fracture Mechanics 79: 312-328.
Chapuis, R.P., and Aubertin, M. 2003. On the use of the Kozeny Carman equation to predict the hydraulic conductivity of soils, Canadian Geotechnical Journal 40(3): 616-628.
Chen, D., Pan, Z., Shi, J.-Q., Si, G., Ye, Z., and Zhang, J. 2016. A novel approach for modelling coal permeability during transition from elastic to post-failure state using a modified logistic growth function, International Journal of Coal Geology 163: 132-139.
Chiarelli, A.S., Shao, J.F., and Hoteit, N. 2003. Modeling of elastoplastic damage behavior of a claystone, International Journal of Plasticity 19(1): 23-45.
Choo, J., and Borja, R.I. 2015. Stabilized mixed finite elements for deformable porous media with double porosity, Computer Methods in Applied Mechanics and Engineering 293: 131-154.
Choo, J., and Sun, W. 2018a. Coupled phase-field and plasticity modeling of geological materials: From brittle fracture to ductile flow, Computer Methods in Applied Mechanics and Engineering 330: 1-32.
Choo, J., and Sun, W. 2018b. Cracking and damage from crystallization in pores: Coupled chemo-hydro-mechanics and phase-field modeling, Computer Methods in Applied Mechanics and Engineering 335: 347-379.
Choo, J., White, J.A., and Borja, R.I. 2016. Hydromechanical modeling of unsaturated flow in double porosity media, International Journal of Geomechanics 16(6): D4016002.
Conil, N., Djeran-Maigre, I., Cabrillac, R., and Su, K. 2004. Poroplastic damage model for claystones, Applied Clay Science 26(1-4): 473-487.
Coussy, O. 2004. Poromechanics. Wiley Online Library.
Coussy, O. 2007. Revisiting the constitutive equations of unsaturated porous solids using a Lagrangian saturation concept, International Journal for Numerical and Analytical Methods in Geomechanics 31(15): 1675-1694.
Cueto-Felgueroso, L., and Juanes, R. 2014. A phase-field model of two-phase Hele-Shaw flow, Journal of Fluid Mechanics 758: 522-552.
Cui, L., and Fall, M. 2015. A coupled thermo–hydro-mechanical–chemical model for underground cemented tailings backfill, Tunnelling and Underground Space Technology 50: 396-414.
Cui, Y.J., Tang, A.M., Loiseau, C., and Delage, P. 2008. Determining the unsaturated hydraulic conductivity of a compacted sand-bentonite mixture under constant-volume and free-swell conditions, Physics and Chemistry of the Earth 33: S462-S471.
Cuss, R., Harrington, J., Giot, R., and Auvray, C. 2014a. Experimental observations of mechanical dilation at the onset of gas flow in Callovo-Oxfordian claystone, Geological Society, London, Special Publications 400(1): 507-519.
Cuss, R., Harrington, J., Graham, C., Sathar, S., and Milodowski, A. 2012. Observations of heterogeneous pore pressure distributions in clay-rich materials, Mineralogical Magazine 76(8): 3115-3129.

Cuss, R.J., Harrington, J.F., Noy, D.J., Graham, C.C., and Sellin, P. 2014b. Evidence of localised gas propagation pathways in a field-scale bentonite engineered barrier system; results from three gas injection tests in the large scale gas injection test (Lasgit), Applied Clay Science 102: 81-92.

Cuss, R.J., Harrington, J.F., Noy, D.J., Wikman, A., and Sellin, P. 2011. Large scale gas injection test (Lasgit): Results from two gas injection tests, Physics and Chemistry of the Earth 36(17-18): 1729-1742.

Dagher, E., Nguyen, T., and Sedano, J.I. 2018. Development of a mathematical model for gas migration (two-phase flow) in natural and engineered barriers for radioactive waste disposal, Geological Society, London, Special Publications 482: SP482. 414.

Daniels, K.A., and Harrington, J. 2017. The response of compact bentonite during a 1-D gas flow test. British Geological Survey. OR/17/067.

de Borst, R., and Verhoosel, C.V. 2016. Gradient damage vs phase-field approaches for fracture: Similarities and differences, Computer Methods in Applied Mechanics and Engineering 312: 78-94.

De Lorenzis, L., McBride, A., and Reddy, B. 2016. Phase‐field modelling of fracture in single crystal plasticity, GAMM‐Mitteilungen 39(1): 7-34.

Delahaye, C.H., and Alonso, E.E. 2002. Soil heterogeneity and preferential paths for gas migration, Engineering Geology 64(2-3): 251-271.

Donohew, A.T., Horseman, S.T., and Harrington, J.F. 2000. Gas entry into unconfined clay pastes at water contents between the liquid and plastic limits, Environmental Mineralogy: Microbial Interactions Anthropogenic Influences, Contaminated Land and Waste Management 9: 369-394.

Doughty, C. 2007. Modeling geologic storage of carbon dioxide: comparison of non-hysteretic and hysteretic characteristic curves, Energy Conversion and Management 48(6): 1768-1781.

Ehlers, W., and Luo, C. 2017. A phase-field approach embedded in the Theory of Porous Media for the description of dynamic hydraulic fracturing, Computer Methods in Applied Mechanics and Engineering 315: 348-368.

Elsworth, D., and Bai, M. 1992. Flow-Deformation Response of Dual-Porosity Media, Journal of Geotechnical Engineering-Asce 118(1): 107-124.

Espinoza, D.N., and Santamarina, J.C. 2012. Clay interaction with liquid and supercritical CO_2: The relevance of electrical and capillary forces, International Journal of Greenhouse Gas Control 10: 351-362.

Fall, M., and Nasir, O. 2012. Numerical Modelling of Gas Migration from a DGR in Ontario's Sedimentary Rocks. University of Ottawa.

Fall, M., Nasir, O., and Nguyen, T.S. 2014. A coupled hydro-mechanical model for simulation of gas migration in host sedimentary rocks for nuclear waste repositories, Engineering Geology 176: 24-44.

Francfort, G.A., and Marigo, J.-J. 1998. Revisiting brittle fracture as an energy minimization problem, Journal of the Mechanics and Physics of Solids 46(8): 1319-1342.

Fredlund, D.G., Rahardjo, H., and Fredlund, M.D. 2012. Unsaturated soil mechanics in

engineering practice. Wiley.
Freiesleben, H. 2013. Final disposal of radioactive waste. In EPJ Web of Conferences. EDP Sciences. p. 01006.
Garcia, M., Beattie, T., and Schumacher, S. 2020. EURAD− the European Joint Programme for research on radioactive waste management between EU members states national programmes, EPJ Nuclear Sciences & Technologies 6: 21.
Gasch, T., Malm, R., and Ansell, A. 2016. A coupled hygro-thermo-mechanical model for concrete subjected to variable environmental conditions, International Journal of Solids and Structures 91: 143-156.
Gens, A. 2010. Soil–environment interactions in geotechnical engineering, Géotechnique 60(1): 3-74.
Gens, A., and Alonso, E.E. 1992. A framework for the behavior of unsaturated expansive clays, Canadian Geotechnical Journal 29(6): 1013-1032.
Gerard, P., Harrington, J., Charlier, R., and Collin, F. 2014. Modelling of localised gas preferential pathways in claystone, International Journal of Rock Mechanics and Mining Sciences 67: 104-114.
Gerard, P., Radu, J.-P., Talandier, J., De La Vaissière, R., Charlier, R., and Collin, F. 2010. Numerical modelling of the resaturation of swelling clay with gas injection, Unsaturated Soils: 1383-1388.
Gonzalez-Blanco, L., Romero, E., Jommi, C., Li, X., and Sillen, X. 2016. Gas migration in a Cenozoic clay: Experimental results and numerical modelling, Geomechanics for Energy and the Environment 6: 81-100.
Graham, C.C., Harrington, J.F., Cuss, R.J., and Sellin, P. 2012. Gas migration experiments in bentonite: implications for numerical modelling, Mineralogical Magazine 76(8): 3279-3292.
Graham, C.C., Harrington, J.F., and Sellin, P. 2016. Gas migration in pre-compacted bentonite under elevated pore-water pressure conditions, Applied Clay Science 132-133: 353-365.
Graham, J., Halayko, K.G., Hume, H., Kirkham, T., Gray, M., and Oscarson, D. 2002. A capillarity-advective model for gas break-through in clays, Engineering Geology 64(2-3): 273-286.
Gui, Y., Hu, W., Zhao, Z., and Zhu, X. 2017. Numerical modelling of a field soil desiccation test using a cohesive fracture model with Voronoi tessellations, Acta Geotechnica: 1-16.
Gui, Y., Zhao, Z., Kodikara, J., Bui, H.H., and Yang, S. 2016. Numerical modelling of laboratory soil desiccation cracking using UDEC with a mix-mode cohesive fracture model, Engineering Geology 202: 14-23.
Guo, G., and Fall, M. 2018. Modelling of dilatancy-controlled gas flow in saturated bentonite with double porosity and double effective stress concepts, Engineering Geology 243: 253-271.
Guo, G., and Fall, M. 2019. Modelling of preferential gas flow in heterogeneous and saturated bentonite based on phase field method, Computers and Geotechnics 116: 103206.
Gurtin, M.E. 1996. Generalized Ginzburg-Landau and Cahn-Hilliard equations based on a

microforce balance, Physica D: Nonlinear Phenomena 92(3): 178-192.
Gurtin, M.E., Fried, E., and Anand, L. 2010. The mechanics and thermodynamics of continua. Cambridge University Press.
Gutiérrez-Rodrigo, V., Villar, M.V., Martín, P.L., Romero, F.J., and Barcala, J.M. 2015. Gas-breakthrough pressure of FEBEX bentonite, Geological Society, London, Special Publications 415(1): 47-57.
Harrington, J., and Horseman, S. 2003. Gas migration in KBS-3 buffer bentonite. Sensitivity of test parameters to experimental boundary conditions. Swedish Nuclear Fuel and Waste Management Co.
Harrington, J., Milodowski, A., Graham, C., Rushton, J., and Cuss, R. 2012. Evidence for gas-induced pathways in clay using a nanoparticle injection technique, Mineralogical Magazine 76(8): 3327-3336.
Harrington, J., Tamayo-Mas, E., Shao, H., Dagher, E.E., Lee, J., Kim, K., Lai, S.H., Chittenden, N., Wang, Y., P. Damians, I., and Olivella, S. 2019a. Modelling advective gas flow in a compact clay: Application and assessment of different numerical approaches. In 6th EAGE Shale Workshop, Bordeaux, France.
Harrington, J.F., Cuss, R.J., and Talandier, J. 2017a. Gas transport properties through intact and fractured Callovo-Oxfordian mudstones, Geological Society, London, Special Publications 454: SP454. 457.
Harrington, J.F., Graham, C.C., Cuss, R.J., and Norris, S. 2017b. Gas network development in a precompacted bentonite experiment: Evidence of generation and evolution, Applied Clay Science 147: 80-89.
Harrington, J.F., Graham, C.C., Cuss, R.J., and Norris, S. 2019b. Gas network development in compact bentonite: key controls on the stability of flow pathways, Geofluids 2019: 3815095.
Hoch, A.R., Cliffe, K.A., Swift, B.T., and Rodwell, W.R. 2004. Modelling gas migration in compacted bentonite. POSIVA OY.
Horseman, S.T., Harrington, J.F., and Sellin, P. 1997. Gas migration in MX80 buffer bentonite, Scientific Basis for Nuclear Waste Management Xx 465: 1003-1010.
Horseman, S.T., Harrington, J.F., and Sellin, P. 1999. Gas migration in clay barriers, Engineering Geology 54(1-2): 139-149.
Houlsby, G. 1997. The work input to an unsaturated granular material, Géotechnique 47(1): 193-196.
Hu, R., Chen, Y., and Zhou, C. 2011. Modeling of coupled deformation, water flow and gas transport in soil slopes subjected to rain infiltration, Science China Technological Sciences 54(10): 2561.
Hu, R., Chen, Y.F., Liu, H.H., and Zhou, C.B. 2016. A coupled two‐phase fluid flow and elastoplastic deformation model for unsaturated soils: theory, implementation, and application, International Journal for Numerical and Analytical Methods in Geomechanics 40(7): 1023-1058.
IAEA. 2019. Options for management of spent fuel and radioactive waste for countries developing new nuclear power programmes. IAEA.

Jain, A.K., and Juanes, R. 2009. Preferential mode of gas invasion in sediments: Grain‐scale mechanistic model of coupled multiphase fluid flow and sediment mechanics, Journal of Geophysical Research: Solid Earth 114(B8).

Jove-Colon, C.F. 2013. Disposal systems evaluations and tool development-Engineered Barrier System (EBS) evaluation. Sandia National Laboratories (SNL-NM), Albuquerque, NM (United States).

Juanes, R., Spiteri, E., Orr, F., and Blunt, M. 2006. Impact of relative permeability hysteresis on geological CO_2 storage, Water Resources Research 42(12).

Khalili, N. 2008. Two-phase fluid flow through fractured porous media with deformable matrix, Water Resources Research 44.

Khalili, N., Geiser, F., and Blight, G. 2004. Effective stress in unsaturated soils: review with new evidence, International Journal of Geomechanics 4(2): 115-126.

Killough, J. 1976. Reservoir simulation with history-dependent saturation functions, Society of Petroleum Engineers Journal 16(01): 37-48.

Kodikara, J., and Costa, S. 2013. Desiccation cracking in clayey soils: Mechanisms and modelling, Multiphysical Testing of Soils and Shales: 21-32.

Kosugi, K.i. 1994. Three‐parameter lognormal distribution model for soil water retention, Water Resources Research 30(4): 891-901.

Kosugi, K.i. 1996. Lognormal distribution model for unsaturated soil hydraulic properties, Water Resources Research 32(9): 2697-2703.

Kumar, S., Zielonka, M., Searles, K., and Dasari, G. 2017. Modeling of hydraulic fracturing in ultra-low permeability formations: The role of pore fluid cavitation, Engineering Fracture Mechanics 184: 227-240.

Land, C.S. 1968. Calculation of imbibition relative permeability for two-and three-phase flow from rock properties, Society of Petroleum Engineers Journal 8(02): 149-156.

Laplace, P.S. 1805. Traité de mécanique céleste: Tome quatrième. Courcier.

Lee, S., Mikelic, A., Wheeler, M., and Wick, T. 2017. Phase-field modeling of two-phase fluid-filled fractures in a poroelastic medium, submitted for publication.

Lee, S., Min, B., and Wheeler, M.F. 2018. Optimal design of hydraulic fracturing in porous media using the phase field fracture model coupled with genetic algorithm, Computational Geosciences: 1-17.

Lenhard, R., and Parker, J. 1987. A model for hysteretic constitutive relations governing multiphase flow: 2. Permeability‐saturation relations, Water Resources Research 23(12): 2197-2206.

Levasseur, S., Charlier, R., Frieg, B., and Collin, F. 2010. Hydro-mechanical modelling of the excavation damaged zone around an underground excavation at Mont Terri Rock Laboratory, International Journal of Rock Mechanics and Mining Sciences 47(3): 414-425.

Li, D.-Q., Jiang, S.-H., Cao, Z.-J., Zhou, W., Zhou, C.-B., and Zhang, L.-M. 2015. A multiple response-surface method for slope reliability analysis considering spatial variability of soil properties, Engineering Geology 187: 60-72.

Li, J., Yin, Z.-Y., Cui, Y., and Hicher, P.-Y. 2016. Work input analysis for soils with double

porosity and application to the hydromechanical modeling of unsaturated expansive clays, Canadian Geotechnical Journal 54(2): 173-187.

Li, W., and Wei, C. 2018. Stabilized low‐order finite elements for strongly coupled poromechanical problems, International Journal for Numerical Methods in Engineering 115(5): 531-548.

Liu, J.-F., Song, Y., Skoczylas, F., and Liu, J. 2016. Gas migration through water-saturated bentonite–sand mixtures, COx argillite, and their interfaces, Canadian Geotechnical Journal 53(1): 60-71.

Liu, J.F., Skoczylas, F., and Talandier, J. 2015. Gas permeability of a compacted bentonite-sand mixture: coupled effects of water content, dry density, and confining pressure, Canadian Geotechnical Journal 52(8): 1159-1167.

Luckner, L., van Genuchten, M.T., and Nielsen, D.R. 1989. A consistent set of parametric models for the two-phase flow of immiscible fluids in the subsurface, Water Resources Research 25(10): 2187-2193.

Mahjoub, M., Rouabhi, A., Tijani, M., Granet, S., M'jahad, S., and Talandier, J. 2017. Numerical study of Callovo-Oxfordian argillite expansion due to gas injection, International Journal of Geomechanics 18(1): 04017134.

Marschall, P., Horseman, S., and Gimmi, T. 2005. Characterisation of gas transport properties of the Opalinus Clay, a potential host rock formation for radioactive waste disposal, Oil & gas science and technology 60(1): 121-139.

Mašín, D. 2013. Double structure hydromechanical coupling formalism and a model for unsaturated expansive clays, Engineering Geology 165: 73-88.

Mauthe, S., and Miehe, C. 2017. Hydraulic fracture in poro-hydro-elastic media, Mechanics Research Communications 80: 69-83.

Mazars, J. 1986. A description of micro-and macroscale damage of concrete structures, Engineering Fracture Mechanics 25(5-6): 729-737.

Metcalfe, R., Watson, S., Rees, J., Humphreys, P., and King, F. 2008. Gas generation and migration from a deep geological repository for radioactive waste. A review of Nirex/NDA's work.

Miehe, C., Hofacker, M., and Welschinger, F. 2010a. A phase field model for rate-independent crack propagation: Robust algorithmic implementation based on operator splits, Computer Methods in Applied Mechanics and Engineering 199(45-48): 2765-2778.

Miehe, C., and Mauthe, S. 2016. Phase field modeling of fracture in multi-physics problems. Part III. Crack driving forces in hydro-poro-elasticity and hydraulic fracturing of fluid-saturated porous media, Computer Methods in Applied Mechanics and Engineering 304: 619-655.

Miehe, C., Mauthe, S., and Teichtmeister, S. 2015a. Minimization principles for the coupled problem of Darcy–Biot-type fluid transport in porous media linked to phase field modeling of fracture, Journal of the Mechanics and Physics of Solids 82(Supplement C): 186-217.

Miehe, C., Schänzel, L.-M., and Ulmer, H. 2015b. Phase field modeling of fracture in multi-physics problems. Part I. Balance of crack surface and failure criteria for brittle crack

propagation in thermo-elastic solids, Computer Methods in Applied Mechanics and Engineering 294: 449-485.

Miehe, C., Welschinger, F., and Hofacker, M. 2010b. Thermodynamically consistent phase‐field models of fracture: Variational principles and multi‐field FE implementations, International Journal for Numerical Methods in Engineering 83(10): 1273-1311.

Miller, W., Alexander, R., Chapman, N., McKinley, J.C., and Smellie, J. 2000. Geological disposal of radioactive wastes and natural analogues. Elsevier.

Mobasher, M.E., Berger-Vergiat, L., and Waisman, H. 2017. Non-local formulation for transport and damage in porous media, Computer Methods in Applied Mechanics and Engineering 324: 654-688.

Mobasher, M.E., Waisman, H., and Berger-Vergiat, L. 2018. Thermodynamic framework for non-local transport-damage modeling of fluid driven fracture in porous media, International Journal of Rock Mechanics and Mining Sciences 111: 64-83.

Mohammadnejad, T., and Khoei, A. 2013a. An extended finite element method for hydraulic fracture propagation in deformable porous media with the cohesive crack model, Finite Elements in Analysis and Design 73: 77-95.

Mohammadnejad, T., and Khoei, A. 2013b. Hydro‐mechanical modeling of cohesive crack propagation in multiphase porous media using the extended finite element method, International Journal for Numerical and Analytical Methods in Geomechanics 37(10): 1247-1279.

Monroy, R., Zdravkovic, L., and Ridley, A. 2010. Evolution of microstructure in compacted London Clay during wetting and loading, Géotechnique 60(2): 105-119.

Mualem, Y. 1976. A new model for predicting the hydraulic conductivity of unsaturated porous media, Water Resources Research 12(3).

Mualem, Y. 1978. Hydraulic conductivity of unsaturated porous media: generalized macroscopic approach, Water Resources Research 14(2): 325-334.

Müller, S., and Schüler, L. 2019. GeoStat-Framework/GSTools: Reverberating Red.

Na, S., and Sun, W. 2018. Computational thermomechanics of crystalline rock, Part I: A combined multi-phase-field/crystal plasticity approach for single crystal simulations, Computer Methods in Applied Mechanics and Engineering 338: 657-691.

Nagra. 2008. Effects of post-disposal gas generation in a repository for low- and intermediate-level waste sited in the Opalinus Clay of Northern Switzerland. National Cooperative for the Disposal of Radioactive Waste.

Nair, R., Abousleiman, Y., and Zaman, M. 2005. Modeling fully coupled oil–gas flow in a dual-porosity medium, International Journal of Geomechanics 5(4): 326-338.

Nash, P., Swift, B., Goodfield, M., and Rodwell, W. 1998. Modelling gas migration in compacted bentonite, Posiva Report: 98-08.

Navarro, V., Asensio, L., De la Morena, G., Pintado, X., and Yustres, Á. 2015. Differentiated intra- and inter-aggregate water content models of Mx-80 bentonite, Applied Clay Science 118(Supplement C): 325-336.

Nguyen, T., and Le, A. 2014. Simultaneous gas and water flow in a damage-susceptible bedded argillaceous rock, Canadian Geotechnical Journal 52(1): 18-32.

Nguyen, T.T., Yvonnet, J., Zhu, Q.Z., Bornert, M., and Chateau, C. 2016. A phase-field method for computational modeling of interfacial damage interacting with crack propagation in realistic microstructures obtained by microtomography, Computer Methods in Applied Mechanics and Engineering 312: 567-595.

Nguyen, V.P., Lian, H., Rabczuk, T., and Bordas, S. 2017. Modelling hydraulic fractures in porous media using flow cohesive interface elements, Engineering Geology 225(Supplement C): 68-82.

Nuth, M., and Laloui, L. 2008. Effective stress concept in unsaturated soils: Clarification and validation of a unified framework, International Journal for Numerical and Analytical Methods in Geomechanics 32(7): 771-801.

Olivella, S., and Alonso, E.E. 2008. Gas flow through clay barriers, Géotechnique 58(3): 157-176.

Parisio, F., and Laloui, L. 2017. Plastic-damage modeling of saturated quasi-brittle shales, International Journal of Rock Mechanics and Mining Sciences 93: 295-306.

Parisio, F., Samat, S., and Laloui, L. 2015. Constitutive analysis of shale: a coupled damage plasticity approach, International Journal of Solids and Structures 75-76: 88-98.

Parker, J., and Lenhard, R. 1987. A model for hysteretic constitutive relations governing multiphase flow: 1. Saturation‐pressure relations, Water Resources Research 23(12): 2187-2196.

Pusch, R. 1980. Permeability of highly compacted bentonite. Swedish Nuclear Fuel Supply Company.

Pusch, R., and Forsberg, T. 1983. Gas migration through bentonite clay. Svensk Kaernbraenslefoersoerjning AB.

Pusch, R., and Hökmark, H. 1990. Basic model of water-and gas-flow through smectite clay buffers, Engineering Geology 28(3-4): 379-389.

Pusch, R., Hökmark, H., and Börgesson, L. 1987. Outline of models of water and gas flow through smectite clay buffers. Swedish Nuclear Fuel and Waste Management Co.

Pusch, R., Ranhagen, L., Nilsson, K., and Geological, S. 1985. Gas migration through Mx-80 bentonite. Final report. NAGRA Technical Report 85-36.

Qi, S., and Vanapalli, S.K. 2016. Influence of swelling behavior on the stability of an infinite unsaturated expansive soil slope, Computers and Geotechnics 76: 154-169.

Qi, S., and Vanapalli, S.K. 2018. Simulating hydraulic and mechanical responses of unsaturated expansive soil slope to rainfall: Case Study, International Journal of Geomechanics 18(6): 05018002.

Qiao, Y., Xiao, Y., Laloui, L., Ding, W., and He, M. 2019. A double-structure hydromechanical constitutive model for compacted bentonite, Computers and Geotechnics 115: 103173.

Rodwell, W. 2005. Summary of a GAMBIT Club Workshop on gas migration in bentonite. A Report produced for the GAMBIT Club. Swedish Nuclear Fuel and Waste Management Co.

Rodwell, W.R., Harris, A.W., Horseman, S.T., Lalieux, P., Muller, W., Amaya, L.O., and Pruess, K. 1999. Gas migration and two-phase flow through engineered and geological barriers for a deep repository for radioactive waste. Nuclear Energy Agency.

Rutqvist, J., Borgesson, L., Chijimatsu, M., Kobayashi, A., Jing, L., Nguyen, T.S., Noorishad, J., and Tsang, C.F. 2001. Thermohydromechanics of partially saturated geological media: governing equations and formulation of four finite element models, International Journal of Rock Mechanics and Mining Sciences 38(1): 105-127.

Rutqvist, J., Kim, K., Xu, H., Guglielmi, Y., and Birkholzer, J. 2018. Investigation of coupled processes in Argillite Rock: FY18 Progress. Lawrence Berkeley National Lab.(LBNL), Berkeley, CA (United States).

Rutqvist, J., and Stephansson, O. 2003. The role of hydromechanical coupling in fractured rock engineering, Hydrogeology Journal 11(1): 7-40.

Salimzadeh, S., and Khalili, N. 2015a. Fully coupled XFEM model for flow and deformation in fractured porous media with explicit fracture flow, International Journal of Geomechanics 16(4): 04015091.

Salimzadeh, S., and Khalili, N. 2015b. Three-dimensional numerical model for double-porosity media with two miscible fluids including geomechanical response, International Journal of Geomechanics 16(3): 04015065.

Salimzadeh, S., and Khalili, N. 2015c. A three-phase XFEM model for hydraulic fracturing with cohesive crack propagation, Computers and Geotechnics 69: 82-92.

Sanchez, M., Gens, A., Guimaraes, L.D., and Olivella, S. 2005. A double structure generalized plasticity model for expansive materials, International Journal for Numerical and Analytical Methods in Geomechanics 29(8): 751-787.

Sánchez, M., Gens, A., Villar, M.V., and Olivella, S. 2016. Fully coupled thermo-hydro-mechanical double-porosity formulation for unsaturated soils, International Journal of Geomechanics 16(6): D4016015.

Sanchez, M., Manzoli, O.L., and Guimaraes, L.J.N. 2014. Modeling 3-D desiccation soil crack networks using a mesh fragmentation technique, Computers and Geotechnics 62: 27-39.

Santillán, D., Juanes, R., and Cueto‐Felgueroso, L. 2017a. Phase field model of fluid‐driven fracture in elastic media: Immersed‐fracture formulation and validation with analytical solutions, Journal of Geophysical Research: Solid Earth 122(4): 2565-2589.

Santillán, D., Juanes, R., and Cueto‐Felgueroso, L. 2018. Phase‐field model of hydraulic fracturing in poroelastic media: fracture propagation, arrest and branching under fluid injection and extraction, Journal of Geophysical Research: Solid Earth 123: 2127–2155.

Santillán, D., Mosquera, J.-C., and Cueto-Felgueroso, L. 2017b. Fluid-driven fracture propagation in heterogeneous media: Probability distributions of fracture trajectories, Physical Review E 96(5): 053002.

Seiphoori, A., Ferrari, A., and Laloui, L. 2014. Water retention behaviour and microstructural evolution of MX-80 bentonite during wetting and drying cycles, Géotechnique 64(9): 721-734.

Selvadurai, A., and Głowacki, A. 2008. Permeability hysterisis of limestone during isotropic compression, Groundwater 46(1): 113-119.

Shehata, A. 2015. Engineering Properties, Micro-and Nano-Structure of Bentonite-Sand Barrier Materials in Aggressive Environments of Deep Geological Repository for

Nuclear Wastes. Université d'Ottawa/University of Ottawa.

Shin, H., and Santamarina, J. 2011. Desiccation cracks in saturated fine-grained soils: particle-level phenomena and effective-stress analysis, Géotechnique 61(11): 961.

SKB. 2011. Environmental Impact Statement: Interim storage, encapsulation and final disposal of spent nuclear fuel. Svensk Kärnbränslehantering AB.

Song, X., Ye, M., and Wang, K. 2017. Strain localization in a solid‐water‐air system with random heterogeneity via stabilized mixed finite elements, International Journal for Numerical Methods in Engineering 112(13): 1926-1950.

Spiteri, E.J., and Juanes, R. 2006. Impact of relative permeability hysteresis on the numerical simulation of WAG injection, Journal of Petroleum Science and Engineering 50(2): 115-139.

Spiteri, E.J., Juanes, R., Blunt, M.J., and Orr, F.M. 2008. A new model of trapping and relative permeability hysteresis for all wettability characteristics, SPE journal 13(03): 277-288.

Sun, W., Ostien, J.T., and Salinger, A.G. 2013. A stabilized assumed deformation gradient finite element formulation for strongly coupled poromechanical simulations at finite strain, International Journal for Numerical and Analytical Methods in Geomechanics 37(16): 2755-2788.

Swift, B., Hoch, A., and Rodwell, W. 2001. Modelling gas migration in compacted bentonite: GAMBIT Club Phase 2–Final report, Posiva Report 2.

Tamayo-Mas, E., Harrington, J., Shao, H., Dagher, E., Lee, J., Kim, K., Rutqvist, J., Lai, S.-H., Chittenden, N., and Wang, Y. 2018. Numerical modelling of gas flow in a compact clay barrier for DECOVALEX-2019. In 2nd International Discrete Fracture Network Engineering Conference. American Rock Mechanics Association.

Tawara, Y., Hazart, A., Mori, K., Tada, K., Shimura, T., Sato, S., Yamamoto, S., Asano, H., and Namiki, K. 2014. Extended two-phase flow model with mechanical capability to simulate gas migration in bentonite, Clays in Natural and Engineered Barriers for Radioactive Waste Confinement 400: 545-562.

Tripathy, S., Sridharan, A., and Schanz, T. 2004. Swelling pressures of compacted bentonites from diffuse double layer theory, Canadian Geotechnical Journal 41(3): 437-450.

van Genuchten, M.T. 1980. A closed-form equation for predicting the hydraulic conductivity of unsaturated soils, Soil Science Society of America Journal 44(5): 892-898.

Vanapalli, S.K., Fredlund, D.G., Pufahl, D.E., and Clifton, A.W. 1996. Model for the prediction of shear strength with respect to soil suction, Canadian Geotechnical Journal 33(3): 379-392.

Vilarrasa, V., Bolster, D., Olivella, S., and Carrera, J. 2010. Coupled hydromechanical modeling of CO_2 sequestration in deep saline aquifers, International Journal of Greenhouse Gas Control 4(6): 910-919.

Vilarrasa, V., Rutqvist, J., Blanco Martin, L., and Birkholzer, J. 2015. Use of a dual-structure constitutive model for predicting the long-term behavior of an expansive clay buffer in a nuclear waste repository, International Journal of Geomechanics 16(6): D4015005.

Villar, M. 2005. MX-80 bentonite. Thermo-hydro-mechanical characterisation performed at CIEMAT in the context of the Prototype Project, Informes Técnicos CIEMAT 1053: 39.

Villar, M.V., Gutierrez-Rodrigo, V., Martín, P.L., Romero, F.J., and Barcala, J.M. 2014a. Gas transport in bentonite. 1135-9420.

Villar, M.V., and Lloret, A. 2008. Influence of dry density and water content on the swelling of a compacted bentonite, Applied Clay Science 39(1-2): 38-49.

Villar, M.V., Martin, P.L., and Romero, F.J. 2014b. Gas transport properties of compacted bentonite, Unsaturated Soils: Research & Applications, Vols 1 and 2: 1735-1740.

Vo, T.D., Pouya, A., Hemmati, S., and Tang, A.M. 2017. Numerical modelling of desiccation cracking of clayey soil using a cohesive fracture method, Computers and Geotechnics 85: 15-27.

Wang, J.J., Zhu, J.G., Chiu, C.F., and Zhang, H. 2007. Experimental study on fracture toughness and tensile strength of a clay, Engineering Geology 94(1-2): 65-75.

Wang, Q., Cui, Y.-J., Tang, A.M., Barnichon, J.-D., Saba, S., and Ye, W.-M. 2013a. Hydraulic conductivity and microstructure changes of compacted bentonite/sand mixture during hydration, Engineering Geology 164: 67-76.

Wang, Q., Tang, A.M., Cui, Y.J., Barnichon, J.D., and Ye, W.M. 2013b. Investigation of the hydro-mechanical behaviour of compacted bentonite/sand mixture based on the BExM model, Computers and Geotechnics 54: 46-52.

Wang, Q., Tang, A.M., Cui, Y.J., Delage, P., and Gatmiri, B. 2012. Experimental study on the swelling behaviour of bentonite/claystone mixture, Engineering Geology 124: 59-66.

Warren, J., and Root, P.J. 1963. The behavior of naturally fractured reservoirs, Society of Petroleum Engineers Journal 3(03): 245-255.

White, J.A., and Borja, R.I. 2008. Stabilized low-order finite elements for coupled solid-deformation/fluid-diffusion and their application to fault zone transients, Computer Methods in Applied Mechanics and Engineering 197(49-50): 4353-4366.

Wilson, Z.A., Borden, M.J., and Landis, C.M. 2013. A phase-field model for fracture in piezoelectric ceramics, International Journal of Fracture 183(2): 135-153.

Wilson, Z.A., and Landis, C.M. 2016. Phase-field modeling of hydraulic fracture, Journal of the Mechanics and Physics of Solids 96: 264-290.

Wiseall, A., Cuss, R., Graham, C., and Harrington, J. 2015. The visualization of flow paths in experimental studies of clay-rich materials, Mineralogical Magazine 79(6): 1335-1342.

Xia, L., Yvonnet, J., and Ghabezloo, S. 2017. Phase field modeling of hydraulic fracturing with interfacial damage in highly heterogeneous fluid-saturated porous media, Engineering Fracture Mechanics 186: 158-180.

Xu, L., Ye, W.-M., and Ye, B. 2017. Gas breakthrough in saturated compacted GMZ bentonite under rigid boundary conditions, Canadian Geotechnical Journal 54(8): 1139-1149.

Xu, L., Ye, W.M., Chen, B., Chen, Y.G., and Cui, Y.J. 2016. Experimental investigations on thermo-hydro-mechanical properties of compacted GMZ01 bentonite-sand mixture using as buffer materials, Engineering Geology 213: 46-54.

Xu, L., Ye, W.M., Ye, B., Chen, B., Chen, Y.G., and Cui, Y.J. 2015. Investigation on gas migration in saturated materials with low permeability, Engineering Geology 197: 94-102.

Xu, R., and Zhao, K. 2018. Corrosive fracture of electrodes in Li-ion batteries, Journal of the

Mechanics and Physics of Solids 121: 258-280.

Xu, W.J., Shao, H., Hesser, J., Wang, W., Schuster, K., and Kolditz, O. 2013. Coupled multiphase flow and elasto-plastic modelling of in-situ gas injection experiments in saturated claystone (Mont Terri Rock Laboratory), Engineering Geology 157: 55-68.

Ye, W.M., Xu, L., Chen, B., Chen, Y.G., Ye, B., and Cui, Y.J. 2014. An approach based on two-phase flow phenomenon for modeling gas migration in saturated compacted bentonite, Engineering Geology 169: 124-132.

Yin, P., and Vanapalli, S.K. 2018. Model for predicting tensile strength of unsaturated cohesionless soils, Canadian Geotechnical Journal 55(9): 1313-1333.

Yoshioka, K., and Bourdin, B. 2016. A variational hydraulic fracturing model coupled to a reservoir simulator, International Journal of Rock Mechanics and Mining Sciences 88: 137-150.

Young, T. 1805. An essay on the cohesion of fluids, Philosophical Transactions of the Royal Society of London 95: 65-87.

Yu, L., and Weetjens, E. 2009. Summary of gas generation and migration. Belgian Nuclear Research Centre.

Zhao, C., Liu, Y., and Gao, F. 2010. Work and energy equations and the principle of generalized effective stress for unsaturated soils, International Journal for Numerical and Analytical Methods in Geomechanics 34(9): 920-936.

Zheng, L., Rutqvist, J., Xu, H., Kim, K., Voltolini, M., and Cao, X. 2017. Investigation of coupled processes and impact of high temperature limits in argillite rock: FY17 Progress. Ernest Orlando Lawrence Berkeley National Laboratory, Berkeley, CA (US).

Zhou, S., Zhuang, X., and Rabczuk, T. 2018. A phase-field modeling approach of fracture propagation in poroelastic media, Engineering Geology.

Zhou, S., Zhuang, X., and Rabczuk, T. 2020. Phase field method for quasi-static hydro-fracture in porous media under stress boundary condition considering the effect of initial stress field, Theoretical and Applied Fracture Mechanics 107: 102523.

Zhu, C.-M., Ye, W.-M., Chen, Y.-G., Chen, B., and Cui, Y.-J. 2013. Influence of salt solutions on the swelling pressure and hydraulic conductivity of compacted GMZ01 bentonite, Engineering Geology 166: 74-80.

Appendices

Appendix A Introduction of Task A of DECOVALEX-2019

The Task A of DECOVALEX-2019, i.e. modElliNg Gas INjection ExpERiments (ENGINEER), was proposed for better understanding the gas migration process in two low permeability materials, including compacted bentonite and Callovo-Oxfordian claystone (Rutqvist et al. 2018). The task focuses on developing new numerical models to quantitatively predict the gas flux and the associated hydromechanical behaviors. The developed models are expected to be used as tools for assessing the effect of gas migration on the barrier material. The benchmark tests for validating the new numerical models were conducted by British Geological Survey, as seen in (Daniels and Harrington 2017; Harrington et al. 2017). The clay material for the gas injection tests is Mx80 bentonite. The prepared sample is a cylinder with length of 120mm and diameter of 60mm. The dry density of the sample is 1.56kg/m3. A hole with a diameter of 6.35 mm was drilled along the center line of the sample to a depth of 64.8 mm. The drilled hole allows a stainless-steel to be inserted into the sample for measuring gas pressure or injecting gas. The sample was installed in a constant volume pressure vessel, see Figure A.1(a), which was instrumented with two axial and three radial load cells, as well as three arrays of porewater pressure transducers, see Figure A.1(b). The load cells and transducers were used to monitor the evolution of stress and porewater pressure during the gas flow process.

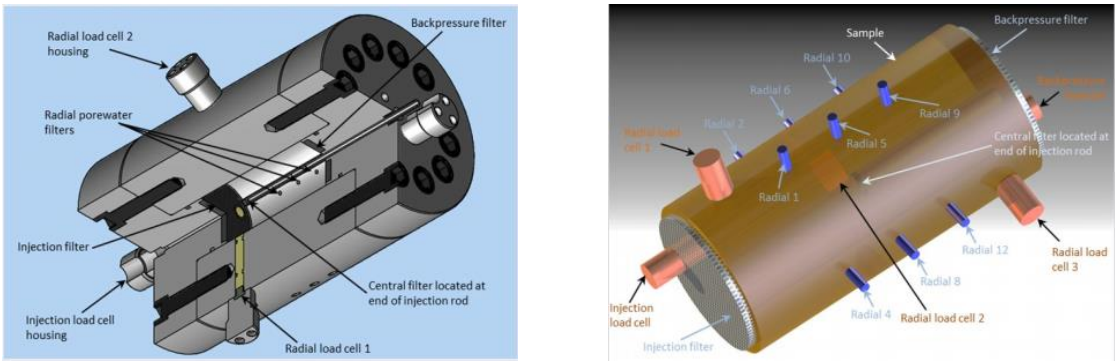

(a) Constant volume pressure vessel (b) Positions of the load cells and transducers

Figure A.1 Apparatus components and instrumentation (Harrington et al. 2017)

Two gas injection tests, i.e., 1-D flow test and 3-D spherical flow test, were conducted on the bentonite sample under constant volume condition. The environmental temperature for the tests was controlled around 20℃ (Daniels and Harrington 2017; Harrington et al. 2017). The bentonite sample in both tests experienced two stages in sequence, i.e. sample hydration and gas injection. In the stage of hydration, the sample was hydrated through all radial and backpressure filter until a saturated state was achieved. The hydration process leads to the development of swelling pressure. Once the monitored total stress reaches a plateau, the helium gas was injected into bentonite sample through either one side surface or the center point, thus leading to the 1-D flow or 3-D spherical flow, respectively, as seen in Figure A.2. As the gas

migrates in the bentonite, the evolutions of gas pressure, porewater pressure, total stress and gas outflow rate were continuously monitored. The detailed results have been presented in (Daniels and Harrington 2017; Harrington et al. 2017).

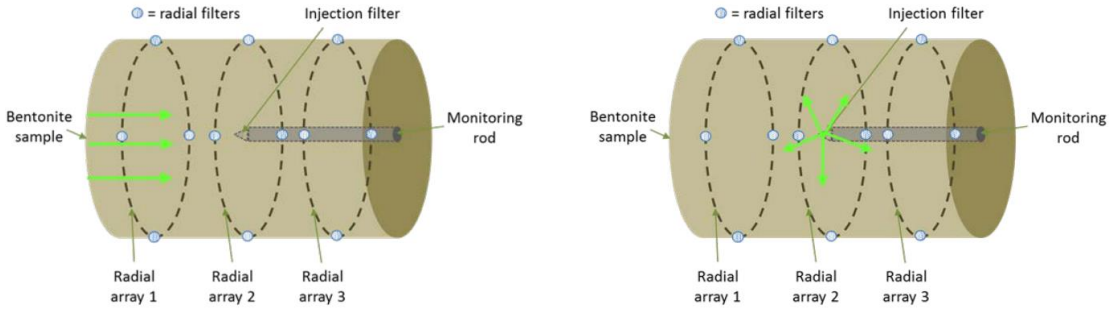

Figure A.2 Schematic graph of gas flow direction (Left: 1-D gas flow; Right: 3-D spherical flow) (Harrington et al. 2017; Rutqvist et al. 2018)

Appendix B Introduction of FEM Used in This Thesis

1. Basic steps for FEM to solve the developed model

The developed governing equations in this thesis are expressed in terms of Partial Differential Equations (PDEs) which cannot be solved analytically. Thus, the developed PDEs were solved numerically by using FEM which has four basic steps:

(1) Derivation of weak forms

The strong form of each governing equation is multiplied by an appropriate test function. The resultant product is integrated over the space domain of the problem. Then, the order of the derivative is reduced by using integration by parts. Finally, boundary conditions are introduced (Zienkiewicz et al. 2013). Through this way, the strong forms that require the governing equations should hold at all points of the domain, has been converted to their weak forms that only need to be held in the test function space.

(2) Temporal discretization

The time integration for the transient problem in this thesis is achieved by an implicit method, i.e. the backwards differentiation formula (BDF) method. The formula for the BDF at the time, t_k, can be expressed as (Ascher and Petzold 1998; Weiss 2019)

$$U^k \approx \sum_{i=1}^{q} \alpha_{k,i} U^{k-i} + \tau_k \beta_k \dot{U}(t_k) \tag{B.1}$$

where τ_k is a variable step size, U^k is the approximated solution at the time t_k, $\alpha_{k,i}$ and β_k are coefficients that depend on the order, q, and the time step size. The BDF solver embedded in COMSOL can automatically adjust the time step size, τ_k, and the order of BDF, q, based on the evolution of the solution with time. More details about this technique are given

below.

(3) Spatial discretization

The exact solutions of the PDEs are approximated in space by linear combinations of basis functions. The forms of the approximated solutions depend on the order of the basis function and the type of the selected element. Substituting the approximated solutions into the weak forms gives a series of algebraic equations for the coupled HM problem.

(4) Solving strategy

The coupled multi-physical model can be solved by either a fully coupled approach or a segregated approach. For the fully coupled approach, the developed governing equations are solved simultaneously, and therefore, all of the couplings between different physics can be considered. However, this approach for a multi-physical problem is both memory- and time-intensive. In contrast, the segregated approach solves the coupled equations in a separated way. Specifically, there are several steps followed by the approach (Frei 2013):

1) Set initial conditions for all physics involved in the model;
2) Solve the first physics (or the first group of physics) by using the solution evaluated in the previous step;
3) …
4) Solve the *n*th physics (or the *n*th group of physics) by using the solution evaluated in the previous step;
5) Check the convergency criterion. If it is satisfied, the next step proceeds. Otherwise, repeat steps 2-4 until the convergency criterion is satisfied.

Compared with the fully coupled approach, the segregated approach may take more iterations to reach convergency. However, the total solution time and memory usage are lower for the segregated approach, since each sub-step needs less time solution time and memory space.

2. Galerkin Finite Element Method

The adopted FEM is based on the Galerkin method that is one of the weight residual methods to solve PDEs. In this method, the weighting function, i.e., the test function in COMSOL, is the same with the basis function used for approximating the exact solution. Compared with other FEMs, such as Petrov-Galerkin FEM and Least-Squares FEM, the Galerkin FEM (GFEM) is more computationally efficient (Romão et al. 2011). The GFEM may give rise to oscillation solutions when applied to heat transfer and fluid flow problems. However, these issues can be solved by introducing a stabilized term, as seen in (Burman 2008). Currently, the GFEM has been widely used to solve coupled HM problems in porous media. A stabilized technique has been developed in (Choo and Borja 2015; White and Borja 2008) to avoid the pore pressure oscillation when a lower equal-order element is adopted to discretize the domain.

3. Adaptive time-stepping approach

Here the basic steps for the adjustment of the time step size and the order of BDF are given below. More details about this approach can be found in (Ascher and Petzold 1998; Weiss 2019).

For a coupled model that have M physical fields and N_j degrees of freedom for the field

j, the time step is accepted if the weighted root mean square (WRMS) norm of the error at the time t_k, which is estimated as Eq. (B.2), is less one (Weiss 2019).

$$\left\|\bar{e}_k\right\|_{WRMS}^2 := \frac{1}{M}\sum_j \frac{1}{N_j}\sum_i \frac{\left|\bar{e}_{k,i}(q,\tau)\right|^2}{\left(A_i + R\left|U_i^k\right|\right)^2} \tag{B.2}$$

where $\bar{e}_{k,i}$ is the local truncation error, U_i^k is the approximated solution of ith degree of freedom, A_i is the absolute tolerance specified by the user and R is the relative tolerance depending on the physics setting.

In the initial steps, both the time step size and the order are increased until $\left\|\bar{e}_k\right\| > 1$. Then, the order is adjusted according to the monotonicity of $T(q) := (q+1)\bar{e}_k$. The order is increased or decreased if $T(q)$ monotonically decreases or increases, respectively, with the order q. Otherwise, the order q keeps the same. Then, $\left\|\bar{e}_k\right\|$ is estimated again. If $\left\|\bar{e}_k\right\| < 1$ fails, a new step size, τ', is defined as

$$\tau' = \left(\frac{A + R|U|}{\bar{e}_{k,\tau}}\right)^{1/(q+1)} \tau \tag{B.3}$$

If $\left\|\bar{e}_k\right\| < 1$, the time step size is increased by a factor of two on the precondition that the error has decreased to a value that is 16 times smaller than the allowed one. The time step size and the order in the next step depend on their adjustment history. If the order was changed in the previous step, it remains the same. If the order and time step size keep constant in the last $q+1$ ($q < 5$) steps, the increase or decrease of the order again depends on the monotonicity of $T(q)$, as previously stated (Weiss 2019).

Appendix C Advances in Modelling of Hydro-Mechanical Processes of Gas Migration in Saturated Bentonite

Guanlong Guo, Mamadou Fall, Engineering Geology (submitted)

Abstract

Bentonite is a key material for the construction of Engineered Barrier Systems (EBSs) in deep geological repositories (DGRs) for radioactive waste. Modelling of gas migration in saturated bentonite, as well as the accompanied hydromechanical (HM) processes is crucial for conducting a performance assessment for the safety of a deep geological repository (DGR). The objective of this paper is to review the state-of-the-art of coupled HM models for simulating the gas migration behaviors in saturated bentonite, and then identify the pros and cons of these models that can be referenced by future numerical works. To this end, the paper has summarised and discussed the coupled HM models from several aspects, including governing equations, HM constitutive models, fracture theories and related numerical approaches. It is found that the visco-capillary two-phase flow model with enriched intrinsic permeability is the most used hydraulic model to simulate the fluid flow, while the previous mechanical models have covered plasticity, damage, swelling and consolidation of clay matrix. The development of preferential pathways was commonly considered in an implicit way by using the embedded fracture model as intrinsic permeability model or by adopting plastic or damage models to describe the mechanical behaviors. Current numerical models that can explicitly simulate the gas-driven fracturing process in saturated bentonite were not frequently reported. The existing ones are not enough to simulate all the key experimental behaviors associate with the preferential pathways. Advanced numerical approaches, such as XFEM or DEM based approaches, and proper fracture theories, such as the cohesive zone model, need to be employed to explicitly describe the development of preferential pathways. At the end of this paper, conclusions and recommendations for future studies are given.

Keywords: Gas migration; Dilatancy-controlled flow; Nuclear Wastes; Bentonite; Deep geological repository; Coupled hydromechanical processes

1 Introduction

Management of nuclear waste has been one of the critical problems that affect the sustainable development of nuclear power. Depositing the nuclear waste in a deep geological repository (DGR) is a widely-accepted approach to deal with the radioactive material (Fall et al. 2012; Liu et al. 2016; Nasir et al. 2011; Nasir et al. 2015; Rodwell et al. 1999; Rutqvist et al. 2018). A DGR consists of an engineering barrier system (EBS) and a natural barrier system. Bentonite is commonly used as the buffer or sealing material for the EBS, as it has several desirable properties, such as low hydraulic conductivity, proper swelling property, low diffusion coefficient and high sorption capacity (Liu et al. 2014b; Nasir et al. 2013; Shehata et al. 2020; Tawara et al. 2014; Xu et al. 2018; Xu et al. 2015). However, over the lifespan of a DGR, a large amount of gas may be generated from some physicochemical processes, such as corrosion of metallic materials, radiolysis of water and microbial degradation (Miller et al. 2000; Rodwell et al. 1999; Rutqvist et al. 2018). Transport of the generated gas could jeopardize the desirable properties of bentonite for sealing the nuclear wastes (Graham et al. 2012; Ye et al. 2014). Thus, a comprehensive understanding of gas transport in bentonite is crucial to conducting a reliable performance assessment for a DGR.

There are four basic gas transport mechanisms, i.e., advection/diffusion of dissolved gas, visco-capillary two-phase flow, dilatancy-controlled flow, and macro-fracture-controlled flow (Marschall et al. 2005; Ye et al. 2014; Yu and Weetjens 2009). The specific transport mechanism taken by the generated gas depends on the rate of gas generation. At a low rate of gas generation, the generated gas can totally dissolve into the porewater and then be transported through the advection/diffusion mechanism (Ye et al. 2014; Yu and Weetjens 2009). When the rate of gas generation exceeds the dissolution rate, a free gas phase is formed. The gas pressure increases with the continuous generation of gas. When gas pressure reaches the gas entry value of bentonite, the highly-pressurized gas infiltrates the initially saturated porous media and then migrates by replacing the porewater, which results in the visco-capillary two-phase flow (Rodwell et al. 1999). As the rate of gas generation further increases, the advection/diffusion and visco-capillary two-phase flow may not be sufficient to transport all the generated gas, thus inducing a further increase in gas pressure. When the gas pressure approaches the minimum principal stress to which the porous medium is subjected at a local scale, microfractures are developed (Graham et al. 2012; Rodwell et al. 1999). As a result, both the intrinsic permeability and the desaturation process are significantly enhanced. This transport mechanism is called dilatancy-controlled flow. If this mechanism is yet not efficient enough to transport the generated gas, the gas pressure may exceed the sum of the minimum principal stress and the tensile strength at a global scale (Marschall et al. 2005). In such a circumstance, macroscopic fractures will be triggered, which can increase the fracture transmissivity by many orders of magnitude.

To examine the effect of gas migration on the sealing ability of the buffer material, both experimental (laboratory or in situ) tests and numerical modelling have been conducted over the past four decades. The earliest study on this topic may be dated back to the early 1980s. Pusch and Forsberg (1983) proposed a physical model in which gas may flow in highly compacted bentonite through wider passages. This model was further improved based on

quantitative microstructural data and basic physical relationships (Pusch and Hökmark 1990). Experimental studies in (Pusch et al. 1985) showed that a critical gas pressure of the same order of magnitude as the swelling pressure is required for gas breakthrough in dense bentonite. In the 1990s, more gas injection tests were conducted on different types of bentonite, such as French Fo-Ca clay, Kunigel VI bentonite, Canadian Avonlea bentonite and Mx80 bentonite. These experimental studies examined the effects of dry density and initial degree of saturation on the gas migration process. It was found that higher dry density and higher initial degree of saturation contribute to more significant gas breakthrough behaviors, as detailed in (Gallé and Tanai 1998; Hume 1999; Tanai et al. 1997). The gas injection test on saturated Mx80 bentonite showed that gas breakthrough occurred when gas pressure was slightly larger than the sum of the swelling pressure and the backpressure (Horseman et al. 1997, 1999). This breakthrough phenomenon was attributed to the development of preferential pathways.

In the past 20 years, gas transport in bentonite has been an integrated subject of many international research programs related to nuclear waste disposals, such as GAMBIT Club, FORGE project, DECOVALEX-2019/-2023 and EURAD. Both experimental and numerical studies have been (are being) systematically conducted in these projects. Several types of bentonite, such as MX-80, FEBEX and GMZ bentonite, have been investigated in terms of their performances during the gas migration process, as seen in (Cuss et al. 2014; Daniels and Harrington 2017; Graham et al. 2012; Gutiérrez-Rodrigo et al. 2015; Harrington and Horseman 2003; Harrington et al. 2017; Harrington et al. 2019; Villar et al. 2014b; Xu et al. 2017; Xu et al. 2018). During this period, experimental studies were mainly conducted on saturated bentonite under constant volume condition in order to realistically reproduce the field condition. Strong couplings between stress, water pressure, gas pressure and gas flow rate have been highlighted in these experimental studies, as seen in (Graham et al. 2012; Harrington and Horseman 2003; Harrington et al. 2017). These coupled HM behaviors are closely associated with the development of preferential pathways (Graham et al. 2012). In addition, the self-sealing behaviors, including the recoveries of the tensile strength, breakthrough pressure and low permeability, were observed in experiments conducted on the tested bentonite that has experienced re-saturation process.

Along with the experimental studies, many numerical models have been developed to simulate the gas migration process in bentonite. Some numerical studies mainly focused on simulating the hydraulic behaviors, such as the evolution of gas pressure, degree of saturation or gas flow rate. These behaviors are generally simulated by the generalized Darcy's law in which the hydraulic properties, such as intrinsic permeability, relative permeability or gas entry value, are coupled with the gas pressure or/and external confining pressure, as seen in (Birgersson et al. 2008; Calder et al. 2006; Graham et al. 2002; Tanaka et al. 2010; Tawara et al. 2014; Ye et al. 2014). As these models are not fully coupled with the mechanical process, the mechanical responses cannot be captured. To account for the mechanical effect, more numerical models were constructed in the framework of Biot's consolidation theory or mixture theory, as in (Alonso et al. 2006; Arnedo et al. 2008; Dagher et al. 2018; Fall et al. 2014; Gerard et al. 2008; Gerard et al. 2014; Gerard et al. 2010; Olivella and Alonso 2008; Puig Damians et al. 2019; Xu et al. 2013; Yamamoto et al. 2015). As the coupled hydromechanical (HM)

behaviors observed in experiments are very complex, some conceptual models, such as the embedded fracture model, double porosity model, stochastic model, single gas flow model, etc., were proposed to ease the modelling work. Furthermore, the plastic and damage models were employed in some coupled HM models to account for the effect of the development of preferential pathways, as seen in (Dagher et al. 2018; Fall et al. 2014; Nguyen and Le 2014; Xu et al. 2013). Although these models are beneficial to achieving the gas breakthrough and some mechanical behaviors, they are not able to explicitly simulate the preferential pathways. By far, the numerical models that can explicitly simulate the preferential gas flow in bentonite are not frequently reported. However, such numerical approaches have been paid more attention in the latest international project for nuclear waste disposal, i.e. DECOVALEX-2023.

This review paper is organized as follows. In Section 2, bentonite materials and key experimental findings associated with this topic are briefly discussed. Section 3 presents the governing equations for fluid flow and mechanical deformation. The stress state variables adopted in previous numerical models are discussed in detail. Section 4 mainly focuses on the constitutive models that were proposed to simulate the hydraulic and mechanical processes during the gas migration process. The pros and cons of these models are discussed. In Section 5, fracture theories that can be used to simulate the fracturing process in bentonite are reviewed. Then, the existing approaches and potential approaches for simulating the preferential pathways are discussed. In section 6, conclusions and recommendations for future works are given.

2 Materials and Experimental Findings

As the copper canister used to store nuclear wastes is highly resistant to corrosion, it is expected to take thousands of years after the closure of a DGR for groundwater penetrating the canister and reacting with the iron inserts (Rodwell et al. 1999). Thus, at the onset of gas generation, the bentonite material is expected to have reached a fully saturated state and the heat release phase has finished (Rodwell et al. 1999). In addition, as the buffer material is constrained by the copper canister and the rigid host rock, the volume change is not allowed during gas migration. To realistically reproduce these field conditions, most of previous gas injection tests were conducted on saturated bentonite under constant volume and isothermal condition.

2.1 Materials

2.1.1 HM Properties

There are several types of bentonite that were widely used to conduct gas injection tests, e.g. Mx80 bentonite, FEBEX bentonite and GMZ bentonite. Mineralogical compositions of these bentonites are listed in Table C.1. More physicochemical information for these three types of bentonite has been summarised in (Ye et al. 2010).

Table C.1 Mineralogical composition of three bentonites (wt.%) (Modified from (Ye et al. 2010))

Materials	Montmorillonite	Quartz	Cristobalite	Feldspar	Plagioclase	Kaolinite	References
MX80	65-82	4-12		5-8			(Villar 2005)
FEBEX	92±3	2±1	2±1		3±1		(Villar et al. 2014a)
GMZ	75.4	11.7	7.3	4.3		0.8	(Ye et al. 2010)

As Table C.1 shows, montmorillonite, a clay mineral of high swelling potential, is the dominant component of the three bentonites. The HM properties of a bentonite sample highly depend on the amount of montmorillonite it contains. Previous experimental studies showed that some key HM properties of saturated samples, including intrinsic permeability, gas entry value and swelling pressure, are directly controlled by the dry density (Seiphoori et al. 2014; Villar 2005; Villar et al. 2014a; Xu et al. 2017). For the bentonite sample with high dry density, there are more expansive clay minerals per unit volume of the sample that can adsorb water molecules. Thus, a high swelling pressure is expected to develop when the sample reaches a fully saturated state under constant volume condition. As the adsorbed water film is relatively immobile, the porous space available for fluid flow significantly decreases with the increase of dry density. As a result, the saturated bentonite sample with high dry density has a very low intrinsic permeability (ranging between 10^{-20}~10^{-21} m^2) and a high gas entry value (which is 18MPa in (Rutqvist et al. 2018)). Previous experimental studies showed that the swelling pressure, intrinsic permeability and gas entry value can be predicted by an exponential function of dry density, as seen in (Gutiérrez-Rodrigo et al. 2015; Seiphoori et al. 2014; Villar 2005; Ye et al. 2010).

2.1.2 Heterogeneity

The dry density for real compacted bentonite materials may distribute heterogeneously in space, especially for the case in the field. As discussed in Section 2.1.1 of this appendix, the dry density directly controls the intrinsic permeability, gas entry value and swelling pressure. Thus, both the HM properties and stress state may vary from place to place in the bentonite sample. The highly pressurised gas is expected to preferentially flow through the areas that are less resistant to both flow and fracturing. To account for the heterogeneity, the hydraulic properties or parameters, such as intrinsic permeability, gas entry value, fracture aperture and spacing, were randomly assigned with several discrete values in different locations of the sample (Damians et al. 2020; Gonzalez-Blanco et al. 2018). Some features of the preferential flow have been qualitatively captured by these models. However, this simple approach seems not sufficient to realistically reproduce the heterogeneous distribution of HM properties in saturated bentonite. The random field for a specific property of geomaterials generally follows a lognormal distribution law (Li et al. 2015; Santillán et al. 2017). In addition, a property at one position is more associated with this property at closer positions than that at far positions (Kasama et al. 2012; Li et al. 2015). This natural feature is generally described by a spatially autocorrelated random field that is developed on a correlation function. The spatially autocorrelated random field that follows a lognormal distribution has been adopted in

(Delahaye and Alonso 2002) to simulate the preferential gas flow in heterogeneous bentonite. The preferential gas flow was observed in the weak layers of soils. This approach can be further extended to other HM properties to enhance its ability to simulate the preferential gas flow. Except for the HM properties, the heterogeneous distribution of swelling pressure is also expected to have significant effects on the preferential gas flow. Nevertheless, the heterogeneity in stress state has not yet been examined in previous studies in terms of its effect on the gas migration process.

2.1.3 Pore Structure

It is commonly accepted that unsaturated expansive soils have double pore structures, i.e. inter-aggregate pores and intra-aggregate pores, thus presenting a bimodal pore size distribution (Alonso et al. 1999; Dieudonne et al. 2017; Gens and Alonso 1992; Sánchez et al. 2016). As the hydration process proceeds, the inter-aggregate pores gradually reduce due to the swelling of clay particles (Gens and Alonso 1992). At saturated state, the soil primarily presents a unimodal pore size distribution. However, recent Mercury Intrusion Porosimetry (MIP) results showed that the saturated bentonite also exhibits a bimodal pore size distribution which, however, is less significant than that of the as-compacted bentonite (Madaschi and Laloui 2018), as seen in Figure C.1.

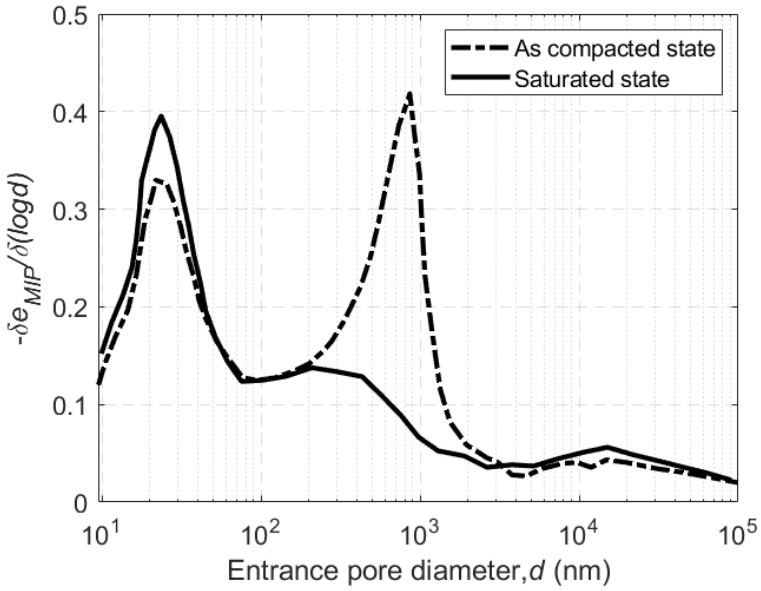

Figure C.1 Pore size distribution of as-compacted and saturated bentonite (Madaschi and Laloui 2018)

Moreover, the μ-CT images obtained by Gonzalez-Blanco et al. (2018) also confirmed that the saturated bentonite has double pore structures, i.e. fissures between clay grains and pores in grains. As seen in Figure C.2, fissures between clay grains can be easily identified from the saturated bentonite, although they are not as obvious as those in bentonite at compacted state. Under high gas pressure, these fissures may be activated and then serve as the preferential pathways for gas flow. This has been observed in the right image in Figure C.2. In addition, the existence of wider passages in highly compacted bentonite was also confirmed in (Pusch and Forsberg 1983; Pusch and Hökmark 1990; Xu et al. 2017).

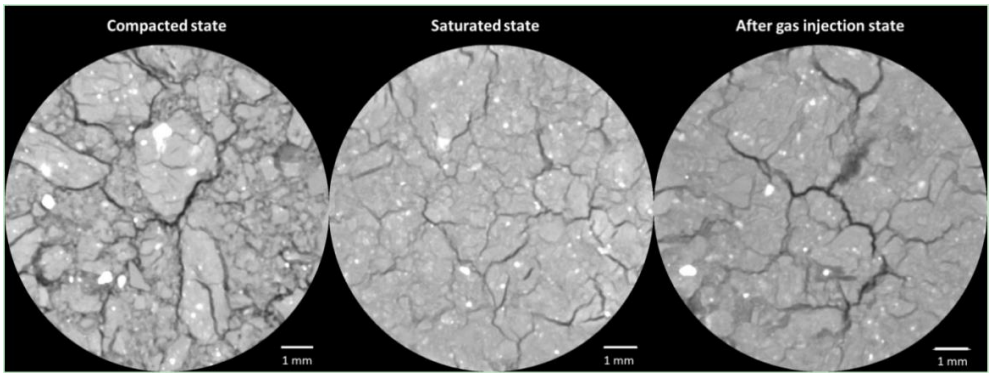

Figure C.2 Grain structure of bentonite at compacted, saturated and after-injection states (Gonzalez-Blanco et al. 2018)

It is worth noting that whether the saturated bentonite can be considered as a porous medium having double pore structures really depends on the specific physical process of concern. For traditional research topics that focus on the overall mechanical behavior, it may be appropriate to regard the saturated bentonite as a single-porosity medium, since a small amount of larger pore may not have significant influence on the mechanical behavior. In contrast, for the current research topic in which the saturated bentonite is subjected to a highly pressurized gas, the existence of larger connected pores, even with a small amount, will significantly influence the gas transport process. This is because the larger connected pores may be utilised by the highly pressurized gas as the preferential flow pathways. Under such a situation, it is reasonable to regard the saturated bentonite as double porosity media in which the larger connected pores serve as the potential flow pathways and the pores in matrix keep saturated.

2.2 Experimental Findings

Previous experimental studies showed that the gas migration in saturated bentonite is accompanied by some characteristic behaviors, including gas breakthrough phenomenon, development of preferential pathways, build-up of porewater pressure and total stress, localised consolidation of clay matrix, almost saturated state after gas injection test and self-sealing behaviors. These behaviors are discussed as follows in an integrated way.

As the effective pore size of saturated bentonite for fluid flow is extremely small, the gas entry value is so high that the gas can hardly infiltrate the bentonite. In general, gas entry takes place when the gas pressure reaches the sum of porewater pressure and swelling pressure (Cuss et al. 2014; Cuss et al. 2011; Graham et al. 2012). The swelling capability of the bentonite material can be significantly influenced by the salinity of porewater (Navarro et al. 2017; Shehata et al. 2020; Zhu et al. 2013). The swelling pressure of bentonite exposed to NaCl or $CaCl_2$ solution is significantly less than that exposed to distilled water (Shehata et al. 2020; Zhu et al. 2013). In addition, the salinity of porewater also contributes to the increase of the hydraulic conductivity (Zhu et al. 2013). Therefore, gas migration in saturated bentonite is expected to be influenced by the geochemical environment of the repository. However, the chemical effect has not yet been widely considered in previous gas injection tests on bentonite.

As gas migrates through the bentonite sample, strong couplings between stress, water pressure, gas pressure and gas outflow rate have been observed in experiments (Harrington and

Horseman 2003; Harrington et al. 2017; Harrington et al. 2019). Specifically, the gas breakthrough events are accompanied by a localized build-up of porewater pressure and total stress (Graham et al. 2012; Harrington and Horseman 2003). Significant perturbations of stress field generally precede the major gas outflow events (Harrington et al. 2017). These strong couplings are closely associated with the development of preferential pathways (Harrington et al. 2017). The developed pathways may exhibit strong instabilities. The aperture size and orientation of the pathways may evolve spatially and temporally during the gas transport process. Consequently, the monitored gas outflow rate, porewater pressure and total stress will experience strong fluctuations (Harrington and Horseman 2003; Harrington et al. 2017; Harrington et al. 2019).

Under constant volume condition, the dilation of the buffer material is considerably inhibited. The opening of the developed pathways mainly results from the consolidation of clay matrix surrounding the pathways and/or the compression of the porewater in the clay matrix (Graham et al. 2012; Harrington et al. 2017; Hoch et al. 2004). This process eventually leads to the build-up of porewater pressure and total stress, as observed in (Harrington and Horseman 2003; Harrington et al. 2017; Harrington et al. 2019) and the water exchange between the developed microfractures and the clay matrix (Harrington and Horseman 2003; Harrington et al. 2017; Wiseall et al. 2015).

When the developed pathways are fully connected with outlet boundaries, gas rapidly flows out of the sample, thus inducing gas breakthrough phenomenon. The gas breakthrough may also take place in subsequent injection cycles, but it is less obvious than the first one due to the preferential pathways formed in the first cycle (Harrington and Horseman 2003; Villar et al. 2014a). On the other hand, the developed pathways may close or self-seal when gas pressure decreases to a certain value. As a result, the pathways developed in previous injection cycles may not be used as the flow pathways in the following cycles (Harrington and Horseman 2003). The self-sealing capability of the tested bentonite is also observed when the material is subjected to a rehydration process. The rehydrated sample can recovery its tensile strength, permeability and gas breakthrough pressure to a certain degree (Graham et al. 2012; Villar et al. 2014a).

The tested bentonite can keep an almost saturated state after the gas injection test (Graham et al. 2012; Harrington and Horseman 2003; Harrington et al. 2017; Hoch et al. 2004; Horseman et al. 1999). As the aperture size of the developed pathways is much larger than the pore size of the clay matrix, gas preferentially flows through the fracture network, while leaving the clay matrix at a saturated state. Since the void space of the developed pathways only accounts for a tiny percentage of the total void space, the whole sample can remain a saturated state.

In addition to the developed preferential pathways, interfaces between the bentonite sample and its other materials, such as hard rocks or metal container, may also serve as the pathways for the preferential gas outflow (Davy et al. 2009; Liu et al. 2014a; Popp et al. 2013; Xu et al. 2017). However, the gas pressure required to trigger a breakthrough phenomenon varies from case to case. The gas breakthrough pressure is distinctly less than the swelling pressure in (Davy et al. 2009), while it is equal to or slightly higher than the swelling pressure in (Liu et

al. 2014a). Thus, the interface may significantly control the gas flow in the field where interfaces exist between the buffer material and the canister and host rocks.

To summarize, gas transport in saturated bentonite is accompanied by complex coupled HM behaviors which may pose great challenges to the numerical modelling work. However, these behaviors need to be appropriately accounted for in numerical models in order to get a comprehensive understanding of the gas migration process.

3 Governing Equations

As discussed in Section 2.2 , gas migration in saturated bentonite involves strong couplings between hydraulic and mechanical processes. To simulate the HM behaviors observed in experiments, previous coupled HM models were generally developed within the framework of Biot's consolidation theory or mixture theory. In this section, the governing equations used in previous models are presented and discussed.

3.1 Mass Balance Equations

Most of previous models regarded the saturated bentonite as a porous medium having a single pore structure, as seen in (Chittenden et al. 2020; Dagher et al. 2018; Damians et al. 2018; Olivella and Alonso 2008). A set of comprehensive governing equations that have accounted for gas dissolution, water evaporation, diffusion, dispersion and advection, was adopted in (Dymitrowska et al. 2014; Olivella and Alonso 2008) to simulate the gas migration behavior in bentonite. The mass balance equation for fluid component, α, which represents w and g for water and generated gas, respectively, is expressed as (Dymitrowska et al. 2014)

$$\begin{aligned}&\phi\frac{\partial}{\partial t}\left(\omega_\alpha^l\rho^l S^l+\omega_\alpha^g\rho^g S^g\right)+\left(\omega_\alpha^l\rho^l S^l+\omega_\alpha^g\rho^g S^g\right)\frac{\partial\varepsilon_v}{\partial t}+\\&\nabla\cdot\left(\boldsymbol{i}_\alpha^l+\omega_\alpha^l\rho^l\boldsymbol{q}^l+\boldsymbol{i}_\alpha^g+\omega_\alpha^g\rho^g\boldsymbol{q}^g\right)=0\end{aligned}\qquad\text{(C.1)}$$

where S^ϖ is the degree of saturation for a fluid phase, ϖ, which represents l and g for liquid and gas respectively, ρ^ϖ is the phase density, ϕ is the porosity, ε_v is the volumetric strain, ω_α^ϖ is the mass fraction of the component α in the fluid phase ϖ, $\boldsymbol{i}_\alpha^\varpi$ is a non-advective flux due to diffusion and dispersion and $\boldsymbol{q}^\varpi$ is the advective flux. The specific forms for the mass fraction of each component and the non-advective/advective fluxes are given in Section 4.1.1.

As the transport capacity of diffusion/advection of dissolved gas is several orders of magnitude lower than that of the visco-capillary two-phase flow (Nagra 2008), the contribution of diffusion/advection of dissolved gas can be neglected for the current research topic that

involves gas flow through preferential pathways. Then, the governing equation for the fluid component α is simplified as

$$\rho_\alpha \phi \left(\frac{S_\alpha}{K_\alpha} - \frac{\partial S_e}{\partial p_c} \right) \frac{\partial p_\alpha}{\partial t} + \nabla \cdot (\rho_\alpha \boldsymbol{q}_\alpha) = -\phi \rho_\alpha \frac{\partial S_e}{\partial p_c} \frac{\partial p_{\alpha'}}{\partial t} - S_\alpha \rho_\alpha \frac{\partial \varepsilon_v}{\partial t} \tag{C.2}$$

where K_α is the bulk modulus of fluid component α, S_e is the effective degree of saturation, $p_c = p_g - p_w$ is the capillary pressure, $\boldsymbol{q}_\alpha$ is Darcy's velocity, ε_v is the volumetric strain of porous media and α' denotes the other fluid component besides the component α.

3.2 Momentum Balance Equation

The momentum balance equation used for governing the mechanical behavior during gas migration in bentonite is expressed as

$$\nabla \cdot \boldsymbol{\sigma} + \rho \boldsymbol{g} = \boldsymbol{0} \tag{C.3}$$

where $\boldsymbol{\sigma}$ is the total stress tensor, ρ is the average density of the unsaturated porous media and $\boldsymbol{g}$ is the gravitational acceleration.

To determine the total stress tensor used in Eq. (C.3), an appropriate stress state variable that can capture the main mechanical behaviors during gas migration process needs to be defined. Currently, two types of stress state variables are used to simulate the mechanical behavior of bentonite, i.e. the Bishop-type effective stress, see Eq. (C.4), and the independent stress state variables (net normal stress and suction), see Eq. (C.5).

$$\boldsymbol{\sigma}' = \left(\boldsymbol{\sigma} + p_g \boldsymbol{I} \right) - \chi \left(p_g - p_w \right) \boldsymbol{I} \tag{C.4}$$

$$\boldsymbol{\sigma}_n' = \boldsymbol{\sigma} + p_g \boldsymbol{I}, \quad s = p_g - p_w \tag{C.5}$$

where $\boldsymbol{\sigma}'$ is the effective stress, χ is the Bishop's coefficient, $\boldsymbol{\sigma}_n'$ is the net normal stress, and s is the suction. In most of previous models on this topic, the effective degree of saturation, S_e, was taken as the Bishop's coefficient, as suggested by Alonso et al. (2010). Alternatively, the Bishop's coefficient used in (Dagher et al. 2018) is defined as a function of the ratio between suction and gas-entry value, p_{gev} (Khalili and Khabbaz 1998):

$$\chi = \begin{cases} \left[\dfrac{s}{p_{gev}}\right]^{-0.55}, & \text{if } s > p_{gev} \\ 1, & \text{otherwise} \end{cases} \tag{C.6}$$

Using Bishop-type effective stress to construct mechanical models has several advantages. Firstly, a complex porous medium containing multiphase material can be converted to a mechanically equivalent single-phase continuum (Khalili et al. 2004; Nuth and Laloui 2008). Furthermore, the pre-existing mechanical constitutive models for solid continuum or saturated porous media can be readily extended to model the mechanical behavior of unsaturated soils. In addition, the Bishop-type effective stress can seamlessly recover the Terzaghi's effective stress when the degree of saturation reaches unity (Lu et al. 2010). This feature is beneficial to the mathematical treatment in numerical simulations. Due to these advantages, the Bishop-type effective stress was widely adopted in previous numerical models to simulate the mechanical behavior of bentonite during the gas migration process, as those in (Dagher et al. 2018; Fall et al. 2014; Xu et al. 2013).

Nevertheless, using Bishop-type effective stress may underestimate the contribution of gas pressure on the mechanical behavior of the bentonite sample. The gas entry value of the saturated bentonite is very high due to the extremely small pore size. Therefore, the Bishop's coefficient, no matter it is the effective degree of saturation or the one defined by Eq. (C.6), can remain almost 1 even when the gas pressure has reached a high value. Consequently, the Bishop-type effective stress may change a little even though the gas pressure is very high. In such a situation, the strong coupling between the hydraulic and the mechanical process cannot be realistically described. The tensile failure may not be achieved even when gas pressure has exceeded the sum of the total stress and the tensile strength. To remedy this issue, an appropriate Bishop's coefficient that can rapidly decrease when gas pressure reaches a certain value needs to be defined. Alternatively, an initial flaw where the gas entry value is small needs to be predefined to trigger the desaturation process.

Compared with the Bishop-type effective stress, the independent stress state variables, i.e., net normal stress and suction, have clear experimental meanings (Laloui and Nuth 2009). Two sets of constitutive models corresponding to the net normal stress and suction, are necessary to be defined to describe the overall mechanical behavior of unsaturated soils. As seen in Eq. (C.5), the gas pressure fully contributes to the net normal stress. This is beneficial to simulating the tensile failure when the gas pressure exceeds the sum of the total stress and the tensile strength. On the other hand, the net normal stress may overestimate the contribution of gas pressure to the mechanical behaviors in areas of a high degree of saturation. Although the increase of suction may offset the overestimation to some extent, the mechanical constitutive model corresponding to suction is not readily available for the current research topic.

4 Constitutive Models

4.1 Hydraulic Models

4.1.1 Advection/diffusion of Dissolved Gas

Previous numerical models on this research topic mainly focused on the coupled HM behaviors during gas migration in saturated bentonite. Thus, the model for simulating the advection/diffusion of dissolved gas in saturated bentonite is relatively standard. More details about this gas transport mechanism can be found in (Amann-Hildenbrand et al. 2015; Horseman et al. 1996). The gas transport mechanism is controlled by three basic laws, i.e., Darcy's law, Fick's law and Henry's law. The non-advective transport due to diffusion and dispersion is described by Fick's law (Delahaye and Alonso 2002; Dymitrowska et al. 2014):

$$\boldsymbol{i}_\alpha^\varpi = -\rho_\alpha \left(D_\alpha^\varpi \boldsymbol{I} + \boldsymbol{D}'^\varpi \right) \nabla \omega_\alpha^\varpi \tag{C.7}$$

where $\boldsymbol{i}_\alpha^\varpi$ is the diffusion flux of fluid component α in the fluid phase ϖ, D_α^ϖ is the apparent diffusion coefficient of the fluid component α in fluid phase ϖ in porous media, $\boldsymbol{D}'^\varpi$ is the dispersion tensor and ω_α^ϖ is the mass fraction of the fluid component α in the fluid phase ϖ.

The apparent diffusion coefficient D_α^ϖ can be modelled as (Dagher et al. 2018; Delahaye and Alonso 2002)

$$D_\alpha^\varpi = \phi_e S_\alpha \tau_d \bar{D}_\alpha^\varpi \tag{C.8}$$

where ϕ_e is the accessible porosity for diffusion that is generally smaller than the overall porosity, τ_d is the tortuosity for the diffusion and $\bar{D}_\alpha^\varpi$ is the diffusion coefficient in a free solution.

The dispersion tensor $\boldsymbol{D}'^\varpi$ is expressed as (Dymitrowska et al. 2014; Rodwell et al. 1999)

$$\boldsymbol{D}'^\varpi = d_T^\varpi \left| \boldsymbol{q}^\varpi \right| \boldsymbol{I} + \left(d_L^\varpi - d_T^\varpi \right) \frac{1}{\left| \boldsymbol{q}^\varpi \right|} \boldsymbol{q}^\varpi \otimes \boldsymbol{q}^\varpi \tag{C.9}$$

where d_L^ϖ and d_T^ϖ are the longitudinal and transversal dispersivity coefficients of the fluid phase ϖ.

In unsaturated porous media, there is a phase transformation between the liquid phase and gas phase. For example, gas can dissolve into water and water can evaporate into gas. The mass fraction of water vapour in gas phase can be determined by the psychrometric law: (Dymitrowska et al. 2014)

$$\omega_w^g = p_w^{g0} \frac{M_w}{RT\rho^g} \exp\left(\frac{-\left(p^g - p^l\right) M_w}{RT\rho^l} \right) \tag{C.10}$$

where M_α is the molar mass of the fluid component α, R is the ideal gas constant, T is the absolute temperature and p_w^{g0} is the water vapour pressure in equilibrium with liquid water at a planar surface.

The mass fraction of gas that dissolves in water is determined by Henry's law: (Dymitrowska et al. 2014)

$$\omega_g^l = \left(\omega_g^g \rho_g\right) \frac{RT}{HM_g} \tag{C.11}$$

where H is the Henry's constant.

4.1.2 Visco-Capillary Two-Phase Flow

The visco-capillary two-phase flow in porous media is commonly described by the generalized Darcy's law:

$$\boldsymbol{q}_\alpha = -\frac{\boldsymbol{k}_{in} k_{r\alpha}}{\mu_\alpha} \nabla\left(\boldsymbol{p}_\alpha - \rho_\alpha \boldsymbol{g}\right) \tag{C.12}$$

where $\boldsymbol{k}_{in}$ is the intrinsic permeability tensor, $k_{r\alpha}$ is the relative permeability, μ_α is the fluid dynamic viscosity, p_α is the pore fluid pressure, ρ_α is the density, and $\boldsymbol{g}$ is the gravitational acceleration.

Gas migration in saturated bentonite is accompanied by complex coupled HM processes. To account for the mechanical effect on the fluid flow, the conventional Darcy's law was enhanced by coupling the intrinsic permeability with mechanical variables, e.g. damage variable, plastic strain, volumetric strain, etc., thus leading to various intrinsic permeability models.

4.1.2.1 Intrinsic Permeability

Intrinsic permeability directly controls the gas flow behaviors in bentonite, including the evolution of gas pressure, the gas breakthrough and the gas outflow rate. The previously proposed models can be classified as five categories, as shown in Table C.2.

Gas-pressure-based models were phenomenologically developed based on the experimental observation that gas pressure needs to reach a critical value (which may be associated with the external confining stress) to trigger the gas breakthrough event. As indicated by Eq. (C.13)-(C.15), the intrinsic permeability will experience a significant increase when the gas pressure

reaches a critical value. These phenomenologically based models contain less information about the evolutions of either pore size or pore structure which are the fundamental factors affecting the intrinsic permeability. In order to account for the evolution of the available pore space for fluid flow, a scaling coefficient, M_k, was introduced into the intrinsic permeability model in (Ye et al. 2014). The scaling coefficient, which was interpreted as the cumulative percentage of the intruded pores in MIP test, will increase with the rise of gas pressure. However, the pore size distribution taken by the scaling coefficient is the one measured prior to the gas injection test. During the gas migration process, the pore size distribution may experience significant changes. Therefore, the scaling coefficient cannot reflect the dynamic evolution of pore size distribution.

The porosity-based model, as given by Eq. (C.16), can capture the contribution from the change of pore volume to the evolution of intrinsic permeability. By calibrating the introduced empirical parameter, a significant rise of intrinsic permeability may be achieved by the model. However, the development of preferential pathways not only involves the change in pore size, but also the evolution of pore structure which is a more important factor controlling the intrinsic permeability. Clearly, this simple porosity-based model is not able to reflect this feature.

The strain-based model, as expressed by Eq. (C.17), has incorporated the equivalent plastic strain and the volumetric strain. The equivalent plastic strain, which is defined with respect to the deviatoric plastic strain, can be regarded as a measure of pore structure evolution. Meanwhile, the volumetric strain is a measure of pore size evolution. In addition, introducing the plastic strain in the model is beneficial to achieving a rapid increase of permeability once the yield criterion is reached. This permeability model is originally adopted to simulate gas flow in rocks which may experience shear failure. If the tensile failure is preferable, the equivalent plastic strain in the model can be replaced by the maximum principal strain to account for the possible opening of the developed fractures.

The damage-based permeability model, as expressed by Eq. (C.18), consists of two parts, i.e., an undamaged part controlled by the porosity and a damaged part by the damage variable. The damage is a combination of the tensile-induced and the compression-induced damage (Dagher et al. 2018; Fall et al. 2014). Therefore, this damage-based model also accounts for the effect of both volume change and pore structure evolution on the permeability. As seen from Eq. (C.18), this model can capture the rapid increase of intrinsic permeability when the damage initiates. However, it is too simple to reflect the geometric features of the microfracture network, such as the aperture size, fracture density or orientation.

Table C.2 Models for intrinsic permeability for gas migration in barrier materials

Categories	Models for intrinsic permeability	Eq.	References
Gas pressure based models	$k_{in}=\begin{cases}\left(1+C_1 p_g\right)k_{\text{in}0}, & p_g \le p_{cr}\\ \left[C_2\left(p_g-p_{cr}\right)+1+C_1 p_{cr}\right]k_{\text{in}0}, & p_g \le p_{cr}\end{cases}$	(C.13)	(Xu et al. 2013)
	$k_{in}=\begin{cases}k_{in0}, & \text{when } p_g \le p_w + p_{sw}\\ k_{in0}C_3\left(\begin{matrix}1+c_r\left(p_{sw}-p_0\right)\\ +C_5 c_r\left(p_g-p_{sw}\right)\end{matrix}\right)^{C_4}, & \text{once } p_g > p_w + p_{sw}\end{cases}$	(C.14)	(Tawara et al. 2014)
	$k_{in}=k_{in0}+C_6\exp\left[C_7\left(p_{\min}-p_g-p_{cr}\right)\right]$ $M_k=P_{cum}=\sum_{i=1}^{n_M}C_i\left[\log\left(p_g-p_w\right)\right]^{i-1}$	(C.15)	(Ye et al. 2014)
Porosity-based model	$k_{in}=k_{in0}\exp\left[C_8\left(\phi-\phi_0\right)\right]$	(C.16)	(Tamayo-Mas et al. 2018)
Strain-based model	$k_{in}=k_{in0}\exp\left(C_9\varepsilon_v+C_{10}\bar{\varepsilon}_{pl}\right)$	(C.17)	Nguyen and Le (2014)
Damage-based model	$k_{in}=k_{UD}+k_D$ $k_{UD}=k_{in0}\exp\left[C_{11}\left(\phi-\phi_0\right)\right]$ $k_D=\frac{d}{d_{\max}}\left(k_{\max}-k_{UD}\right)$	(C.18)	(Dagher et al. 2018; Fall et al. 2014)
Embedded fracture model	$\boldsymbol{k}_{in}=k_{mat}\boldsymbol{I}+\frac{b^3}{12a}\boldsymbol{n}_f\otimes\boldsymbol{n}_f$ $b=b_0+a\left\langle\varepsilon_n-\varepsilon_0\right\rangle$	(C.19)	(Olivella and Alonso 2008)

Note: k_{in} is the intrinsic permeability, k_{in0} is the initial intrinsic permeability, p_0 is the atmospheric pressure, p_g is the gas pressure, p_w is the water pressure, p_{cr} is a critical gas pressure, p_{sw} is the swelling pressure, c_r is the mineral compressibility, $p_{\min}$ is the minimum principal stress, ϕ is the porosity, ϕ_0 is the initial porosity, ε_v is the volumetric strain, $\bar{\varepsilon}_{pl}$ is the equivalent plastic strain, k_{UD} is the undamaged permeability, k_D is the damaged permeability, d is the damage variable, $d_{\max}$ is the maximum damage variable, $k_{\max}$ is the maximum permeability corresponding to $d_{\max}$, k_{mat} is the permeability of clay matrix, b is the aperture, b_0 is the initial aperture, a is the fracture spacing, $\boldsymbol{n}_f$ is the normal vector of fracture, ε_n is the strain normal to the fracture, ε_0 is a critical strain controlling the opening of fracture and C_i is the empirical parameter for calibration.

Embedded fracture model (EFM) was widely adopted in previous numerical models to simulate the gas migration in saturated bentonite (Alonso et al. 2006; Dymitrowska et al. 2014; Gerard et al. 2010; Olivella and Alonso 2008). In this model, the developed fractures are conceptualized as a series of parallel fractures that are embedded in a porous matrix, as seen in Figure C.3. This permeability model, as expressed by Eq. (C.19), is a combination of the permeability for porous matrix and the permeability for the embedded fractures. Clearly, the EFM has incorporated the key geometric features of fractures, including aperture size, fracture density and orientation. In addition, the open/closure of the fracture is described by the evolution of the strain normal to the fracture. Therefore, compared with the aforementioned permeability models, EFM is more powerful to describe the evolution of intrinsic permeability caused by the development of microfracture network.

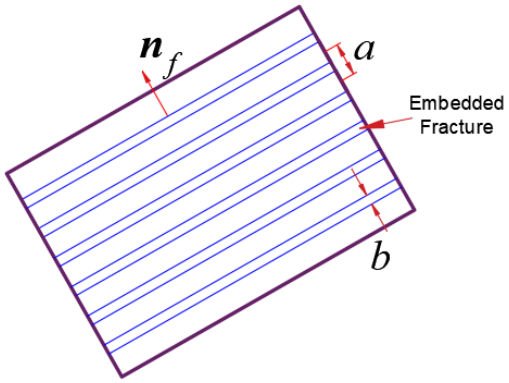

Figure C.3 Schematic graph of the embedded fracture model (a is the fracture spacing, b is the fracture aperture and $\boldsymbol{n}_f$ is the unit vector normal to the fracture)

It is worth noting that there are several variants for the original EFM. For example, the fracture aperture was defined with respect to the volumetric strain in (Dymitrowska et al. 2014) and to the stress normal to the fracture in (Rutqvist et al. 2018). Furthermore, the permeability tensor for embedded fractures, $\boldsymbol{k}_{ef}$, has been reformulated in (Levasseur et al. 2010) as

$$\boldsymbol{k}_{ef} = k_{ef0}\left(1 + C_k \left\langle \varepsilon_n - \varepsilon_0 \right\rangle\right)^3 \left(\boldsymbol{I} - \boldsymbol{n}_f \otimes \boldsymbol{n}_f\right) \tag{C.20}$$

where k_{ef0} is the initial permeability of the embedded fractures and C_k is a dimensionless parameter to be determined by model calibration.

In the original EFM, the embedded fractures only affect the hydraulic properties, such as intrinsic permeability and gas entry value. In the real case, the development of microfractures also degrades the mechanical properties, such as Young's modulus. Hence, the original EFM is not a fully coupled HM model. To account for the effect of embedded fractures on the mechanical behaviors, the normal stiffness of embedded fractures has been incorporated into the effective stiffness of fractured porous media (Martinez et al. 2013). Specifically, the increase of fracture aperture can reduce both the fracture stiffness and the overall stiffness of

the porous media. This improved EFM model was further extended to account for two sets of embedded fractures in an anisotropic clay matrix (Yang et al. 2020). However, it should be noted that the improved EFM was mainly applied to rocks where a certain amount of microfractures originally exist. However, the mechanical behavior of pre-existing fractures in soils has not yet been widely studied. More studies need to be performed to validate the applicability of this improved EFM to the saturated bentonite.

4.1.2.2 Water Retention Model

Water retention model significantly influences the response of bentonite to gas injection and the accuracy of model prediction (Madaschi and Laloui 2018). This is because the water retention model governs both effective stress and relative permeability through the degree of saturation. By far, the widely used water retention model for simulating gas migration in bentonite is van Genuchten model (van Genuchten 1980):

$$S_e = \left[1 + \left(\frac{p_c}{p_{gev}}\right)^n\right]^{-m} \tag{C.21}$$

$$S_e = \frac{S - S_{rw}}{1 - S_{rw}} \tag{C.22}$$

where S_e is the effective degree of saturation of the water phase, p_c is the capillary pressure, p_{gev} is the gas entry value, S_{rw} is the residual degree of saturation, m and n are shape parameters and $n = 1/(1-m)$.

The gas entry value is an important hydraulic property that controls the gas migration process. At intact state, the saturated bentonite has a very high gas entry value due to the extremely small pore size. Thus, the gas migration process is considerably inhibited at the beginning of the gas injection test. Once microfractures develop in bentonite sample under high gas pressure, the gas entry value decreases significantly, as the size of the microfractures is much larger than the pore size in clay matrix. As a result, the desaturation process is accelerated. In (Olivella and Alonso 2008), the evolution of gas entry value was described by a cubic root model (CRM) that was derived by combining the cubic law for intrinsic permeability of fractures and the Young-Laplace equation. The CRM is written as:

$$p_{gev} = p_{gev0}\left(\frac{k_{in0}}{k_{in}}\right)^{1/3} \tag{C.23}$$

where p_{gev0} is the initial gas entry value of the intact bentonite sample.

Based on Kozeny-Carman model, Young-Laplace equation and hydraulic radius concept, a similar CRM can also be derived to predict the gas entry value of porous media (Rodwell et al. 1999). Moreover, this CRM was also verified by in-situ dataset (Rodwell et al. 1999). Because of the solid physical meaning and in-situ evidence, this model has been widely used in previous coupled HM models, such as (Alonso et al. 2006; Arnedo et al. 2013; Arnedo et al. 2008; Dymitrowska et al. 2014; Gerard et al. 2014). In contrast, the gas entry value was defined as an exponential function of void ratio or porosity in some numerical studies, such as (Dagher et al. 2018; P. Damians et al. 2019). Compared with the CRM, this type of model is less physically based and therefore, was not widely used in previous numerical models.

Considering that the saturated bentonite presents bimodal pore size distribution, Madaschi and Laloui (2018) adopted an advanced water retention model originally developed by Dieudonne et al. (2017) to simulate the gas migration in compacted bentonite. This model has accounted for different retention mechanisms at two scales of pores, i.e., the adsorption in intra-aggregate pores and the capillarity in inter-aggregate pores. Nevertheless, the adsorption mechanism may be irrelevant to the gas migration process in bentonite, since the adsorbed water molecules are relatively immobile even under high gas pressure. Thus, considering the adsorption mechanism in water retention model may contribute little to reproducing the real gas migration process. In fact, it is the development of preferential pathways that significantly affects the water retention behavior of the tested bentonite. Currently, the effect of the developed pathways on the water retention model is solely reflected by the degradation of gas entry value. The evolution of shape parameters during the development of preferential pathways has not yet been examined in previous models. To realistically reproduce the gas migration process, the dynamic evolution of preferential pathways needs to be incorporated into the water retention model. In addition, water retention behavior is expected to experience strong hysteresis during the wetting and drying process. However, both the dynamic features and hysteretic behaviors are difficult to be modelled due to the complex process involved in this topic.

4.1.2.3 Relative Permeability

At present, there are two groups of relative permeability models that are commonly used to simulate the gas migration behavior in barrier materials, i.e. Mualem-van Genuchten model (MGM)(used in (Dagher et al. 2018; Sedighi et al. 2015; Senger et al. 2014; Xu et al. 2013; Ye et al. 2014)) and power law model (PLM) (used in (Damians et al. 2017; Gerard et al. 2014; Olivella and Alonso 2008; P. Damians et al. 2019; Puig Damians et al. 2019)).

The MGM is a closed-form analytical model to predict the relative permeability for unsaturated soils (Fredlund et al. 1994; Mualem 1976; van Genuchten 1980). The relative permeabilities for water, k_{rw}, and for gas, k_{rg}, are respectively expressed as

$$k_{rw}\left(S_e\right)=\sqrt{S_e}\left[1-\left(1-S_e^{1/m}\right)^m\right]^2 \tag{C.24}$$

$$k_{rg}\left(S_e\right)=\sqrt{1-S_e}\left(1-S_e^{1/m}\right)^{2m} \tag{C.25}$$

where S_e is the effective degree of saturation and m is a fitting parameter.

The PLM was developed from the macroscopic approach by Mualem (1978). In this approach, the wetting fluid is assumed to cover the whole surface of the soil matrix as a continuous component, whereas the nonwetting fluid resides in the internal pore volume (Mualem 1978). The derived power law model is expressed as

$$k_{r\alpha}\left(S_{e\alpha}\right)=S_{e\alpha}^{n_\alpha} \tag{C.26}$$

where $S_{e\alpha}$ is the effective degree of saturation of fluid component α and n_α is a parameter depending on soil type. The theoretical analysis in (Mualem 1978) indicated that n_α is lower than 3.0 for granular porous media and higher than 3.0 for fine-textured soils.

Figure C.4 compares the relative permeability of gas predicted by MGM and that by PLM with order of 3. It can be seen that the relative permeability predicted by the PLM is distinctly lower than that by the MGM over the whole range of degree of saturation. In particular, when the degree of saturation exceeds 0.8, the relative permeability of gas predicted by PLM is much smaller than that by MGM. Thus, it seems that the PLM with a higher order is more suitable to describe the localized gas flow. To enhance the flexibility of the PLM to fit the experimental data, Eq. (C.26) has been scaled by a coefficient, as seen in (Dymitrowska et al. 2014; Gonzalez-Blanco et al. 2016). Due to the limited experimental data and dynamic evolution of microfractures, the parameters included in the PLM have to be determined by model calibration.

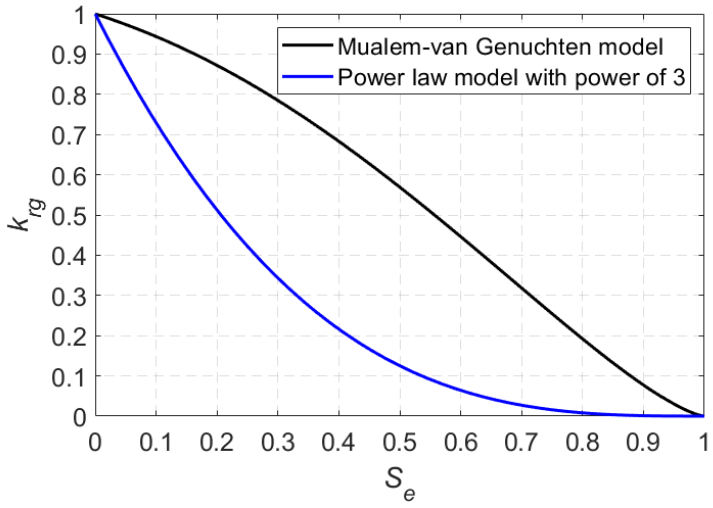

Figure C.4 Comparison between Mualem-van Genuchten model and power law model

4.1.3 Single Gas Flow Model

A single gas flow model was developed by Chittenden et al. (2020) based on the experimental finding that the bentonite sample can keep fully saturated after the gas injection test. The mechanical behavior is described by a simple linear elastic model. Therefore, the performance of the model to simulate the complex HM behavior primarily relies on the capability of the permeability model. Figure C.5 presents the conceptual model in which the single gas phase flows through a series of capillary tubes that account for a tiny percentage of the total pore space.

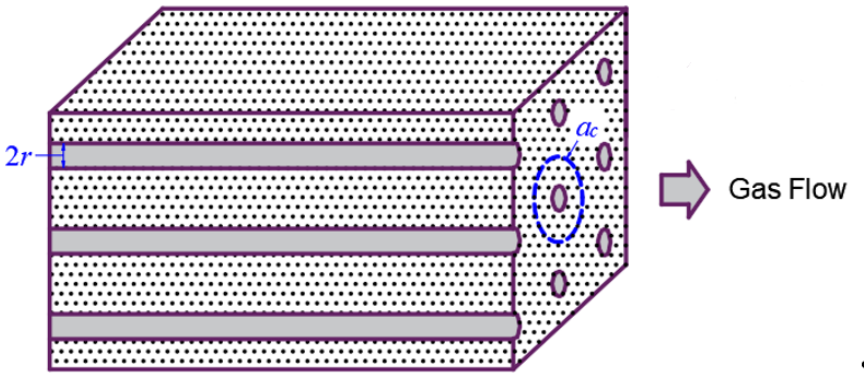

Figure C.5 Conceptual model for single gas flow (modified from (Chittenden et al. 2020))

Darcy's law is adopted to describe the single gas flow. The gas permeability consists of a capillary component and a creep component (Bond et al. 2020; Chittenden et al. 2020). The creep component is defined with respect to the creep porosity controlled by gas pressure. This component is introduced to account for the residual gas permeability when the gas injection is terminated. The capillary component is defined with respect to the capillary radius that is governed by gas pressure and total stress (Bond et al. 2020; Chittenden et al. 2020).

Compared with the standard multiphase flow model, the single gas flow model has considerably simplified the gas migration process, since the water retention model and relative permeability model were not considered. This simple model performs well in reproducing the experimentally observed behaviors, as seen in (Chittenden et al. 2020). This may be attributed to the consideration of several important mechanical behaviors, including the dilation of capillary tubes, the creep deformation and the pathways consolidation (i.e., several narrow capillaries emerge into a larger one). However, it is still not clear how the build-up of porewater pressure is simulated in this simple model. In addition, the complete removal of water transport process may exclude some possible HM processes. For example, the development of microfracture network may be accompanied by the localized consolidation of clay matrix which may involve the water transfer between the clay matrix and the developed fractures. Moreover, after the gas breakthrough event, water may infiltrate the tested sample through the developed pathways, thus leading to the closure and self-sealing of the developed fractures. Furthermore, the deviation in porewater pressure (caused by the glacial loading/unloading in the field) may influence the gas entry into the saturated bentonite (Graham et al. 2016). Therefore, the capability of this simple model to account for these coupled HM processes needs to be further examined.

4.2 Mechanical Models

Gas migration in saturated bentonite is accompanied by complex mechanical behaviors, such as the development of microfractures, the localized consolidation of clay matrix and the swelling behavior. In order to properly account for the effect of these mechanical behaviors in the coupled HM framework, previous mechanical constitutive models have covered various mechanical processes, such as plasticity, damage and swelling. These processes can be lumped into a general mechanical constitutive model:

$$\boldsymbol{\sigma}'_C = \mathbb{D}(d) : \left(\boldsymbol{\varepsilon} - \boldsymbol{\varepsilon}_{pl} - \boldsymbol{\varepsilon}_{sw}\right) \tag{C.27}$$

where $\boldsymbol{\sigma}'_C$ is the constitutive stress tensor (effective stress tensor or net normal stress tensor), $\mathbb{D}$ is the stiffness tensor, d is the damage variable, $\boldsymbol{\varepsilon}$ is the total strain tensor, $\boldsymbol{\varepsilon}_{pl}$ is the plastic strain tensor and $\boldsymbol{\varepsilon}_{sw}$ is the strain tensor due to swelling.

4.2.1 Elastic Models

Both linear and nonlinear elastic models were used to simulate the mechanical behavior of bentonite during the gas migration process. The linear elastic model developed in (Damians et al. 2020), was enriched by adding a dilatancy term due to the deviatoric strain to the volumetric strain. This enrichment may enhance the ability of the model to simulate the dilation of the pore space. The proposed nonlinear elastic models are generally pressured dependent. As defined in the Barcelona Basic Model (Alonso et al. 1990), the bulk modulus of the material, K, is proportional to the net mean stress, p'_n. Thus, p'_n is not allowed to be negative (note: the compressive stress is taken positive here) in the nonlinear elastic model. This means the tensile behavior of bentonite under high gas pressure cannot be accounted for by this nonlinear model. To achieved that, a constant minimum bulk modulus was assumed in (Dymitrowska et al. 2014), when the pressure-dependent bulk modulus decreases to this value.

Here, it is worth noting that the elastic stiffness of unsaturated soils can be affected by suction or water content (Qi and Vanapalli 2018; Yin and Vanapalli 2018). This nonlinearity was considered in (Mahjoub et al. 2017; Yamamoto et al. 2015) when studying the gas migration in barrier materials. However, it was widely observed that the tested bentonite sample can remain a fully saturated state after the gas injection test. The matric suction may be highly localized in the discrete pathways which only accounts for a tiny percentage of the pore space. It is still not clear for this topic whether the matric suction can have any significant influence on the elastic stiffness. Therefore, this coupling was generally neglected in previous numerical models for this topic.

4.2.2 Elastoplastic Models

Elastic models may not be strong enough to describe the complex mechanical behaviors of bentonite during gas flow process. Thus, the elastoplastic models have been introduced into the coupled HM framework. These elastoplastic models include Barcelona Basic Model (BBM), Drucker-Prager Model (DPM) and Mohr-Coulomb Model (MCM). As both BBM and

DPM are defined with respect to mean stress and deviatoric stress, the analysis to DPM is similar to that of BBM. Thus, only BBM and MCM will be analyzed as follows.

4.2.2.1 BBM

BBM was originally developed by Alonso et al. (1990) based on the independent stress state variables to simulate the elastoplastic behavior of unsaturated soils. This model was widely used to simulate the mechanical behavior of bentonite during the gas migration process, as seen in (Alonso et al. 2006; Dymitrowska et al. 2014; Olivella and Alonso 2008). The yield surface for the BBM at a given suction is presented in Figure C.6.

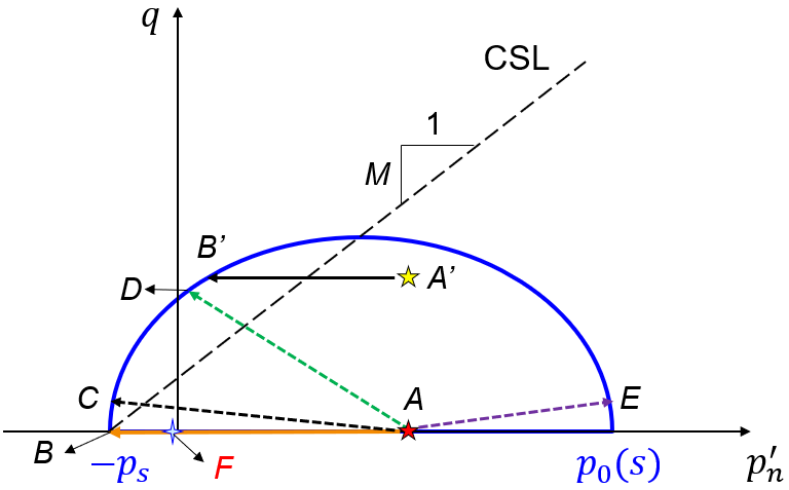

Figure C.6 Yield surface of BBM at a certain suction (Modified from (Alonso et al. 1990)) (CSL: Critical State Line; M: Slope of CSL)

According to Eq. (C.5), the increase of gas pressure is equivalent to an unloading process. For a material initially at an isotropic stress state, like point A in Figure C.6, with the increase of gas pressure, the stress state may evolve along three paths, such as A-B, A-C and A-D in Figure C.6. Under constant external stress condition, the increase of gas pressure only reduces the net mean stress, p'_n, whereas the deviatoric stress, q, remains constant. Thus, the stress state point will move along path A-B, and the sample is expected to experience a nonlinear elastic expansion with the increase of gas pressure. When the gas pressure exceeds the external confining stress, the sample will be subjected to tensile stress. In contrast, if the external boundaries are constrained, the total stress to which the material is subjected is expected to increase due to the rise of gas pressure. At a specific point in the material, if the constraint level varies with the change of direction, certain deviatoric stress may develop. Thus, the stress state may evolve along paths A-C or A-D in Figure C.6. However, the value that the deviatoric stress can reach depends on the specific constraint level. For the saturated bentonite under constant volume condition, the constraint to the sample is strong in each direction. Therefore, the developed deviatoric stress may not be significant, which means the stress state is more likely to evolve along path A-C. The stress state on this line may first become tensile stress before touching the yield surface of BBM. By far, the performance of BBM to describe the material in tensile state was rarely examined. For the bentonite material with a small tensile strength, it

is expected to experience a tensile failure after small tensile stress is reached (possibly represented by Point F in Figure C.6). This has been verified to some extent by the experimental finding that gas initially entries the saturated bentonite when the gas pressure reaches the sum of swelling pressure and porewater pressure, i.e. the total stress (Graham et al. 2012). It is worth noting that the effect of suction on the increase of tensile strength of bentonite is still not clear. However, the rise in suction can increase the pre-consolidation pressure, i.e. $p_0(s)$, thus leading to the expansion of the yield surface. This may further inhibit the occurrence of shear failure. As discussed above, the bentonite sample is more likely to experience a tensile failure during the gas migration process if it is initially in an isotropic stress state.

On the other hand, if the bentonite is initially subjected to a strong anisotropic stress state, like Point A' in Figure C.6, the shear failure is preferable to take place in the sample. However, most of previous experimental and numerical studies assumed the bentonite sample was initially in an isotropic stress state. In fact, previous numerical studies on this topic that adopted BBM or its extended version rarely reported the occurrence of plastic strain due to the rise of gas pressure, as seen in (Alonso et al. 2006; Dymitrowska et al. 2014; Olivella and Alonso 2008). In (Dagher 2020), the plastic behavior during gas injection was numerically observed and analyzed. This may be attributed to the introduced heterogeneity for the HM properties, as well as initial defects introduced in the sample before the gas injection. In addition, it is found that the simulated stress state in (Dagher 2020) after the hydration stage is less than the measured swelling pressure in the experiment. Therefore, it needs to be further examined whether the plastic process could appear in the real stress state.

Once the preferential pathways develop in the bentonite sample, the highly pressurized gas may significantly compress the porous matrix surrounding the pathways, thus leading to the localized consolidation. The stress state in the porous matrix may evolve along path A-E in Figure C.6. Once the stress reaches the yield surface, the surface expands outwards and volumetric plastic strain develops in the porous matrix. This plastic strain may inhibit the closure of the developed pathways after the gas breakthrough event. By far, this volumetric plastic strain has not yet been considered in previous numerical models.

4.2.2.2 MCM

MCM has been used to simulate the plastic behavior of natural barrier materials during the gas migration process, as seen in (Nguyen and Le 2014; Xu et al. 2013). Figure C.7 presents the Mohr-Coulomb failure line and two Mohr circles, i.e. C1 and C2, at two stress states. The size of the Mohr circle depends on the difference between the maximum and the minimum principal stress. The size of C1 is smaller than that of C2, which means C2 is subjected to a more significant anisotropic stress state. With the increase of gas pressure, the Mohr circle, C2, will move towards the left side. When the circle touches the yield line, both shear and volumetric plastic strain appear. The resulted shear failure zone may serve as the preferential pathways for gas migration. In contrast, the Mohr circle, C1, will not touch the Mohr-Coulomb line as the gas pressure increases because of its small size. Therefore, with the increase of gas pressure, the shear failure is more likely to occur in the sample that is initially subjected to larger deviatoric stress. This is consistent with the previous analysis of the BBM. Thus, MCM seems more suitable to model the shear failure of natural rock formations (that are generally

subjected to an anisotropic stress state) due to the CO_2 injection (Cappa and Rutqvist 2011; Rutqvist and Tsang 2002). In contrast, the bentonite is more likely to be subjected to a nearly isotropic stress state (resulting in a very small Mohr circle, like C1 in Figure C.7). With the increase of gas pressure, the Mohr circle may not touch the yield line before the tensile strength is reached. In analogy to the analysis in the previous section, the Mohr circle may be enlarged due to the different constraint level in different directions. However, this effect may not be significant for bentonite under constant volume condition. Therefore, the rise of pore pressure is more likely to induce a tensile failure in the material that is initially in an isotropic state. To account for the tensile failure, a tensile cut-off line has been added to the Mohr-Coulomb line, as seen in Figure C.7. This improved MCM has been adopted in (Xu et al. 2013) to simulate the tensile failure of claystone driven by the high gas pressure. This enriched MCM may also be suitable to simulate the tensile induced failure in bentonite material if the required parameters are available.

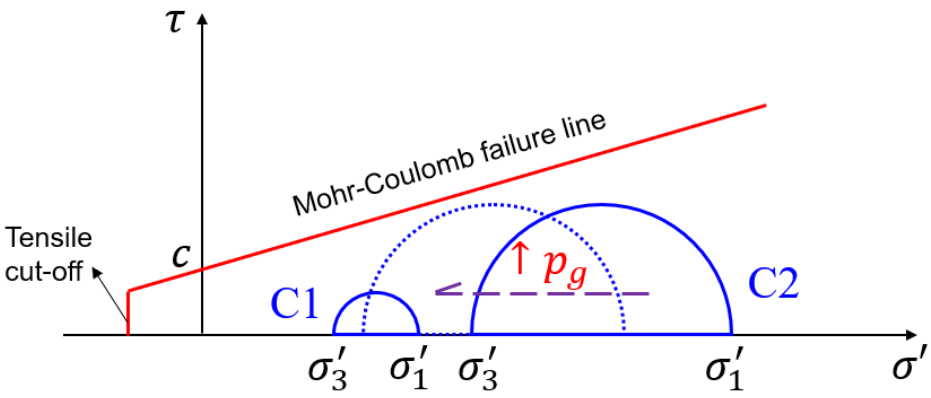

Figure C.7 Movement of Mohr circle with the increase of gas pressure

4.2.3 Damage Models

When gas pressure exceeds the sum of total stress and tensile strength, a series of microfractures are developed in the saturated bentonite (Harrington et al. 2017; Rodwell et al. 1999). These microfractures can degrade the material stiffness and provide preferential pathways for gas flow. Explicitly simulating the microfractures is mathematically complex and computationally demanding. To avoid that, damage models were commonly employed in previous studies to implicitly simulate the fracturing process. The fracturing process is described by the evolution of the damage field. For a simple isotropic damage model, the damaged Young's modulus can be defined as

$$E(d) = (1-d)E_0 \tag{C.28}$$

where $E(d)$ is the damaged Young's modulus, E_0 is the original Young's modulus and d is the damage variable.

Dagher et al. (2018) adopted a damage model, which has incorporated both the tensile-induced damage and the compressive/shear-induced damage, to simulate the development of microfracture network in bentonite. The tensile-induced damage is expressed as (Dagher et al. 2018):

$$d=\begin{cases}0 & \varepsilon<\varepsilon_{to}\\ 1-\dfrac{f_{tr}}{E_0\varepsilon} & \varepsilon_{to}\le\varepsilon<\varepsilon_{tu}\\ 1 & \varepsilon\ge\varepsilon_{tu}\end{cases} \tag{C.29}$$

where f_{tr} denotes the residual tensile strength, ε is the uniaxial tensile strain, ε_{to} is the strain that corresponds to the tensile strength and ε_{tu} is the tensile strain corresponding to a complete tensile failure.

It can be seen from (C.29) that the damage variable may experience two discrete jumps at $\varepsilon=\varepsilon_{to}$ and $\varepsilon=\varepsilon_{tu}$. This discontinuous feature may lead to some convergency issues in the simulation. In addition, this simple damage model was originally developed by Tang et al. (2002) for rocks, and then adopted in (Fall et al. 2014; Pazdniakou and Dymitrowska 2018) to simulate the gas-driven fracturing process in rocks. The application of this damage model in simulating the fracturing process in bentonite is questionable. As seen in Eq. (C.29), the residual tensile strength may be a property that is specific to the rock material. This property is not available for the bentonite material.

It should be noted that the damage variable predicted by the previously mentioned models is a scalar value. This means the damage caused by the high gas pressure can only be isotropic. In fact, the fracture may propagate along a preferential direction according to the specific stress state and the distribution of material properties. To realistically simulate the damaging process, advanced damage models that can account for the fracture orientation, aperture size and fracture density need to be developed.

4.2.4 Swelling Models

Once the developed microfracture network has connected with the outflow boundaries, a large amount of gas rapidly flows out of the sample, leading to the gas breakthrough phenomenon. As the gas pressure decreases, the external water may infiltrate the sample through the developed microfracture network. The changes in suction or water content may induce the swelling or shrinkage of the tested bentonite. The swelling of the clay is closely associated with the fracture closure and self-healing process. Thus, properly simulating the swelling process is critical to simulating the self-sealing behavior of tested bentonite. The swelling/shrinkage process has been simulated by a nonlinear elastic model in (Olivella and Alonso 2008), see Eq.(C.30), or a linear elastic model in (Tamayo-Mas et al. 2018), see Eq. (C.31).

$$\dot{\varepsilon}_{sw}=-\kappa_s\frac{\dot{s}}{s+p_{atm}} \tag{C.30}$$

$$\dot{\varepsilon}_{sw} = -K_{sc}\dot{s} \tag{C.31}$$

where ε_{sw} is the volumetric strain due to swelling, κ_s is the elastic stiffness parameter corresponding to suction, p_{atm} is the atmospheric pressure and K_{sv} is the swelling coefficient.

Another swelling/shrinkage model is defined with respect to the degree of saturation (Rutqvist et al. 2018):

$$\dot{\varepsilon}_{sw} = \beta_{sw}\dot{S}_w \tag{C.32}$$

where β_{sw} is a moisture swelling coefficient determined by model calibration. The numerical results in (Rutqvist et al. 2018) showed that considering the swelling/shrinkage due to the change in water content can offset part of the poroelastic stress changes, thus resulting in a good agreement between the numerical and experimental results.

It can be identified from the above swelling models that the swelling process is described in a rather simple way. In the real case, the swelling behavior may involve complex interactions between clay minerals, adsorbed water, capillary water and the gas phase. These coupling mechanisms need to be considered in future numerical works.

4.3 Discussions on the Pre-existing Numerical Models

The pre-existing numerical models for simulating gas migration in saturated bentonite are summarized in Table C.3.

As seen from Table C.3, all numerical models, except for Model 4, adopted the visco-capillary two-phase flow model to simulate the fluid flow in bentonite. Models for predicting relative permeability and gas entry value are relatively uniform. The MGM and PLM are commonly selected for predicting the relative permeability, while the CRM is dominantly used to describe the evolution of gas entry value because of its solid theoretical basis. In contrast, there are various intrinsic permeability models available for simulating the gas flow. As seen in Table C.3, the EFM and its variants are more favourable than the others, since they convey more information about the fracturing process and the fracture features. The first three models (Models 1-3) that only incorporate the two-phase flow model cannot capture the mechanical behavior of bentonite during the gas migration process. The permeability models that are defined with respect to the external stress may not be appropriate to describe the gas flow behavior under constant volume condition, because the total stress will increase as the highly pressurized gas infiltrates the saturated bentonite.

Most of previous numerical models were developed in the coupled HM framework to simulate the HM behaviors observed in experiments. To account for the development of preferential pathways, plastic and damage models have been incorporated into the framework. As analyzed in Section 4.2.2 in this appendix, with the increase of gas pressure, the tensile failure is more possible to occur in the bentonite sample that is initially subjected to a nearly isotropic stress state. Thus, the tensile failure needs to be properly accounted for in the plastic models, such as BBM and DPM. However, this does not mean that the shear failure could not

occur in a real bentonite sample. From a local viewpoint, the stress state may distribute heterogeneously in the real sample due to the heterogeneous distribution of dry density. This may lead to a high deviatoric stress state in specific areas. Once the highly pressurized gas reaches these areas, the shear failure may occur. Thus, the heterogeneity in stress state needs to be further examined in terms of its effect on the development of preferential pathways. The previous damage model provided an approach to implicitly simulate the development of preferential pathway under high gas pressure. However, it needs to be further improved to account for the fracture orientation, aperture size and density. Swelling models need to be further improved to account for the fundamental physics at the microscale.

The numerical models listed in Table C.3, except for Model 9 which will be introduced in the following section, have not yet explicitly considered the development of preferential pathways. Thus, these models may not be strong enough to realistically evaluate the effect of gas transport on the sealing ability of the saturated bentonite.

Table C.3 Numerical models for gas migration in saturated bentonite

No. of models	Hydraulic models			Mechanical models				Stress state variable		
	k_{in}	k_r	p_{gev}	Elastic ($\boldsymbol{\varepsilon}_{el}$)	Plastic ($\boldsymbol{\varepsilon}_{pl}$)	Damage (d)	Swelling (ε_{sw})	$\boldsymbol{\sigma}'$	$\boldsymbol{\sigma}'_n$	s
1	$k_{in}(\sigma, p_g)$	MGM	CRM	/	/	/	/	/	/	/
2	$k_{in}(p_g)$	MGM	Const	/	/	/	/	/	/	/
3	$k_{in}(p_g)$	MGM	CRM	/	/	/	/	/	/	/
4	$k_{in}(p_g, \sigma)$	/	/	Linear	/	/	/	✓	/	/
5	EFM	PLM	CRM	Linear	/	/	/	/	✓	/
6	EFM	PLM	?	Linear	DPM?	/	/	?	?	?
7	$k_{in}(d, \phi)$	MGM	$p_{gev}(e)$	Nonlinear	xBBM?	$d(\boldsymbol{\varepsilon}_{pl})$	$\varepsilon_{sw}(s)$	✓	/	/
8	$k_{in}(d, \phi)$	MGM	$p_{gev}(e)$	Linear	/	$d(\varepsilon_t, \varepsilon_c)$	$\varepsilon_{sw}(s)$	✓	/	/
9	vEFM	CM	CRM	Linear	/	MC	$\varepsilon_{sw}(S_w)$	✓	/	/
10	vEFM	CM	CRM	Linear	/	/	$\varepsilon_{sw}(S_w)$	/	✓	/
11	EFM	PLM	CRM	Nonlinear	BBM?	/	$\varepsilon_{sw}(s)$	/	✓	✓
12	vEFM	PLM	CRM	Nonlinear	BBM?	/	$\varepsilon_{sw}(s)$	/	✓	✓

References for the corresponding models listed above:

1: (Ye et al. 2014); 2: (Tawara et al. 2014); 3: (Calder et al. 2006); 4: (Chittenden et al. 2020); 5: (Damians et al. 2020); 6: (Damians et al. 2018); 7: (Dagher 2020); 8: (Dagher et al. 2018); 9: (Rutqvist et al. 2020); 10: (Rutqvist et al. 2018); 11: (Alonso et al. 2006; Gonzalez-Blanco et al. 2016; Olivella and Alonso 2008); 12: (Dymitrowska et al. 2014)

Note: EFM: Embedded Fracture Model; vEFM: variant of EFM; MGM: Mualem-van Genuchten Model; PLM: Power Law Model; CM: Corey's Model; CRM: Cubic Root Model; DPM: Drucker-Prager Model; BBM: Barcelona Basic Model; xBBM: extended BBM; MC: Mohr-Coulomb criterion.

5 Fracture Propagation Models

Both laboratory and in-situ tests, as discussed in Section 2.2, have shown that the coupled HM behaviors during gas migration are highly associated with the development of preferential pathways. To explore the fundamental physics involved in the gas migration process, it is necessary to simulate the development of preferential pathways in an explicit way. In this section, the fracture theories and numerical approaches for explicitly modelling the fracturing process will be reviewed and discussed.

5.1 Fracture Theories

5.1.1 Rankine-type Fracture Criterion

The extremely small pore size of saturated bentonite leads to a very high gas entry pressure that considerably inhibits the gas entry into the barrier material. As a result, the development of preferential pathways is a prerequisite for the gas entry. As discussed in Section 2.2, gas initially enters the saturated bentonite when the gas pressure exceeds the sum of the swelling pressure and the porewater pressure. This fracturing process is suitable to be described by the Rankine-type fracture criterion (RFC). Theoretically, this criterion can be interpreted from the viewpoint of Gibbs free energy that consists of water pressure, solute, adsorption, and gravitational components (Rodwell et al. 1999). The total potential of the porewater in bentonite is defined as the difference of Gibbs free energy, ΔG, between pore water and free water at a reference state. At an equilibrium state, the difference of Gibbs free energy, ΔG, should be zero (Rodwell et al. 1999):

$$\Delta G = \nu_w \left(\Delta p_w - \Delta \Pi_{SF} - \Delta \Pi_A \right) = 0 \tag{C.33}$$

where Δp_w is the change in the water pressure component, $\Delta \Pi_{SF}$ is the change in the immobile solute component, $\Delta \Pi_A$ is the change in the adsorption component, and ν_w is a partial molar volume of water.

The above equation infers that the porewater pressure exceeds the external free water pressure by an incremental water pressure Δp_w, i.e., $\Delta \Pi_{SF} + \Delta \Pi_A$, at the equilibrium state. The force caused by the incremental water pressure can be transmitted from point to point throughout the clay medium to the rigid boundary (Rodwell et al. 1999). The averaged force applied on the boundary is interpreted as the effective stress or swelling pressure. It is the incremental pressure lying along the midplanes between two adjacent clay particles that determines the swelling pressure (Rodwell et al. 1999). The averaged total stress is the sum of the calculated swelling pressure and the external water pressure. For the RFC, when gas pressure reaches the total stress (plus the tensile strength if applicable), the fracture starts to form and propagate. At the microscale, the gas pressure should reach the sum of the incremental water pressure at the midplanes and the external water pressure to create fractures. This is consistent with the assumption that the fracture initiation is caused by the rupturing of thin water films absorbed on the surface of clay minerals (Nash et al. 1998). Due to the non-uniform distribution of dry density or the orientation of clay particles, the local porewater pressure may differ from point to point, thus leading to the heterogeneous distribution of fractures in clayey

barrier materials. This microscale fracturing mechanism has not yet been considered in previous numerical models. It is expected that considering this fracturing mechanism will make the developed model more powerful to simulate the fundamental physics during gas migration process.

5.1.2 Linear Elastic Fracture Mechanics

Linear elastic fracture mechanics (LEFM) is developed based on the Griffith fracture criterion (GFC) which states that a fracture starts to propagate when the decrease in the elastic strain energy of the fractured material, is equal to the increase in the surface energy of the fracture (Rodwell et al. 1999). LEFM only concerns the contribution of elastic strain energy to the fracture propagation. Thus, it may not be suitable to simulate the fracturing process in saturated bentonite that may undergo plastic deformation (Hallett and Newson 2005; Hoch et al. 2004; Nash et al. 1998; Swift et al. 2001). In addition, LEFM can lead to a stress singularity at the fracture tip. This is not allowed in real geomaterials that have finite tensile strength. From the viewpoint of numerical implementation, a remeshing strategy is required to refine the mesh around the fracture tip in order to resolve the convergence issues caused by the stress singularity (Amarasiri and Kodikara 2010). Due to these limitations, LEFM was rarely used to simulate the fracturing process in clays.

5.1.3 Cohesive Zone Model

Cohesive Zone Model (CZM) introduces a fracture process zone to account for the micro-fracturing process ahead of the fracture tip, see the red zone in Figure C.8(a). The fracture process zone around the fracture tip consists of two cohesive surfaces that are held together by cohesive traction. The separation between the cohesive surfaces is controlled by cohesive traction and fracture energy, which is described by a traction-separation law (TSL), as seen in Figure C.8(b).

Compared with LEFM, CZM has eliminated the stress singularity at the fracture tip and can describe the nonlinear behavior in the fracture process zone. Moreover, CZM accommodates inelastic deformation in the material surrounding the developed fracture. Thus, CZM is more appropriate to simulate the fracturing process in saturated bentonite. At present, CZM has been used to simulate the desiccation cracking in unsaturated clays, as seen in (Amarasiri and Kodikara 2011; Gui et al. 2017; Gui et al. 2016; Vo et al. 2017). In recent literature, mixed-mode fracture and plastic effects were also incorporated in the CZM (Gui et al. 2016). Furthermore, CZM is also widely adopted to simulate the hydraulic fracturing in rocks (Carrier and Granet 2012; Chen et al. 2009; Dahi Taleghani et al. 2018; Guo et al. 2017; Li et al. 2017; Nguyen et al. 2017). Extending these models to account for the multiphase flow is relatively straightforward, as done in (Mohammadnejad and Khoei 2013; Salimzadeh and Khalili 2015a). It can be seen that the CZM-based fracturing models for either hydraulic fracturing or desiccation cracking have covered the main characteristics of the gas-driven fracturing in saturated bentonite, such as the fluid-driven fracturing process, multiphase flow and the possible plastic behavior. In addition, CZM is an approach that can be compatible with various numerical approaches, such as FEM, extended Finite Element Method (XFEM), FDEM, FEM with zero-thickness interfaces and DEM. Therefore, the CZM seems a suitable approach to

simulate the gas-driven fracturing process in saturated bentonite. However, the mechanical properties that are used to define the TSL, including the tensile strength and the fracture energy are still not available for saturated bentonite. More experimental works need to be conducted to determine these properties.

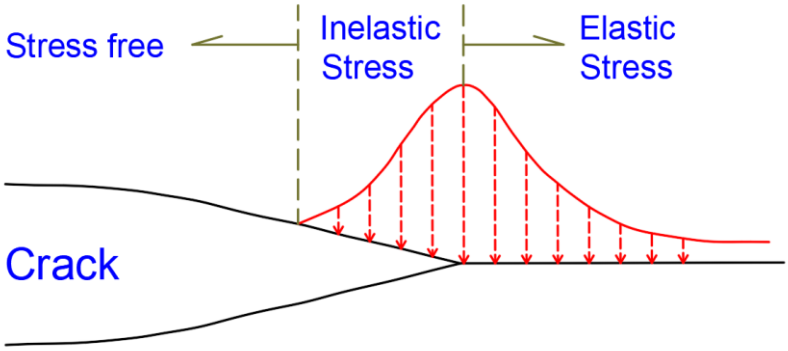

(a) Cohesive zone at the crack tip

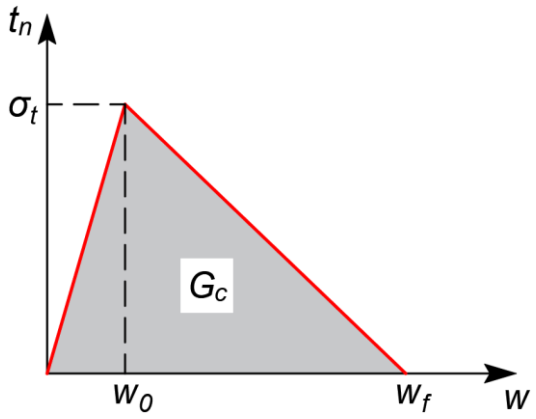

Note: σ_t : Tensile strength; w_0 : Separation at fracture initiation; w_f : Separation at full failure; G_c : Fracture energy

(b) Traction-separation law

Figure C.8 Schematic of crack zone model and an example of traction-separation law (Papanastasiou and Sarris 2017)

5.2 Numerical Methods

Above-introduced fracture theories can be implemented in different numerical methods. In this subsection, the existing and the potential numerical approaches for simulating the development of preferential pathways are introduced.

5.2.1 Existing Approaches

By far, explicit approaches for simulating the development of preferential pathways were not frequently reported in previous literature. Nash et al. (1998) developed a fracture propagation model based on the GFC to simulate the gas migration in saturated bentonite. The

fracture propagation is controlled by the gas pressure and the external total stress. This model can well simulate the evolutions of gas pressure and the gas outflow rate. However, it is rather simple to simulate other HM behaviors as discussed in Section 2.2 of the appendix. Since the model has not yet considered the mobile water, the build-up of water pressure and the water exchange between the fracture and the clay matrix cannot be simulated. In addition, as the model is not a fully coupled HM model, the fracture propagation model is not applicable to simulate the fracturing process under constant volume condition.

Lawrence Berkeley National Laboratory (LBNL) proposed a rigid-body-spring network (RBSN), a type of discrete fracture network (DFN) model, to simulate the development of preferential pathways in bentonite, as seen in (Rutqvist et al. 2018). The fracturing process of a local rigid-body-spring element is represented by the degradation of stiffness between springs (Kim et al. 2017). The well-known code, TOUGH, is used to simulate the multiphase flow behavior. The evolutions of both porewater pressure and total stress as observed in experiments can be well simulated, as seen in (Rutqvist et al. 2018). However, the numerical results showed that the localized gas flow was less satisfactorily described. Specifically, the fractures uniformly propagated through the whole cross-section in 2-D simulations, while the fractures formed clusters and then extended to the circumferential surface in 3-D simulations. These results may be caused by either the relatively larger element or the relatively homogeneous HM properties that were applied to the coupled TOUGH-RBSN model. Applying fine elements or more heterogeneous HM properties may contribute to a more distinct preferential gas flow. In addition, the bulk element in RBSN approach is nondeformable. Therefore, the localized consolidation of clay matrix and the possible water exchange between clay matrix and developed fractures may not be captured by this model.

5.2.2 Potential Approaches

There are various explicit approaches having been used to simulate hydraulic fracturing and desiccation cracking. These approaches may become the potential approaches for simulating the gas-driven fracturing in saturated bentonite. Based on the type of numerical method, these approaches can be classified into FEM-based approaches and DEM-based approaches.

The standard FEM is a continuous numerical method that is not able to describe the displacement jump. To simulate the discrete fracture by using FEM, a common treatment is to insert a zero-thickness interface element between two adjacent bulk elements. The mechanical behavior of the interface element was generally described by a CZM. This numerical approach has been used to simulate the hydraulic fracturing, as seen in (Carrier and Granet 2012; Chen et al. 2009; Nguyen et al. 2017). However, for most of the interface-enriched FEM models, the propagation direction needs to be predefined. In contrast, the XFEM, in which a new shape function is defined, can simulate the arbitrary fracture propagation without introducing the interface element. In (Mohammadnejad and Khoei 2013; Salimzadeh and Khalili 2015b), the XFEM, combined with CZM, was used to simulate the fracturing process in unsaturated porous media. In these models, the two-phase fluid flow has been considered and the average pore pressure serves as the driving force for the fracturing process. As the displacement jump is described by an enriched shape function in XFEM, the remeshing strategy is not required to

track the fracture trajectory. Therefore, this approach seems a good candidate to simulate the arbitrary fracture propagation during the gas transport in saturated bentonite.

In recent years, phase field (PF) method has been a popular approach to explicitly simulate the fracture propagation. The PF method is a numerical approach that can regularize a sharp discontinuity into a diffusive fracture zone by introducing a fracture density functional (Mauthe and Miehe 2017). The evolution of the PF variable is controlled by a governing equation that is derived from either the microforce balance law or the variational principle of free energy minimization. The governing equation can be easily implemented into the standard FEM. Compared with the discontinuous approaches, as introduced in the preceding paragraph, the PF method is more suitable to simulate the fracture branching and kinking, as this approach does not involve any special treatments on the mesh or the shape function. Currently, this approach has been widely used to simulate hydraulic fracturing in rocks (Chen et al. 2020; Lee et al. 2016) and desiccation cracking in soils (Cajuhi et al. 2018; Heider and Sun 2020). Therefore, the PF method would be a potential approach to simulate the development of preferential pathways.

DEM-based approaches are more suitable to simulate strong discontinuities. Universal Distinct Element Code (UDEC) has been widely adopted to simulate the desiccation cracking in soils, as seen in (Amarasiri and Kodikara 2011; Amarasiri et al. 2011; Gui et al. 2016). Moreover, the UDEC has been coupled with TOUGH to simulate the coupled multiphase flow and discontinuous deformation in fractured porous media (Lee et al. 2019). This coupled TOUGH-UDEC method seems a powerful tool to simulate the development of preferential pathways in saturated bentonite, since it can incorporate the fracture propagation, the consolidation of clay matrix, the multiphase flow and the possible water transport between fractures and clay matrix.

Jain and Juanes (2009) proposed a grain-scale model based on PFC2D to simulate gas migration in saturated deformable media. The numerical results showed that gas migration may take place either by capillary invasion or by fracture propagation. The capillary invasion is favoured in coarse-grain porous media, while fracture propagation mainly takes place in fine-grain porous media. This numerical result is qualitatively consistent with the experimental finding in this topic that the development of a microfracture network is a prerequisite for gas transport in saturated bentonite (Harrington et al. 2017). However, it is worth noting that the multiphase flow and capillary effect were treated in a very simple way in (Jain and Juanes 2009). To realistically account for the fluid flow, the lattice Boltzmann method (LBM) coupled with DEM can be adopted to simulate the multiphase flow in deformable porous media, as in (Kano et al. 2020; Montellà et al. 2019; Wang et al. 2020). This coupled LBM-DEM method may be a potential candidate to examine the gas migration in bentonite from a grain scale.

6 Summary and Conclusions

The review paper focuses on summarising and discussing previous coupled HM models for simulating gas migration in saturated bentonite. The reviewed models have covered governing equations, HM constitutive models, fracture theories and numerical approaches for simulating the development of preferential pathways in saturated bentonite.

The gas transport in saturated bentonite is generally modelled by a generalized Darcy's law. To account for the mechanical effect on fluid flow, previous intrinsic permeability models has been coupled with some mechanical variables, such as porosity, volumetric strain, tensile strain, plastic strain and damage variable. The capability of an intrinsic permeability model highly depends on the amount of physical or geometrical information it conveys. EFM has accounted for the fracturing mechanism and incorporated more geometrical features of fractures. Thus, EFM and its variants are the most widely used permeability models to simulate the gas migration in saturated bentonite. Compared with the diverse intrinsic permeability models, the adopted relative permeability models are relatively uniform, mainly including MGM and PLM. In almost all numerical models, van-Genuchten model was used to describe the water retention behavior. To account for the effect of the development of preferential pathways on the water retention behavior, the gas entry value was generally coupled with the intrinsic permeability (which is also controlled by the pathways) through a CRM.

At present, both the Bishop-type effective stress and the independent stress state variables have been adopted to develop the mechanical models for this research topic. Both stress state variables have their benefits and limitations. It is still open for discussion that which stress state variable is more appropriate for the current research topic. The adopted mechanical models include linear/nonlinear elastic models, elastoplastic models, damage models and swelling models. The elastoplastic models and damage models are proposed for simulating the possible shear failure and tensile failure caused by the high gas pressure. These inelastic models have accounted for the development of microfracture network in an implicit way. The hydration-induced swelling is associated with the closure and the self-sealing of the developed fractures. It is generally modelled in a simple way in which the swelling strain was defined with respect to degree of saturation or suction.

The development of preferential pathways that directly controls the complex HM couplings is desirable to be simulated in an explicit way. Current numerical approaches that can explicitly simulate the gas-driven fracturing in saturated bentonite are not frequently reported. Three fracture theories are introduced, including LEFM, Rankine-type fracture criterion and CZM. LEFM mainly concerns the elastic strain energy, it is not suitable to simulate the fracturing in saturated bentonite which may undergo plastic deformation. Rankine-type fracture criterion has been examined from the viewpoint of Gibbs free energy. Its rationality has been verified by the experimental finding that gas starts to enter the saturated bentonite when gas pressure reaches the sum of swelling pressure and porewater pressure. CZM introduces a fracture process zone ahead of the fracture tip which contributes to avoiding the issue of stress singularity. It can be well compatible with numerous numerical approaches, including FEM, XFEM, FDEM and DEM. Moreover, CZM has been widely used to simulate the hydraulic fracturing in rocks and desiccation cracking in soils. Therefore, CZM is a promising approach to simulate the gas-driven fracturing in saturated bentonite.

In light of the current research status of this topic, several aspects can be considered in future numerical works:

(1) Introducing the double pore structure of compacted bentonite in numerical models can be beneficial to simulating the localized consolidation of clay matrix, the water

exchange between pores and developed fractures and the almost saturated state after gas injection test.

(2) Advanced damage models that can capture the fracturing mechanism and account for the geometric features of the developed fractures, such as fracture orientation, aperture size and fracture density, are necessary to be developed.

(3) The dry density of the real bentonite sample may distribute heterogeneously, thus leading to the heterogeneity in both HM properties and stress state. Considering the heterogeneity of stress state is expected to significantly enhance the ability of the numerical model to simulate the development of preferential pathways.

(4) To reliably evaluate the effect of gas transport on the sealing capability of the saturated bentonite, the development of preferential pathways needs to be simulated in an explicit way. Some potential numerical approaches, such as PF method, XFEM and TOUGH-UDEC, can be further studied and improved to simulate the gas-driven fracturing process. CZM is a promising approach to describe the fracturing process in bentonite.

(5) Self-sealing behaviors of the tested bentonite sample were rarely examined in previous numerical studies, although they are crucial for the performance assessment of the DGR. Self-sealing of bentonite may involve complex couplings between clay minerals, adsorbed water, capillary water and gas phase at a microscopic scale. These couplings need to be properly accounted for in future numerical models for obtaining a comprehensive understanding of the self-sealing process.

Appendix D Derivation of Double Effective Stress Concept

Borja and Koliji (2009) derived a thermodynamically based effective stress model for unsaturated soils with double porosity based on the mixture theory. This approach is extended to derive a double effective stress concept based on the assumption of small deformation and incompressible solid grains. The porosity of the submixture β, and the degree of saturation of the fluid α are defined respectively as:

$$\phi_\beta = \frac{V_\beta}{V_t} \tag{D.1}$$

$$S_{\beta\alpha} = \frac{V_{\beta\alpha}}{V_\beta} \tag{D.2}$$

where V_β, V_t are the void volume of the submixture β and the total volume of the porous media, respectively, and $V_{\beta\alpha}$ is the volume of the fluid α in the submixture β.

According to Eq. (46) in (Borja and Koliji 2009), and substituting the $\phi^{\beta\alpha}$ in the original equation with $S_{\beta\alpha}\phi_\beta$, the mass balance equation for fluid α in the submixture β can be expressed as:

$$\begin{aligned}&\frac{d(S_{\beta\alpha}\phi_\beta)}{dt}+\frac{S_{\beta\alpha}\phi_\beta}{K_{\beta\alpha}}\frac{dp_{\beta\alpha}}{dt}+S_{\beta\alpha}\phi_\beta\nabla\cdot\boldsymbol{v}_s\\&=c_{\beta\alpha}-S_{\beta\alpha}\phi_\beta\nabla\cdot\tilde{\boldsymbol{v}}_{\beta\alpha}-\tilde{\boldsymbol{v}}_{\beta\alpha}\cdot\nabla(S_{\beta\alpha}\phi_\beta)-\frac{S_{\beta\alpha}\phi_\beta}{K_{\beta\alpha}}\tilde{\boldsymbol{v}}_{\beta\alpha}\cdot\nabla p_{\beta\alpha}\end{aligned}\tag{D.3}$$

where $p_{\beta\alpha}$, $c_{\beta\alpha}$, $K_{\beta\alpha}$ *and* $\tilde{\boldsymbol{v}}_{\beta\alpha}$ are the fluid pressure, rate of mass density exchange, bulk modulus and relative velocity of the fluid α in the submixture β respectively, and $\boldsymbol{v}_s$ is the velocity of the solid.

Instead of introducing the pore fraction ψ^β as in the original approach, this paper will introduce the volumetric strain to the submixture β, for deriving its corresponding work-conjugated effective stress concept. The details are elaborated as below.

The first term on the left side of Eq. (D.3) can be decomposed as:

$$\frac{d(S_{\beta\alpha}\phi_\beta)}{dt}=S_{\beta\alpha}\frac{d\phi_\beta}{dt}+\phi_\beta\frac{dS_{\beta\alpha}}{dt}\tag{D.4}$$

The change in the rate of porosity in the above equation is obtained by taking the derivative of Eq. (D.1) as:

$$\frac{d\phi_\beta}{dt}=\frac{dV_\beta}{V_t dt}-\phi_\beta\frac{dV_t}{V_t dt}\tag{D.5}$$

Following the definition in Li et al. (2016) and the assumption of small deformation, the volumetric strain rates for the submixture β, $\dot{\varepsilon}_{\beta v}$, and for the entire mixture, $\dot{\varepsilon}_v$, are defined as:

$$\dot{\varepsilon}_{\beta v}=\frac{dV_\beta}{V_t dt}\tag{D.6}$$

$$\dot{\varepsilon}_v=\frac{dV_t}{V_t dt}\tag{D.7}$$

By using equality, i.e. $\nabla \cdot \boldsymbol{v}_s = \dot{\varepsilon}_v$, and the third term on the left side of Eq. (D.3) is rewritten as:

$$S_{\beta\alpha}\phi_\beta \nabla \cdot \boldsymbol{v}_s = S_{\beta\alpha}\phi_\beta \dot{\varepsilon}_v \tag{D.8}$$

Combining Eqs. (D.3) to (D.8), the mass balance equation for the fluid α in the submixture β is expressed as:

$$\begin{aligned} S_{\beta\alpha}\phi_\beta \nabla \cdot \tilde{\boldsymbol{v}}_{\beta\alpha} &= -S_{\beta\alpha}\dot{\varepsilon}_{\beta v} - \phi_\beta \frac{dS_{\beta\alpha}}{dt} - \frac{S_{\beta\alpha}\phi_\beta}{K_{\beta\alpha}} \frac{dp_{\beta\alpha}}{dt} + c_{\beta\alpha} \\ &- \tilde{\boldsymbol{v}}_{\beta\alpha} \nabla (S_{\beta\alpha}\phi_\beta) - \frac{S_{\beta\alpha}\phi_\beta}{K_{\beta\alpha}} \tilde{\boldsymbol{v}}_{\beta\alpha} \nabla p_{\beta\alpha} \end{aligned} \tag{D.9}$$

The rate of change in the internal energy density of the unsaturated double porous media as derived in Borja and Koliji (2009), is expressed as:

$$\rho \dot{e} = \boldsymbol{\sigma} : \dot{\boldsymbol{\varepsilon}} - \sum_{\beta=1}^{2} \sum_{\alpha=l,g} p_{\beta\alpha} S_{\beta\alpha}\phi_\beta \nabla \cdot \tilde{\boldsymbol{v}}_{\beta\alpha} + \frac{1}{2} \sum_{\beta=1}^{2} \sum_{\alpha=l,g} c_{\beta\alpha} \boldsymbol{v}_{\beta\alpha} \cdot \boldsymbol{v}_{\beta\alpha} + r_T - \nabla \cdot \boldsymbol{q} \tag{D.10}$$

where ρ is the density of the mixture, $\dot{e}$ is the rate of change in the internal energy per unit total mass of the mixture, $\dot{\boldsymbol{\varepsilon}}$ is the rate of change in the strain tensor, $\boldsymbol{\sigma}$ is the total stress tensor, $v_{\alpha\beta}$ is the velocity of the fluid α in the submixture β, r_T is the heat supplied per unit volume of the mixture, and $\boldsymbol{q}$ is a heat flux vector.

Substituting Eq. (D.9) into Eq. (D.10), and neglecting the heat supply and heat flux terms provide:

$$\rho \dot{e} = \boldsymbol{\sigma} : \dot{\boldsymbol{\varepsilon}} + \sum_{\beta=1}^{2} \sum_{\alpha=l,g} p_{\beta\alpha} S_{\beta\alpha} \dot{\varepsilon}_{\beta v} - \sum_{\beta=1}^{2} \sum_{\alpha=l,g} p_{\beta\alpha} G_{\beta\alpha} + \frac{1}{2} \sum_{\beta=1}^{2} \sum_{\alpha=l,g} c_{\beta\alpha} \boldsymbol{v}_{\beta\alpha} \cdot \boldsymbol{v}_{\beta\alpha} \tag{D.11}$$

$$G_{\beta\alpha} = -\phi_\beta \frac{dS_{\beta\alpha}}{dt} - \frac{S_{\beta\alpha}\phi_\beta}{K_{\beta\alpha}} \frac{dp_{\beta\alpha}}{dt} + c_{\beta\alpha} - \tilde{\boldsymbol{v}}_{\beta\alpha} \nabla (S_{\beta\alpha}\phi_\beta) - \frac{S_{\beta\alpha}\phi_\beta}{K_{\beta\alpha}} \tilde{\boldsymbol{v}}_{\beta\alpha} \nabla p_{\beta\alpha} \tag{D.12}$$

Here, it should be noted that $G_{\beta\alpha}$ in the above equation is different from that in the original equation because of the introduction of Eqs. (D.4)-(D.8).

The second term on the right side of Eq. (D.11) can be expressed as:

$$\sum_{\beta=1}^{2}\sum_{\alpha=l,g} p_{\beta\alpha}S_{\beta\alpha}\dot{\varepsilon}_{\beta v} = \bar{p}_1\dot{\varepsilon}_{1v} + \bar{p}_2\dot{\varepsilon}_{2v} \tag{D.13}$$

$$\bar{p}_1 = p_{1l}S_{1l} + p_{1g}S_{1g} \tag{D.14}$$

$$\bar{p}_2 = p_{2l}S_{2l} + p_{2g}S_{2g} \tag{D.15}$$

where $\bar{p}_1$, $\bar{p}_2$ are the average fluid pressure in submixtures 1 and 2, respectively, and $\dot{\varepsilon}_{1v}$, $\dot{\varepsilon}_{2v}$ are the volumetric strain rate of submixture 1 and 2, respectively.

Note that the rate of volumetric strain of subcontinuum β, $\dot{\varepsilon}_{\beta v}$, can be expressed with respect to the strain tensor as

$$\dot{\varepsilon}_{\beta v} = \dot{\boldsymbol{\varepsilon}}_\beta : \boldsymbol{I} \tag{D.16}$$

where $\boldsymbol{\varepsilon}_\beta$ is the strain tensor for subcontinuum β and $\boldsymbol{I}$ is a second-order identity tensor.

Combining Eqs. (D.11) to (D.16), and only considering the contribution of deformation to the rate of internal energy, Eq. (D.11) is reformulated as

$$\rho\dot{e}_d = \boldsymbol{\sigma}_1' : \dot{\boldsymbol{\varepsilon}}_1 + \boldsymbol{\sigma}_2' : \dot{\boldsymbol{\varepsilon}}_2 \tag{D.17}$$

$$\boldsymbol{\sigma}_1' = \boldsymbol{\sigma} + \bar{p}_1\boldsymbol{I} \tag{D.18}$$

$$\boldsymbol{\sigma}_2' = \boldsymbol{\sigma} + \bar{p}_2\boldsymbol{I} \tag{D.19}$$

where e_d is the internal energy without considering the contribution from fluid flow, $\boldsymbol{\sigma}_1'$ and $\boldsymbol{\sigma}_2'$ are the derived double effective stress tensors which are work-conjugated to their corresponding strain tensors $\dot{\boldsymbol{\varepsilon}}_1$ and $\dot{\boldsymbol{\varepsilon}}_2$, respectively.

Appendix E Simulation of Mx80-8 Test with Fine Mesh

To examine the effect of element size on the numerical result, the simulated domain for Mx80-8 test in Section 3.2 is meshed by elements of different size. As seen in Figure E.1, the element size reduces from the normal mesh to the finer mesh. In each meshing strategy, the gas injection boundary and the outflow boundaries are further refined, as the fluid flow on these

boundaries is the major concern of this study. This nonuniform element size and the curved injection boundary need to be meshed by an unstructured grid. The triangle element is adopted to generate such an unstructured mesh, since this element type can make a smooth transition from the smallest element to the largest element. Figure E.2 compares the evolutions of gas pressure simulated by using the three meshing strategies. It can be seen that the numerical result almost coincides with each other, which indicates the change of element size in the three meshing strategies has little influence on the numerical results.

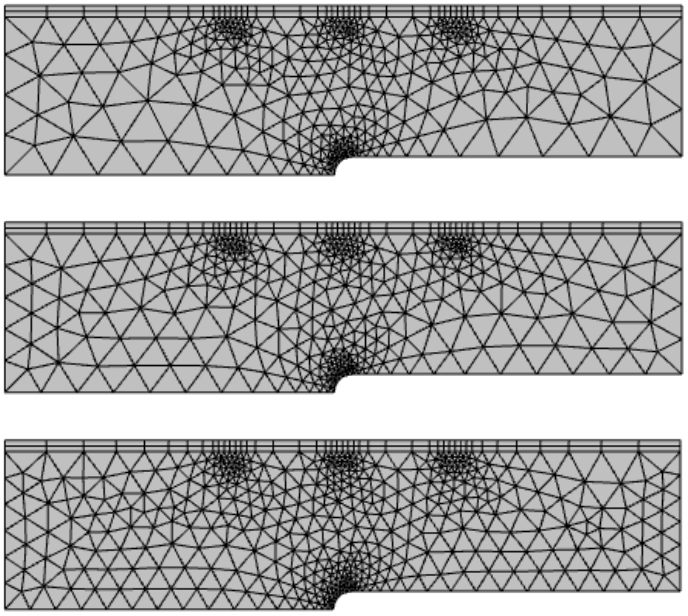

(a) Normal mesh

(b) Fine mesh

(c) Finer mesh

Figure E.1 Different meshing strategies for simulating Mx80-8 test in Section 3.2

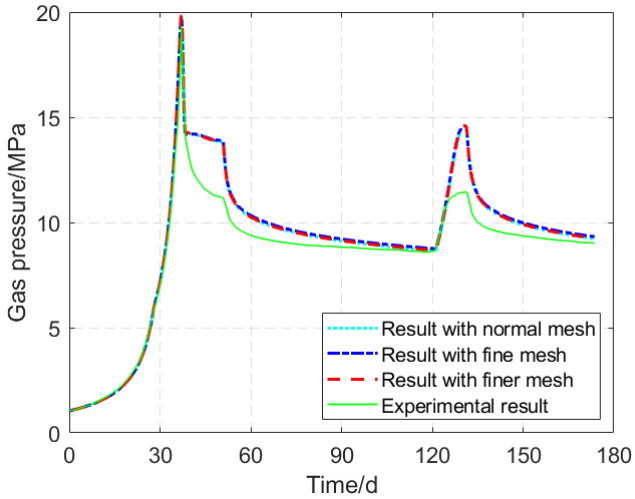

Figure E.2 Comparison of numerical results with different meshing strategies

The element size around the outflow boundaries (OFBs) of Mx80-8 test in Section 3.3 has also been examined in terms of its effect on the evolution of gas pressure. As seen in Figure E.3, the number of elements on the OFBs has increased from two to six. The quadrilateral

element is adopted to discretize the domain. Using the quadrilateral element to construct an unstructured grid may generate some malformed elements. However, since the mesh is very fine over the entire domain, a smooth transition between small elements and larger elements can be achieved. In addition, the Q4P4 quadrilateral element that is enriched by a stabilized technique can make the simulation more stable and efficient. The numerical results corresponding to the three meshing strategies are presented in Figure E.4. The evolution curves of gas pressure almost coincide with each other, which demonstrates that the numerical result is insensitive to the change of element size around the outflow boundaries.

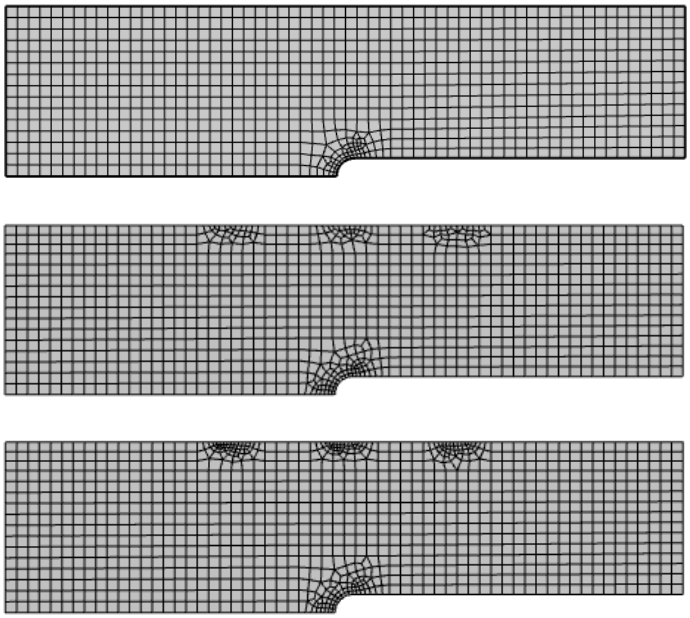

(a) Two elements on OFBs

(b) Four elements on OFBs

(c) Six elements on OFBs

Figure E.3 Different meshing strategies on OFBs of Mx80-8 test in Section 3.3 (OFB: Outflow boundary)

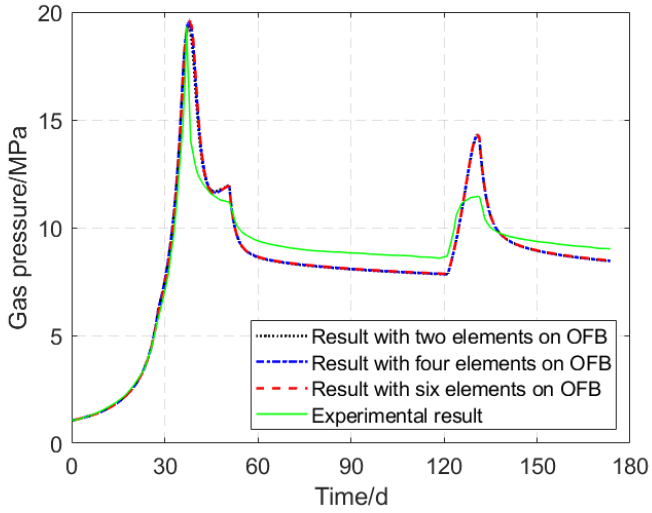

Figure E.4 Comparison of numerical results with different quantity of elements on OFBs

Appendix F 1D Terzaghi's Consolidation Problem

To solve the one-dimensional Terzaghi's consolidation problem, the analytical solution for the water pressure at position $z=z_1$ derived by (Terzaghi 1951) and cited in (Nguyen et al. 2017) is:

$$\frac{p(z_1)}{p_0}=\frac{4}{\pi}\sum_{j=1}^{\infty}\left\{\frac{(-1)^{j-1}}{2j-1}\cos\left[(2j-1)\frac{\pi}{2}\left(\frac{z_1}{h}\right)\right]\exp\left[-(2j-1)^2\frac{\pi^2}{4}\frac{c_v t}{h^2}\right]\right\} \tag{F.1}$$

where c_v is the coefficient of consolidation, m_v is the confined compressibility and p_0 is the initial pore pressure. These three parameters are determined by the following equations:

$$c_v=\frac{k_w}{\mu_w}\frac{1}{S+{\alpha_B}^2 m_v} \tag{F.2}$$

$$m_v=\frac{(1+v)(1-2v)}{(1-v)E} \tag{F.3}$$

$$p_0=\frac{\alpha_B m_v}{S+{\alpha_B}^2 m_v}\bar{t} \tag{F.4}$$

where S is the fluid storage coefficient and $\bar{t}$ is the load applied on the top boundary.

In Section 4.2.5.3, the solid grains and water are assumed incompressible, and therefore the fluid storage coefficient, S, and Biot's coefficient, α_B, are 0 and 1, respectively.

Appendix G Formulas for Spatially Auto-correlated Random Field

A random field $R(\boldsymbol{x})$ in a two-dimensional domain follows the lognormal distribution law with a mean of μ_R, and variance of σ_R^2. Then, its logarithm, $\ln R(\boldsymbol{x})$, follows the normal distribution law, i.e. $\ln R \sim N\left(\mu_{\ln R},\sigma_{\ln R}^2\right)$, where the mean, $\mu_{\ln R}$, and the variance, $\sigma_{\ln R}^2$, are expressed as (Santillán et al. 2017):

$$\mu_{\ln R}=\ln\mu_R-\frac{1}{2}\sigma_{\ln R}^2 \tag{G.1}$$

$$\sigma_{\ln R}^2=\ln\left(1+\sigma_R^2/\mu_R^2\right) \tag{G.2}$$

The random field $\ln R(\boldsymbol{x})$ is then expressed as:

$$\ln R(\boldsymbol{x}) = \mu_{\ln R} + \sigma_{\ln R} Z(\boldsymbol{x}) \tag{G.3}$$

where $Z(\boldsymbol{x})$ is a spatially auto-correlated random field that follows a standard normal distribution, $\ln R \sim N(0,1)$. For simplicity, the cross-correlation between different properties is neglected in this study. In addition, the random field is assumed stationary, which means that the means and variances remain the same at any point within the domain of interest.

The squared exponential type correlation function, as expressed by Eq. (G.4) (Li et al. 2015), is used to describe the spatially correlated features of the random field:

$$\rho(\tau) = \exp\left[-\pi\left(\frac{\tau_x^2}{\vartheta_h^2} + \frac{\tau_y^2}{\vartheta_v^2}\right)\right] \tag{G.4}$$

where τ_x and τ_y are the distance between two locations in the horizontal and the vertical directions, respectively; and ϑ_h and ϑ_v are the correlation length in the horizontal and the vertical directions, respectively. In this paper, ϑ_h is assumed equal to ϑ_v, which results in an isotropic auto-correlated random field.

Due to its theoretical simplicity and ease of implementation, the well-known Cholesky decomposition technique is used to generate the spatially auto-correlated random field. More details about this technique can be found in (Kasama et al. 2012; Li et al. 2015).

References

Alonso, E.E., Gens, A., and Josa, A. 1990. A constitutive model for partially saturated soils, Géotechnique 40(3): 405-430.

Alonso, E.E., Olivella, S., and Arnedo, D. 2006. Mechanisms of gas transport in clay barriers, Journal of Iberian Geology 32(2).

Alonso, E.E., Pereira, J.M., Vaunat, J., and Olivella, S. 2010. A microstructurally based effective stress for unsaturated soils, Geotechnique 60(12): 913-925.

Alonso, E.E., Vaunat, J., and Gens, A. 1999. Modelling the mechanical behaviour of expansive clays, Engineering Geology 54(1-2): 173-183.

Amann-Hildenbrand, A., Kroos, B., Harrington, J., Cuss, R., Davy, C., Skoczylas, F., Jacops, E., and Maes, N. 2015. Gas transfer through clay barriers, Developments in Clay Science 6: 227-267.

Amarasiri, A., and Kodikara, J. 2010. Use of material interfaces in DEM to simulate soil fracture propagation in Mode I cracking, International Journal of Geomechanics 11(4): 314-322.

Amarasiri, A.L., and Kodikara, J.K. 2011. Numerical modeling of desiccation cracking using the cohesive crack method, International Journal of Geomechanics 13(3): 213-221.

Amarasiri, A.L., Kodikara, J.K., and Costa, S. 2011. Numerical modelling of desiccation cracking, International Journal for Numerical and Analytical Methods in Geomechanics 35(1): 82-96.

Arnedo, D., Alonso, E.E., and Olivella, S. 2013. Gas flow in anisotropic claystone: Modelling triaxial experiments, International Journal for Numerical and Analytical Methods in Geomechanics 37(14): 2239-2256.

Arnedo, D., Alonso, E.E., Olivella, S., and Romero, E. 2008. Gas injection tests on sand/bentonite mixtures in the laboratory. Experimental results and numerical modelling, Physics and Chemistry of the Earth 33: S237-S247.

Ascher, U.M., and Petzold, L.R. 1998. Computer methods for ordinary differential equations and differential-algebraic equations. Society for Industrial and Applied Mathematics.

Birgersson, M., Åkesson, M., and Hökmark, H. 2008. Gas intrusion in saturated bentonite–A thermodynamic approach, Physics and Chemistry of the Earth, Parts A/B/C 33: S248-S251.

Bond, A., Chittenden, N., and Thatcher, K. 2020. RWM coupled processes project: Third annual report for DECOVALEX-2019.

Borja, R.I., and Koliji, A. 2009. On the effective stress in unsaturated porous continua with double porosity, Journal of the Mechanics and Physics of Solids 57(8): 1182-1193.

Burman, E. 2008. Pressure projection stabilizations for Galerkin approximations of Stokes' and Darcy's problem, Numerical Methods for Partial Differential Equations: An International Journal 24(1): 127-143.

Cajuhi, T., Sanavia, L., and De Lorenzis, L. 2018. Phase-field modeling of fracture in variably saturated porous media, Computational Mechanics 61(3): 299-318.

Calder, N., Avis, J., Senger, R., and Leung, H. 2006. Modifying TOUGH2 to support modeling of gas transport through saturated compacted bentonite as part of the large-scale gas injection test (LASGIT) in Sweden. In Proceedings of TOUGH Symposium. pp. 15-17.

Cappa, F., and Rutqvist, J. 2011. Modeling of coupled deformation and permeability evolution during fault reactivation induced by deep underground injection of CO2, International Journal of Greenhouse Gas Control 5(2): 336-346.

Carrier, B., and Granet, S. 2012. Numerical modeling of hydraulic fracture problem in permeable medium using cohesive zone model, Engineering Fracture Mechanics 79: 312-328.

Chen, B., Sun, Y., Barboza, B.R., Barron, A.R., and Li, C. 2020. Phase-field simulation of hydraulic fracturing with a revised fluid model and hybrid solver, Engineering Fracture Mechanics 229: 106928.

Chen, Z., Bunger, A., Zhang, X., and Jeffrey, R.G. 2009. Cohesive zone finite element-based modeling of hydraulic fractures, Acta Mechanica Solida Sinica 22(5): 443-452.

Chittenden, N., Benbow, S., Bond, A., and Norris, S. 2020. Development of an upscalable HM model for representing advective gas migration through saturated bentonite, International Journal of Rock Mechanics and Mining Sciences 133: 104415.

Choo, J., and Borja, R.I. 2015. Stabilized mixed finite elements for deformable porous media with double porosity, Computer Methods in Applied Mechanics and Engineering 293:

131-154.

Cuss, R.J., Harrington, J.F., Noy, D.J., Graham, C.C., and Sellin, P. 2014. Evidence of localised gas propagation pathways in a field-scale bentonite engineered barrier system; results from three gas injection tests in the large scale gas injection test (Lasgit), Applied Clay Science 102: 81-92.

Cuss, R.J., Harrington, J.F., Noy, D.J., Wikman, A., and Sellin, P. 2011. Large scale gas injection test (Lasgit): Results from two gas injection tests, Physics and Chemistry of the Earth 36(17-18): 1729-1742.

Dagher, E., Nguyen, T., and Sedano, J.I. 2018. Development of a mathematical model for gas migration (two-phase flow) in natural and engineered barriers for radioactive waste disposal, Geological Society, London, Special Publications 482: SP482. 414.

Dagher, E.E. 2020. A mathematical model for gas migration in natural and engineered barriers for radioactive waste disposal. In Department of Civil Engineering. University of Ottawa, Ottawa, Canada.

Dahi Taleghani, A., Gonzalez-Chavez, M., Yu, H., and Asala, H. 2018. Numerical simulation of hydraulic fracture propagation in naturally fractured formations using the cohesive zone model, Journal of Petroleum Science and Engineering 165: 42-57.

Damians, I.P., Olivella, S., and Gens, A. 2017. Modelling gas flow experiments in Mx80 bentonite. In 9th Workshop on CODE_BRIGHT, Barcelona.

Damians, I.P., Olivella, S., and Gens, A. 2018. Modelling spherical gas flow in Mx80 bentonite. In 10th Workshop on CODE_BRIGHT, Barcelona.

Damians, I.P., Olivella, S., and Gens, A. 2020. Modelling gas flow in clay materials incorporating material heterogeneity and embedded fractures, International Journal of Rock Mechanics and Mining Sciences 136: 104524.

Daniels, K.A., and Harrington, J. 2017. The response of compact bentonite during a 1-D gas flow test. British Geological Survey. OR/17/067.

Davy, C.A., Skoczylas, F., Lebon, P., and Dubois, T. 2009. Gas migration properties through a bentonite/argillite interface, Applied Clay Science 42(3-4): 639-648.

Delahaye, C.H., and Alonso, E.E. 2002. Soil heterogeneity and preferential paths for gas migration, Engineering Geology 64(2-3): 251-271.

Dieudonne, A.-C., Della Vecchia, G., and Charlier, R. 2017. Water retention model for compacted bentonites, Canadian Geotechnical Journal 54(7): 915-925.

Dymitrowska, M., Olivella, S., Arnedo, D., Alcoverro, J., and Alonso, E.E. 2014. Final modelling results and progress in gas transport modelling, FORGE Report D3.31: 71pp.

Fall, M., Nasir, O., and Nguyen, T.S. 2012. Coupled hydro-mechanical modelling of gas migration in Ontario's sedimentary rocks, potential host rocks for nuclear waste repositories. In Proceedings of Canadian Geotechnical Conference - GeoManitoba 2012, Winniped, Manitoba, Canada.

Fall, M., Nasir, O., and Nguyen, T.S. 2014. A coupled hydro-mechanical model for simulation of gas migration in host sedimentary rocks for nuclear waste repositories, Engineering Geology 176: 24-44.

Fredlund, D.G., Xing, A.Q., and Huang, S.Y. 1994. Predicting the Permeability Function for

Unsaturated Soils Using the Soil-Water Characteristic Curve, Canadian Geotechnical Journal 31(4): 533-546.

Frei, W. 2013. Solving multiphysics problems. Available from https://www.comsol.com/blogs/solving-multiphysics-problems/.

Gallé, C., and Tanai, K. 1998. Evaluation of gas transport properties of backfill materials for waste disposal: H2 migration experiments in compacted Fo-Ca clay, Clays and Clay Minerals 46(5): 498-508.

Gens, A., and Alonso, E.E. 1992. A framework for the behavior of unsaturated expansive clays, Canadian Geotechnical Journal 29(6): 1013-1032.

Gerard, P., Charlier, R., Barnichon, J.-D., Su, K., Shao, J.-F., Duveau, G., Giot, R., Chavant, C., and Collin, F. 2008. Numerical modelling of coupled mechanics and gas transfer around radioactive waste in long-term storage, Journal of theoretical and applied mechanics 38(1-2): 25-44.

Gerard, P., Harrington, J., Charlier, R., and Collin, F. 2014. Modelling of localised gas preferential pathways in claystone, International Journal of Rock Mechanics and Mining Sciences 67: 104-114.

Gerard, P., Radu, J.-P., Talandier, J., De La Vaissière, R., Charlier, R., and Collin, F. 2010. Numerical modelling of the resaturation of swelling clay with gas injection, Unsaturated Soils: 1383-1388.

Gonzalez-Blanco, L., Romero, E., Jommi, C., Li, X., and Sillen, X. 2016. Gas migration in a Cenozoic clay: Experimental results and numerical modelling, Geomechanics for Energy and the Environment 6: 81-100.

Gonzalez-Blanco, L., Romero, E., and Marschall, P. 2018. Effect of spatial heterogeneity on gas transport in compacted MX-80. In International Symposium on Energy Geotechnics 2018, Lausanne, Switzerland

Graham, C.C., Harrington, J.F., Cuss, R.J., and Sellin, P. 2012. Gas migration experiments in bentonite: implications for numerical modelling, Mineralogical Magazine 76(8): 3279-3292.

Graham, C.C., Harrington, J.F., and Sellin, P. 2016. Gas migration in pre-compacted bentonite under elevated pore-water pressure conditions, Applied Clay Science 132-133: 353-365.

Graham, J., Halayko, K.G., Hume, H., Kirkham, T., Gray, M., and Oscarson, D. 2002. A capillarity-advective model for gas break-through in clays, Engineering Geology 64(2-3): 273-286.

Gui, Y., Hu, W., Zhao, Z., and Zhu, X. 2017. Numerical modelling of a field soil desiccation test using a cohesive fracture model with Voronoi tessellations, Acta Geotechnica: 1-16.

Gui, Y., Zhao, Z., Kodikara, J., Bui, H.H., and Yang, S. 2016. Numerical modelling of laboratory soil desiccation cracking using UDEC with a mix-mode cohesive fracture model, Engineering Geology 202: 14-23.

Guo, J., Luo, B., Lu, C., Lai, J., and Ren, J. 2017. Numerical investigation of hydraulic fracture propagation in a layered reservoir using the cohesive zone method, Engineering Fracture Mechanics 186: 195-207.

Gutiérrez-Rodrigo, V., Villar, M.V., Martín, P.L., Romero, F.J., and Barcala, J.M. 2015. Gas-breakthrough pressure of FEBEX bentonite, Geological Society, London, Special Publications 415(1): 47-57.

Hallett, P., and Newson, T. 2005. Describing soil crack formation using elastic–plastic fracture mechanics, European Journal of Soil Science 56(1): 31-38.

Harrington, J., and Horseman, S. 2003. Gas migration in KBS-3 buffer bentonite, Sensitivity of Test Parameters to Experimental Boundary ConditionsSwedish Nuclear Fuel and Waste Management Company, Stockholm (Sweden).

Harrington, J.F., Graham, C.C., Cuss, R.J., and Norris, S. 2017. Gas network development in a precompacted bentonite experiment: Evidence of generation and evolution, Applied Clay Science 147: 80-89.

Harrington, J.F., Graham, C.C., Cuss, R.J., and Norris, S. 2019. Gas network development in compact bentonite: key controls on the stability of flow pathways, Geofluids 2019: 3815095.

Heider, Y., and Sun, W. 2020. A phase field framework for capillary-induced fracture in unsaturated porous media: drying-induced vs. hydraulic cracking, Computer Methods in Applied Mechanics and Engineering 359: 112647.

Hoch, A.R., Cliffe, K.A., Swift, B.T., and Rodwell, W.R. 2004. Modelling gas migration in compacted bentonite. POSIVA OY.

Horseman, S., Higgo, J., Alexander, J., and Harrington, J. 1996. Water, gas and solute movement through argillaceous media, Nuclear Energy Agency Rep. CC-96/1. OECD, Paris.

Horseman, S.T., Harrington, J.F., and Sellin, P. 1997. Gas migration in MX80 buffer bentonite, Scientific Basis for Nuclear Waste Management Xx 465: 1003-1010.

Horseman, S.T., Harrington, J.F., and Sellin, P. 1999. Gas migration in clay barriers, Engineering Geology 54(1-2): 139-149.

Hume, H.B. 1999. Gas breakthrough in compacted Avonlea bentonite. University of Manitoba, Winnipeg, Manitoba.

Jain, A.K., and Juanes, R. 2009. Preferential mode of gas invasion in sediments: Grain-scale mechanistic model of coupled multiphase fluid flow and sediment mechanics, Journal of Geophysical Research-Solid Earth 114(B8).

Kano, Y., Sato, T., and Oyama, H. 2020. Numerical study on the formations of gas channels and subsequent bubbles in unconsolidated sandy seabed sediment using a coupled LBM-DEM method, Journal of Natural Gas Science and Engineering 74: 103101.

Kasama, K., Whittle, A.J., and Zen, K. 2012. Effect of spatial variability on the bearing capacity of cement-treated ground, Soils and Foundations 52(4): 600-619.

Khalili, N., Geiser, F., and Blight, G. 2004. Effective stress in unsaturated soils: review with new evidence, International Journal of Geomechanics 4(2): 115-126.

Khalili, N., and Khabbaz, M.H. 1998. A unique relationship for chi for the determination of the shear strength of unsaturated soils, Géotechnique 48(5): 681-687.

Kim, K., Rutqvist, J., Nakagawa, S., and Birkholzer, J. 2017. TOUGH–RBSN simulator for hydraulic fracture propagation within fractured media: Model validations against

laboratory experiments, Computers & Geosciences 108: 72-85.
Laloui, L., and Nuth, M. 2009. On the use of the generalised effective stress in the constitutive modelling of unsaturated soils, Computers and Geotechnics 36(1-2): 20-23.
Lee, J., Kim, K.-I., Min, K.-B., and Rutqvist, J. 2019. TOUGH-UDEC: A simulator for coupled multiphase fluid flows, heat transfers and discontinuous deformations in fractured porous media, Computers & Geosciences 126: 120-130.
Lee, S., Wheeler, M.F., and Wick, T. 2016. Pressure and fluid-driven fracture propagation in porous media using an adaptive finite element phase field model, Computer Methods in Applied Mechanics and Engineering 305: 111-132.
Levasseur, S., Charlier, R., Frieg, B., and Collin, F. 2010. Hydro-mechanical modelling of the excavation damaged zone around an underground excavation at Mont Terri Rock Laboratory, International Journal of Rock Mechanics and Mining Sciences 47(3): 414-425.
Li, D.-Q., Jiang, S.-H., Cao, Z.-J., Zhou, W., Zhou, C.-B., and Zhang, L.-M. 2015. A multiple response-surface method for slope reliability analysis considering spatial variability of soil properties, Engineering Geology 187: 60-72.
Li, J., Yin, Z.-Y., Cui, Y., and Hicher, P.-Y. 2016. Work input analysis for soils with double porosity and application to the hydromechanical modeling of unsaturated expansive clays, Canadian Geotechnical Journal 54(2): 173-187.
Li, Y., Deng, J.G., Liu, W., and Feng, Y. 2017. Modeling hydraulic fracture propagation using cohesive zone model equipped with frictional contact capability, Computers and Geotechnics 91(Supplement C): 58-70.
Liu, J.-F., Song, Y., Skoczylas, F., and Liu, J. 2016. Gas migration through water-saturated bentonite–sand mixtures, COx argillite, and their interfaces, Canadian Geotechnical Journal 53(1): 60-71.
Liu, J.F., Davy, C.A., Talandier, J., and Skoczylas, F. 2014a. Effect of gas pressure on the sealing efficiency of compacted bentonite-sand plugs, Journal of Contaminant Hydrology 170: 10-27.
Liu, J.F., Skoczylas, F., and Liu, J. 2014b. Experimental research on water retention and gas permeability of compacted bentonite/sand mixtures, Soils and Foundations 54(5): 1027-1038.
Lu, N., Godt, J.W., and Wu, D.T. 2010. A closed-form equation for effective stress in unsaturated soil, Water Resources Research 46.
Madaschi, A., and Laloui, L. 2018. A stochastic approach to the modelling of gas transport in bentonite. In 7th International Conference on Unsaturated Soils, Hong Kong, China.
Mahjoub, M., Rouabhi, A., Tijani, M., Granet, S., M'jahad, S., and Talandier, J. 2017. Numerical study of Callovo-Oxfordian argillite expansion due to gas injection, International Journal of Geomechanics 18(1): 04017134.
Marschall, P., Horseman, S., and Gimmi, T. 2005. Characterisation of gas transport properties of the Opalinus Clay, a potential host rock formation for radioactive waste disposal, Oil & gas science and technology 60(1): 121-139.
Martinez, M.J., Newell, P., Bishop, J.E., and Turner, D.Z. 2013. Coupled multiphase flow and

geomechanics model for analysis of joint reactivation during CO2 sequestration operations, International Journal of Greenhouse Gas Control 17: 148-160.

Mauthe, S., and Miehe, C. 2017. Hydraulic fracture in poro-hydro-elastic media, Mechanics Research Communications 80: 69-83.

Miller, W., Alexander, R., Chapman, N., McKinley, J.C., and Smellie, J. 2000. Geological disposal of radioactive wastes and natural analogues. Elsevier.

Mohammadnejad, T., and Khoei, A. 2013. Hydro-mechanical modeling of cohesive crack propagation in multiphase porous media using the extended finite element method, International Journal for Numerical and Analytical Methods in Geomechanics 37(10): 1247-1279.

Montellà, E.P., Yuan, C., Chareyre, B., and Gens, A. 2019. A hybrid multiphase model based on lattice Boltzmann method direct simulations, arXiv preprint arXiv:1906.04722.

Mualem, Y. 1976. A New Model for Predictingthe Hydraulic Conductivity of Unsaturated Porous Media, Water Resources Research 12(3).

Mualem, Y. 1978. Hydraulic conductivity of unsaturated porous media: generalized macroscopic approach, Water Resources Research 14(2): 325-334.

Nagra. 2008. Effects of post-disposal gas generation in a repository for low- and intermediate-level waste sited in the Opalinus Clay of Northern Switzerland. National Cooperative for the Disposal of Radioactive Waste.

Nash, P., Swift, B., Goodfield, M., and Rodwell, W. 1998. Modelling gas migration in compacted bentonite, Posiva Report: 98-08.

Nasir, O., Fall, M., Nguyen, S.T., and Evgin, E. 2011. Modelling of the hydro-mechanical response of sedimentary rocks of southern Ontario to past glaciations, Engineering Geology 123(4): 271-287.

Nasir, O., Fall, M., Nguyen, S.T., and Evgin, E. 2013. Modeling of the thermo-hydro-mechanical–chemical response of sedimentary rocks to past glaciations, International Journal of Rock Mechanics and Mining Sciences 64: 160-174.

Nasir, O., Fall, M., Nguyen, T.S., and Evgin, E. 2015. Modeling of the thermohydromechanical–chemical response of Ontario sedimentary rocks to future glaciations, Canadian Geotechnical Journal 52(7): 836-850.

Navarro, V., Yustres, Á., Asensio, L., la Morena, G.D., González-Arteaga, J., Laurila, T., and Pintado, X. 2017. Modelling of compacted bentonite swelling accounting for salinity effects, Engineering Geology 223: 48-58.

Nguyen, T., and Le, A. 2014. Simultaneous gas and water flow in a damage-susceptible bedded argillaceous rock, Canadian Geotechnical Journal 52(1): 18-32.

Nguyen, V.P., Lian, H., Rabczuk, T., and Bordas, S. 2017. Modelling hydraulic fractures in porous media using flow cohesive interface elements, Engineering Geology 225(Supplement C): 68-82.

Nuth, M., and Laloui, L. 2008. Effective stress concept in unsaturated soils: Clarification and validation of a unified framework, International Journal for Numerical and Analytical Methods in Geomechanics 32(7): 771-801.

Olivella, S., and Alonso, E.E. 2008. Gas flow through clay barriers, Géotechnique 58(3): 157-

176.
P. Damians, I., Olivella, S., and Gens, A. 2019. Modelling a gas flow experiment in Mx80 bentonite. In Proceedings of the XVII ECSMGE-2019, Reykjavík, Iceland.
Papanastasiou, P., and Sarris, E. 2017. 6 - Cohesive zone models. In Porous Rock Fracture Mechanics. Woodhead Publishing. pp. 119-144.
Pazdniakou, A., and Dymitrowska, M. 2018. Migration of gas in water saturated clays by coupled hydraulic-mechanical model, Geofluids 2018.
Popp, T., Rölke, C., and Salzer, K. 2013. Role of Interfaces in Bentonite-Block Assemblies as Favoured Pathways for Gas Transport. In Gas Generation and Migration International Symposium and Workshop 5th to 7th February 2013 Luxembourg. p. 19.
Puig Damians, I., Olivella Pastallé, S., and Gens Solé, A. 2019. Modelling gas flow experiments in Mx80 bentonite: analysis of preferential gas paths. In Workshop of CODE_BRIGHT Users: 16th May 2019, Barcelona, Spain. International Centre for Numerical Methods in Engineering (CIMNE). pp. 1-5.
Pusch, R., and Forsberg, T. 1983. Gas migration through bentonite clay. Svensk Kaernbraenslefoersoerjning AB.
Pusch, R., and Hökmark, H. 1990. Basic model of water-and gas-flow through smectite clay buffers, Engineering Geology 28(3-4): 379-389.
Pusch, R., Ranhagen, L., Nilsson, K., and Geological, S. 1985. Gas migration through Mx-80 bentonite. Final report. NAGRA Technical Report 85-36.
Qi, S., and Vanapalli, S.K. 2018. Simulating hydraulic and mechanical responses of unsaturated expansive soil slope to rainfall: Case Study, International Journal of Geomechanics 18(6): 05018002.
Rodwell, W.R., Harris, A.W., Horseman, S.T., Lalieux, P., Muller, W., Amaya, L.O., and Pruess, K. 1999. Gas Migration and Twophase Flow through Engineered and Geological Barriers for a Deep Repository for Radioactive Waste. Nuclear Energy Agency.
Romão, E., Campos, M., and Moura, L. 2011. Application of the Galerkin and Least-Squares Finite Element Methods in the solution of 3D Poisson and Helmholtz equations, Computers & Mathematics with Applications 62(11): 4288-4299.
Rutqvist, J., Kim, K., Xu, H., Guglielmi, Y., and Birkholzer, J. 2018. Investigation of coupled processes in Argillite Rock: FY18 Progress. Lawrence Berkeley National Lab.(LBNL), Berkeley, CA (United States).
Rutqvist, J., Kim, K., Xu, H., Guglielmi, Y., and Birkholzer, J. 2020. Investigation of Coupled Processes in Argillite Rock: FY20 Progress. Lawrence Berkeley National Lab.(LBNL), Berkeley, CA (United States).
Rutqvist, J., and Tsang, C.F. 2002. A study of caprock hydromechanical changes associated with CO2-injection into a brine formation, Environmental Geology 42(2-3): 296-305.
Salimzadeh, S., and Khalili, N. 2015a. Three-dimensional numerical model for double-porosity media with two miscible fluids including geomechanical response, International Journal of Geomechanics 16(3): 04015065.
Salimzadeh, S., and Khalili, N. 2015b. A three-phase XFEM model for hydraulic fracturing with cohesive crack propagation, Computers and Geotechnics 69: 82-92.

Sánchez, M., Gens, A., Villar, M.V., and Olivella, S. 2016. Fully Coupled Thermo-Hydro-Mechanical Double-Porosity Formulation for Unsaturated Soils, International Journal of Geomechanics: D4016015.

Santillán, D., Mosquera, J.-C., and Cueto-Felgueroso, L. 2017. Fluid-driven fracture propagation in heterogeneous media: Probability distributions of fracture trajectories, Physical Review E 96(5): 053002.

Sedighi, M., Thomas, H.R., Al Masum, S., Vardon, P.J., Nicholson, D., and Chen, Q. 2015. Geochemical modelling of hydrogen gas migration in an unsaturated bentonite buffer, Geological Society, London, Special Publications 415(1): 189-201.

Seiphoori, A., Ferrari, A., and Laloui, L. 2014. Water retention behaviour and microstructural evolution of MX-80 bentonite during wetting and drying cycles, Géotechnique 64(9): 721-734.

Senger, R., Romero, E., Ferrari, A., and Marschall, P. 2014. Characterization of gas flow through low-permeability claystone: laboratory experiments and two-phase flow analyses, Geological Society, London, Special Publications 400(1): 531-543.

Shehata, A., Fall, M., Detellier, C., and Alzamel, M. 2020. Effect of groundwater chemistry and temperature on swelling and microstructural properties of sand–bentonite for barriers of radioactive waste repositories, Bulletin of Engineering Geology and the Environment.

Swift, B., Hoch, A., and Rodwell, W. 2001. Modelling gas migration in compacted bentonite: GAMBIT Club Phase 2–Final report, Posiva Report 2.

Tamayo-Mas, E., Harrington, J., Shao, H., Dagher, E., Lee, J., Kim, K., Rutqvist, J., Lai, S.-H., Chittenden, N., and Wang, Y. 2018. Numerical modelling of gas flow in a compact clay barrier for DECOVALEX-2019. In 2nd International Discrete Fracture Network Engineering Conference. American Rock Mechanics Association.

Tanai, K., Kanno, T., and Galle, C. 1997. Experimental study of gas permeabilities and breakthrough pressures in clays, Scientific Basis for Nuclear Waste Management Xx 465: 995-1002.

Tanaka, Y., Hironaga, M., and Kudo, K. 2010. Gas migration mechanism of saturated highly-compacted bentonite and its modeling. In ASME 2010 13th International Conference on Environmental Remediation and Radioactive Waste Management. American Society of Mechanical Engineers. pp. 7-16.

Tang, C., Tham, L., Lee, P., Yang, T., and Li, L. 2002. Coupled analysis of flow, stress and damage (FSD) in rock failure, International Journal of Rock Mechanics and Mining Sciences 39(4): 477-489.

Tawara, Y., Hazart, A., Mori, K., Tada, K., Shimura, T., Sato, S., Yamamoto, S., Asano, H., and Namiki, K. 2014. Extended two-phase flow model with mechanical capability to simulate gas migration in bentonite, Clays in Natural and Engineered Barriers for Radioactive Waste Confinement 400: 545-562.

Terzaghi, K. 1951. Theoretical soil mechanics. Chapman And Hall, Limited.; London.

van Genuchten, M.T. 1980. A closed-form equation for predicting the hydraulic conductivity of unsaturated soils, Soil Science Society of America Journal 44(5): 892-898.

Villar, M. 2005. MX-80 bentonite. Thermo-hydro-mechanical characterisation performed at CIEMAT in the context of the Prototype Project, Informes Técnicos CIEMAT 1053: 39.

Villar, M.V., Gutierrez-Rodrigo, V., Martín, P.L., Romero, F.J., and Barcala, J.M. 2014a. Gas transport in bentonite. 1135-9420.

Villar, M.V., Martin, P.L., and Romero, F.J. 2014b. Gas transport properties of compacted bentonite, Unsaturated Soils: Research & Applications, Vols 1 and 2: 1735-1740.

Vo, T.D., Pouya, A., Hemmati, S., and Tang, A.M. 2017. Numerical modelling of desiccation cracking of clayey soil using a cohesive fracture method, Computers and Geotechnics 85: 15-27.

Wang, M., Feng, Y.T., Wang, Y., Qu, T.M., and He, W. 2020. A hybrid discrete bubble-lattice Boltzmann–discrete element model for gas-charged sediments, Computational Particle Mechanics 7(3): 509-522.

Weiss, J.-P. 2019. Automatic time step and order selection in time-dependent problems. Available from https://www.comsol.com/blogs/automatic-time-step-and-order-selection-in-time-dependent-problems/.

White, J.A., and Borja, R.I. 2008. Stabilized low-order finite elements for coupled solid-deformation/fluid-diffusion and their application to fault zone transients, Computer Methods in Applied Mechanics and Engineering 197(49-50): 4353-4366.

Wiseall, A., Cuss, R., Graham, C., and Harrington, J. 2015. The visualization of flow paths in experimental studies of clay-rich materials, Mineralogical Magazine 79(6): 1335-1342.

Xu, L., Ye, W.-M., and Ye, B. 2017. Gas breakthrough in saturated compacted GMZ bentonite under rigid boundary conditions, Canadian Geotechnical Journal 54(8): 1139-1149.

Xu, L., Ye, W., Chen, Y., Chen, B., and Cui, Y. 2018. A new approach for determination of gas breakthrough in saturated materials with low permeability, Engineering Geology 241: 121-131.

Xu, L., Ye, W.M., Ye, B., Chen, B., Chen, Y.G., and Cui, Y.J. 2015. Investigation on gas migration in saturated materials with low permeability, Engineering Geology 197: 94-102.

Xu, W.J., Shao, H., Hesser, J., Wang, W., Schuster, K., and Kolditz, O. 2013. Coupled multiphase flow and elasto-plastic modelling of in-situ gas injection experiments in saturated claystone (Mont Terri Rock Laboratory), Engineering Geology 157: 55-68.

Yamamoto, S., Kumagai, M., Koga, K., and Sato, S. 2015. Mechanical stability of engineered barriers in a subsurface disposal facility during gas migration based on coupled hydromechanical modelling, Geological Society, London, Special Publications 415(1): 213-224.

Yang, J., Fall, M., and Guo, G. 2020. A three-dimensional hydro-mechanical model for simulation of dilatancy controlled gas flow in anisotropic claystone, Rock Mechanics and Rock Engineering 53(9): 4091-4116.

Ye, W.M., Chen, Y.G., Chen, B., Wang, Q.O., and Wang, J. 2010. Advances on the knowledge of the buffer/backfill properties of heavily-compacted GMZ bentonite, Engineering Geology 116(1-2): 12-20.

Ye, W.M., Xu, L., Chen, B., Chen, Y.G., Ye, B., and Cui, Y.J. 2014. An approach based on two-

phase flow phenomenon for modeling gas migration in saturated compacted bentonite, Engineering Geology 169: 124-132.

Yin, P., and Vanapalli, S.K. 2018. Model for predicting tensile strength of unsaturated cohesionless soils, Canadian Geotechnical Journal 55(9): 1313-1333.

Yu, L., and Weetjens, E. 2009. Summary of gas generation and migration. Belgian Nuclear Research Centre.

Zhu, C.-M., Ye, W.-M., Chen, Y.-G., Chen, B., and Cui, Y.-J. 2013. Influence of salt solutions on the swelling pressure and hydraulic conductivity of compacted GMZ01 bentonite, Engineering Geology 166: 74-80.

Zienkiewicz, O.C., Taylor, R.L., and Zhu, J. 2013. The finite element method: its basis and fundamentals, The Finite Element Method: its Basis and Fundamentals (Seventh Edition), seventh edition ed., Butterworth-Heinemann, Oxford.